

Thermoelectric Effects in Nanoscale Devices

Inauguraldissertation

zur
Erlangung der Würde eines Doktors der Philosophie
vorgelegt der
Philosophisch-Naturwissenschaftlichen Fakultät
der Universität Basel

von

Oliver Braun

Basel, 2022

Genehmigt von der Philosophisch-Naturwissenschaftlichen Fakultät
auf Antrag von
Prof. Dr. Michel Calame
Prof. Dr. Ilaria Zardo
Prof. Dr. Pascal Gehring

Basel, den 22. Juni 2021

Prof. Dr. Marcel Mayor
Dekan

Contents

1	Introduction	1
1.1	Outline	3
2	Theoretical background and introduction to the fields covered in this thesis	5
2.1	Introduction	5
2.2	Charge transport in graphene	5
2.3	Graphene nanoribbons and their electronic properties	7
2.3.1	Transport in quantum dots	8
2.3.2	Why bottom-up synthesized GNRs	10
2.4	Thermoelectricity	10
2.4.1	Seebeck effect	10
2.4.2	Peltier effect	11
2.4.3	Thomson effect	11
2.5	Thermal conductivity	12
2.6	Thermoelectric figure of merit zT	13
3	Materials and methods	17
3.1	Basics of Raman spectroscopy	18
3.1.1	General concept of the Raman effect	18
3.1.2	Instrumentation for Raman spectroscopy at the Transport at Nanoscale Interfaces Laboratory	19
3.2	Probe stations and cryostats	19
3.2.1	Electronics	19
3.2.2	Lake Shore probe station	20
3.2.3	Heliox cryostat	20
3.2.4	Automated vacuum prober	20
3.3	CVD-graphene	20
3.3.1	Graphene growth and transfer	21
3.3.2	Quality assessment	21
3.4	Electrical breakdown procedure for graphene nanogap formation	23
3.4.1	Procedure and challenges	23
3.4.2	Application to molecular electronics	25
3.5	Graphene nanoribbons (GNRs)	26
3.5.1	Overview of graphene nanoribbons	26
3.5.2	Growth substrates and GNR transfer	26
3.5.3	9-AGNRs	28
3.5.4	5-AGNRs	30
3.5.5	5-AGNRs (with kinks)	31
3.5.6	17-AGNRs	32

3.5.7	Pyrene-GNRs	33
3.6	Optimized substrates and measurement approaches for Raman spectroscopy of graphene nanoribbons	34
3.7	Methods used for determining the thermal conductivity of graphene	36
3.7.1	Preparation of the SiN membrane	36
3.7.2	Synthesis and transfer of graphene	36
3.7.3	Raman setup and spectra analysis	36
3.7.4	Temperature calibration	37
3.7.5	He-ion irradiation	37
4	Optimized graphene electrodes for contacting graphene nanoribbons	39
4.1	Introduction	41
4.2	Graphene electrodes and electronics	42
4.2.1	Graphene patterning	42
4.2.2	Graphene electrode separation	43
4.2.3	Graphene quality after patterning	43
4.2.4	Electronic measurements	43
4.3	Results and discussion	43
4.3.1	Graphene electrodes	43
4.3.2	Characterization of patterned graphene electrodes	45
4.3.3	Electrical characterization and effect of annealing	46
4.4	Conclusions	49
	Appendix 4.A. SEM image of device fabricated with PMMA mask	50
	Appendix 4.B. Raman characterization of transferred 9-AGNRs	51
	Appendix 4.C. Extended gate voltage dependence data	52
5	Electrical transport properties of GNRs	53
5.1	Introduction	55
5.2	Transport measurements on wide band gap GNRs	56
5.2.1	Transport properties of 9-AGNR films	56
5.2.2	Low-temperature measurements of 9-AGNRs with electrodes separated by <15nm	61
5.3	Transport measurements in low band gap GNRs	62
5.3.1	Kinked 5-AGNRs	63
5.3.2	5-AGNRs	64
5.3.3	17-AGNRs	66
5.4	Transport measurements in GNRs near a topological phase boundary	68
5.4.1	Pyrene-GNRs	68
5.5	Conclusion and outlook	71
	Appendix 5.A. 17-AGNRs: Annealing effects	73
	Appendix 5.B. pyrene-GNRs: Additional data	74
5.B.1.	kink defects in pyrene-GNRs	74
5.B.2.	Additional transport measurements on pyrene-GNR devices	75
6	Multi-gate quantum dots from 9-atom-wide armchair graphene nanoribbons	77
6.1	Introduction	79

6.2	Device design and fabrication	79
6.3	Quantum dot formation at low temperature	81
6.3.1	Characterization of the QDs with zero applied side gate voltage	81
6.3.2	Gating efficiency	83
6.3.3	Tunable QD energies using side gates	84
6.3.4	Single QD formation for strongly gated electrodes	85
6.4	Conclusion and outlook	86
	Appendix 6.A. Device fabrication and electrostatic potential	87
	6.A.1 Device fabrication and precharacterization	87
	6.A.2 FEM-calculations of the electrostatic potential	89
	Appendix 6.B. On-surface and post-transfer characterization of 9-AGNRs	90
	Appendix 6.C. Device 1: Additional data	91
	6.C.1. Temperature dependent transport characteristics	91
	6.C.2. Extended data to separately gated electrodes	92
	6.C.3. Current and dI/dV -maps with individually gated electrodes	93
	Appendix 6.D. Devices 1-4: Overview of transport characteristics	94
7	Edge contacts to graphene nanoribbons	95
7.1	Introduction	96
7.2	Challenges in the device fabrication and proposed solutions	97
7.2.1	Dry transfer of 9-AGNRs	97
7.2.2	Wet transfer and encapsulation of 9-AGNRs	98
7.3	Transport results of edge-contacted 9-AGNRs using a silicon gate	100
7.3.1	Interpretation of the temperature-dependent transport data	101
7.4	Transport results of edge-contacted 9-AGNRs using a graphite gate	103
7.5	Conclusion and outlook	104
8	Seebeck coefficient of nanoscale devices	107
8.1	Introduction and motivation	109
8.2	Seebeck coefficient determined using DC-method: Au-nanoparticles	110
8.3	Motivation for vertical thermometer/heater structures	113
8.4	Seebeck coefficient determined using an AC-method	115
8.4.1	Theoretical and experimental considerations	117
8.4.2	Calibration: thermometer vs. heater current	120
8.4.3	Calibration: thermometer vs. cryostat temperature	121
8.5	Thermoelectrical characterization of graphene films	122
8.6	Thermoelectrical characterization of GNR films	124
8.6.1	Conductance and thermocurrent measurements	124
8.6.2	Seebeck coefficient and power factor of GNRs	126
8.6.3	Seebeck coefficient at various heater currents	127
8.7	Conclusion and outlook	129
	Appendix 8.A. Frequency dependence of the thermocurrent	130
	Appendix 8.B. Probe current for resistance thermometers	131
	Appendix 8.C. Thermometer response	132
	Appendix 8.D. Thermocurrents at various heater currents	133

9	Spatially mapping thermal transport in graphene by an opto-thermal method	135
9.1	Introduction	137
9.2	Experimental temperature maps	139
9.3	FEM calculations	140
9.4	Thermal conductivity map based on fitted experimental temperature map	141
9.5	Thermal conductivity of defect-engineered graphene	142
9.6	Unsupervised classification of Raman spectrum in maps of defect engineered graphene	144
9.7	Discussion	146
9.8	Conclusion and outlook	147
	Appendix 9.A. Raman spectra of pristine and defect engineered graphene . .	148
	Appendix 9.B. Laser power and absorption	149
	Appendix 9.C. Laser spot size, beam profile and FEM parameters	150
	Appendix 9.D. Validation of method	151
10	Conclusion & outlook	153
10.1	Results and conclusions	153
10.2	Outlook	154
	Bibliography	157
	Acknowledgments	181
	About the Author	183
	Publications	185

1 Introduction

In 2016, 80% of the produced energy came from fossil fuels, while the remaining 20% was generated from biofuels, nuclear power plants, and renewable sources (e.g. water, wind, and sun). More than 4/5 of this energy is used for transportation and heating purposes, of which less than 1/5 is in the form of electricity.^{1,2} Electrical energy, on top of powering electronic devices, can conveniently be converted to other forms of energy and is therefore seen as the most valuable form of energy.

Electricity is commonly generated using heat engines (e.g. steam turbines) that convert temperature differences – generated by burning coal, oil, gas, etc. - to electricity. The efficiency of this conversion is thermodynamically limited by the Carnot efficiency $\eta = 1 - T_C/T_H$, where T_C and T_H are the absolute temperatures of the cold and hot reservoirs, respectively.³ In practice, Carnot efficiency is never reached and part of the generated heat has no further application and is wasted.

In 1822, Thomas Johann Seebeck laid the foundation for a possible use of this waste heat by discovering the thermoelectric effect.⁴ Ever since its discovery, physicists have wanted to make use of this Seebeck effect to generate electricity directly from a temperature gradient.

The maximum efficiency η_{\max} of this process for a thermoelectric device is defined as follows:⁵

$$\eta_{\max} = \frac{T_H - T_C}{T_H} \frac{\sqrt{1 + ZT}}{\sqrt{1 + ZT} + \frac{T_C}{T_H}} \quad (1.1)$$

Where ZT is the thermoelectric figure of merit of the device at the averaged device temperature $T = (T_H - T_C)/2$. We want to make here the distinction between ZT and zT , where the device thermoelectric figure of merit is written with an upper case Z and always defined at a given temperature T , while the material thermoelectric figure of merit is written with a lower case z and is temperature dependent.

The thermoelectric figure of merit zT of a material for small temperature gradients can be written as:⁵

$$zT = \frac{\sigma S^2}{\kappa} T \quad (1.2)$$

consisting of the Seebeck coefficient S and the electrical and thermal conductivities, σ and κ .

Great efforts have been undertaken to find materials and material combinations with a high zT . Lead telluride (PbTe) and germanium telluride/silver antimony telluride (TAGS), for example, have this property. These material combinations are the core materials of the thermocouples used in the thermoelectric generators powering NASA's Mars 2020 rover, Perseverance.⁶ Besides this extraordinary application in space engineering

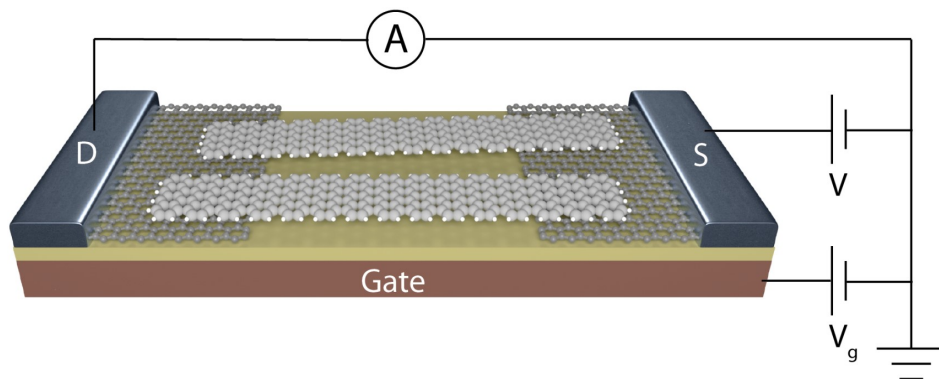


Figure 1.1 Schematic illustration of a graphene nanoribbons field-effect transistor. The 9 atom wide graphene nanoribbons (light gray) are contacted using single-layer graphene electrodes (dark gray) that are in contact with the measurement instruments via source (S) and drain (D) metal leads (silverish). Illustration by M.L. Perrin.

and less well-known ones in niche markets, there are limited use cases of thermoelectric materials due to the low conversion efficiencies.⁷

Almost three decades ago, it was proposed that the nanostructuring of materials could lead to an enhancement of the thermoelectric efficiency due to quantization effects.^{8,9} Graphene nanoribbons (GNRs), narrow strips of graphene, are good candidates to exhibit a high thermoelectric efficiency. For example, if their structure is sufficiently controlled, a band gap can be opened due to lateral confinement and phononic heat transport could be suppressed by boundary scattering, leading to an independent tuning of the electrical and thermal conductivity. Researchers have tried in the past to push the limits of top-down lithography to form graphene nanoribbons by etching processes, leading to signs of band gap opening.^{10,11}

An alternative approach to open a band gap in carbon-based nanostructures is to synthesize atomically precise GNRs by a synthesis process starting from molecular precursors. Such GNRs have attracted considerable interest as future electronic building blocks, due to their highly tunable width and edge structure.¹²

Bottom-up synthesized GNRs are *Designer Quantum Materials*, materials in which the properties can be designed and adjusted on demand. GNRs offer a variety of properties: tunable band gap,¹³ in-situ *pn*-junction formation,¹⁴ quantum dot behavior¹⁵ and even exhibit topologically non-trivial phases.^{16–19}

This shows that graphene nanoribbons are a versatile platform for novel electronic devices. However, many challenges remain in the device integration of these materials, especially regarding contacting and gating strategies. These two challenges directly enter the zT via the electrical conductivity. In this thesis, we mostly use graphene electrodes to explore the transport properties of these nanoobjects and show two possibilities how to improve the contacts to GNRs. In Figure 1.1 an artistic illustration of a typical field-effect transistor (FET) device is shown. Since GNRs are a novel material system, their characterization outside of the ultra-high vacuum conditions is in an early stage.

This thesis covers various aspects of the GNR device integration for thermoelectric characterization. This involves the development of contacting and gating strategies

for assessing the electrical conductivity of GNRs. Further, the Seebeck coefficient of GNR based devices is determined using an advanced measurement platform and scheme. Finally, a novel Raman-based method is established to map thermal conductivity. Although the working principle of this method is demonstrated on defect-engineered graphene membranes, it is extendable to films of GNRs. The thesis concludes by giving a summary of the limitations in the field of GNR based nanoelectronics and presents an outlook on how they might be overcome.

1.1 Outline

The individual chapters are structured as follows:

Chapter 2 provides some basic concepts that are essential for the investigation of the thermoelectric effects in nanoscale devices and gives a general introduction to graphene nanoribbons and their properties. It explains theoretical aspects of charge transport, thermoelectricity, and thermal conductivity as well as the thermoelectric figure of merit.

A broad overview of the materials used in this work and their characterization methods is presented in **Chapter 3**. Graphene growth and transfer are described in detail and selected GNR types that differ in width and edge structure are explained. The properties of GNRs vary significantly for each type of ribbon. Optical and electrical methods to characterize graphene and GNRs are discussed. In particular, Raman spectroscopy and an electrical breakdown procedure for graphene nanogap formation are described.

Chapters 4, 5, 6, and 7 are devoted to the investigation of charge transport in GNRs. A particular difficulty in studying the electrical transport of GNRs is to ensure reliable contacts. A fabrication procedure of graphene electrodes via optimized electron-beam lithography and reactive ion etching is reported in **Chapter 4**. The fabrication is exemplified on uniaxially aligned and non-aligned 9-atom wide armchair graphene nanoribbons integrated into a FET geometry and their electrical properties are determined. The transport results obtained in **Chapter 4** are extended in **Chapter 5** for three different kinds of low band gap GNRs of the armchair family and GNRs with partial zigzag edges. Another challenge in the electrical characterization of GNRs is the limited electrostatic tunability using a single gate in FET devices, which is addressed in **Chapter 6**. A multi-gate FET geometry is presented and discussed there. A different approach to contact GNRs is introduced in **Chapter 7**. The famous edge contacting procedure²⁰ is applied to films of GNRs.

The quantification of the Seebeck effect in nanostructures contacted using graphene electrodes is studied in **Chapter 8**. The Seebeck coefficients of Au-nanoparticle arrays, graphene, and for the first time films of graphene nanoribbons are determined. Two different measurement schemes are employed.

Chapter 9 examines the spatially resolved thermal conductivity, the third part, besides the charge transport and the Seebeck effect, that contributes to the thermoelectric figure of merit. It presents a method for the spatially-resolved assessment of the thermal conductivity of suspended pristine and defect-engineered graphene.

Chapter 10 summarizes the presented results, draws the conclusion regarding the conducted research on thermoelectric effects in nanoscale devices, and gives an outlook for possible improvements, and how to continue the work pioneered in this thesis.

2 Theoretical background and introduction to the fields covered in this thesis

2.1 Introduction

The purpose of this chapter is to introduce the various concepts from a theoretical and/or idealized point of view. It covers charge transport in graphene and graphene nanoribbons as well as an introduction to thermoelectric effects and thermal conductivity. All of these concepts are relevant with respect to the thermoelectric figure of merit, introduced at the end of this chapter.

2.2 Charge transport in graphene

Graphene consists of hexagonally arranged carbon atoms. In Figure 2.1a) an artistic illustration thereof is given. The crystallographic unit cell consists of two atoms. The distance between the two carbon atoms is 1.42 Å. In momentum space, the positions of the carbon atoms are denoted K and K'. The resulting lattice vectors have a length a of 2.46 Å. Carbon has four valence electrons. Three thereof are in planar sp^2 -orbitals and form with the electrons from the neighboring carbon atom σ -bonds. The fourth electron is delocalized in p_z -orbitals, extending above and below the carbon atom plane. Using these p_z -orbitals graphene can form π -bonds with other extended π -systems, a concept that is often referred to as π - π -stacking. In Figure 2.1a) the orbitals are depicted as transparent ellipsoids. These π -orbitals give rise to a band structure, which can be written in a simplified version as follows:²¹

$$E(k_x, k_y) = \pm t \left[1 + 4 \cos \left(\frac{\sqrt{3}k_x a}{2} \right) \cdot \cos \left(\frac{k_y a}{2} \right) + 4 \cos^2 \left(\frac{k_y a}{2} \right) \right]^{1/2} \quad (2.1)$$

In the low energy spectrum, this leads to a linear energy dispersion relation, cause for excitement among solid-state physicists since this is usually only seen for massless Dirac fermions in high-energy physics. In ideal graphene, the valence band is filled with electrons and the conduction band is filled with holes, with the two bands meeting at the Dirac point. In this situation, charge neutrality is achieved. Therefore this point is also referred to as charge neutrality point (CNP). Due to the continuity of the density of states, it is possible to shift these bands up and down with respect to the Fermi energy E_F . This can be achieved for example by applying an electrostatic field from a gate

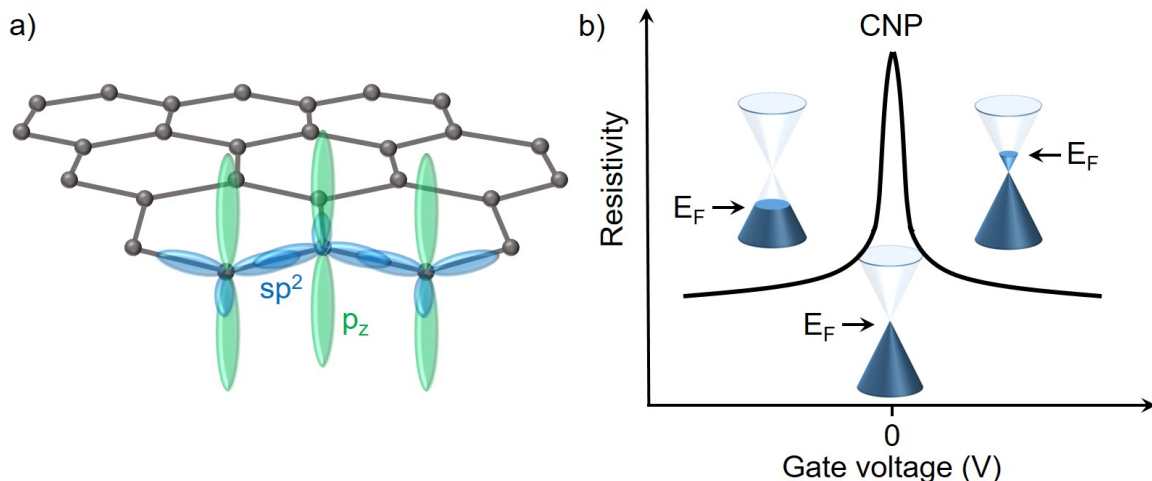


Figure 2.1 Electronic properties of graphene. a) Artistic drawing of the hexagonally arranged carbon atoms. The sp^2 -orbitals (blue) and p_z -orbitals (green) are illustrated for 3 carbon atoms. b) Resistivity of a graphene FET as a function of gate voltage. The small insets illustrate the low energy dispersion of graphene with the Fermi energy E_F .

electrode in a FET geometry, leading to a change in charge carrier majority type and charge carrier density. In Figure 2.1b) the measured resistivity of graphene in a FET geometry is shown as a function of gate voltage. The insets show how the bands are positioned with respect to the Fermi energy for different gate voltages.

Graphene, a material that is widely studied in the solid-state physics community since its isolation in 2004, has recently gained a new twist. By literally twisting two sheets of graphene (single- and multilayers have been investigated) on top of each other by a small angle, a Moiré lattice is formed. This leads to a distortion in the electronic band structure resulting in flat bands. If the twist angle is around 1.1° and the device quality sufficiently high, a superconducting state can emerge at low temperatures. This forms the foundation of a prospering field.

Within this thesis, we use graphene mostly as contact electrodes to the nano-objects. This due to the following advantages compared to metal electrodes:

- Graphene is a covalent crystal that is therefore stable up to temperatures much higher than room temperature.^{22,23}
- The charge carrier density in the graphene electrodes can be tuned.^{24,25}
- Graphene is atomically flat.
- The atomically thin graphene electrodes reduce the screening of an applied electrostatic field drastically, compared to bulky metal electrodes. This leads to an enhanced gate coupling.^{26,27}
- To form an electric contact to GNRs, one could use organic chemistry, to functionalize the edges of the graphene or/and via π - π -stacking of aromatic rings on top of graphene similar as it has been demonstrated for molecules.²⁸⁻³⁰

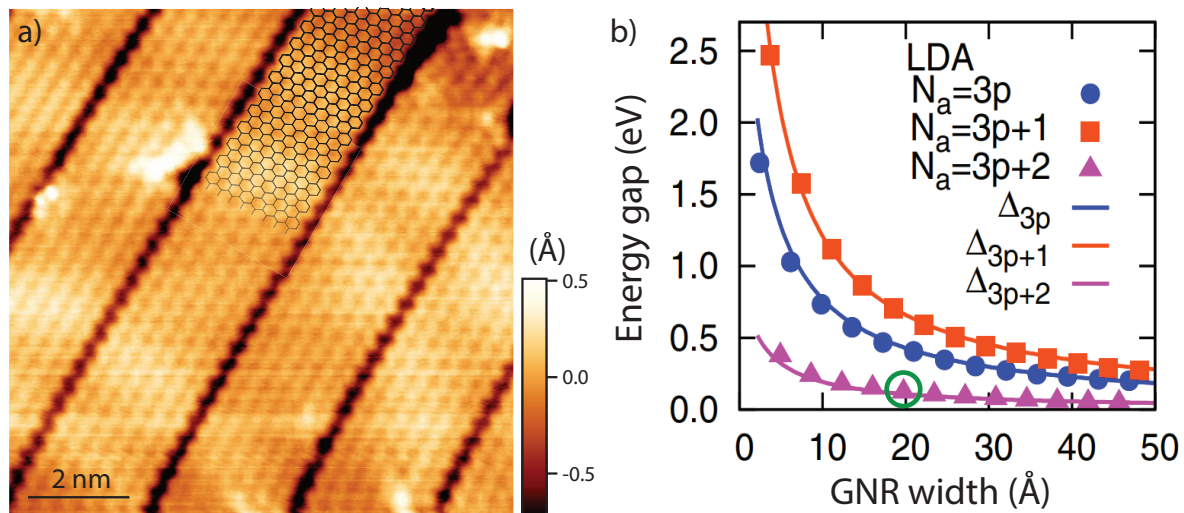


Figure 2.2 STM characterization of GNRs and their calculated electronic band gap. **a)** STM height profile of 17-AGNRs at room temperature ($V_b = -0.2$ V, I_t 30 pA). The chemical structure of the GNR is overlaid. Data provided by Gabriela Borin-Barin. **b)** Band gaps of armchair GNRs as a function of width obtained from first-principle calculations. The 17-AGNR is indicated with a green circle. Figure adapted from Son et al.³¹

In particular, the last point is favorable for the GNRs that are investigated in this thesis since they are also planar and a large number of π -orbitals will overlap at the contact area.

2.3 Graphene nanoribbons and their electronic properties

Graphene nanoribbons are narrow, long strips of graphene and in many theoretical works, they are also treated as such. By using periodic boundary conditions one reduces the computational cost but neglects the finite length that these GNRs usually have, typically varying between a few nanometers up to 50 nanometers. This means graphene nanoribbons are usually treated as one-dimensional objects and therefore possess a one-dimensional density of states. GNRs can have various edge and width structures. For straight GNRs there are the edge configurations *armchair* and *zigzag*. Tight-binding calculations show that a band gap can be opened in graphene nanoribbons with armchair edges due to quantum confinement in width, while GNRs with zigzag edges are always metallic.

Calculations using density functional theory showed that armchair GNRs always exhibit a band gap that varies vastly with their width.^{31,32} GNRs with armchair edges can be separated in 3 families, $3p$, $3p + 1$, $3p + 2$, with p being an integer. The band gap varies from family to family, where the smallest band gap is in the $3p + 2$ -family, medium-sized band gaps are in the $3p$ -family, and large band gaps in the $3p + 1$ -family. Within each family, the band gap scales inversely with the GNR width as shown in Figure 2.2b).³¹

Figure 2.2a) shows a high-resolution scanning tunneling microscope (STM) image

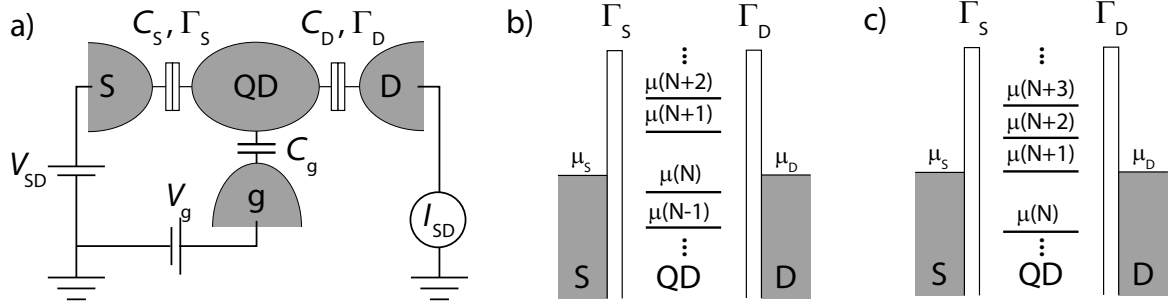


Figure 2.3 Quantum dot capacitor model and energy levels. **a)** Capacitor model of a quantum dot (QD) with source (S), drain (D) and gate (g) electrodes. The QD is coupled to S and D via tunnel barriers $\Gamma_{S,D}$, resulting in a capacitive coupling $C_{S,D}$. The source-drain current I_{SD} is measured for the bias voltage V_{SD} while the gate voltage V_g is varied. **b)** and **c)** Electrochemical potentials $\mu_{S,D}$ of the electrodes and the QD $\mu(N)$ in **b)** Coulomb blockade, **c)** a situation where under a very small V_{SD} current can flow. Figure adapted from^{36–38}.

of 17-atom wide armchair GNRs (17-AGNRs), recorded at room temperature. The chemical structure of a 17-AGNR is overlaid for clarification. From STM images like these and even more clearly in larger area scans as shown in Chapter 3, one can see that GNRs have a very high aspect ratio, serving as a validation of this 1D object picture from a geometrical point of view. This picture is a highly idealized one, as most of the currently available GNRs have a finite size. Hence, the GNRs have to be treated as very large molecules. However, in carbon nanotubes (CNTs), which have an even higher aspect ratio due to their micrometer lengths, quantum dot (QD) behavior has been observed.^{33–35} This shows that from an electronic point of view also geometrically long objects can act as 0D objects. In the following, we therefore briefly discuss the main concepts of a quantum dot.

2.3.1 Transport in quantum dots

Quantum dots exhibit discrete energy levels due to quantum confinement. Charge transport through a quantum dot occurs only if a very small bias voltage is applied between the source and drain leads and one of these discrete levels is aligned with the Fermi level of the leads. If the level of the QD is not aligned with the Fermi level of the leads no current flows. Using an external electrical field, the levels inside the QD can be shifted up or down with respect to the Fermi level of the leads. By recording the current as a function of gate voltage one can probe the spacing between the QD levels.

The QD levels are broadened by temperature. This means, even if the level is only close to the Fermi level of the leads, charge transport can occur. Therefore, such spectroscopy measurements are usually performed at low temperatures to accurately probe the level spacing.

A simplified picture of a capacitively coupled quantum dot with the applied voltages

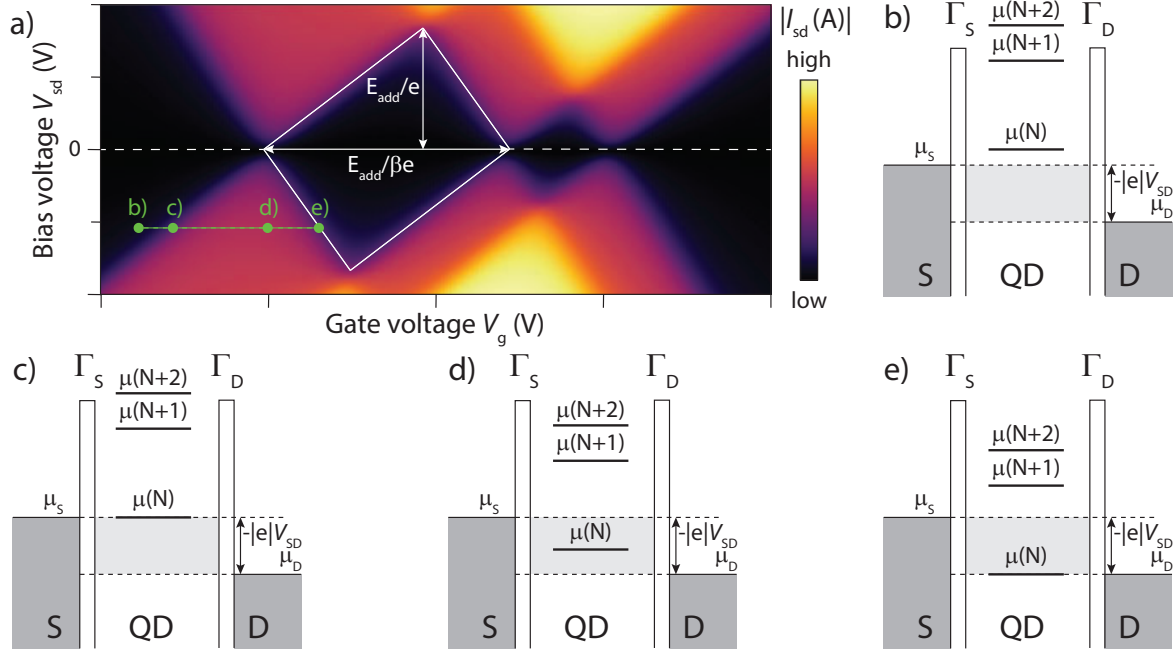


Figure 2.4 Charge transport in a QD under finite bias. **a)** Calculated charge stability diagram of a three level system, assuming asymmetric $\Gamma_{S,D}$. **b) to e)** Energy levels for various applied gate voltages V_g . The corresponding positions are indicated in panel a) in green.

is shown in Figure 2.3a). Figure 2.3b) and c) show the two situations that can occur, either no current can flow due to level misalignment (Coulomb blockade) or a current flows when the QD level is aligned with the source and drain potentials (under very small bias voltage).

An increased bias voltage V_{SD} between the source and drain contacts leads to an energy window (also called bias window) of size $eV_{SD} = \mu_S - \mu_D$, where e is the elementary charge. Now charge transport can occur not only if the QD level is aligned with the energy level of the leads but also when it is within the two levels, or within the bias window. If one monitors the current as a function of bias and gate voltage, one can form a charge stability diagram. A calculated charge stability diagram for a three-level system with different level spacing and asymmetric tunnel barriers is shown in Figure 2.4.

Stability diagrams are typically used to investigate the formation of quantum dots in quantum devices. In the black regions (Coulomb blockade regime), no current flows through the device, as neither the temperature nor the bias voltage provides the energy required for adding an extra electron onto the quantum dot. The edges of this diamond-shaped blocking region correspond to the onset of resonant transport. For bias voltages exceeding the resonance condition, single-electron tunneling (SET regime) occurs.

To investigate spin-dependent transport phenomena, these measurements would ideally also be performed in a magnetic field. For simplicity, we will not discuss the magnetic field dependence since no such measurements are shown in the remainder of this thesis.

2.3.2 Why bottom-up synthesized GNRs

A synthetic approach is probably the best way to generate materials in a controlled way that bridge the size gap in materials fabricated using top-down and bottom-up approaches. Hence, bottom-up synthesized GNRs combine the best properties of the two worlds, atomic precision leading to control over the mass fabricated quantum objects at contactable length scales.

By starting from molecular precursors, such GNRs benefit from the massive diversity of properties these molecules provide. Using molecules a variety of macroscopic phenomena have been realized, e.g. switching devices^{39,40}, diodes⁴¹ or even molecular motors⁴². Further, they are constrained in a planar geometry, which can enhance charge transport⁴³ and leads to a larger overlap with the electrodes improving mechanical stability. Bottom-up synthesized GNRs have lengths that can reach up to several dozens of nanometers, allowing them to be contacted with electrodes that are defined using well-established top-down methods. In chapter 4 this is demonstrated using graphene electrodes. As a potential drawback, one has to mention that carbon based materials with zigzag edges tend to be more reactive than their counterparts with armchair edges only.^{44–46} This can be limiting their processing under ambient conditions towards a device integration. In Chapter 7, a possible solution to this challenge is discussed. We also want to stress here, that most of the theoretical work on GNRs is done in gas phase, meaning that the GNRs are surrounded by vacuum. However, in a real-world experiment, the molecular orbitals of the GNRs can also hybridize with the orbitals of the electrodes, leading to an experimental probing of the complete device rather than the GNRs alone.^{47–49}

2.4 Thermoelectricity

This section describes the three thermoelectric effects. They are named after their discoverers the Seebeck, Peltier, and Thomson effect. Since they all have a temperature gradient as a prerequisite, they are also physically interlinked. This is also briefly discussed.

2.4.1 Seebeck effect

In a material, conductor or semiconductor, that is placed in a temperature gradient the energy distribution of its charge carriers will change.⁵⁰ On the hot side, there will be more charge carriers with higher energy than on the cold side, resulting in a diffusion of charge carriers from the hot to the cold side. This diffusion builds up a potential between the two sides that counteract the diffusion of more charge carriers. In the steady-state, Ohms law is modified by electromotive forces, resulting in a voltage difference without a current flow. The resulting potential difference ΔV is material dependent and given by the Seebeck coefficient S , sometimes referred to as thermopower:

$$\Delta V = -S\Delta T \tag{2.2}$$

with ΔT being the corresponding temperature difference between the hot and cold sides. This effect is called the Seebeck effect named after Thomas Johann Seebeck who

reported it in 1822,⁴ but already earlier hints at discoveries of thermoelectricity can be found in literature.⁵¹

The Seebeck effect is the working principle of a thermoelectric generator that can fulfill work using a temperature difference.

Besides this technological aspect, investigating and determining the Seebeck coefficient of a material is also of fundamental interest. From a theoretical point of view, the Seebeck coefficient can be seen as proportional to the derivative of the transmission function $\tau(E)$ through a material system. It can therefore be expressed as follows:⁵²

$$S = -\frac{\pi^2 k_B^2 T}{3e} \frac{\partial \ln \tau(E)}{\partial E} \Big|_{E=E_F} \quad (2.3)$$

where k_B is the Boltzmann constant and e the elementary charge. This means if the transmission function of a system contains sharp features, so-called resonances, they lead to a high Seebeck coefficient. Molecular systems and GNRs can exhibit such resonances. In general, the Seebeck coefficient is defined in a linear response regime, meaning for small ΔT . However, scientists also studied the Seebeck coefficient under very large temperature gradients of up to several hundreds of Kelvin.⁵³

2.4.2 Peltier effect

The Seebeck effect is thermodynamically reversible, hence one can generate a temperature difference if a current is passed through a material. This effect is then called the Peltier effect.⁵⁴ Since in a system where a current is flowing both effects are present, its detection is challenging. Therefore the Peltier effect was discovered 12 years later than the Seebeck, in 1834. The Peltier effect can be expressed analytically as follows:⁵⁴

$$\dot{Q} = (\Pi_A - \Pi_B)I \quad (2.4)$$

where \dot{Q} is the heat generated per time unit, $\Pi_{A,B}$ are the Peltier coefficients for material A, B respectively, and I is the current that flows. The Seebeck and Peltier effect are closely related as can be seen from the relation between their coefficients: $\Pi = TS$, where T is the temperature.

2.4.3 Thomson effect

The Thomson effect was discovered in 1857 and named after William Thomson, 1st Baron Kelvin.⁵⁵ It describes that if a material with a temperature-dependent Seebeck coefficient is placed in a temperature gradient, then the Peltier effect will take place at each infinitely small junction of the material where the Seebeck coefficient changes. Mathematically it can be expressed as follows:⁵⁵

$$\dot{q} = -\mathcal{K}\mathbf{J} \cdot \nabla T \quad (2.5)$$

where \dot{q} is the heat production rate per unit volume, \mathcal{K} the Thomson coefficient, \mathbf{J} the current density through the material, and ∇T the temperature gradient. Since the Thomson effect is closely related to the Seebeck effect, also its coefficients are related as

follows: $\mathcal{K} = T \cdot dS/dT$. In this equation effects like the thermal conductivity and Joule heating are neglected.

2.5 Thermal conductivity

Heat transfer has fascinated humans ever since. A fire can give warmth during a cold winter night, ice cream can be refreshing on a hot summer day or computers need advanced cooling techniques while performing calculations. The theoretical foundation for understanding and mastering heat conduction is Joseph Fourier's work *The Analytical theory of Heat* from 1822.⁵⁶ The most important theory is compressed in the following formula:

$$\vec{q} = -\kappa \nabla T \quad (2.6)$$

where q is the heat flow, κ is the thermal conductivity and T is the temperature. This equation states that the heat flows in the opposite direction of a temperature gradient and that the two are correlated linearly with the proportionality constant, called thermal conductivity κ .

Several methods have been developed to measure the thermal conductivity of a material of interest. The measurement techniques can be divided into three different classes. The first class consists of optical techniques using lasers, the second consists of scanning techniques with sharp heated or cooled tips and the third one consists of microchips with on-chip heaters and thermometers.

The class of optical techniques to determine the thermal conductivity mostly uses one laser as a heat source and simultaneously to probe the temperature.^{57,58} In some cases two lasers are used to do these tasks separately.⁵⁹ Using the Raman effect, the temperature changes can be related to a shift of the phonon frequency.^{60,61} By scanning the laser beam across a sample, a temperature profile can be extracted that is then used to model the thermal conductivity. To properly determine the thermal conductivity, the absorbed laser power has to be taken into account. This is not a trivial task, since the laser light can be scattered from the edges of the nanostructures or their supports. In the particular case of objects that are smaller than the laser spot, like nanowires, measurements of the optical absorption has only been achieved recently.⁶² This Raman-based method is sometimes referred to as the opto-thermal method. In Chapter 9 this method serves as the basis of a new method that allows to spatially map the thermal conductivity of a suspended graphene membrane.

Using scanning thermal microscopy (SThM) it is possible to map thermal properties with nanometer resolution.⁶³ SThM requires the use of specialized probes. The most common type are thermocouples, that probe the temperature at the thermocouple junction placed at the probe tip, followed by thin-film resistors at the probe tip. This method can be operated in two different configurations. Either scanning the heated tip over a sample and monitoring the heat flow from the tip to the substrate or using the tip as a thermometer while scanning over the substrate with local temperature variations. In general, the sensitivity is higher if the system is operated such that the tip only acts as a thermometer. In both cases the thermal contact to the substrate is essential, allowing only for slow scan speeds with limited mechanical vibrations and

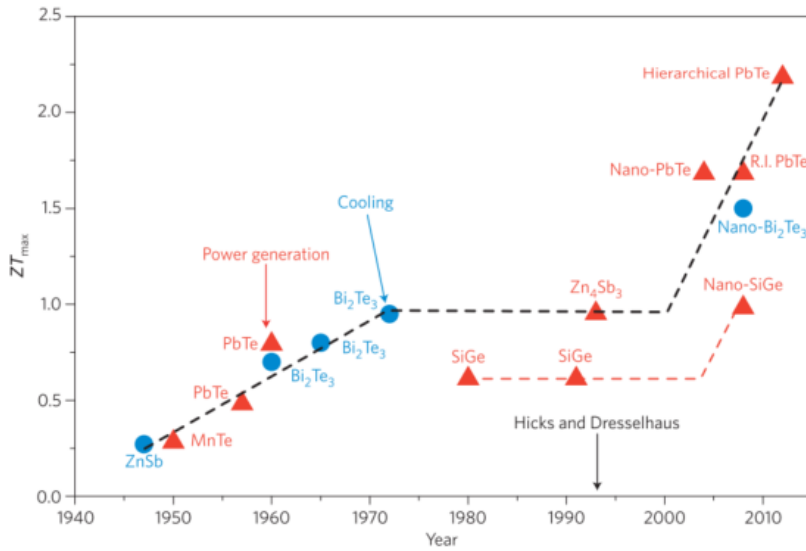


Figure 2.5 Evolution of the maximum zT over time. Materials for thermoelectric cooling are shown as blue dots and for thermoelectric power generation as red triangles. The black dashed line guides the eye. Figure taken from Heremans et al.⁷⁴

thus requires a complex setup to properly measure. This technique was used to observe quantized thermal conductance in single-atom junctions,⁶⁴ thermal conductance of single-molecule junctions,⁶⁵ measure the thermal conductivity of single molecules⁶⁵ and determine temperature profiles on a vast variety of nanoscale systems.^{66–69}

The third class consists of solid-state devices where thin-film wires on a silicon-based chip generate a thermal gradient. This can be either on a bulk chip or on suspended membranes. In both cases, either a DC or AC current is passed through the heater leading to a temperature increase. In some cases the heater also serves as a thermometer, in others separate thermometers are placed nearby. If the nanostructure is electrically conducting and reliable electrical contacts can be made to it, the well established 3ω method can be used to measure the thermal conductivity.^{70–73}

The working principle of this method is that an AC current at frequency ω is passed through the nanostructure, leading to a self-heating effect. The temperature and consequently the resistance of the nanostructure will change at frequency 2ω since Joule heating scales with the square of the current according to $P = RI^2$. The current at frequency ω combined with the resistance change at 2ω results in a voltage modulation at 3ω . This can be used to determine the temperature change of the nanostructure as a function of heating power, and thus can be correlated to its thermal conductivity.

2.6 Thermoelectric figure of merit zT

To quantify how well a material can be used as a building block in a thermoelectric generator, a thermoelectric figure of merit has been defined as follows:^{5,75–77}

$$zT = \frac{\sigma S^2}{\kappa} T \quad (2.7)$$

where zT is the dimensionless figure of merit and σ the electrical conductivity. Optimizing zT is challenging since the parameters are interlinked. In semiconductors, the electrical conductivity can be increased by tuning the concentration of dopants, but this will in general reduce the magnitude of the Seebeck coefficient.⁷⁸ In metals, the electrical conductivity is directly coupled to the electronic part of the thermal conductivity as stated by the empirical Wiedemann-Franz law as follows:⁷⁹

$$\frac{\kappa}{\sigma} = LT \quad (2.8)$$

where L is the proportionality constant, known as the Lorenz number. This Lorenz number has an analytical expression $L = \pi^2/3 \cdot (k_B/e)^2$, where k_B is the Boltzmann constant and e the elementary charge. In 2020, a law applicable to molecular systems, similar to the Wiedemann-Franz law for metals was derived for molecular systems, where the charge carriers can transfer via hopping transport:⁸⁰

$$\frac{\kappa}{\sigma} = L_M \frac{\lambda}{k_B} \quad (2.9)$$

where λ is the reorganization energy for the electron transfer and L_M is the Lorenz number for molecules, given by $L_M = 1/2 \cdot (k_B/e)^2$.

Because the parameters in the figure of merit are dependent on each other, for several decades the maximum value of ZT had remained around 1, as can be seen in Figure 2.5.⁷⁴ Advances in the material sciences have led to improvements, but mostly involving toxic or very rare materials. Another pathway to improve the ZT was proposed by Hicks and Dresselhaus in 1993, where it was suggested that nanostructuring materials could be the key to improvements.^{8,9} This led to increased research activity in the field and also some improvements in ZT values. In a one-dimensional electronic conductor, the density of states has sharp peaks around the quantum levels of the conductor.⁸¹ In a zero-dimensional case, even sharper peaks are present. By now aligning the Fermi level of the conductor with these peaks in the density of states (DOS), a minor change in charge carrier distribution leads to a drastic increase or decrease in high-energy charge carriers. This would massively enhance the Seebeck coefficient. Experiments on nanowires have shown that an increase in the power factor is possible due to one-dimensional confinement.^{82,83}

Besides engineering the power factor, the thermal conductivity of nanostructures can be engineered. In Chapter 9 of this thesis, one example is given; there, the thermal conductivity of graphene is tuned using defect engineering. In general, heat can be transported via electrons and/or phonons. While in metals the majority of the heat is transferred via the electrons, in semiconductors the phonons conduct most of the heat. Recently, the existence of relaxons, quasi-particles of collective behavior of phonons has been proposed.⁸⁴⁻⁸⁶ Relaxons are supposed to be accountable for the majority of heat transfer in a hydrodynamic regime. Also from a more conservative standpoint, there is room to influence the thermal conductivity. Since $\kappa = \kappa_{\text{electrons}} + \kappa_{\text{phonons}}$, and the mean free path (MFP) of electrons in semiconductors is around one order of magnitude smaller than that of phonons (corresponding to approximately 10 nm for electrons and 100 nm for phonons)⁷⁸, thermal transport in nanostructures is dominated by the phononic contribution. If one now designs a nanomaterial system smaller than the

phonon-MFP but larger than the electron-MFP, the two contributions to the thermal conductivity can be influenced separately. Graphene nanoribbons, with an average length of a couple of dozens of nanometers, are in this dimension. It is therefore highly desirable to explore this type of nanomaterial in the context of thermoelectrics. This is addressed in Chapter 8.

A nanomaterial in between a hot and cold lead can also serve as an energy filter, leading to either a heat engine or a refrigerator, depending on the level alignment in the leads with respect to the Fermi level.⁸⁷

In this thesis all components of the thermoelectric figure of merit are discussed, although not all are based on the same material system. An outlook on thermoelectrics is given at the end of the thesis in Chapter 10.

3 Materials and methods

This chapter reports on the synthesis of the materials used in this thesis. Further, the characterization methods are explained, from optical to electrical methods. A strong focus is also laid on the GNR synthesis. Since the precursor molecule defines the exact shape of the GNR, it is of utmost importance to understand the synthesis process. For example, a change in the precursor molecule can still lead to the same GNR but has a drastic influence on the average length or allows for the formation of kinks every ~ 10 nm. These differences do not negatively influence the physical properties of the GNR backbone, however, when it comes to the device integration of GNRs, information like this can help understand the transport data.

Contributions:

O.B. and J.O. did graphene characterization, Raman spectroscopy measurements and developed the Raman optimized substrates. R. Fu. did graphene growth. G.B.B., N.B., and R.D. performed GNR synthesis. K.M. and A.N. synthesized the GNR precursor molecules. M.L.P. did Raman calculations. M.E.A. developed the EB-technique and performed transport measurements on molecular devices. M.C. was involved in discussion and supervised O.B., J.O., R.Fu., M.E.A. and M.L.P.

Parts of this chapter have been adapted from El Abbassi et al.³⁰, Overbeck⁸⁸, Overbeck et al.⁸⁹, El Abbassi et al.¹⁵, Sun et al.¹⁹ and Braun et al.⁹⁰.

3.1 Basics of Raman spectroscopy

3.1.1 General concept of the Raman effect

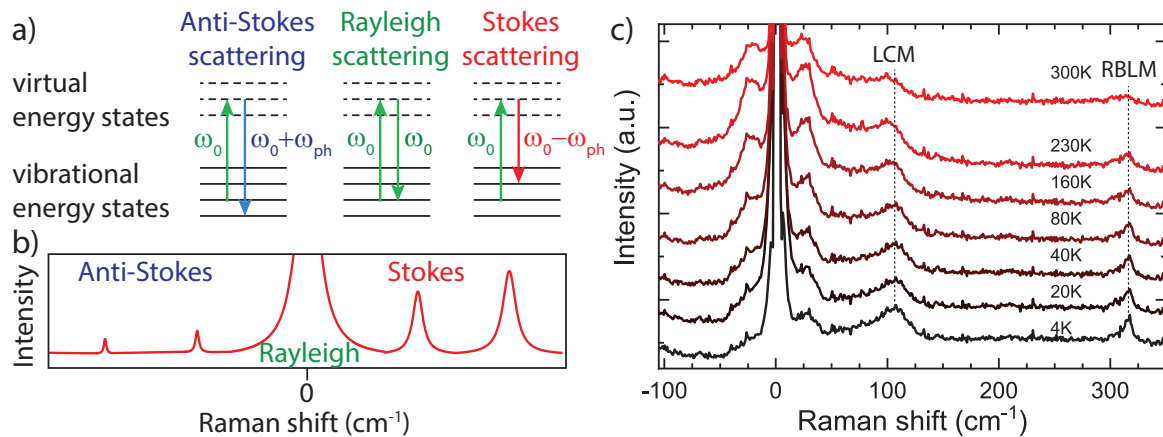


Figure 3.1 Raman spectroscopy: concept and application. a) Concept of the Raman effect, a two phonon effect. Anti-stokes, Stokes and Rayleigh scattering are depicted. b) Schematic Raman spectra showing the Anti-Stokes, Rayleigh, and Stokes peaks. c) Temperature dependent Raman spectra of 9-AGNRs on hBN.

Raman scattering of light was discovered in 1928 by C.V. Raman and K.S. Krishnan, and independently by G. Landsberg and L. Mandelstam.^{91–93} It is based on the inelastic scattering of light in a gas, liquid, or solid. When light interacts inelastically with the lattice vibrations, the light quantum (photon) can gain or lose energy. The amount of that energy is equal to a lattice vibration quantum (phonon). By analyzing the spectrum of the scattered light one can hence gain information about the vibrational modes present in the system under investigation. The Raman effect is a two photon effect. In Figure 3.1a) this is depicted, showing the excitation with a photon of frequency ω_0 . If the photon scatters elastically, it keeps its frequency, this process is called Rayleigh scattering. If the light scatters inelastically, the scattered photon has a frequency of $\omega_0 \pm \omega_{ph}$, where ω_{ph} corresponds to the frequency of the phonon. These processes are called Stokes scattering, (in the case of $-\omega_{ph}$) and Anti-Stokes scattering (in the case of $+\omega_{ph}$). Figure 3.1b) shows a schematic Raman spectrum. The difference in intensity can be understood as follows: Phonons are bosons, and therefore one can describe their average number n by the Bose-Einstein distribution:

$$n = \frac{1}{e^{E_\nu/k_B T} - 1} \quad (3.1)$$

where E_ν is their energy, k_B is the Boltzmann constant, and T is the temperature. One can also view the process as a phonon getting created (n to $n + 1$, Stokes) or annihilated ($n + 1$ to n , Anti-Stokes). The intensity ratio between the Stokes scattering I_S and Anti-Stokes scattering I_{AS} can therefore be expressed as:

$$\frac{I_S}{I_{AS}} \propto \frac{n+1}{n} = e^{E_v/k_B T} \quad (3.2)$$

We see that the intensity ratio is strongly temperature-dependent and hence can be used as a thermometer. In Figure 3.1c) Raman spectra collected at different temperatures are shown. The physical interpretation of the shown peaks is discussed later after introducing the graphene nanoribbons in more detail. One sees that the intensity ratio of the peaks at $\pm 25 \text{ cm}^{-1}$ changes drastically, illustrating the above-discussed temperature. We further see that the peak labeled LCM shows a strong temperature dependence of its peak position. This is quite surprising for such a low-frequency vibrational mode. However, it can be understood by the origin of this mode. It is a longitudinal compressive mode (LCM) in atomically precise graphene nanoribbons and was first identified by Overbeck et al.⁸⁹. For this vibration all atoms of the GNR are involved. Therefore this vibrational mode is in particular sensitive to pinning of the GNR to the substrate and/or different thermal expansion coefficients of the GNR and the underlying substrate. In the remainder of this thesis, we use Raman spectroscopy as a tool to assess the quality of the materials under investigation and in Chapter 9 we use these temperature-induced shifts of the Raman peaks to locally map the temperature.

3.1.2 Instrumentation for Raman spectroscopy at the Transport at Nanoscale Interfaces Laboratory

The Raman spectra shown in this thesis are acquired using a confocal Raman microscope (Alpha 300R, WITec) in back-scattering geometry. It is equipped with three excitation sources (488 nm, 532 nm, and 785 nm) and two corresponding spectrometers, one for visible and one for near-infrared light. The laser light is fiber-coupled to a tower. In this tower, it is linearly polarized by a $\lambda/2$ plate. The polarization of the incoming light can be rotated in an automated manner, which is very convenient to determine the orientation of aligned GNRs as discussed later. The linearly polarized light then gets focused onto the sample, which is placed either directly on a scan table, in a custom build vacuum chamber, or a He-flow cryostat (Microstat HiRes, Oxford Instruments). The backscattered light passes a filter to block the corresponding laser light and optionally an analyzer that controls the outgoing polarization. The light is then fiber-coupled to the spectrometers where it is dispersed by a grating and later collected by the CCD. The following gratings are available for the visible light: 150, 600, and 1800 g/mm and for the near-infrared light 150, 300, and 1200 g/mm. The grating is selected based on the spectral resolution needs. A more detailed description of the setup can be found in the Ph.D. thesis of Jan Overbeck.⁹⁴

3.2 Probe stations and cryostats

3.2.1 Electronics

All electronic measurements were performed in a custom-built vacuum chamber ($< 10^{-6}$ mbar). For regular I-V characterization with or without applied gate voltage, a data acquisition

board (ADwin-Gold II, Jäger Computergesteuerte Messtechnik GmbH) was used to apply the bias and gate voltages and read the voltage output of the I–V converter (DDPCA-300, FEMTO Messtechnik GmbH). A modular electronics system (IVVI-DAC2-rack, Delft University of Technology) in combination with two lock-in amplifiers (SR830, Stanford Research Systems), along with the previously mentioned ADwin-DAQ, were used to determine the Seebeck coefficient.

3.2.2 Lake Shore probe station

The devices were measured in a commercially available probe station (Model CRX-6.5K, Lake Shore Cryogenics) at various temperatures (9 K - 350 K). This probe station is a closed-cycle cooling system, meaning the sample is never in direct contact with the ^4He that provides the cooling power. It is equipped with 6 spring-loaded needles that allow for temperature-dependent measurements over larger ranges.

3.2.3 Heliox cryostat

Parts of the temperature calibration measurements were carried out in a ^3He sample-in-vacuum dipstick. The system is cooled by inserting it into a ^4He Dewar. A specially engineered 1 K condensation stage allows for cooling to around 1.5 K. The ^3He closed cycle system then allows for cooling down to ~ 250 mK. The samples have to be wire bonded into a chip carrier and are contacted via a wire attached to a chip carrier socket. The wiring and sample mounting was developed by the author with the help of O.V.. In order to make little thermal contact to the outside world are the wires connecting the sample to the measurement instruments chosen to be thin and long. This causes them to have a resistance of $\sim 140 \Omega$. In the temperature calibration measurements, this is accounted for as we use a voltage-controlled current source.

3.2.4 Automated vacuum prober

Some precharacterization of the graphene electrodes was been performed in a custom-built vacuum prober. This probe station was developed in parts by the author and further developed by M.L.P. with help of O.V.. It allows for automated three-terminal measurements (source-drain-gate) under vacuum conditions ($< 10^{-6}$ mbar).

3.3 CVD-graphene

Single-layer graphene can be synthesized using chemical vapor deposition (CVD) at a large scale on various substrates. This procedure is well established since 2008/2009.^{95–99} It allows for the production of hundreds of graphene-based devices in parallel. Here are the recipe and key properties of CVD-graphene synthesized on copper within the Laboratory for Transport at Nanoscale Interfaces at Empa are described. We follow mostly the procedure developed by Thodkar et al.^{100,101}

3.3.1 Graphene growth and transfer

Polycrystalline graphene is synthesized via CVD in a tube furnace (Three-zone HZS, Carbolite). A 25 μm thick copper (Cu) foil (Foil 2017, No. 46365, Alfa Aesar) is prepared at room temperature by first cleaning in acetone (15 min), rinsing in isopropanol (IPA), immersing in deionized (DI) water (5 min), acetic acid (30 min), DI-water (20 min + 5 min in an ultrasonic bath), ethanol (1 min) and blowing dry with N_2 before reduction annealing in a H_2 -rich atmosphere (20 sccm H_2 in 200 sccm Ar) at 1000 $^\circ\text{C}$ and <1 mbar for 60 min. Before the growth, the pressure inside the tube is increased to 110 mbar by partially closing the downstream valve. Graphene growth is initiated by the addition of 0.04 sccm CH_4 to the chamber for 22 min. The growth is terminated by stopping the CH_4 flow, reducing the pressure by opening the downstream valve, opening the lid of the tube furnace, and circulating air with a fan to allow for an abrupt drop in temperature. The cool-down procedure (to <100 $^\circ\text{C}$) takes 45 min. The as-grown single-layer graphene is transferred onto the target substrate using a wet transfer method¹⁰² described in the following:

Poly(methyl methacrylate) (PMMA) 50K (AR-P 632.12, Allresist GmbH) is spun onto the graphene-coated Cu foil and the backside graphene is etched using reactive ion etching (RIE). A Ar-/O₂-plasma (15/30 sccm) with a power of 25 W and a pressure of 20 mTorr during 30 s was used. Cu is etched away using a copper etchant (PC COPPER ETCHANT-100, Transene) for 60 min leaving the graphene/PMMA film floating on top. The etchant is then replaced by DI-water in a stepwise dilution process. The DI-water is then replaced by a 10 % HCl solution for 5 min. After a final rinsing in DI-water, the graphene/PMMA film is fished out with the target substrate. After settling under ambient conditions for 30 min, the target substrate/graphene/PMMA stack is placed in an oven and heated to 80 $^\circ\text{C}$ for 1 h followed by a second heating step at 80 $^\circ\text{C}$ for at least 12 h under vacuum conditions (<1 mbar) to ensure good adhesion of the graphene to the target substrate. PMMA is removed by placing in acetone for 10 min at room temperature, 60 min at 56 $^\circ\text{C}$, followed by a 30 min cool down period. Finally, we perform an IPA rinsing step followed by N_2 blow drying. This process yields clean, single-layer graphene with low defect density on the target substrate, as assessed in Subsection 3.3.2.

3.3.2 Quality assessment

After transferring graphene to the target substrate a quality assessment can be performed before further fabrication steps.

Raman spectroscopy

Raman spectroscopy is a widely used technique to assess the graphene quality due to its, at first sight, simple data interpretation. By Raman mapping the graphene over a large area a qualitative interpretation can be done. We used large area Raman scans to assess the graphene quality after transfer to SiO_2 . All spectra were acquired in air using a 100x objective (NA = 0.9) with an excitation wavelength of 532 nm and a laser power of 2 mW. After data acquirement, a cosmic ray removal (CRR), as well as a constant

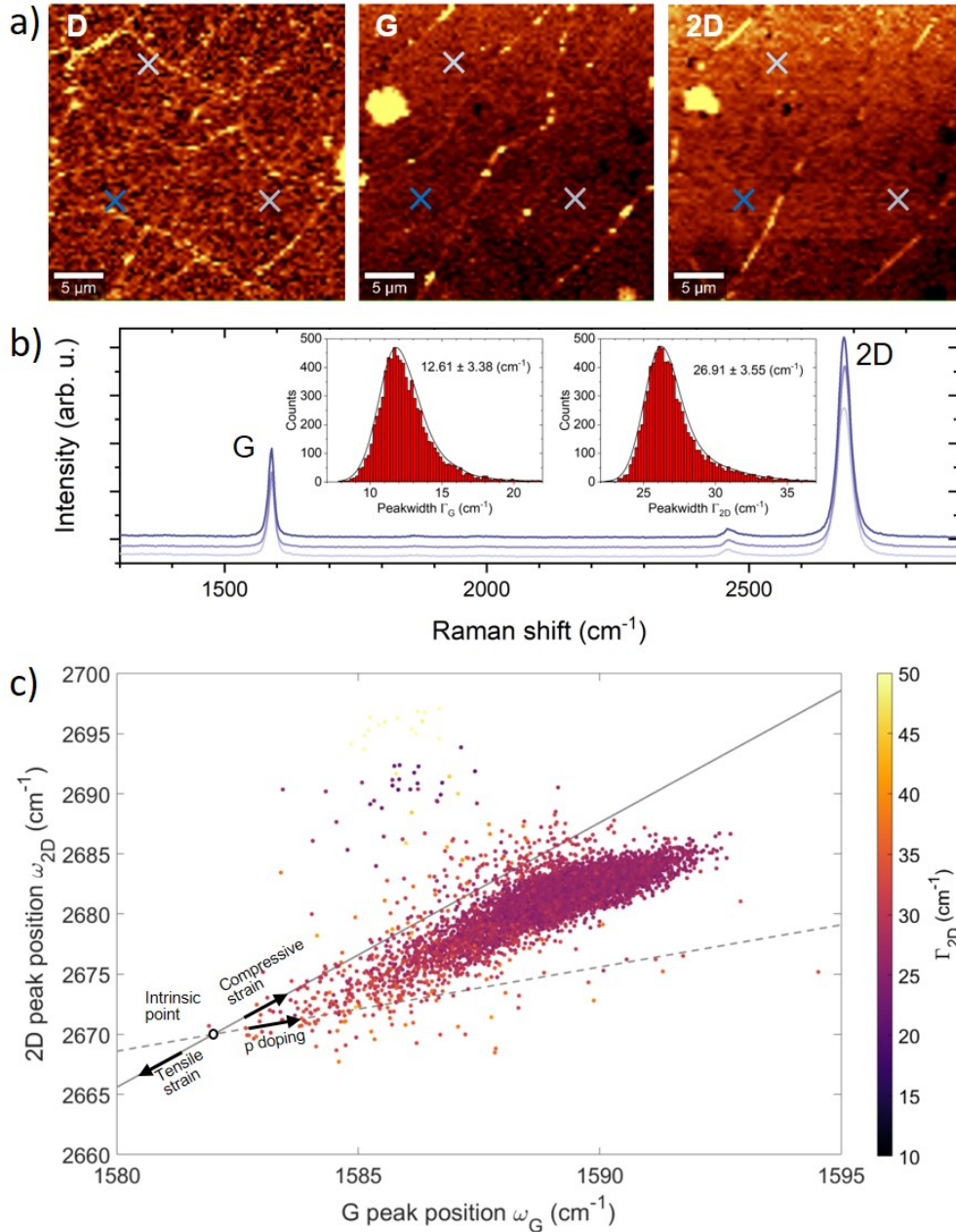


Figure 3.2 Raman mapping of graphene on SiO₂. **a)** Intensity maps of the D-, G- and 2D-Raman band. **b)** 3 individual representative Raman spectra collected at the positions indicated by the crosses in a). The insets show histograms of the extracted full-width at half-maximum of the G and 2D peak (Γ_G and Γ_{2D} , respectively). **c)** Scatter plot of the Raman G and 2D peak position (ω_G and ω_{2D} , respectively). The color map represents Γ_{2D} . The open circle indicates the peak positions of intrinsic graphene, which is neither doped nor strained.^{103,104} Figure taken from Braun et al.⁹⁰

background (at the minimum) subtraction, was applied to each spectrum. The visible bilayer graphene region in the top left corner was excluded from all further data analyses. For each spectrum, the G- and 2D-band are fitted with a single Lorentzian to extract

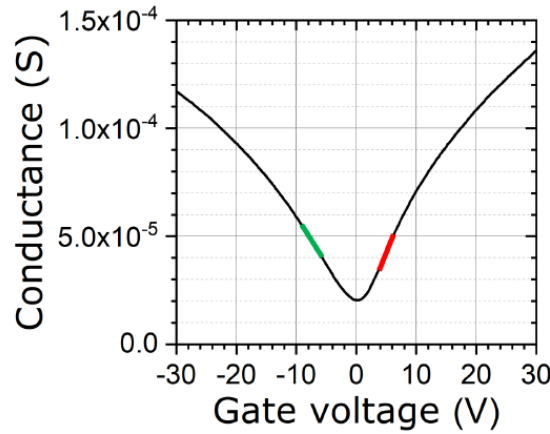


Figure 3.3 Electrical behavior of graphene FET at room temperature. Conductance as a function of applied gate voltage at fixed bias voltage of $V_b = 0.1$ V, indicating typical graphene FET behavior. Field-effect mobilities are $2'500 \text{ cm}^2/\text{Vs}$ for electrons (red) and $1'800 \text{ cm}^2/\text{Vs}$ for holes (green), assuming the geometrical factor being dominated by the central constriction of $350 \times 820 \text{ nm}$.¹⁰⁵ Figure taken from Braun et al.⁹⁰

the peak positions and full-width at half maximum.

Electrical

A further indicator for the graphene quality is the field-effect mobility $\mu_{\text{FE}} = L_{\text{ch}}G/W_{\text{ch}}C_GV_{\text{DS}}$. Where L_{ch} is the channel length, G is the source-drain conductance, W_{ch} is the channel width, C_G is the gate capacity and V_{DS} is the source drain voltage.¹⁰⁵ Electrical behavior of a reference device (on a normally processed chip, device without 2nd electron-beam exposure for gap formation) after fabrication is shown in Figure 3.3.

3.4 Electrical breakdown procedure for graphene nanogap formation

3.4.1 Procedure and challenges

The electrical breakdown procedure allows for the formation of nanogaps in graphene. Originally inspired by the electromigration of Au-nanojunctions for molecular electronics this procedure, although with slightly varied fabrication recipes, is well established within the molecular electronics community.^{23,26,29,30,106–108} First, graphene on an insulating substrate was patterned into a bow tie shape with a constriction 400 nm wide and 800 nm long (ditto) which quickly flares into wide graphene leads that are then connected to large metal contact pads. Second, a feedback-controlled voltage is applied to the device inducing a current to flow between source and drain. By steadily or pulsed increasing of the bias voltage, also the corresponding current scales leading to a temperature at the nanoconstriction increases due to Joule heating.²³ The temperature profile along the constriction follows the 1-D heat equation, with its hot-spot in the center.

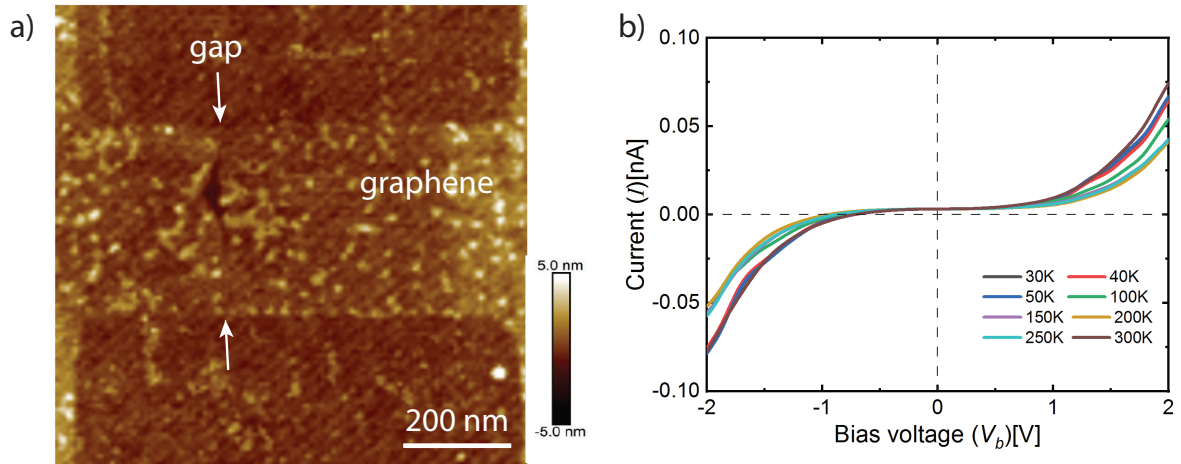


Figure 3.4 Junction geometry and electrical characterization. a) AFM height profile of a graphene nanoconstriction after performing electrical breakdown procedure on a typical device. The nanogap is indicated with white arrows, showing clear size variations. b) Tunneling current curves recorded at various temperatures indicating no temperature dependence. Figure adapted from El Abbassi et al.³⁰.

This procedure provides locally enough thermal energy for rearrangements and later evaporation/sublimation of contaminants on the graphene surface. In a later stage, the current density becomes so large that the graphene starts to crack at its weakest points, usually at the grain boundaries, defects, or edges, leading to an abrupt change in resistance, which can be detected and leads to an immediate ramping down of the applied bias voltage.

After the successful formation, a careful electrical inspection of the nanogap is needed. By fitting the observed S-shaped I-V characteristics to the Simmons model,¹⁰⁹ the size of the nanogap can be estimated. This model has its limitations and only partially reflects the experimental reality since for example, it assumes a plate capacitor for calculating the distance, while experimentally we have two atomically flat electrodes. Further as can be seen in the AFM measurement in Figure 3.4a), the geometry in particular the graphene edges are not as well defined as one would like to have for a model. However, this model can serve as a qualitative estimate in comparing the variation in gap sizes between devices, as well as whether a nanogap has formed or not, i.e. a gap >5 nm would lead to a nondetectable tunneling current.

Besides the I-V measurements, it is also necessary to do gate voltage dependent measurements since isolated graphene islands could be trapped between the two graphene electrodes serving as an electronic island and at low temperature behave like a quantum dot.¹¹⁰ Also distinguishing lead- and molecule-states in graphene-based single-electron transistors is challenging and requires profound know how.¹¹¹ Additionally quantum interference has been reported in nanoconstrictions created using the electrical breakdown procedure.¹¹² To identify and exclude such devices it is necessary to cool down to low temperatures, creating the drawback that the sample undergoes thermal cycling, which may lead to unwanted modifications of the sample. Since the observed current arises

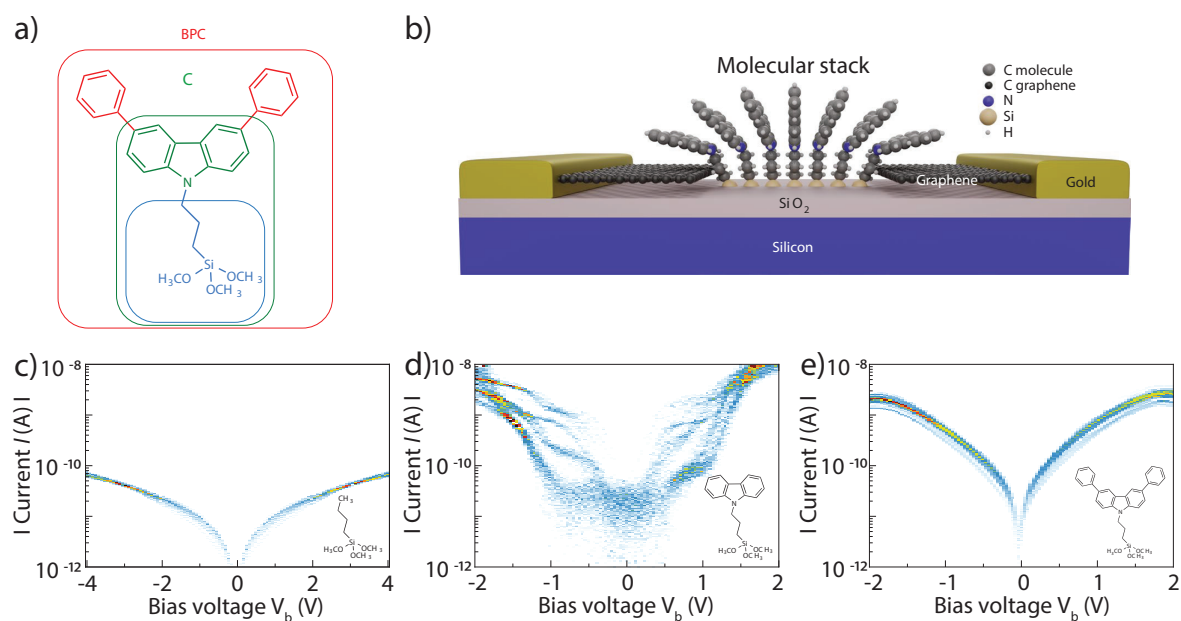


Figure 3.5 Junction geometry, molecular design and electrical characterization.

a) Drawing of the three molecules, constituted of three main parts: the silane group for the covalent anchoring to the substrate, the alkane chain that decouples the silane group from the different head groups (CH₃ (molecule N) and N-carbazole (molecule C)) and biphenyl N-carbazole (molecule BPC). **b)** Schematic illustration of a molecular junction that contains a series of π - π -stacked molecules bridging a graphene nanogap. The atomic positions of the molecules are for illustrative purposes only, and do not correspond to the DFT-relaxed geometry shown in Figure 4 of El Abbassi et al.³⁰. For clarity, different sizes and colors are used to distinguish the carbon atoms of the molecule from those of the graphene. **c)-e)** The electrical measurements that correspond to the three molecules under study with different head groups are displayed as density plots of the measured I–V curves, of which the absolute value of the current is plotted on a logarithmic scale. For each molecule, 100 I–V curves without data selection were measured at room temperature on a specific device per molecule. Figure adapted from El Abbassi et al.³⁰

only from the tunneling of electrons through the vacuum in the nanogap, no temperature dependence is expected. Temperature dependence is a key feature to disentangle signals arising from molecules, graphene islands, graphene nanoribbons, etc. in the nanogap.

These nanogaps have been shown to help to overcome the problem of mechanical instabilities in the field of molecular electronics as laid out in Subsection 3.4.2 and are used to contact GNRs of very short length as described in Chapter 5.

3.4.2 Application to molecular electronics

The workhorse of molecular electronics, the so-called mechanically controlled break junction (MCBJ), where a thin metal strip within a solution of molecules is bent using a piezo-controlled bending mechanism until it breaks, relies its power on a statistical

approach, mostly due to mechanical instabilities. For example, the molecule can leave or also enter the junction while the metal electrodes separate. These gap formations can be performed several thousands of times. The collected current vs. displacement curves are then plotted as a histogram revealing molecular features that can be detected by the experienced observer or advanced clustering approaches.¹¹³ A major drawback of the MCBJ technique is that the gap formation is not very robust and therefore can not be directly used in a solid state device. It has been shown in El Abbassi et al.³⁰ that by using graphene nanogaps formed by the electrical breakdown procedure in combination with the anchoring of the molecule to the substrate within the nanogap as well as an extension of the molecule with side-groups, robust molecular junctions can be formed. This allows for longer measurement times at an individual device and hence one can gain valuable information about the particular molecular junction and foresee the application of molecules in solid state devices.

3.5 Graphene nanoribbons (GNRs)

3.5.1 Overview of graphene nanoribbons

Bottom-up synthesized graphene nanoribbons can have a variety of shapes and as a result vary in their properties. The shape is given by the selected precursor molecules. Besides this, they can either be synthesized in solution or on-surface via CVD or under ultra-high vacuum (UHV) conditions. GNRs synthesized in solution usually have long side groups to avoid agglomeration, however, they can be synthesized at a large scale and drop cast onto a sample similar to molecules. A nice feature, but also a limitation, is that the GNRs can move inside the solution. For example, this can lead to self-alignment of GNRs on hBN. If the GNRs are synthesized using CVD, the substrate tends to show more contaminants after growth than in the UHV synthesized case. We therefore only integrate GNRs that are synthesized under UHV conditions in the nanotech@surfaces laboratory of Prof. Roman Fasel at Empa. In the following an overview of the properties of the GNRs studied in this thesis is given. Electrical characterizations on single GNR level are done using scanning tunneling spectroscopy (STS). The synthesis, as well as scanning tunneling microscopy (STM) images of these GNRs, are shown in the following subsections.

3.5.2 Growth substrates and GNR transfer

Using Au(788) as growth substrate results in uniaxially aligned GNRs (GNRs grown along the narrow (111) terraces) while using Au(111)/mica leads to non-aligned GNRs.^{12,120} Optical images as well as a schematic illustration of the Au terraces can be seen in Figure 3.6. In both cases, Au(788) single crystal (MaTeK, Germany) or Au(111)/mica (Phasis, Switzerland), the growth substrates are cleaned in ultrahigh vacuum by sputtering/annealing cycles. After this cleaning procedure, the precursor molecule is deposited on the surface. The density can be controlled by monitoring a crystal gauge. The polymerization of the precursor molecules, as well as the cyclodehydrogenation steps to form GNRs, are usually initiated by a temperature increase (for exact experimental

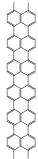
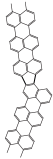


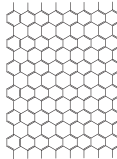
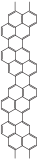
GNR type	5	5, kinked	7	9	17	pyrene
Chemical structure						
Armchair family	3p+2	3p+2	3p+1	3p	3p+2	-
Width (Å)	4.8	4.8	7.2	9.6	19.3	7.2
Average length (nm)	15	80	20	40-45	<20	35
Polymerization temperature (°C)	225 ¹⁵	230	200 ¹¹⁴	200 ¹¹⁵	250 ¹¹⁶	180 ¹⁹
Cyclodehydrogenation temperature (°C)	350 ¹¹⁷	345	400 ¹¹⁴	400 ¹¹⁵	400 ¹¹⁶	300 ¹⁹
Controlled alignment	yes	no	yes	yes	no	no
Controlled density	yes	yes	yes	yes	no	no
Band gap DFT (eV)	0.43 ³¹	0.43 ³¹	1.56 ³¹	0.73 ³¹	0.13 ^{31,116}	0.18 ¹⁹
Band gap STS (eV)	0.85 ¹¹⁸ 0.29 ^a	0.85	2.30 ¹¹⁹	1.40 ¹¹⁵	0.17 ¹¹⁶	0.23 ¹⁹
RBLM (cm ⁻¹)	531	531	396	314	169	459 ^b

Table 3.1 Overview of selected GNRs presenting structural, electronic and vibrational properties.

^aEnd-states within the band gap as reported by Lawrence et al.¹¹⁸

^bLabeled as RBLM* according to Sun et al.¹⁹

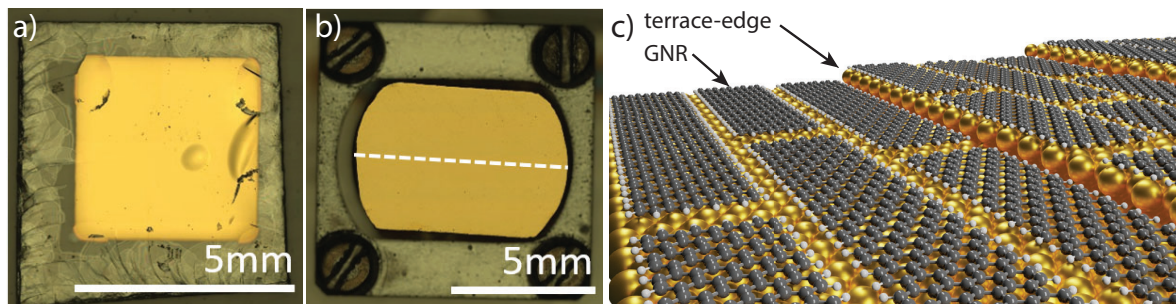


Figure 3.6 Au-growth substrates for on-surface synthesis of GNRs. a) and b) Optical images of Au(111)/mica and Au(788) GNR growth substrate, respectively. In b) the dashed white line indicates the crystal axis. Figure adapted from Braun et al.⁹⁰. c) Artistic illustration of 9-AGNRs on Au(788), aligned along the crystal axis. Figure adapted from Overbeck⁸⁸.

parameters see individual GNR subsections of this section and the references therein). GNRs are transferred from their growth substrate to the silicon-based target substrates with predefined graphene electrodes by two different transfer approaches. GNRs grown on Au(788) crystals are transferred by an electrochemical delamination method using PMMA as an intermediate transfer substrate as reported in Senkovskiy et al.¹²¹, Overbeck⁸⁸ and Overbeck et al.⁸⁹ GNRs grown on Au(111)/mica are transferred using a polymer-free method as described in Fairbrother et al.¹²², Borin Barin et al.¹²³, Backes et al.¹²⁴.

3.5.3 9-AGNRs

9-AGNRs were first synthesized and reported by Talirz et al.¹¹⁵. For the studies reported in this work 9-AGNRs were synthesized from 3,6-diiodo-1,1':2',1'-terphenyl (DITP).¹²⁵ Two types of GNRs, uniaxially aligned and randomly oriented, are transferred onto the sample. The growth substrates are cleaned in ultrahigh vacuum by two sputtering/annealing cycles: 1 kV Ar⁺ for 10 min followed by annealing at 420 °C for Au(788) and 470 °C for Au(111)/mica for 10 min. Next, the precursor monomer DITP is sublimed onto the Au surface from a quartz crucible heated to 70 °C, with the growth substrate held at room temperature. After deposition of 1 monolayer of DITP, the growth substrate is heated (0.5 K/s) to 200 °C with a 10 min holding time to activate the polymerization reaction, followed by annealing at 400 °C (0.5 K/s with a 10 min holding time) to form the GNRs via cyclodehydrogenation.

As can be seen in the STM images of Figure 3.7, even the 9-AGNRs grown on Au(111)/mica which are described as non-aligned films tend to be locally aligned. As it has been shown by Di Giovannantonio et al.¹²⁵ this effect is stronger for 9-AGNRs grown with iodine instead of bromine in the precursor molecule. A further advantage of the iodine-based precursor molecule is the statistically longer 9-AGNRs, which is favorable for device integration. The average GNR length is between 40 and 45 nm,

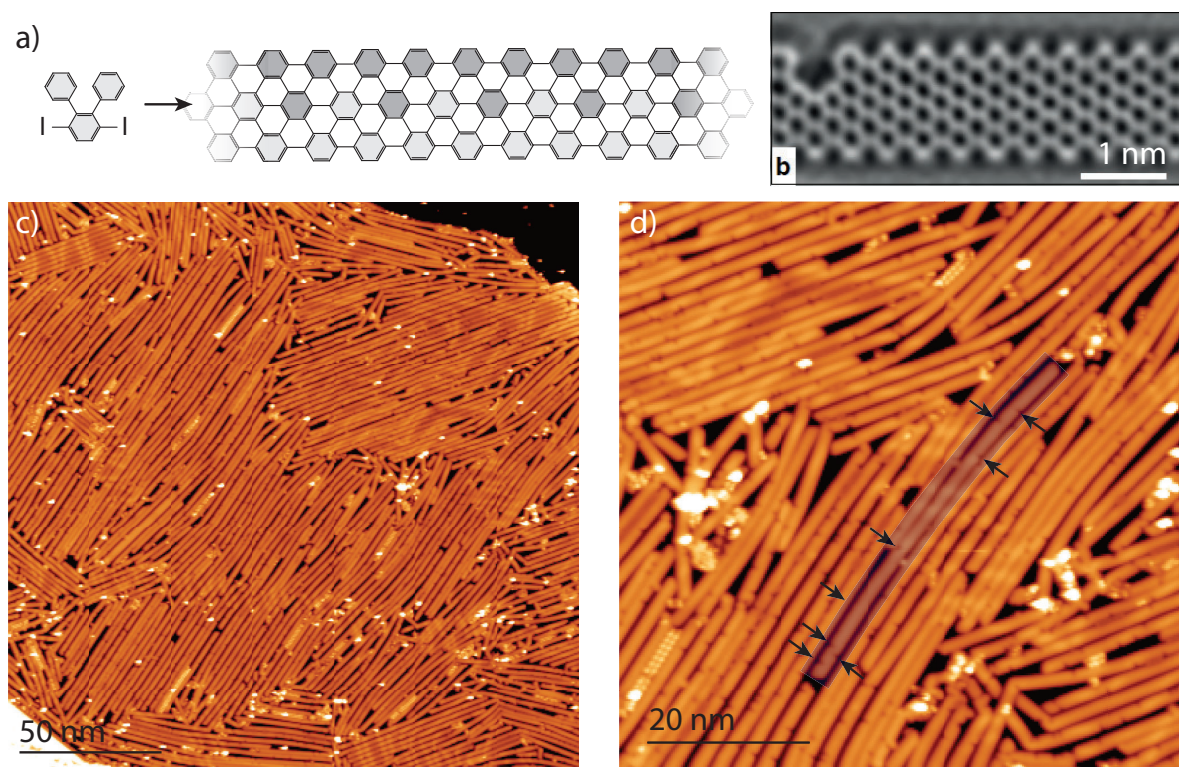


Figure 3.7 9-AGNR synthesis, on-surface characterization and bite-defects. **a)** Schematic representation of the on-surface synthesis route from the molecular precursor to the 9-AGNR. **b)** non-contact AFM image acquired with a CO-functionalized tip ($V_s = 10$ mV, $I_t = 2$ pA). Figure adapted from Pizzochero et al.¹²⁶. **c) and d)** High-resolution STM image of 9-AGNRs on Au(111) ($V_s = -1.5$ V and $I_t = 50$ pA) at liquid helium temperatures. In d) a 9-AGNR is highlighted and all its bite defects are indicated with black arrows. Data provided by Gabriela Borin Barin.

while for 9-AGNRs grown with the bromine-based precursor molecule the average GNR length is around 15 nm.¹²⁵

The presence of bite defects as shown in Figure 3.7 can not be avoided. They originate from the C-C bond scission that occurs during the cyclodehydrogenation step of the reaction.¹¹⁵ A detailed study on the effect of these bite defects on the quantum electronic transport across GNRs has been reported recently by Pizzochero et al.¹²⁶. Their first-principles calculations revealed that such imperfections substantially disrupt the conduction properties at the band edges.

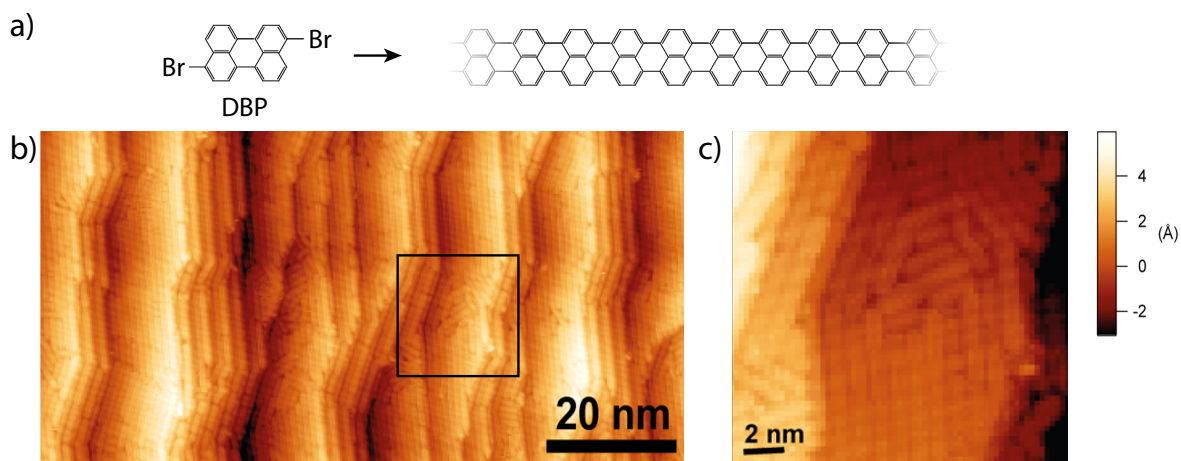


Figure 3.8 5-AGNR synthesis and on-surface characterization. a) Schematic representation of the on-surface synthesis route from the molecular precursor to the 5-AGNR. b) and c) STM image of as-synthesized aligned 5-AGNR on a Au(788) surface ($V_s = -1.5$ V and $I_t = 60$ pA). c) shows a high resolution scan of the area indicated by a black square in b). Figure adapted from El Abbassi et al.¹⁵.

3.5.4 5-AGNRs

5-AGNRs are synthesized by sublimating the precursor molecules, an isometric mixture of 3,9-dibromoperylene and 3,10-dibromoperylene (DBP), at 160 °C onto a Au(788) surface kept at room temperature.¹¹⁷ A slow annealing process (0.2 K/s) up to 225 °C allow the formation of 5-AGNRs via polymerization and cyclodehydrogenation.¹⁵

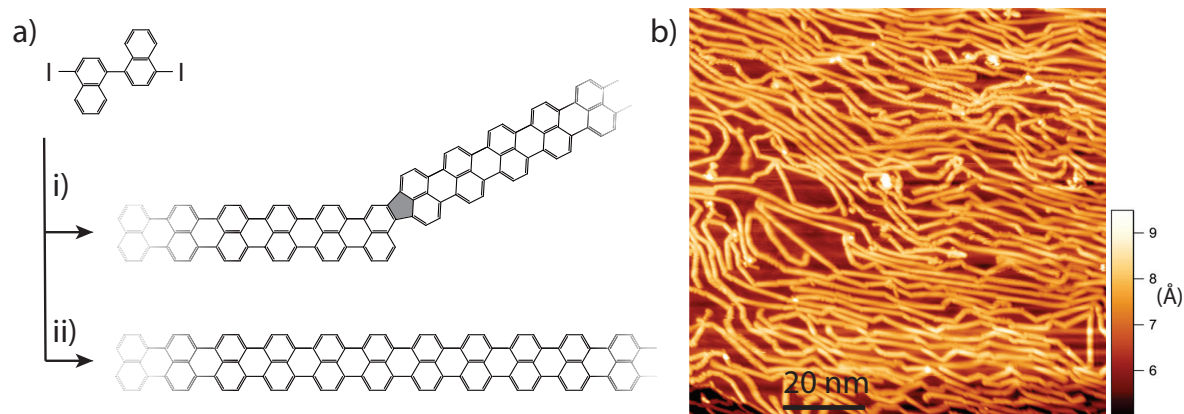


Figure 3.9 kinked 5-AGNR synthesis and on-surface characterization. a) Schematic representation of the on-surface synthesis route from the molecular precursor to the 5-AGNR. Route i) shows the formation of a kink. ii) shows a straight 5-AGNR segment. b) STM image of as-synthesized kinked 5-AGNR on a Au(111) surface ($V_s = -1.5$ V and $I_t = 30$ pA). Data provided by Gabriela Borin Barin.

3.5.5 5-AGNRs (with kinks)

5-AGNRs can also be synthesized by starting from a different precursor molecule than described in Subsection 3.5.4. After the polymerization, this molecule needs to rotate along its axis to form a straight 5-AGNR. If this rotation does not take place a kink in the 5-AGNR is formed. Since this process can (so far) not be completely controlled kinked 5-AGNRs are formed. Despite this unwanted formation of kinks, the GNRs grow very long, some longer than 100 nm. STS measurements revealed that these kinks do not electrically isolate the straight segments from one another. This raises the potential for exploration in a FET geometry. A detailed study by Borin Barin et al. is therefore in preparation.

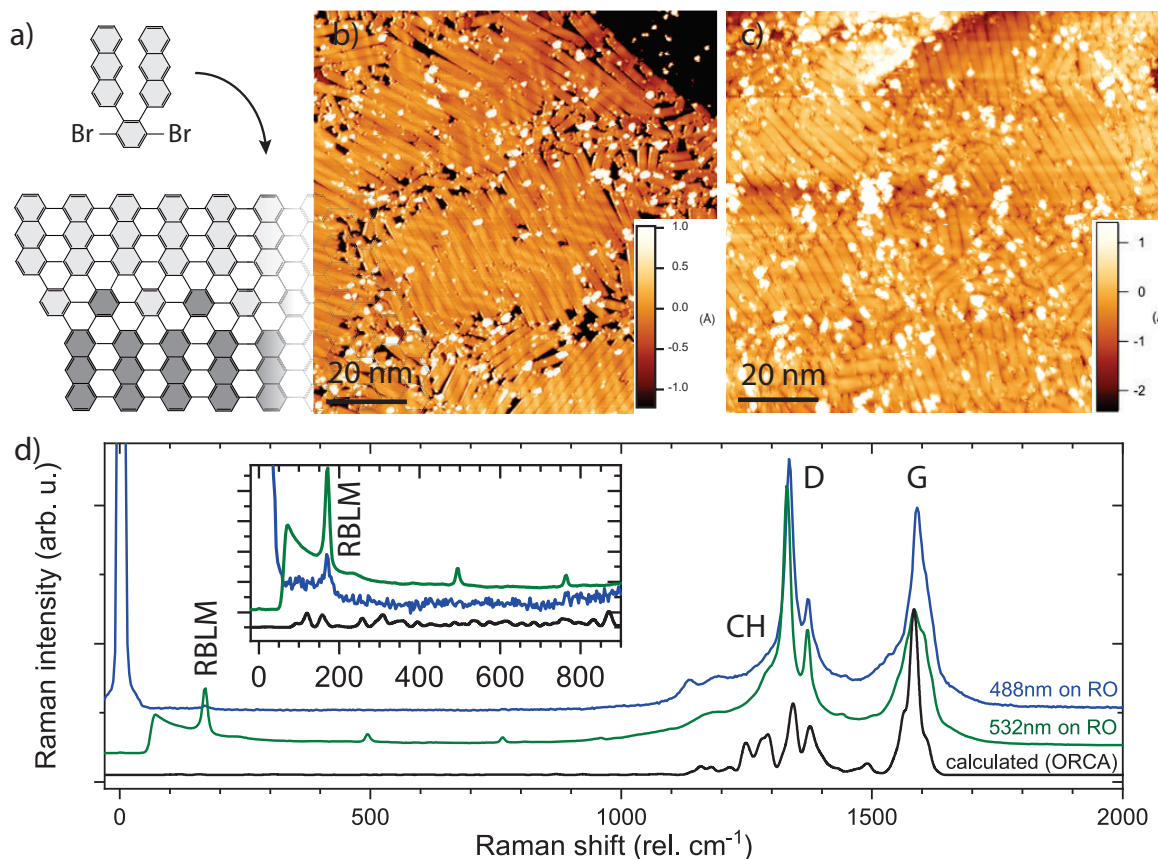


Figure 3.10 17-AGNR synthesis and on-surface characterization. a) Schematic representation of the on-surface synthesis route from the molecular precursor to the 17-AGNR. Note the zigzag edges at the left GNR end. b) and c) STM image of as-synthesized 17-AGNRs on a Au(111) surface ($V_s = -1.5$ V and $I_t = 30$ pA). b) shows the local alignment of longer 17-AGNRs with shorter GNRs in between. c) longer 17-AGNRs after optimizing the growth parameters. Data provided by Gabriela Borin Barin. d) Averaged Raman spectra of transferred 17-AGNRs on Raman optimized substrate. A calculated spectrum is shown for comparison.

3.5.6 17-AGNRs

17-AGNRs are synthesized following the route proposed by Yamaguchi et al.¹¹⁶ on Au(111)/mica and further optimized for length by Nicolò Bassi and Gabriela Borin Barin in the nanotech@surfaces laboratory at Empa. These 17-AGNRs have an electronic band gap of 0.19 eV as measured by STS on Au(111)¹¹⁶. This makes them further appealing for electronic devices. Raman spectroscopy measurements as shown in Figure 3.10d) revealed that the 17-AGNRs can also be transferred and show the typical GNR Raman peaks (G, CH, D, and RBLM). The Raman spectrum was calculated with the ORCA 4.2 DFT code¹²⁷ using the GGA PBE exchange-correlation functional and the def2-SVP basis set, and numerically calculated frequencies. However, we noticed during the ex-situ characterization using thermal annealing and Raman spectroscopy that this GNR is particularly sensitive to heat. We assume this being caused by the zigzag ends of the 17-AGNRs that are chemically more reactive (see Figure 3.10).

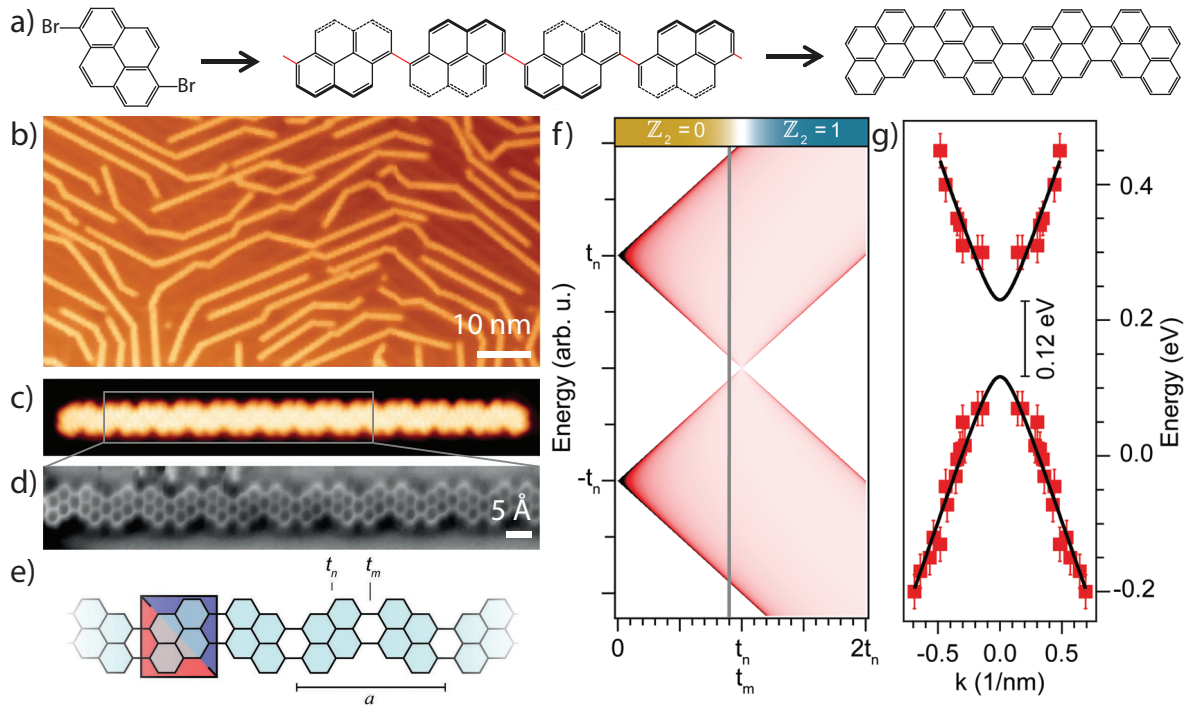


Figure 3.11 On-surface synthesis of the pyrene-GNR and its calculated electronic properties. **a)** Schematic representation of the on-surface synthesis route from a molecular precursor over a polymer phase to the pyrene-GNR. The structure of the intermediate polymer is non-planar due to steric hindrance between neighboring pyrene units. **b)** STM image of the pyrene-GNR on Au(111). **c)** High-resolution STM image of a pyrene-GNR ($V_s = -0.2$ V and $I_t = 120$ pA) **c)** Non-contact-AFM image of the area indicated by the gray rectangle in c) ($V_s = 5$ mV and oscillation amplitude: ~ 80 pm). **e)** Structural model of the pyrene-GNR shown with the relevant intramolecular (t_n) and intermolecular (t_m) coupling constants used in the SSH model. a is the unit cell length. **f)** SSH-derived DOS as a function of the intermolecular coupling constant t_m . The corresponding topological class is indicated by \mathbb{Z}_2 . The gray line marks the position $|t_m - t_n|/t_n = 0.1$. **g)** Plot of the experimental dispersions of the valence band and the conduction band of the pyrene-GNR based on length-dependent energy position of the frontier states (red squares) using $k = \pm p\pi/((N + 1)a)$. The black curve is a fit to the experimental data using the dispersion relation of massive Dirac fermions. Figure adapted from Sun et al.¹⁹.

3.5.7 Pyrene-GNRs

The large band gaps of the currently available AGNRs severely limit device performances due to significant barriers at the contacts. The synthesis of GNRs with smaller band gaps would hence be highly desirable. To this end, width-modulated AGNRs as described in Sections 3.5.4, 3.5.5 and 3.5.6 of this chapter are promising candidates, because their periodically arranged and overlapping electronic states give rise to 1D topological bands

within the band gap of the pristine AGNR backbone.^{17,18}

Here, the synthesis and properties of another ultralow band gap GNR are highlighted. Via on-surface synthesis, based on readily available pyrene-based precursors, pyrene-GNRs can be formed. A schematic representation of the synthesis route can be seen in Figure 3.11a) and is described in detail in Sun et al.¹⁹. The edges of the pyrene-GNR are partially zigzag and partially armchair, leading to a higher chemical reactivity outside of UHV conditions than for GNRs with purely armchair edges. The integrity of the pyrene-GNRs outside of UHV as well as after transfer to device substrates was confirmed using Raman spectroscopy.¹⁹

The charge carriers within the pyrene-GNR behave as massive Dirac fermions since their valence electrons represent a Su–Schrieffer–Heeger (SSH) chain close to the topological phase boundary, this means when the intra- and interdimer coupling become approximately equal (see Figure 3.11e) and f)). This results in an ultralow band gap of ~ 200 meV as confirmed by STS measurements as shown in Figure 3.11g).

3.6 Optimized substrates and measurement approaches for Raman spectroscopy of graphene nanoribbons

Significant challenges remain for GNR processing and characterization. Herein, Raman spectroscopy is used to characterize different types of GNRs on their growth substrate and track their quality upon target substrate transfer.

Here, and in more detail in Overbeck⁸⁸, the fabrication and advantages of Raman-optimized (RO) device substrates for Raman spectroscopy of GNRs are described. These RO-substrates rely on the interference-based intensity enhancement provided by an amorphous dielectric layer on a metal, which blocks the background of the silicon underneath. Together with an advanced mapping approach, this results in high signal-to-noise (S/N) ratios for several excitation wavelengths while limiting radiation damage to the GNRs under investigation.

In Figure 3.12a), we highlight in red the spectral regions for which the Si background masks the signal in a representative 9-AGNRs sample. To address this issue, we developed a layered, interference-optimized substrate that is suitable for both Raman and transport measurements.

The RO structure we designed and fabricated is shown in Figure 3.12b) and consists of an atomic layer deposition (ALD)-grown aluminum-oxide layer patterned on optically thick (typically 80–90 nm) metal source-drain contacting pads (labeled S/D) on a silicon device substrate, that acts as a support and optional gate (G). The result is enhanced optical visibility of the GNRs on top of the metal, allowing for easy identification of film inhomogeneity and a strongly enhanced Raman intensity. This is the result of the GNR layer being placed into the region of a field antinode, and it allows the acquisition of spectra at much lower excitation powers or shorter integration times.

In Figure 3.12c), we show the Raman intensity of the GNR G-mode as a function of oxide thickness for a 9-AGNR sample measured with three different excitation wavelengths. For each wavelength, there is an optimal thickness resulting in maximum Raman intensity. A good compromise suitable for multiwavelength investigations of

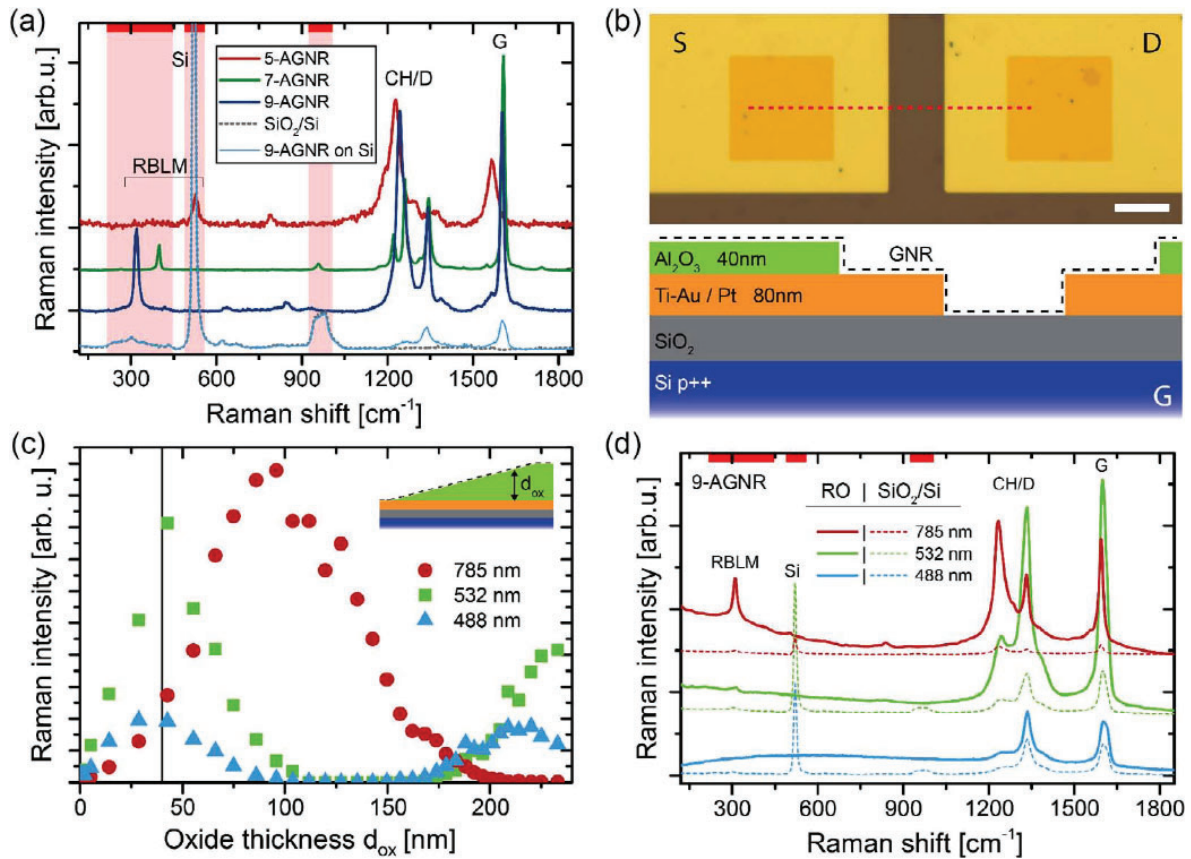


Figure 3.12 Raman optimized device substrates. a) Raman spectra of 5-, 7-, and 9-AGNRs on Au ($\lambda_{\text{ex}} = 785/532/785$ nm, arbitrarily scaled) compared with SiO₂/Si and 9-AGNRs transferred to SiO₂/Si ($\lambda_{\text{ex}} = 488$ nm), scaled to the second-order Si peak. b) Optical micrograph of an RO device substrate based on standard p-doped silicon with thermal oxide. The layers are sketched in the lower half of the panel, corresponding to a cross section at the dashed red line in the optical image. c) Raman intensity of the 9-AGNR G-peak on top of an RO substrate as a function of Al₂O₃ thickness on a sample with an oxide gradient. Measured with 100 \times objective (NA = 0.9) in air. d) Raman spectra of transferred 9-AGNRs measured in the interference-optimized region (RO, solid lines) and on adjacent SiO₂/Si (dashed lines) with different wavelengths. Measured with 100 \times objective (NA = 0.9) in air, no background subtraction. Figure adapted from Overbeck et al.⁸⁹.

GNRs is found at an oxide thickness of about 40 nm (indicated by a vertical line). Figure 3.12d) shows a comparison of the Raman spectra of 9-AGNRs transferred onto a 40 nm RO substrate and the adjacent Si/SiO₂ substrate. Note that, these values are for an oxide thickness of 40 nm, which is a compromise between the wavelengths available within our laboratory and constraints from sample fabrication.

Overall, both the RO substrate and the optimized measurement approach allow for unprecedented insight into the low-frequency modes of GNRs and demonstrated their usefulness in monitoring GNR quality upon device fabrication as shown in later chapters of this thesis.

3.7 Methods used for determining the thermal conductivity of graphene

3.7.1 Preparation of the SiN membrane

Two types of Si/Si₃N₄-membranes were used. First, commercially available Si/Si₃N₄-membranes (Norcada Inc., NORCADA Low Stress SiNx Membrane NX5200D) were patterned with arrays of holes of various diameters using a Gallium-FIB (FEI, Strata). Second, silicon nitride frames are fabricated using dry and wet etch processes as described elsewhere.¹²⁸ Further a Ti/Au (5/40 nm) layer is deposited using an electron beam evaporator to ensure thermal anchoring.

3.7.2 Synthesis and transfer of graphene

The CVD-graphene is synthesized as described here and previously.^{100,129,130} The single-layer graphene samples were synthesized using a Cu metal catalyst by CVD. A 25 μm thick Cu-foil was cleaned with acetic acid for 20 min and rinsed with DI-water and ethanol. The Cu-foil was then heated up to 1000 °C inside a quartz tube under Ar atmosphere for 3 h, and the graphene was then grown with flowing gas mixtures of Ar:H₂:CH₄ = 200:20:0.1 (sccm) for 60 min. After synthesizing the graphene, PMMA 50K was coated on the graphene at 3000 RPM for 30 s. Using reactive ion etching (Ar/O₂-Plasma, 60 s) the graphene on the back-side of the PMMA/graphene/metal catalyst was removed. The metal catalyst was then etched by floating on a 0.1 M ammonium persulfate solution overnight. After rinsing the PMMA/graphene with DI-water, the PMMA/graphene was transferred onto the target substrate and baked at 110 °C for 30 min with an intermediate step at 80 °C for 10 min, increasing the adhesion between the graphene and target substrate. The PMMA was removed with acetone, IPA followed by DI-water. For this study also graphene grown with a slightly different recipe as reported elsewhere was used. Besides graphene grown by us, also commercially available graphene (Easy Transfer, Graphenea, and graphene grown and transferred by Applied Nanolayers) was used.

3.7.3 Raman setup and spectra analysis

Raman spectra were acquired with a confocal Raman microscope (WITec, Alpha 300 R) in backscattering geometry, equipped with 100x (NA = 0.9) and 50x (NA = 0.55, long working distance) objective lenses. The backscattered light was coupled to a 300 mm lens-based spectrometer with gratings of 600 g/mm or 1800 g/mm equipped with a thermoelectrically cooled CCD. The excitation laser with a wavelength of 532 nm from a diode laser was used for all Raman measurements. The laser power was set using WITec *TruePower*. The 2D-peak properties were extracted from the full-spectrum mapping results by fitting a single Lorentzian after linear background subtraction.

3.7.4 Temperature calibration

Measurements were carried out under ambient conditions by placing the sample on a hotplate (Kammrath & Weiss GmbH, LNT 250). The prepared membranes were clamped on a hot plate fixed on the piezo stage of the Raman microscope for mapping. To ensure thermalization of the membrane, a waiting time of ~ 45 min was considered before each Raman map was acquired.

3.7.5 He-ion irradiation

For the irradiation of freestanding graphene membranes, we used a He ion microscope (Orion, Zeiss) equipped with a pattern generator (Elphy MultiBeam, Raith) operated at 30 keV using a probe current of ~ 0.5 pA at a chamber pressure of $\sim 7 \cdot 10^{-5}$ mbar. The ion dose was controlled by the exposure dwell time of each pixel ranging from 0.3 ms to 1.5 ms.

4 Optimized graphene electrodes for contacting graphene nanoribbons

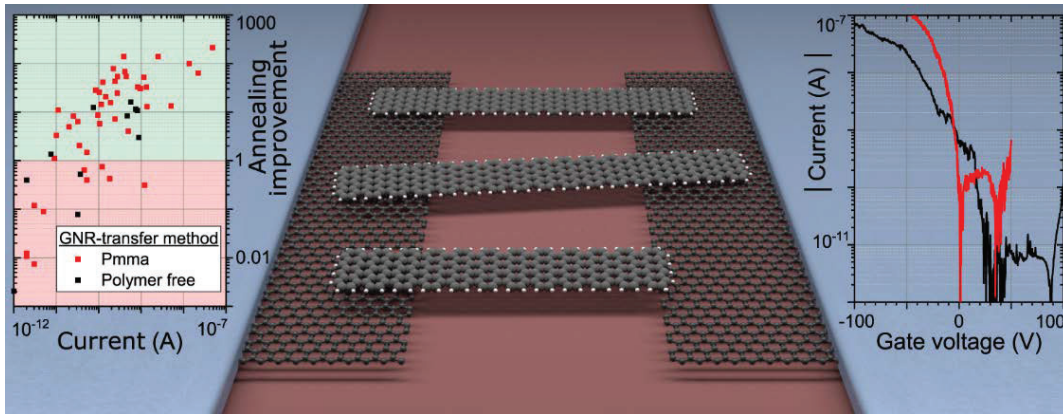


Figure 4.1 Artistic illustration showing the well defined graphene electrodes for contacting graphene nanoribbons. The left inset shows the improvement in on-state current due to thermal annealing. The right inset shows gate dependent transport for two devices transferred using two different methods revealing high on-off ratios. Figure taken from Braun et al.⁹⁰

Atomically precise graphene nanoribbons are a promising emerging class of designer quantum materials with electronic properties that are tunable by chemical design. However, many challenges remain in the device integration of these materials, especially regarding contacting strategies. We report on the device integration of uniaxially aligned and non-aligned 9-atom wide armchair graphene nanoribbons (9-AGNRs) in a field-effect transistor geometry using electron beam lithography-defined graphene electrodes. This approach yields controlled electrode geometries and enable higher fabrication throughput compared to previous approaches using an electrical breakdown technique. Thermal annealing is found to be a crucial step for successful device operation resulting in electronic transport characteristics showing a strong gate dependence. Raman spectroscopy confirms the integrity of the graphene electrodes after patterning and of the GNRs after device integration. Our results demonstrate the importance of the GNR-graphene electrode interface and pave the way for GNR device integration with structurally well-defined electrodes.

Contributions:

R.F. performed the graphene synthesis and O.B. transferred the graphene to the target substrate. A.O. performed the electron beam lithography. S.M. and A.F. helped with the determination of the gap size. G.B.B and R.D. performed on-surface GNR synthesis and STM-imaging, providing samples and performed the GNR transfer. Electrical measurements were performed and analyzed by the author, with help by S.K., J.O., M.E.A., M.L.P. and M.C.

4

This chapter has been adapted from Braun et al.⁹⁰

4.1 Introduction

New classes of electronic nanomaterials often require several years to decades of research to develop reliable electrical contacting approaches. For example, it took more than two decades to go from the first carbon nanotube (CNT) field-effect transistors to their successful integration into microprocessors.^{131–135} Similar timescales were also needed to develop the field of semiconducting nanowires from the first reporting of Si-whiskers to their reliable use for quantum computing.^{136–138} In the case of Si-nanowires, surface passivation of the contact area and thermal annealing were found to increase device performance significantly.¹³⁹ More recently, bottom-up synthesized atomically precise graphene nanoribbons (GNRs) have attracted a lot of attention as their electronic and magnetic properties can be tailored by bottom-up synthesis. However, contacting GNRs using top down fabrication processes turned out to be highly demanding, in particular, because of their nanoscale dimensions of around 1 nm in width and lengths reaching typically 5–50 nm.^{13,15,19,116,125} Standard electron beam lithography and metallization processes have been used by several groups for contacting GNRs.^{13,122,140} However, these methods involve processing and metallization on top of transferred GNRs and can lead to the introduction of contaminants at the contact-GNR interface and/or GNR damage. This approach is particularly problematic for GNRs with reactive and/or functionalized edges.^{17,18,141,142} Alternatively, GNRs have also been transferred on top of predefined metal electrodes.¹⁴³ This approach may be suitable for GNR films in which hopping of charge carriers over larger distances is the dominating effect on transport properties but may lead to ill-defined 3-dimensional junction geometries when contacting a single GNR. Furthermore, metal electrodes in short-channel devices lead to the formation of image charges and screen the applied electrostatic gate field used to tune the electronic transport, requiring advanced gating approaches such as ionic liquid gating for reaching a sufficient gating efficiency.^{13,144–146} Finally, we expect that the disorder of metallic electrodes at the atomic scale leads to uncontrolled local electrostatic potential surrounding the nanoscale object, a problem that 2D covalent crystals have the potential to overcome. The above-mentioned issues can be addressed by the use of graphene electrodes. Graphene, with its monoatomic thickness, allows for the GNRs to be transferred on top of the electrodes, without introducing significant bending of the GNRs bridging the source and drain electrodes. The π - π orbital overlap is widely used for contacting two-dimensional materials^{147,148} and the charge carrier density in the graphene leads can be tuned by electrostatic gating. Graphene electrodes fabricated using the well-established electrical breakdown procedure result in gaps separating the electrodes by a few nanometers and are a suitable way to contact graphene nanoribbons of various types.^{15,19,30,107,149,150} However, inherent geometric variation in such electrodes requires particular care during data analysis. This is necessary to disentangle the signal of the material under study from the direct tunneling current contributions, potential localized lead states, and to exclude reconnected graphene electrodes or connected graphene islands.^{29,110,112,151} Moreover, the long fabrication time of each gap impacts the scalability of this approach. Here, we report on graphene electrodes fabricated by electron beam lithography using the combination of an optimized etch mask and etching recipe, which results in electrode separations down to <15 nm. This clean and well-defined electrode geometry helps to overcome the challenges emphasized above

and represents an appealing platform to contact GNRs with a length of length above 15 nm. Moreover, the availability of large-scale graphene produced by chemical vapor deposition allows us to fabricate up to 1'680 devices per chip. We demonstrate the suitability of our nanofabrication approach by integrating atomically precise 9-AGNRs in a field-effect transistor device.¹¹⁵ 9-AGNRs are the ideal testing material due to their long-term stability and their well-studied transport properties.^{123,126} In addition, we show that thermal annealing is an efficient way to enhance the electrical device properties leading to an increase in the on-state current of up to an order of magnitude at room temperature. Moreover, our gate-dependent electrical transport measurements show on-off ratios reaching values as high as 10^4 . The results obtained in this work open perspectives for the integration of different types of GNRs in more complex device geometries.

4.2 Graphene electrodes and electronics

4.2.1 Graphene patterning

To define graphene electrodes, graphene on Si/SiO₂ with predefined metal electrodes and optimized areas for Raman spectroscopy is patterned by EBL as detailed below. Two exposure steps (100 kV write mode, EBPG5200, Raith GmbH) are done, each followed by an RIE step.⁸⁸ For the first exposure step, the sample with graphene is spin-coated with 160 nm thick PMMA 50K (AR-P 632.06, Allresist GmbH) and 90 nm thick PMMA 950K (AR-P 672.02, Allresist GmbH), each baked at 180 °C on a hotplate for 5 min. Following a first electron beam exposure, the resist is developed in Methyl-isobutyl-ketone (MIBK):IPA (1:3) at room temperature for 60 seconds. RIE (15 sccm Ar, 30 sccm O₂, 25 W, 18 mTorr) for 30 s is used to remove the accessible graphene. PMMA is removed using acetone, IPA, and N₂ dry blow. After this prepatterning of the graphene, a second EBL and RIE step (same etching plasma parameters as above, time reduced to 6 s) are carried out to separate the graphene electrodes. Two different approaches for the fabrication of etch masks were investigated:

i) **CSAR mask:** In the first approach, a 60 nm thick CSAR resist (AR-P 6200.04, Allresist GmbH) is spin-coated. Following the second electron beam exposure, the resist is developed using a suitable developer (AR 600-546, Allresist GmbH) at room temperature for 1 min followed by an IPA rinse. After RIE, the etch mask is removed by immersing in 1-Methyl-2-pyrrolidinone (NMP, Sigma Aldrich) at room temperature for 10 min followed by 60 min at 80 °C, cooled down for 30 min, rinsed with IPA, and blown dry with N₂.

ii) **PMMA mask and cold development:** In the second approach, a 60 nm thick layer of PMMA 950K (AR-P 672.02, Allresist GmbH) diluted in anisole (1:1) is spin-coated. The development of the resist after electron beam exposure is done in MIBK:IPA (1:3) at 2 °C for 45 s followed by an IPA rinse at 2 °C for 10 s. After RIE the etch mask is removed in the same way as after the first RIE step.

Both approaches yield clean and well-separated graphene electrodes with reproducible gap sizes (see Subsection 4.3.2 and Appendix 4.4).

4.2.2 Graphene electrode separation

The separation of graphene electrodes (gap size) is assessed using scanning electron microscopy (SEM) (Helios 450, FEI) and atomic force microscopy (AFM) (Icon, Bruker) to independently determine the electrode separation. The AFM is equipped with a sharp cantilever (tip radius = 2 nm) (SSS-NCHR-20, Nanosensors) operated in soft-tapping mode. The electrode separation by AFM is determined via a Python script, based on the nanoscope library. Each line scan is smoothed individually using a Savitzky-Golay filter and the edges of the gap are determined by selecting the local maxima and minima in the first derivative on either side of the gap minimum. It was not possible to apply the same procedure to the SEM data due to the low contrast between the graphene and the SiO₂ of the target substrate and the small separation of the graphene electrodes. Therefore, the average and standard deviation are obtained from 20 manual measurements that are equally spaced along the gap.

4.2.3 Graphene quality after patterning

The patterned graphene electrodes are analyzed in air by 2D Raman mapping (Alpha300R, WITec) using a 488 nm incident laser beam at 1.5 mW and a 100x objective (NA = 0.9) with a pixel spacing of 100 nm.⁸⁸

4.2.4 Electronic measurements

All electronic measurements are performed under vacuum conditions ($<10^{-6}$ mbar) in two different probe stations.

The FETs consisting of aligned GNRs using the polymer-assisted transfer are characterized in a custom-built probe station equipped with nanoprobe (miBot, Imina Technologies SA). A data acquisition board (USB-6289, National Instruments) is employed to apply the bias and gate voltages and read the voltage output of a custom-made I-V converter (Model SP983, Basel Precision Instruments GmbH).

The FETs consisting of GNRs using the polymer-free transfer method are characterized in a commercially available probe station (Lake Shore Cryogenics, Model CRX-6.5K). A data acquisition board (ADwin-Gold II, Jäger Computergesteuerte Messtechnik GmbH) is employed to apply the bias and gate voltages and read the voltage output of the I-V converter (DDPCA-300, FEMTO Messtechnik GmbH).

4.3 Results and discussion

4.3.1 Graphene electrodes

The fabrication process yielding graphene electrodes for contacting graphene nanoribbons is illustrated in Figure 4.2 and described in detail in the Section 4.2.

We stress that for etching nanogaps into graphene the interplay of the used etch masks, their removal, as well as the chosen etching parameters, plays an even more crucial

The nanoscope library source: <https://github.com/jmarini/nanoscope>, October 2020

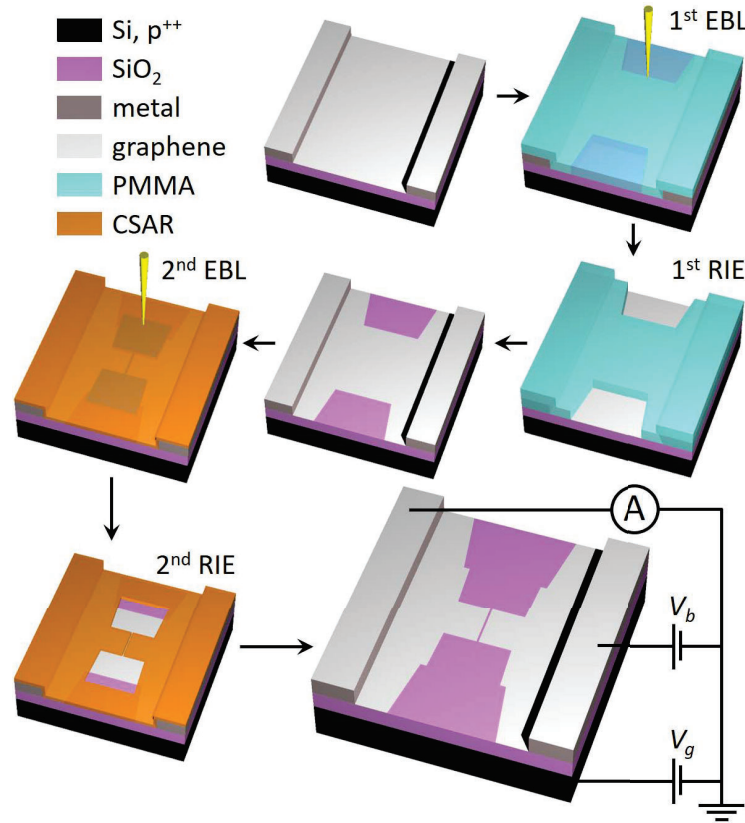


Figure 4.2 Fabrication procedure and electrical measurement configuration. Three-dimensional illustration describing the fabrication steps of the EBL-defined graphene electrodes. The resist regions exposed during electron beam lithography are marked with darker colors. Arrows indicate fabrication order. The electrical measurement configuration is schematically shown in the last, slightly larger, illustration. See main text for details. Figure taken from Braun et al.⁹⁰

role in obtaining the wanted feature resolution than for evaporated features. First, it is crucial to split the resist exposure by electron beam into two steps to ensure the proximity-effect while writing the coarse features does not affect the sensitive exposure of the nanogap. For the second exposure, we use a beam step size of 5 nm and beam current of 3 nA resulting in a beam diameter of 5 nm. Second, for the first RIE step to pattern the coarse features, a double layer etch mask is employed that helps reduce contaminations on graphene by using a low molecular weight resist in direct contact with the graphene and a high molecular weight resist on top for high contrast and feature definition. We note that the undercut in the double layer resist does not pose a problem, as the feature sizes in this first RIE step are not critical. For the second RIE step, an undercut is unwanted since it would result in a larger electrode separation. The smallest graphene electrode separation (<15 nm) is achieved using CSAR resist, due to its excellent performance in terms of resolution, sensitivity, and etch resistance.¹⁵² Third, we emphasize that the duration of the second RIE step has to be short enough to avoid a sideways etching of the resist mask but long enough that the monolayer graphene is fully etched. This trade-off leads to a delicate balance between device yield

and electrode separation. Last, the removal of the etch mask has to be done using processes that are sufficiently mild to preserve graphene's quality but sufficiently harsh to leave little residues on the electrodes. We, therefore, employed only acetone and NMP since their effects on graphene's quality are well studied.^{101,153–155} Since the used GNR growth substrates do not exceed 5×5 mm in size, after fabrication the chip is broken into smaller pieces with 100-200 devices each before the GNRs are transferred to the target substrate.

4.3.2 Characterization of patterned graphene electrodes

Before the electrode separation is assessed, an optical inspection of the graphene electrodes is carried out. Graphene electrodes containing graphene folds in the central region or those damaged during the fabrication process are excluded from further investigation. A typical optical image of the graphene electrodes can be seen in Figure 4.3a). The electrode separation is assessed by SEM and AFM and representative scans are shown in Figures 4.3b) and c), respectively, with the extracted gap sizes displayed in Figure 4.3d).

We find that the graphene electrodes fabricated with the CSAR etch mask (see experimental section) are separated by <15 nm for the smallest designed geometry. The fabrication method using the PMMA etch mask yields a slightly larger electrode separation of ~ 27 nm in the smallest case (See Appendix 4.A.). Hence, these electrodes are only used for the uniaxially aligned 9-AGNRs to have high device yields. Figure 4.3d) also shows that the measured electrode separation for the CSAR etch mask does not scale linearly with the width of the gap in the design. We attribute this behavior to the proximity-effect correction procedure that is applied for the exposure dose calculation. For a successful device integration of GNRs, we consider it important to have graphene electrodes with little to no defects after patterning. Raman spectroscopy maps confirm the high quality of the graphene electrodes after processing (see Figure 4.3e). The D-band intensity map shows negligible intensity in the pristine area and an intensity increase at the edges and in the nanogap region. Raman spectroscopy further revealed a clear drop in the intensity of the G- and 2D- bands where the graphene electrodes are separated, indicating a lower amount of carbon and breaking of the crystal structure. The 488 nm excitation source was chosen to reach a minimal laser spot size for the best spatial resolution. The high graphene quality was also confirmed by measuring the current versus applied gate voltage of a reference device that underwent the same fabrication procedure except for the 2nd RIE step, revealing field-effect mobilities of $\sim 2'500$ cm²/Vs for electrons and $\sim 1'800$ cm²/Vs for holes (see Chapter 3). We optically assessed 91 devices for the two transfer methods based on which we excluded 24 devices. After the initial optical assessment and before the 9-AGNR transfer, each device is characterized electrically. A schematic illustration of the electronic wiring for the latter is depicted in figure 4.4 a). As shown in figure 4.4 b) a high yield of clearly separated graphene electrodes (>1 T Ω) of 79.1 % is found. The remaining 20.9 % of graphene electrodes are either weakly (<1 T Ω) or fully connected (<1 G Ω). Representative I-V characteristics for the three cases are shown in Figure 4.4c). Possible explanations for the poorly formed nanogaps may include the presence of (partially etched) multilayer graphene at the constriction and contamination during/after processing. These devices are not investigated further.

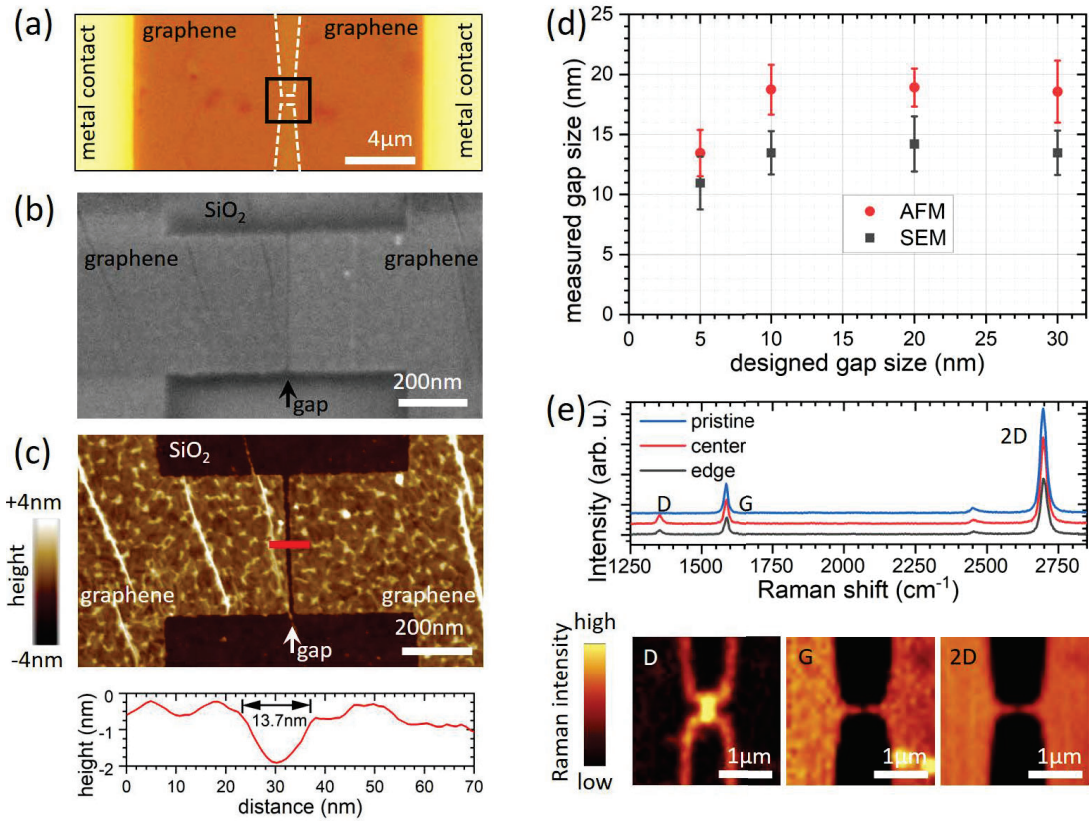


Figure 4.3 Electrode separation of devices fabricated using CSAR mask. **a)** Optical image of a representative device. The central region of the same device is shown in **b)** an SEM image and in **c)** a height profile (AFM scan) including a line cut through the central region (red) showing the electrode separation. **d)** Electrode separations measured by SEM and AFM for four devices with different gap sizes. **e)** Raman intensity maps for D-, G- and 2D-bands in the area indicated with a black square in **a)** and spectra extracted at representative positions. Figure taken from Braun et al.⁹⁰

4.3.3 Electrical characterization and effect of annealing

After the initial characterization of the devices, 9-AGNRs were transferred on top of the graphene electrodes. Figure 3.7 shows high-resolution scanning tunneling microscope (STM) images of 9-AGNRs on the growth substrates presenting their alignment. We note that the growth and transfer methods were adapted to the gap size. For the devices fabricated using the PMMA mask (gap size ~ 27 nm), uniaxially aligned GNRs were transferred oriented perpendicular to the gap to maximize the chance of bridging both electrodes. For the devices fabricated using the CSAR mask (gap size < 15 nm), based on geometrical considerations, we anticipate a higher probability of bridging that allows for investigating non-aligned 9-AGNRs transferred using a polymer-free method. In both cases, the integrity of the 9-AGNRs after the transfer process was confirmed by Raman spectroscopy (see Appendix 4.4). In particular, the presence of the longitudinal compressive mode (LCM) is strong evidence for the high quality of the 9-AGNRs after the transfer process due to its high sensitivity to structural damage.⁸⁹ Figure 4.5a) shows typical I-V characteristics recorded at room temperature under

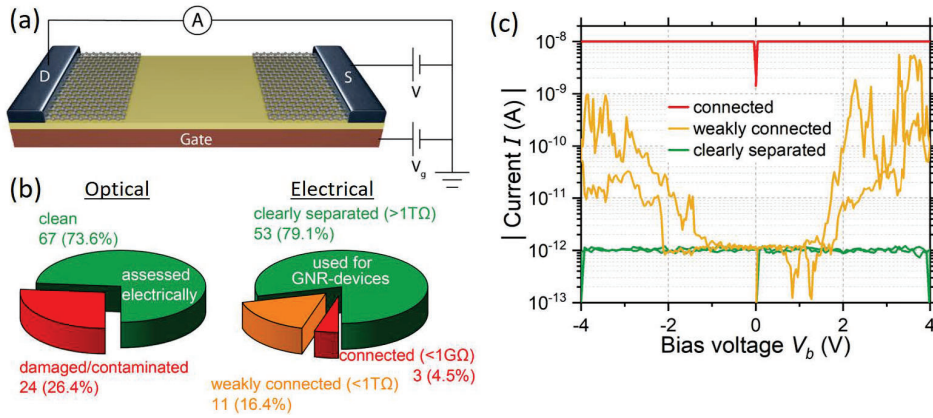


Figure 4.4 Electrical characterization of electrode separation .a) Illustration of the electrical measurement scheme for characterizing the separation of the graphene electrodes. **b)** Statistics on electrode separation by optical and electrical assessment. **c)** I-V characteristics of three representative devices before 9-AGNR transfer Figure taken from Braun et al.⁹⁰

vacuum conditions ($<10^{-6}$ mbar) on different devices fabricated using the two transfer methods. We observe highly nonlinear I-V curves with currents up to 0.5 nA at 1 V bias voltage. The inset presents a schematic of the device and the electrical characterization scheme. To improve the maximum currents through the devices, we investigated the effect of thermal annealing. As the transfer of the 9-AGNRs onto the target substrate exposes the graphene to humidity and even water in the case of the polymer-assisted transfer, the samples were heated to 150 °C for 30 minutes at 10^{-6} mbar to remove water residues at the graphene/GNR interface. The heating also provides energy for local geometric rearrangements. To evaluate the benefit of this thermal treatment, the maximum currents observed at a gate voltage of 0 V and a bias voltage of 1 V are compared before (as transferred, $I_{\text{transferred}}$) and after thermal annealing (I_{annealed}). Figure 4.5b) shows a scatter plot of the ratio $I_{\text{annealed}}/I_{\text{transferred}}$ for all devices. In all samples, an increase by one order of magnitude or higher in 50 % of the devices is observed, with individual junctions showing an increase as high as a factor of 100. During annealing, several processes can take place and affect the conductance of the junctions. By reducing the number of water adsorbates at the GNR-graphene interface, the two nanomaterials can go into a more intimate contact, which can lead to an increased electronic coupling similar to what has been observed for decoupled graphene monolayers.^{156,157} Water removal may also result in reduced doping of the GNRs, leading to a probing of the more intrinsic GNR transport properties, similar to what has been reported for graphene FETs on SiO₂.^{158,159} Studies of molecules with planar anchor groups on graphene electrodes revealed that the binding energy to allow sliding and bending is around 0.01 eV, significantly lower than the energy $k_B T$ (~ 0.04 eV) provided during the thermal annealing process.^{160–162} Hence, this energy is likely sufficient to cause local displacement and geometrical rearrangements of the GNRs that can lead to both improved contacts but also loss of GNRs within the junction resulting in a decrease of overall conductance in multi-GNR junctions as can be seen by a conductance decrease in about 20 % of the devices after annealing. We note that at the annealing temperature

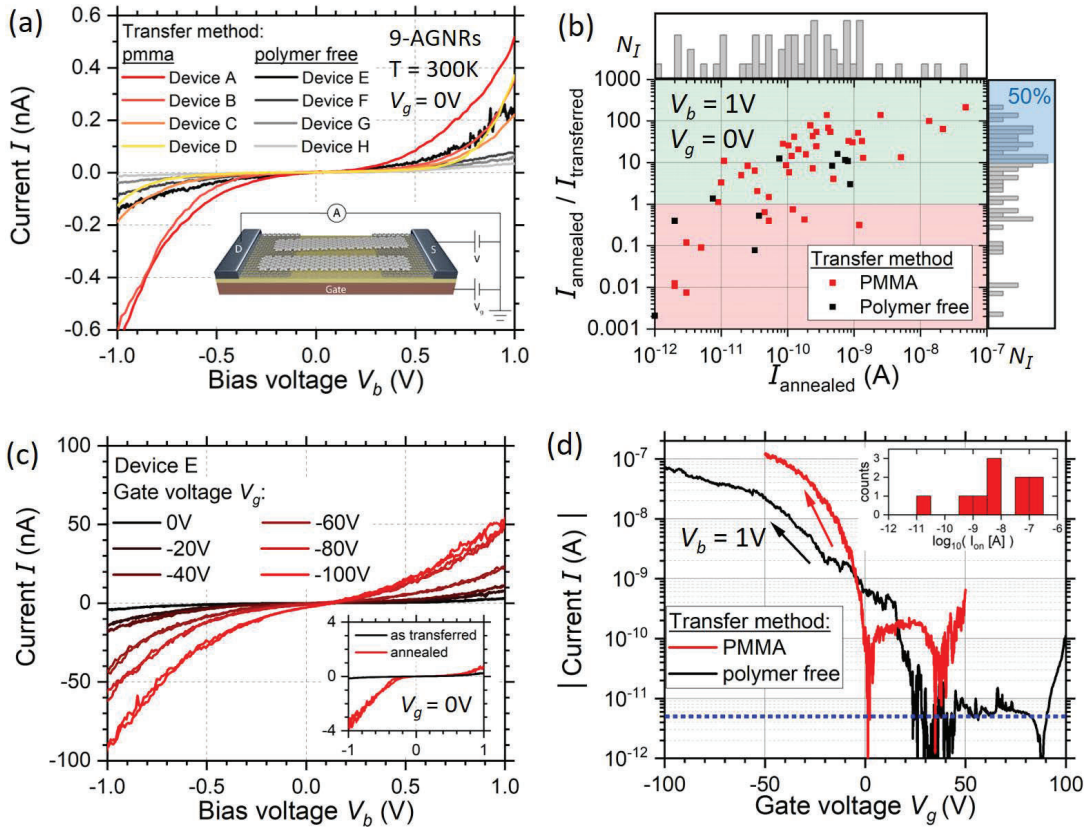


Figure 4.5 Electrical characterization of 9-AGNR based devices and annealing effects . a) I-V characteristics of four representative 9-AGNR devices for each of the two transfer methods before thermal annealing. **b)** The main panel shows the ratio of current values measured before and after the annealing of the devices. Current increase and decrease are highlighted in green and red respectively. Histograms of $I_{\text{transferred}}$ and $I_{\text{annealed}}/I_{\text{transferred}}$ are shown in the outer panels on the top and the right respectively. Highlighted in blue are 50 % of the devices. **c)** I-V characteristics of device E were recorded at different applied gate voltages after annealing. Inset shows the effect of annealing on the I-V characteristics. **c)** Current – gate voltage dependence at fixed bias voltage for two devices. Arrows indicate the direction of the gate sweep. The blue dashed line indicates the noise floor of the I-V converter. The inset shows a histogram of the on-currents. Figure taken from Braun et al.⁹⁰

used, no lateral fusion of GNRs is expected.^{117,149}

In figure 4.5c), we measured current-voltage characteristics at various applied gate voltages. The plot indicates slightly asymmetric characteristics with a strong gate dependence. The presence of only little hysteresis effects between the up and down sweep of the applied bias voltage indicates high device stability. The observed hysteresis is attributed to the influence of trap states in the oxide.¹⁶³ Figure 4.5d) shows a measurement of the current as a function of gate voltage for two devices, recorded at a fixed applied bias voltage of 1 V (see Appendix 4.C.). The traces show a drastic increase of the conductance for negative gate voltages, pointing towards hole transport through the valence band (or highest occupied molecular orbital (HOMO)).¹³ The

gentle increase in conductance at positive gate voltages suggests the presence of another transport channel entering the bias window, presumably the conduction band (or lowest unoccupied molecular orbital (LUMO)). In the gate sweeps, we obtain maximal on-off ratios of up to 10^4 , with an on-current of 70 nA at a gate voltage of -100 V and an off-current of 5 pA at a gate voltage of +40 V for the black curve in figure 4.5d). The maximum observed values for the on-off ratios is about a factor of 100 higher than reported by Martini et al. and El Abbassi et al. contacting 9-AGNRs using graphene electrodes fabricated by electrical breakdown, and about a factor 50 higher than reported by Jangid et al. for top-down fabricated GNRs.^{15,149,164}

4.4 Conclusions

We successfully integrated 9-AGNRs in a FET geometry using graphene electrodes fabricated via optimized e-beam lithography and reactive ion etching resulting in electrode separations as small as <15 nm. Room-temperature electrical transport measurements revealed nonlinear current-voltage characteristics and a strong gate dependence. Furthermore, we found that thermal annealing improves the on-currents after annealing by at least one order of magnitude in 50 % of the investigated devices. In addition, we performed gate sweeps revealing on-off ratios as high as 10^4 with the highest on-currents of 70 nA at a bias voltage of 1 V. The developed technology to fabricate graphene electrodes separated by <15 nm is a major step forward towards all-carbon electronics and offers encouraging prospects for room-temperature ambipolar 9-AGNR-FET behavior. The presented platform could also be applied to short channel FETs using two-dimensional materials as channel material, as reported for MoS₂ or phase-change memory devices.^{165,166} Importantly, this platform will allow for the integration of GNRs of different widths as well as different edge structures for exploring more exotic transport properties.^{19,167}

Appendix 4.A. SEM image of device fabricated with PMMA mask

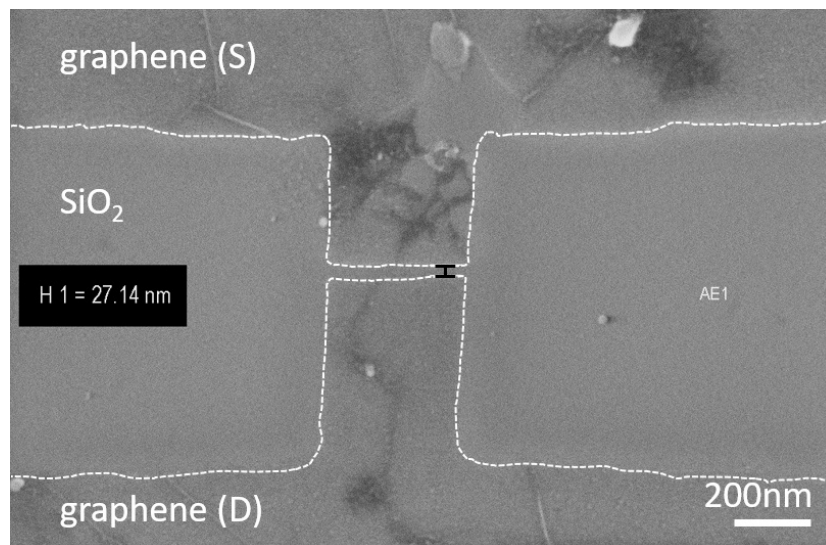


Figure 4.6 Scanning electron micrograph of the central region of a device made with a PMMA etch mask. The graphene source and drain (S and D, respectively) electrodes are separated by around 27 nm (indicated in black). White dashed line as guides to the eye.

Appendix 4.B. Raman characterization of transferred 9-AGNRs

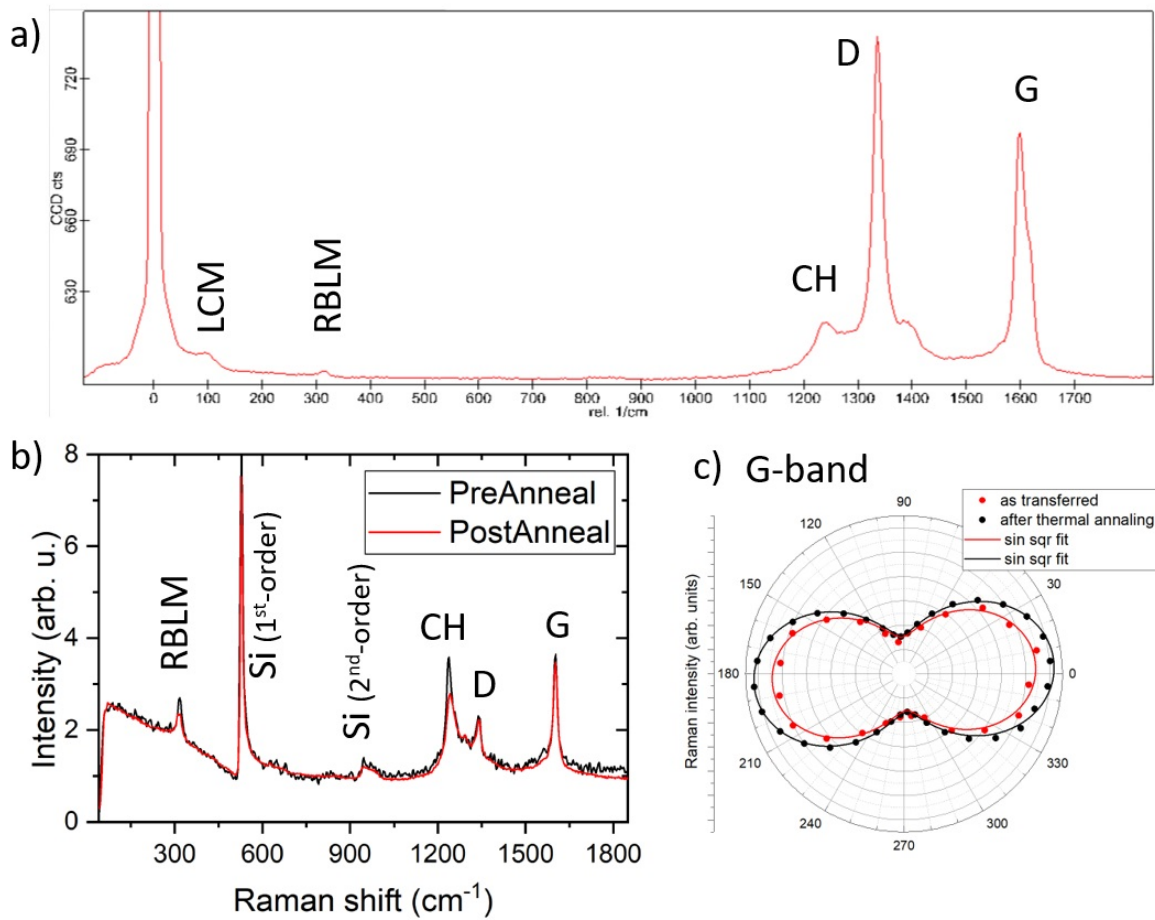


Figure 4.7 Raman characterization of 9-AGNRs after transfer. Acquired under vacuum conditions in a custom-built vacuum chamber as reported elsewhere.⁸⁸ **a)** Average Raman spectra acquired with 488 nm excitation on a Raman optimized area after the transfer of 9AGNRs revealing the typical Raman bands: G, D, CH, RBLM, and LCM.^{89,115,123} **b)** Raman spectra acquired with 785 nm excitation close to the electrical device on SiO_2 before and after thermal annealing (PreAnneal and PostAnneal, respectively) showing no clear difference, hence showing the preservation of the GNR integrity upon annealing. **c)** Polarization dependence of the 9-AGNRs G-band. The sinus-squared fit, reveals a misalignment of the GNRs with respect to the source-drain axis (0°) of around 4° . This small difference is attributed to a not identical placement of the sample for the Raman measurements. The data after annealing is linearly scaled in intensity for better distinction.

Appendix 4.C. Extended gate voltage dependence data

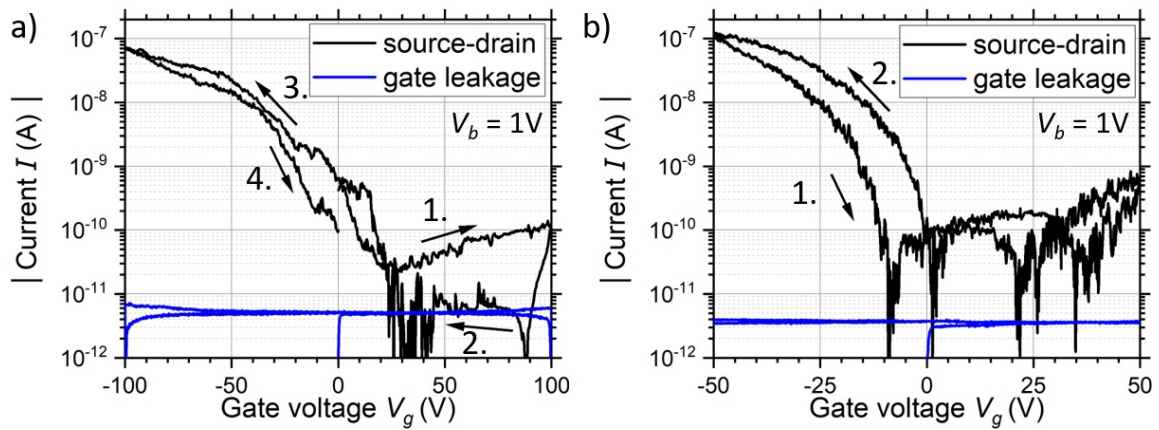


Figure 4.8 Extended gate voltage dependence data. Current vs. gate voltage curves at fixed bias voltage (black) including corresponding gate leakage curves of two devices shown in the main text. GNRs transferred using **a)** polymer free and **b)** PMMA based method. Numbered arrows indicate the direction of the gate voltage sweep.

5 Electrical transport properties of GNRs

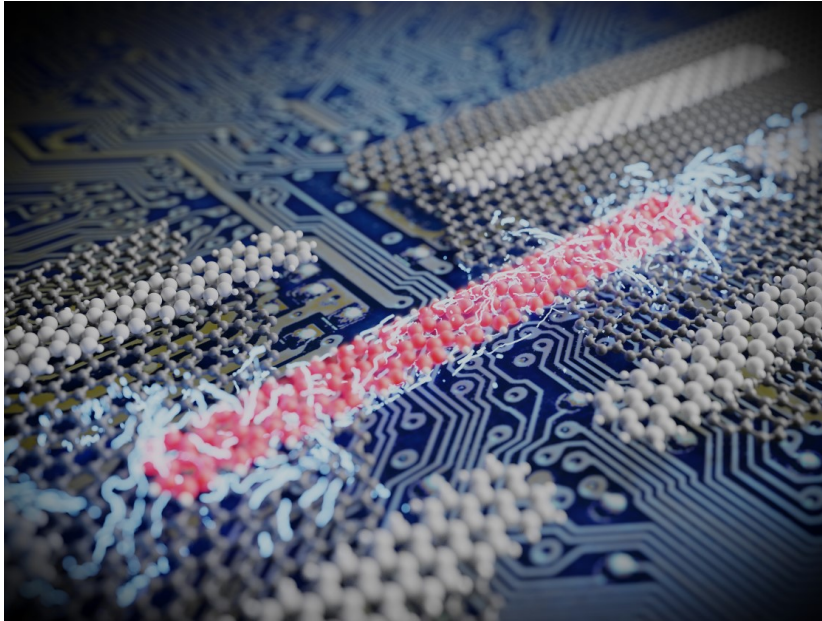


Figure 5.1 Artistic illustration of an individual 5 atom wide armchair graphene nanoribbon (5-AGNR) contacted using graphene electrodes. Visualization: Mickael L. Perrin

This chapter presents the latest results of device integration of GNRs, contacted using graphene electrodes. We start by motivating the use of graphene electrodes instead of metal electrodes which allow for an integration of the GNRs in the very last fabrication step. Transport results obtained on films of wide band gap 9-AGNRs are presented, showing a hopping of charge carriers over distances longer than the average GNR length. This film behavior is studied for various densities and temperatures. Next, we report on transport measurements of 3 different kinds of low band gap GNRs of the armchair family. Finally, we demonstrate that also GNRs with partially zigzag edges can be integrated into devices. This is challenging since the zigzag edges are more reactive than their armchair counterpart. Due to their edge morphology, these so-called pyrene-GNRs exhibit electronic states close to a topological phase boundary, which additionally results in a very low band gap. We conclude with a summary and give an outlook on where the field is heading to.

Parts of this chapter have been adapted from El Abbassi et al.¹⁵ and Sun et al.¹⁹.

Contributions:

O.B. fabricated all the devices and performed transport measurements on the 9-AGNRs films, on the kinked-5-AGNRs, on the 17-AGNRs and, with help of J.O., on the pyrene-GNRs. M.E.A. developed the electric breakdown technique and performed transport measurements on 5-AGNR. R. Fu. performed CVD graphene growth with feedback from O.B. and J.O. M.E.A. analyzed the data on the 5-AGNRs. O.B. analyzed the data on all other GNRs. G.B.B and R.D. performed the synthesis of 9-AGNRs. G.B.B. performed the synthesis of kinked-5-AGNRs and 17-AGNRs. Q.S. performed pyrene-GNR synthesis. M.L.P. and M.C. provided support on the transport measurements and data analysis. M.C. supervised the presented studies.

5.1 Introduction

Field-effect transistors are the core of integrated circuits (IC). Their main function is to efficiently conduct current in the on-state or block it in the off-state. State of the art CMOS based FinFETs operate with current on/off ratios¹⁰⁵ $I_{\text{on}}/I_{\text{off}}$ of 10^7 .¹⁶⁸ Competing with the well-established CMOS technology would be like taking Don Quixotes stand against the windmills.¹⁶⁹ However, the *International roadmap for devices and systems (IRDS)* points out that there is room for *More than Moore*, pointing towards integration of 2D-materials and novel computing architectures.¹⁶⁸ The integration of these novel materials in the last possible fabrication step has lead to some drastic improvement in the device performance and scalability, for example in MoS₂.^{170,171} Along similar lines, we are pushing this approach one step further by integrating the material of interest, in our case graphene nanoribbons, at the very last step by transferring it on top of substrates with predefined graphene electrodes.

Bottom-up synthesized GNRs have attracted considerable interest as one of these future electronic building blocks. This mainly due to their atomic precision, which top-down etched GNRs lack, and their tunable edge structure and width.¹⁰⁻¹² Bottom-up GNRs can therefore be seen as a *Designer Quantum Materials*, where the material properties can be designed by selecting the appropriate precursor molecule(s). The designed materials can vary in their band gap,¹⁶ form pn-junctions,¹⁴ quantum dots,¹⁵ spin-chains,¹⁷² and even exhibit topologically non-trivial phases.^{17,18,173} Synthesized under UHV-conditions, GNRs can reach lengths of several dozens of nanometers.¹²⁵ This allows for contacting them with electrodes that are defined by well-controlled top-down processes. In the following, we will discuss the contacting of GNRs, which is not a trivial task due to their nanometer-scale dimension.

GNRs that are contacted with metal electrodes suffer from performance limitations by screening of the electric field by the electrodes.¹²² Additionally, the contact resistances, arising from the formed Schottky barriers at the GNR/metal interface, limit the achievable on-currents.¹³

Graphene is selected as a contact material due to its flatness, the π - π -stacking to the GNRs, and, as discussed later in Chapter 6, the option to individually tune the charge-carrier density in the electrodes and the GNRs. The charge-carrier density in graphene is also much lower than in metal electrodes and hence cannot fully screen the electrostatic field from the gate.^{27,174} Also from a material perspective, it can be favorable to build a device with only one atomic species (if one neglects the hydrogen termination), in particular, if it can be avoided to use heavy metal ions. The graphene electrodes are separated by two different methods, resulting in either sub-5 nm gaps by using the electrical breakdown technique (see Chapter 3) or $d < 15$ nm gaps by using electron beam lithography (see Chapter 4). The choice of electrode separation method is based on the length L of the GNRs. Figure 5.2 illustrates the device integration process. The illustration shows that a few processes have to work well, separately and together, to fabricate a working device. We want to emphasize that the GNRs are always transferred as a film. By selecting the graphene electrode separation d larger than the average GNR length L , one can probe the film behavior, while by choosing $d < L$, one can assume that the transport is dominated by single/few GNRs.

This chapter shows that using graphene electrodes, GNRs with different edges and

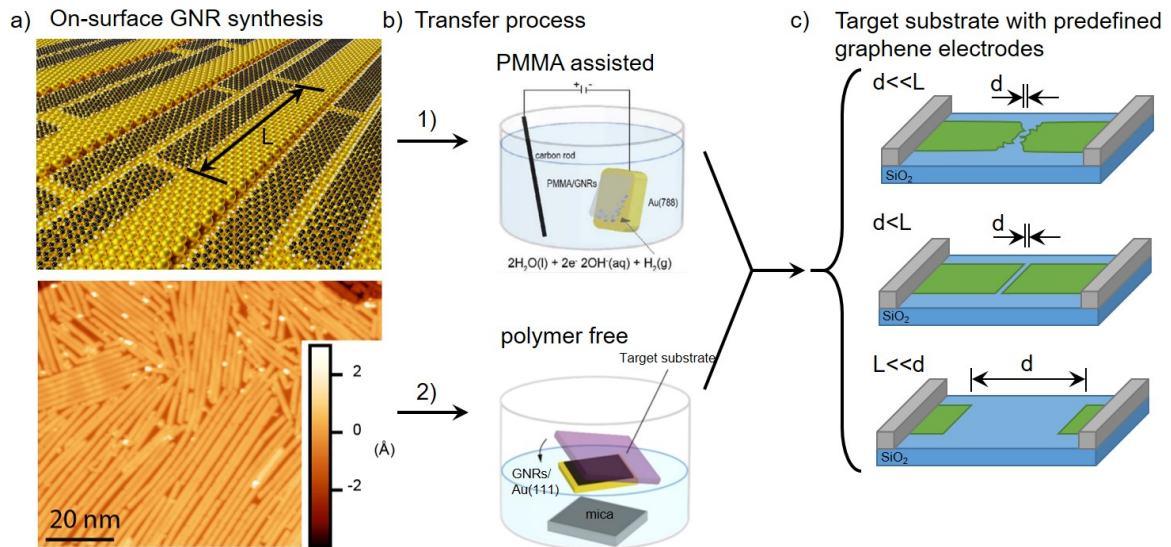


Figure 5.2 Device integration of GNRs for electrical transport characterization. a) Top: Schematic of GNRs on growth surface, here uniaxially aligned 9-AGNRs with a medium dense coverage on Au(788). The GNR length is indicated by L . Bottom: STM image of highly dense, nonaligned 9-AGNRs on Au(111)/mica ($V_b = -1.5$ V, $I_t = 5$ pA) b) The transfer process to the target substrate is determined by the growth process and happens via two routes. 1) PMMA assisted: Electrochemical delamination of PMMA/GNRs from Au(788) and PMMA removal on target substrate. 2) polymer free: GNRs/Au delamination from mica and gold etching on target substrate. c) The target substrate has predefined graphene electrodes, separated by a distance d and are selected with respect to L . Figure adapted from Borin Barin et al.¹²³ and Overbeck⁸⁸

widths can be successfully integrated into FETs and their intrinsic electronic properties are probed. Since we always transfer films of GNRs, we start with discussing the properties thereof, demonstrated with the example of wide band gap 9-AGNRs. The transport properties of low band gap armchair GNRs are studied in the second section, while in the last section we present transport results on pyrene-GNRs that are, due to their edge structure, close to a topological phase boundary.

5.2 Transport measurements on wide band gap GNRs

9-AGNRs are the ideal material system for starting to explore the transport properties of GNRs. This due to their long-term stability, their average length of ~ 45 nm, and the controlled growth process allowing for different densities.

5.2.1 Transport properties of 9-AGNR films

Although there is a fundamental interest in characterizing an individual graphene nanoribbon, the on-surface synthesis approach employed in the nanotech@surfaces-Laboratory at Empa allows only for growing GNRs at a large scale, i.e: $\sim 3 \times 10^{11}$ GNRs

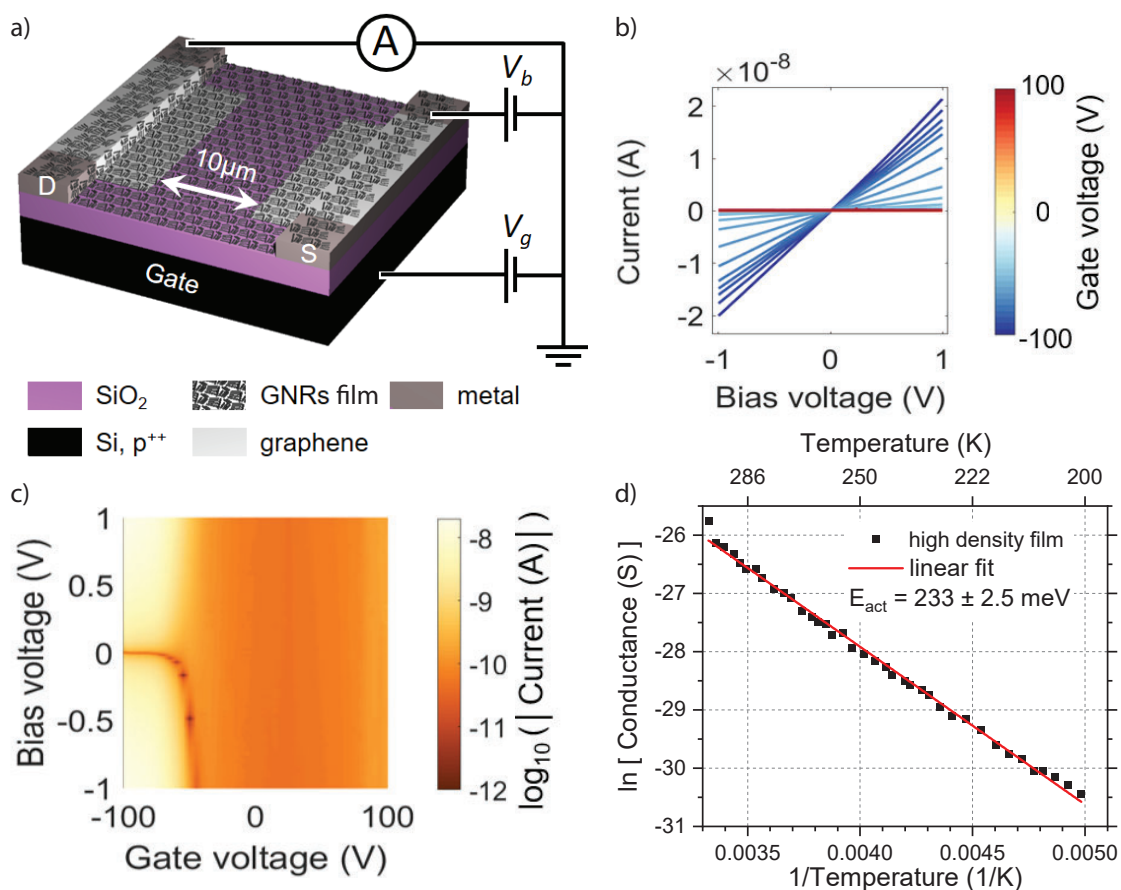


Figure 5.3 9-AGNR films: device layout and temperature dependent transport characterization. **a)** Schematic of the device including electrical measurement configuration. **b)** I-V characteristics at room temperature for various gate voltages. **c)** Current as a function of bias and gate voltages at room temperature. **d)** Arrhenius plot: The logarithm of the electrical conductance, measured at $V_g = -80$ V, is plotted against the inverse of the temperature. The slope of the linear fit to the data corresponds to $-E_{\text{act}}/k_B$ according to Equation 5.1.

on a 4×4 mm growth substrate. Subsequently, in our approach, *films* of GNRs are transferred on the target substrates with predefined electrodes.

Control devices with graphene electrodes separated by a much larger distance than the average GNR length were also characterized, the device geometry is depicted in Figure 5.3a). The graphene electrodes have a width of $\sim 150 \mu\text{m}$ and are separated by $10 \mu\text{m}$. In such a configuration, a hopping mechanism is expected to dominate electronic transport.

In Figure 5.3b) and c) the room temperature transport characteristics are depicted. Almost linear I-Vs are observed. This is similar to the results obtained on films of Au-nanoparticles as will be discussed in Chapter 8. The shape of the I-Vs is in strong contrast to the results presented in Chapter 4, where on 9-AGNR devices with an electrode separation of < 15 nm, S-shaped I-Vs were recorded. Interestingly, the strong gate dependence is very similar in both cases, showing a strong increase in currents by

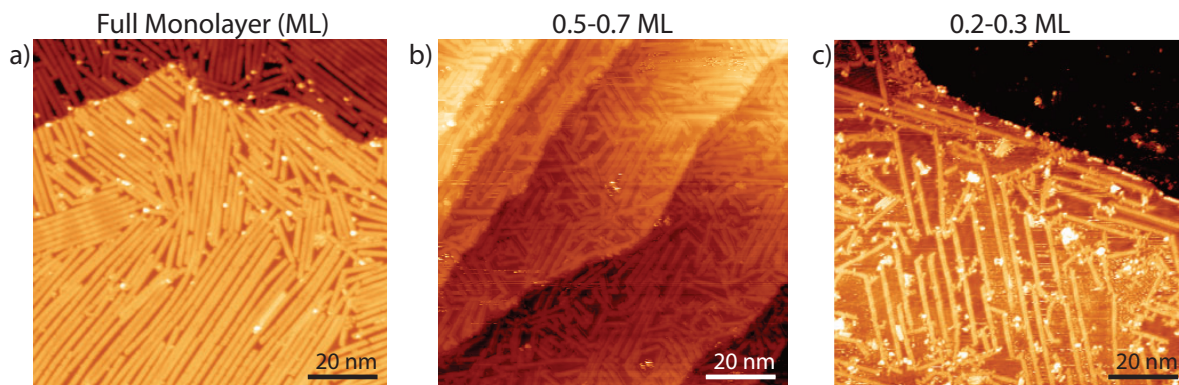


Figure 5.4 Different 9-AGNR densities on Au(111)/mica. STM images of 3 different GNR densities recorded at room temperatures. **a)** Full Monolayer (ML). **b)** 0.5-0.7 ML. **c)** 0.2-0.3 ML. STM data provided by Gabriela Borin Barin.

applying negative voltages to the back gate. Since we assume hopping of charge carriers to be the dominant transport mechanism, a strong temperature dependence is expected, according to:¹⁷⁵

$$G \propto e^{-\frac{E_{\text{act}}}{k_{\text{B}}T}} \quad (5.1)$$

where G is the conductance, E_{act} is the hopping activation energy, k_{B} is the Boltzmann constant and T is the absolute temperature in Kelvin.

Motivated by Equation 5.1, one can make a so-called Arrhenius plot to determine the activation energy. Such a plot is made by plotting the inverse temperature on the X-axis and the natural logarithm of the measured quantity on the Y-axis. In Figure 5.3b) the conductance of a device, consisting of a highly dense 9-AGNR film, is plotted in an Arrhenius plot, the fit reveals an activation energy of $E_{\text{act}} \sim 230$ meV. In a classical semiconductor band diagram picture, it is possible to interpret this activation energy further. In an intrinsic semiconductor at $T = 0$ K, where the Fermi energy is in the middle of the band gap, $E_{\text{act}} = E_{\text{gap}}/2$, where E_{gap} represents the electronic band gap, is valid.¹⁷⁶ Our measured E_{act} would lead to an $E_{\text{gap}} = 460$ meV. However, this relation can not be applied directly to the present case. As the measurement was done with an applied negative gate voltage and hence the Fermi energy lies closer to the conduction band than to the valence band. Further, we only investigated the temperature dependence of the conductance in the 200-300 K range. Below 200 K the conductance through the high-density 9-AGNR film was below the detection limit of our setup. These circumstances lead to the fact that the extracted E_{gap} is only a lower bound for the band gap of the 9-AGNR film.

To gain more insights into the hopping transport mechanism in GNR films, the density of the 9-AGNRs is lowered. The idea is that in high-density films, a hopping of charge carriers is more likely due to the dense package of the GNRs. By lowering the density, at some point, the density should be so low that the charge carriers can not hop from one GNR to the next.

Low-density films of 9-AGNRs can be achieved in a controlled way by evaporating

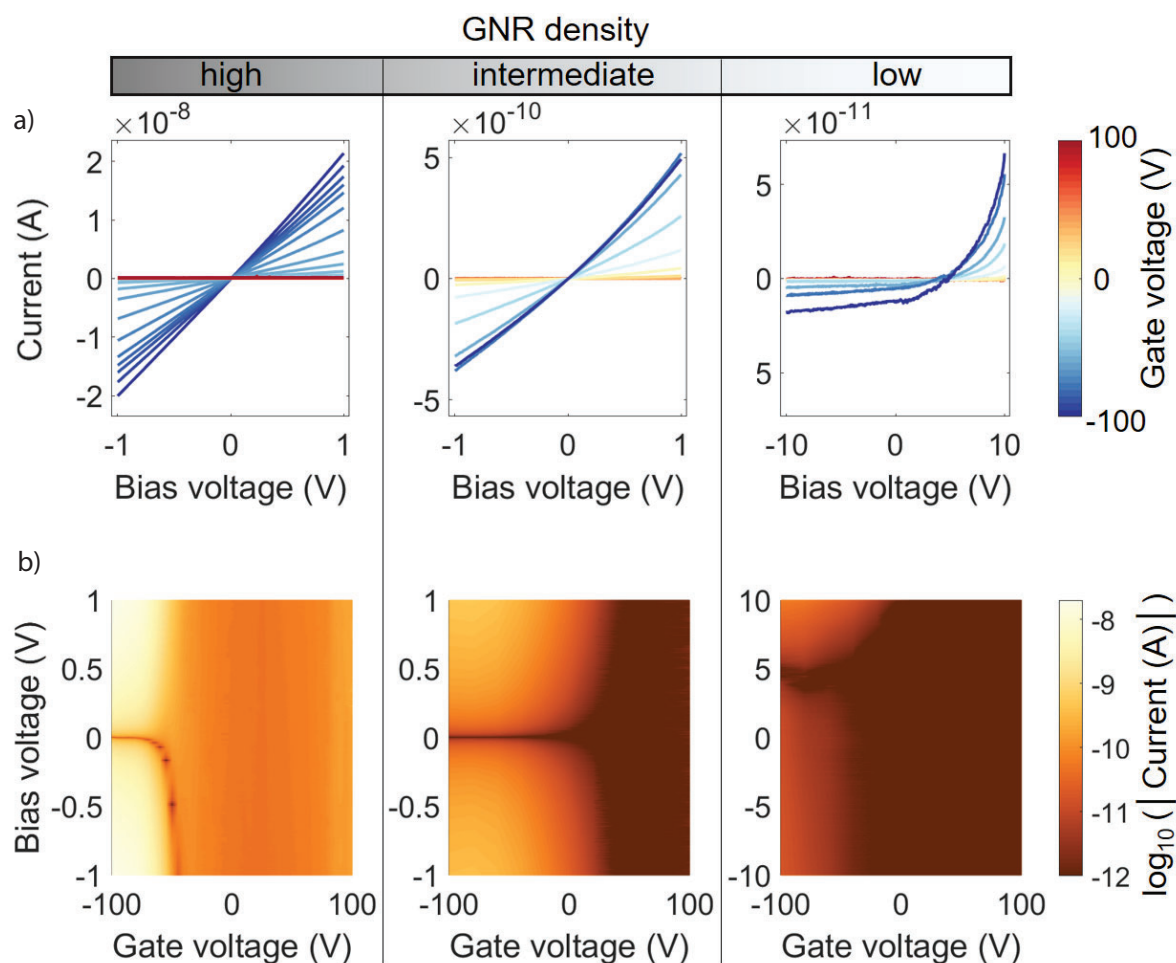


Figure 5.5 Electrical characterization of 9-AGNR films with varying GNR-densities. a) I-V curves measured on three devices with GNR densities ranging from high to low at various gate voltages. Note the increased bias range for low GNR-density. b) Same measurement as in a) plotted on a logarithmic scale. Note the varying offset. All measurements were performed at room temperature.

less than a full monolayer (ML) of precursor molecules on the Au(111) growth substrate. STM images of three different samples with varying 9-AGNRs densities are shown in Figure 5.4.

After transferring these high, intermediate, and low-density films of 9-AGNRs onto device substrates, the electrical characterization revealed quite surprising results. While in the high-density films, linear I-Vs are observed, in the intermediate dense films, the I-Vs, are slightly bent. In the very low-density films, an almost rectifying behavior is observed. What all three have in common is that they conduct more when negative gate voltages are applied to the gate. This can be interpreted that the individual GNRs influence the hopping transport substantially. The rectifying behavior in the low-density films might be caused by some self-gating effect due to the large applied bias voltages. This means, by applying -10 V in bias the potential difference to the gate is only -90 V,

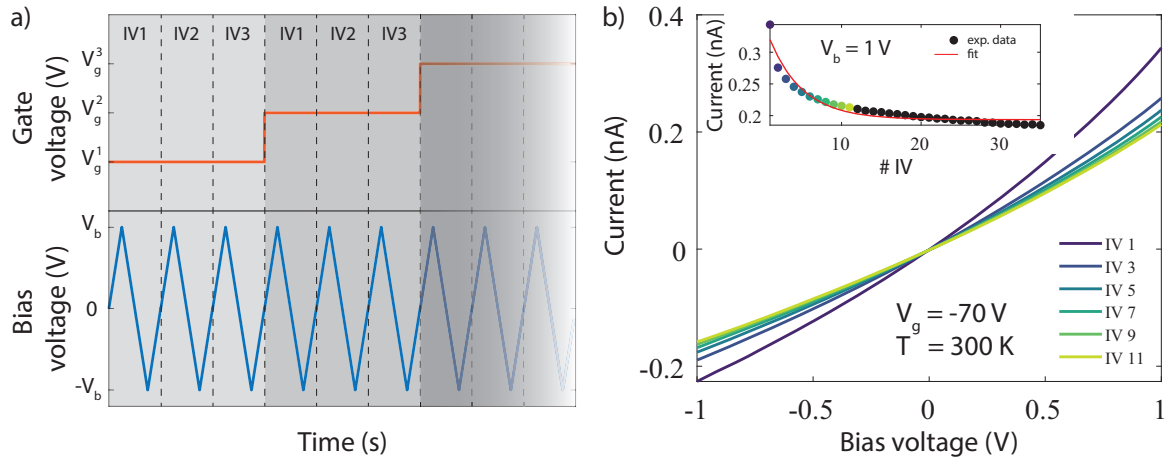


Figure 5.6 Charging effects in high-density films of 9-AGNRs. a) Schematics of the multi-IV-multi-Gate measurement procedure. b) Multiple I-V characteristics were recorded immediately after each other, after changing the gate voltage to -70 V. The inset shows the decay of the current at a fixed bias voltage of 1 V. Note the non-linearity in the I-V characteristics. All measurements are performed at room temperature.

while by applying $+10$ V, the resulting potential difference is -110 V. This effect is also present in the other two cases, but less dominant due to the higher overall currents and lower bias voltages. Additionally, the larger variety at the contacts due to the low GNR density can also cause some asymmetry in the IVs. To better understand the shape of the I-Vs of the intermediate and in particular the high-density films, we investigate in the following section potential charging effects and their evolution.

Time dependent measurements in films of 9-AGNRs

In the following, the potential charging effects on highly dense films of 9-AGNRs are investigated. This since the as transferred high-density films of 9-AGNRs cover a large area of 4×4 mm, it can be seen as building a plate capacitor to the gate. By gaining insights into the charging dynamics of this capacitor, one gains insights into the present transport mechanisms in the GNR film. The metal contact pads to the graphene are 180×180 μm , separated by 20 μm . However the dominating transport channel is 10 μm in length and ~ 150 μm in width, limited by the graphene electrodes. To study the charging effects, we measure a set of n I-Vs and then change the voltage applied to the gate, followed by an immediate measurement of a new set of n I-Vs and so on. In Figure 5.6a), the schematics of this measurement procedure is illustrated for 3 I-V curves. We call this procedure a "multi-IV-multi-gate"-procedure.

An example of the recorded I-Vs is given in Figure 5.6b), where I-Vs are shown at room temperature after changing the gate voltage from -60 V to -70 V. A clear decay in current can be observed by comparing the first I-V with the 11th I-V. To better illustrate this decay, the inset shows the current at a fixed bias voltage of various I-Vs. To model the data we apply the following exponential fit to the data:

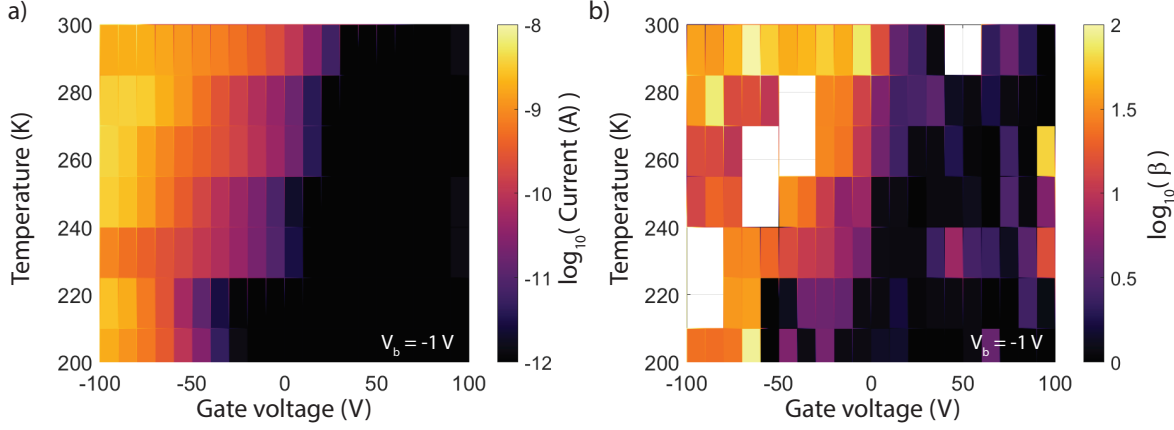


Figure 5.7 Temperature dependence of the current decay over time in high density films of 9-AGNRs. **a)** Fitted current values of the first I-V as a function of gate voltage and temperature. **b)** Decay parameter β as a function of gate voltage and temperature.

$$I = A \cdot e^{-\beta \cdot t} \quad (5.2)$$

where A and β are fitting parameters and t the I-V number (each I-V takes 12 s to measure). We do this to each set of I-Vs after changing the gate from +100 V to -100 V, in steps of -10 V. Figure 5.7 shows the evolution of the current as well as the fitted decay parameter β as a function of temperature. As we would have expected from the previous results, we see a strong temperature dependence of the current. Also the decay parameter β decreases with decreasing temperature, mainly caused by the lower currents.

An intermediate result is that these high-density films of 9-AGNRs show lower currents at lower temperatures and their capacitive behavior can be modeled using a simple, time-dependent multi-IV-multi-gate measurement approach. For further modeling it would be good to have the GNR film in a controlled shape, to take geometrical effects into account.

5.2.2 Low-temperature measurements of 9-AGNRs with electrodes separated by <15nm

After the investigation of the film behavior, and the room temperature characterization of 9-AGNRs in Chapter 4, we want to study this type of GNR at low temperature. As discussed previously, the film contribution should be suppressed at low temperatures, so the only possible transport channel would be through GNRs that bridge the graphene electrodes. A sample with graphene electrodes separated by <15 nm is prepared and high-density 9-AGNRs films are transferred onto, after a subsequent annealing step as proposed in Chapter 4,⁹⁰ the sample is cooled down to 9 K.

Figure 5.8a) shows I-V characteristics at low temperatures, showing highly non-linear behaviour. In the current vs bias and gate voltage map (see Figure 5.8b)) a strong

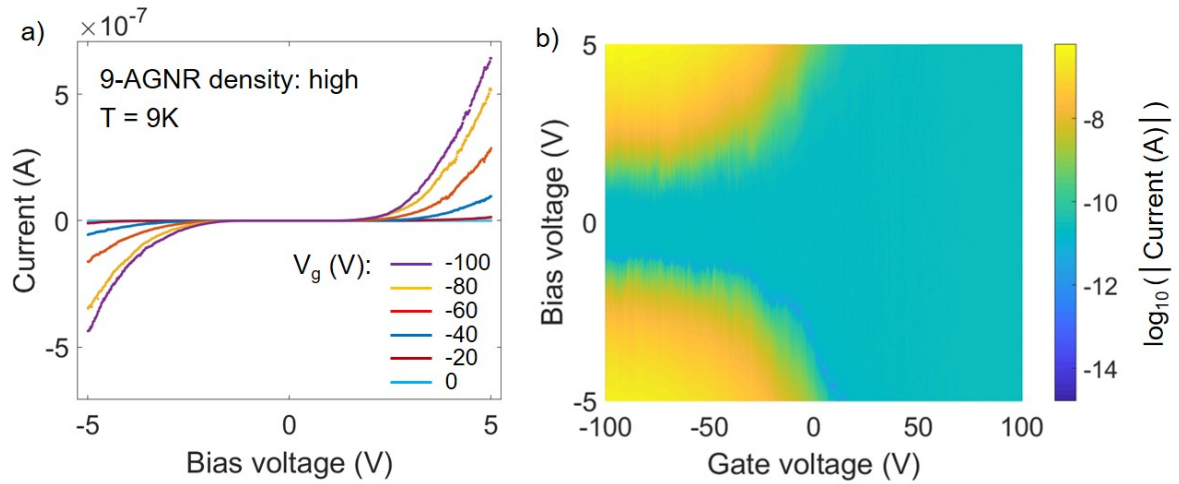


Figure 5.8 Transport characterization of 9-AGNRs device at low temperature. a) Current-voltage characteristics for various applied gate voltages. Recorded at $T = 9$ K. b) Current map as a function of bias and gate voltages. Recorded at $T = 9$ K.

gate voltage dependence is visible. Further, the absence of Coulomb blockade and single-electron tunneling, which would give rise to sharp distinct features in such a map, indicates that many GNRs dominate the transport mechanism. Interestingly, we see at negative gate voltages some blocking of the current up to ~ 1 V in bias voltage. This points towards an electronic barrier being present in the current path, that has to be overcome before a current can flow.

The type of electronic barrier is hard to determine. It could be limited by the contact resistances formed at the graphene/GNR interface, or within the GNRs themselves by for example bite defects¹²⁶. The large band gap of the 9-AGNRs, STS measurements revealed a band gap of 1.4 eV¹¹⁵, can not directly be attributed to this electronic barrier since it would be more dominant in the gate dependence, rather than the bias dependence. Still, the large band gap is limiting the current through the devices. In the following we therefore turn to GNRs with lower band gaps, but initially stay within the same armchair family.

5.3 Transport measurements in low band gap GNRs

After investigating wide band gap GNRs, we now focus on low band gap materials. They are interesting from an electronics device perspective. To perform logic operations a device has to change its state from a charge carrier conducting one to a blocking state. This switching usually happens by applying a voltage(pulse) to the gate electrode. By using a low band gap material as the active material, the required voltages can be kept low, which is favorable for a fast operation. We turn therefore to the exploration of low band gap GNRs. Namely long kinked 5-AGNRs, short straight 5-AGNRs, and 17-AGNRs. They all belong to the armchair-family $3p+2$, which has the lowest band gap of the armchair GNRs.³¹ The following subsections discuss the obtained transport results.

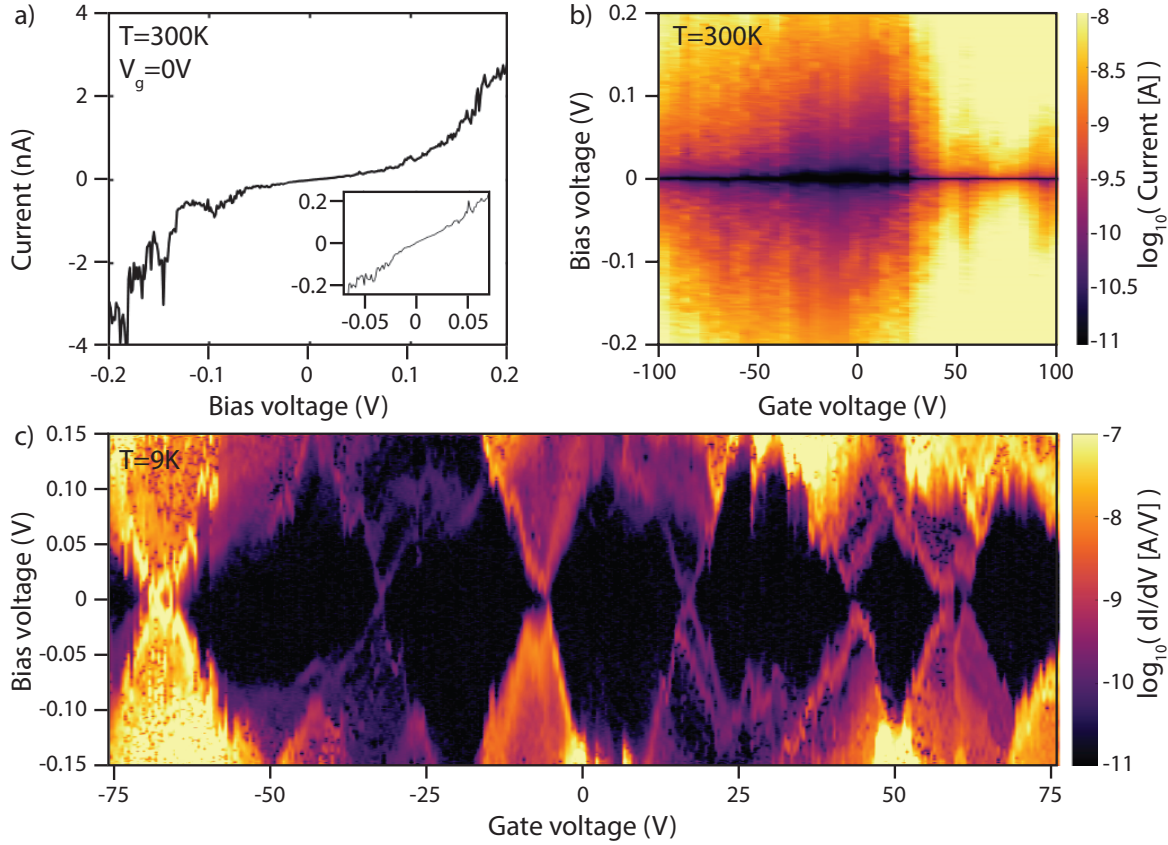


Figure 5.9 Electrical device characterization of kinked-5AGNRs. **a)** I-V curve measured at room temperature. The inset highlights the linear current-voltage behaviour in the low bias voltage regime. **b)** Current as a function of applied bias and gate voltages measured at room temperature. **c)** dI/dV map as a function of applied bias and gate voltages. The black regions indicate the Coulomb blockade region.

5.3.1 Kinked 5-AGNRs

Figure 5.9a) presents an I-V curve recorded at zero gate voltage on a kinked 5-AGNR device characterized at room temperature. At a low bias voltage range, we observe a nonzero conductance value with mostly linear behavior in the voltage range $\pm 0.07\text{ V}$, while the current is below our detection limit before the GNR transfer (see Chapter 4). This metal-like behavior was observed in two devices investigated at room temperature. Beyond this regime, we observe nonlinearities in the I-V curves. Figure 5.9b) shows the current as a function of applied bias and gate voltages (stability diagram), revealing strong gate-dependent transport. The shape of this map points towards a Coulomb blockade being present at room temperature with a crossing point at a gate voltage of around $+70\text{ V}$. Observing a Coulomb blockade at room temperature has been previously reported for quantum dots carved out of few-layer graphene.¹¹⁰

The devices were cooled and electrically characterized at 9 K to perform a spectroscopic characterization of the energy levels in the kinked 5-AGNRs. Figure 5.9c) presents the differential conductance map. We observe several Coulomb blockade diamonds, demonstrating that the kinked 5-AGNRs also behave like quantum dots at cryogenic

temperatures. We extract the energy required to add an electron to the quantum dot E_{add} , by taking half the height of the Coulomb diamonds. We observe characteristic addition energies in the range of 80-120 meV. Several resonances are visible, which form the edges of the Coulomb diamonds. The edge widths depend on the thermal energy ($k_{\text{B}}T$) and the coupling Γ of the ribbon to the graphene leads. Also, additional resonances running parallel to the diamond edge in the SET regime at a gate voltage of +20 V are observed. This resonance corresponds to an electronic or vibrational excited state of the ribbons that creates an additional transport channel. The energy of this excitation can be extracted from the graph by measuring the intersection between the excitation lines and the edge of the Coulomb diamond and is ~ 30 meV. The presence of such excitations is commonly interpreted as a sign of a single quantum dot dominating transport in a particular gate voltage range.^{145,177}

Note that we can observe partially overlapping diamonds together with the absence of a crossing point at $V_g = -30$ V and $+30$ V, suggesting that two or more GNRs contribute to the transport.^{145,177} In semiconducting quantum dots formed in systems such as two-dimensional electron gasses (2DEGs), top-down patterned graphene, or carbon nanotubes, the addition energies are typically < 10 meV, and several Coulomb diamonds can be observed.^{33,178,179} In our case, the addition energies are at least one order of magnitude larger, making the diamond structure apparent up to temperatures as high as room temperature.

To conclude, we have demonstrated the successful integration of kinked 5-AGNRs in a device geometry using graphene electrodes separated by < 15 nm. At room temperature, we observe a strong gate dependence with a thermally smeared-out Coulomb blockade region. At cryogenic temperatures, we observe single-electron transistor (SET) behavior, with addition energies reaching 120 meV. The observation of additional resonances in the SET regime with energies around 30 meV supports the fact that transport through the junction in a particular gate voltage range is dominated by a single quantum dot. This validates the use of graphene electrodes to contact ultra-narrow GNRs as well as the prospects of GNR-based electronic devices.

5.3.2 5-AGNRs

Straight 5-AGNRs are difficult to grow longer than 10 nm, this due to a different precursor molecule/growth procedure (See Chapter 3 Materials and Methods). Hence, we transferred films of aligned 5-AGNRs on graphene electrodes separated by the electrical breakdown procedure, resulting in gaps < 5 nm.

To perform a spectroscopic characterization of the energy levels in 5-AGNR junctions, the devices were cooled and electrically characterized at 13 K. Figure 5.10a) and b) show color-coded stability diagrams, recorded on devices E and F. The general aspect of the stability diagrams reveals the formation of quantum dots in the 5-AGNR devices. We extract the energy required to add an electron to the quantum dot as illustrated in Figure 5.10b) for two diamonds (E_{small} and E_{large} correspond to half of the height of the Coulomb diamonds). Typically, weakly-coupled quantum dots give rise to stability diagrams exhibiting alternating small and larger Coulomb diamonds due to the interplay between the quantum mechanical level spacing and charging energy.¹⁷⁷ We observe such size variations experimentally, and, following this logic, we tentatively divided the

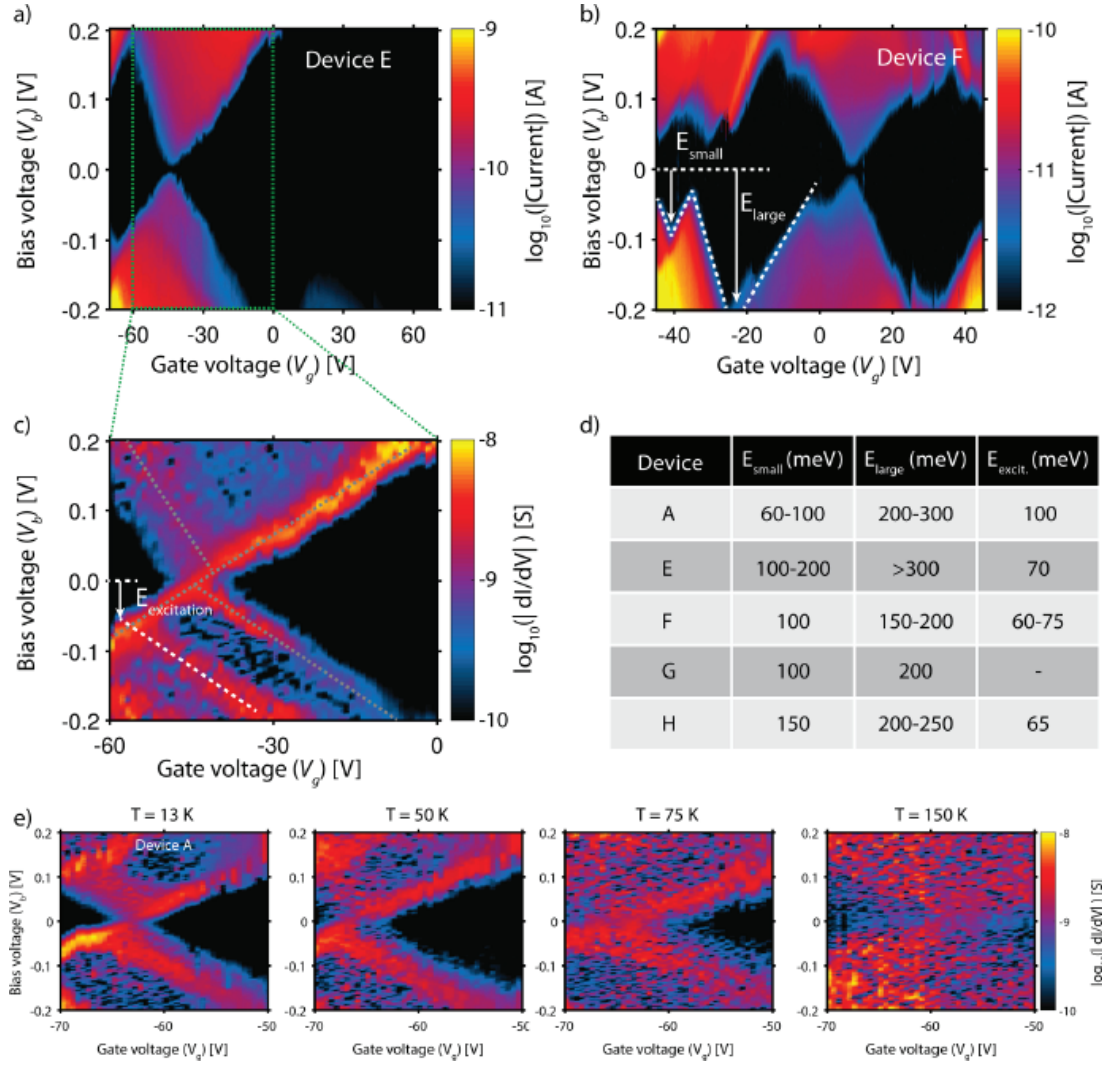


Figure 5.10 Electrical characterization of two devices at 13 K. a), b) Color-coded current maps as a function of gate and bias voltage for devices E and F, respectively. c) Differential conductance recorded on device E. The black area corresponds to a blockade regime, while the areas with high currents are in the single-electron tunneling regime. d) Overview table containing devices A and E-H with the corresponding addition and excitation energies. e) Stability diagrams recorded on device A at 13, 50, 75, and 150 K. Figure taken from El Abbassi et al.¹⁵

diamonds into these two categories. We observe characteristic energies in the range 50-300 meV (see table in Figure 5.10d).

Figure 5.10c) presents the differential conductance map of device E, zoomed in to the SET region. Here, several resonances are visible (gray dashed lines) which form the edges of the Coulomb diamonds. Some of the resonances are asymmetric upon bias polarity inversion, which may be attributed to an asymmetric coupling to the source and drain electrodes as a result of different overlap between the ribbon and the two leads. Also, an additional resonance (white dashed line) running parallel to the diamond edge in the SET regime is observed. We do not consider non-closing and irregular Coulomb

diamonds that may be related to the signature of several ribbons bridging the gap. The extracted excitation energies are listed in Figure 5.10d) for all devices, all lying in the range from 60 to 100 meV.

Note that in device F (Figure 5.10b)), we can observe partially overlapping diamonds together with the absence of a crossing point at $V_g = -35$ V, suggesting that two or more GNRs contribute to the transport.^{145,177} Figure 5.10e) shows four stability diagrams between 10 and 150 K on device A in the gate voltage range of -70 to -50 V. The plots show a crossing point around -63 V, where the diamond edges meet. Upon increasing the temperature, the resonances running along the diamond edges broaden, until about 150 K, where thermal broadening is sufficient to blur the diamond shapes. The large addition energies in our system limit the number of diamonds visible in the experimentally accessible gate range. For some devices, only a lower boundary on the addition energy can be set (for instance, about 300 meV for the right diamond in device E).

To conclude, we have demonstrated the successful integration of short 5-AGNRs in a device geometry using sub 5 nm graphene junctions. At room temperature, we observe linear, metal-like I-V curves. This indicates that the band gap of the 5-AGNR is very small, which qualitatively agrees with DFT calculations and STM measurements. At 13 K, we observe single-electron transistor behavior, with addition energies reaching a few hundred meV. Our first-principles transport calculations (see El Abbassi et al.¹⁵) attribute this small energy gap to the finite size of the ribbons, and the resulting presence of end states at the two termini of the ribbon. Finally, the observation of additional resonances in the SET regime with energies around 70 meV supports the fact that transport through the junction in a particular gate voltage range is dominated by a single quantum dot.

5.3.3 17-AGNRs

The relatively large width of the 17-AGNRs as well as their belonging to the 3p+2-family of armchair graphene nanoribbons gives rise to a low band gap of 0.17 eV.¹¹⁶ This makes this type of GNR favorable for integration and exploration of its transport properties in FET-geometry. Room temperature measurements revealed an S-shape of the I-V-characteristics with source-drain currents reaching the nanoampere range at an applied bias voltage of 1 V (see Figure 5.11a)). A thermal annealing step as proposed by Braun et al.¹³⁰, which for 9-AGNRs lead to an improved device performance due to mainly local rearrangements and removal of water at the GNR/graphene interface, was not possible. This since a degradation of the 17-AGNRs upon thermal annealing was observed and verified using Raman spectroscopy. (See Appendix 5.A.). Figure 5.11b) shows a histogram of 13 measured 17-AGNR-devices. Due to the non-linearity of the I-Vs, the resistance values were extracted at an applied bias voltage of 1 V. The spread in resistance values can be explained by the device to device variations caused by variations in the GNR film (orientation of GNRs, holes, . . .) or slightly varying electrodes (amount of bilayer, folds, wrinkles, contaminants, . . .). The applied gate voltage had little to no effect on the recorded I-V characteristics as it is shown in Figure 5.11c) for a representative device. At low temperature, the I-V characteristics become highly non-linear and as can be seen from the differential conductance map revealed Coulomb

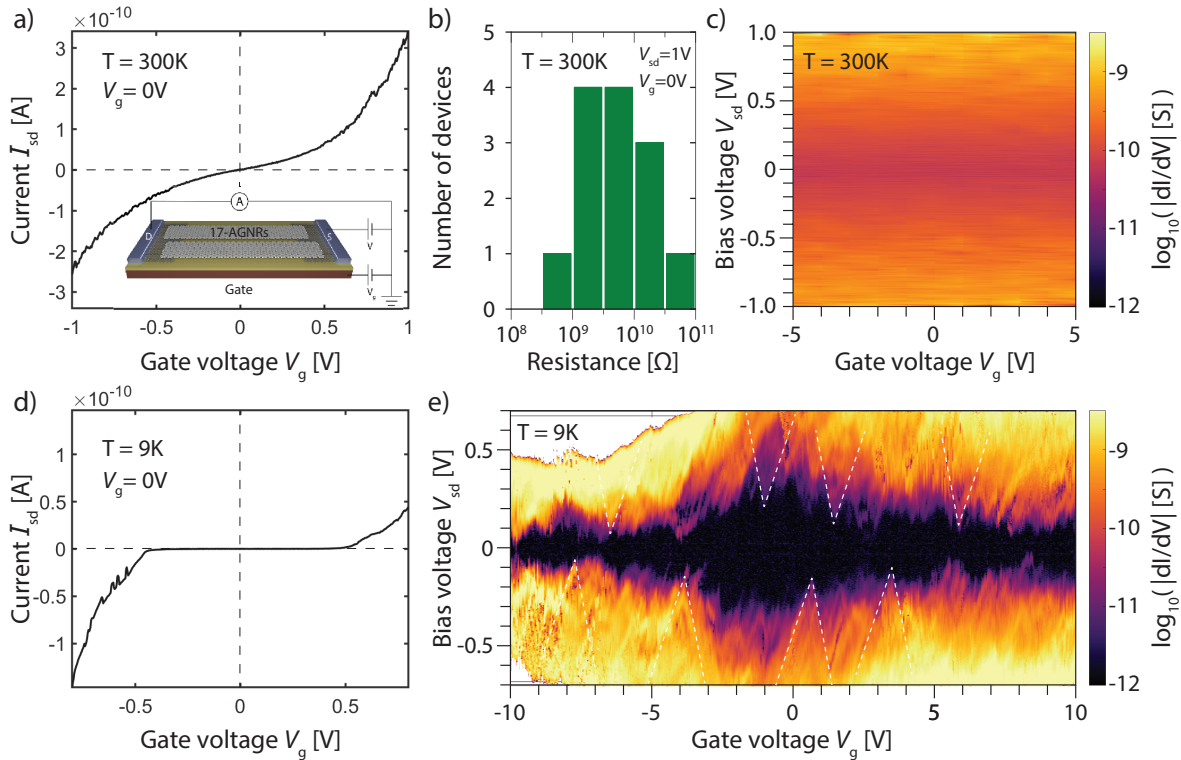


Figure 5.11 Electrical characterization of 17-AGNR devices. **a)** Current-voltage (I - V) trace of a typical device at 300 K. The inset shows the schematic of the device and measurement layout. **b)** Histogram of the room temperature device resistance for all 17-AGNR devices extracted at a bias voltage of 1 V due to the non-linearity of the I - V curve. **d)** Differential conductance dI/dV map of the device in a) at room temperature. **d)** I - V trace of the same device as in a) recorded at 9 K. **e)** dI/dV map as a function of applied bias and gate voltages. The black region indicates the Coulomb blockade. White dashed lines are guides to the eye.

blockade and single-electron tunneling regimes (see Figures 5.11d) and e)). Although at an applied gate voltage of -9.7 V the observed Coulomb blockade diamonds almost close, most of them do not. This observation can be interpreted that somewhere in the current path is a barrier. The extraction of what type of barrier is hard and would mainly be speculation. However, that many sharp features (a few are indicated by white dashed lines) in the dI/dV map can be observed leads to the conclusion that electronic transport happens through various channels, meaning that several 17-AGNRs are probed at the same time. The controlled graphene electrode geometry suggests that the contributing transport channels through 17-AGNRs can be seen as in parallel.

The observed results at room temperature are in agreement with what has been observed for other low band gap GNRs where also no strong gate dependent transport has been observed.^{15,19}

5.4 Transport measurements in GNRs near a topological phase boundary

In bottom-up synthesized GNRs with varying edge shapes, one can speak of several segments of the GNR. If the electronic inter-segment coupling is smaller than the intra-segment coupling, the GNR is in a topologically trivial phase and acts as an interconnect. However, if the inter-segment coupling is larger than the intra-segment coupling, the electronic segments are connected in a chain, forming a unique band structure. This quantum state is then topologically protected. In Gröning et al.¹⁸, an similar in Rizzo et al.¹⁷ the synthesis of such GNRs is reported. However, these GNRs have in parts zigzag edges which are more reactive, what makes it challenging for the exploration in a FET geometry including processing under ambient conditions. In Sun et al.¹⁹ we reported on a pyrene-GNR that is near such a topological phase boundary. In the following the transport results are highlighted.

5.4.1 Pyrene-GNRs

The small but finite band gap of the pyrene-GNR calls for exploring its performance in an FET configuration. The first step towards device integration is to demonstrate the robustness of pyrene-GNRs under ambient conditions. We use Raman spectroscopy to verify the structural integrity of the ribbons after exposing them to air (see Sun et al.¹⁹ for Raman spectra).

The pyrene-GNRs are integrated into FET devices in order to probe their electrical properties by measuring the current as a function of both the bias and gate voltage. Due to the relatively long length of the pyrene-GNRs of about several dozens of nanometers, the GNRs were transferred onto graphene electrodes separated by an electron beam lithography processes as described in Chapter 4, resulting in <15 nm gaps. Figure 5.12a) I-V characteristics of a typical device recorded at room temperature are shown.

At room temperature, we observe a linear dependence of the current on the applied bias voltage, and a negligible dependence of the applied gate (see Figure 5.12). We attribute this quasi-metallic behavior to the small band gap of the pyrene-GNR. This was the case in all 21 measured devices. We therefore extracted the resistance values at a fixed bias and gate voltage, revealing strong device to device variations. Reasons for this could be non-aligned GNRs, transport dominating GNRs having different orientations to the source-drain axis, substantially varied overlap between the graphene electrodes and the GNRs, as well as local contaminants having significant influence on the transport characteristics.

The transport measurements at low temperatures on as-transferred pyrene-GNRs revealed no well defined features (see Figure 5.12c)). To improve the device performance by local rearrangements we also applied a thermal annealing step as described in Chapter 4. This step, however, is more delicate than in the case of 9-AGNRs, since the pyrene-GNRs have partially zigzag edges which are more reactive than purely armchair edges.

Although some sharp(er) features are visible in the low temperature transport measurements after thermal annealing (see Figure 5.12d)). The observed Coulomb blockade

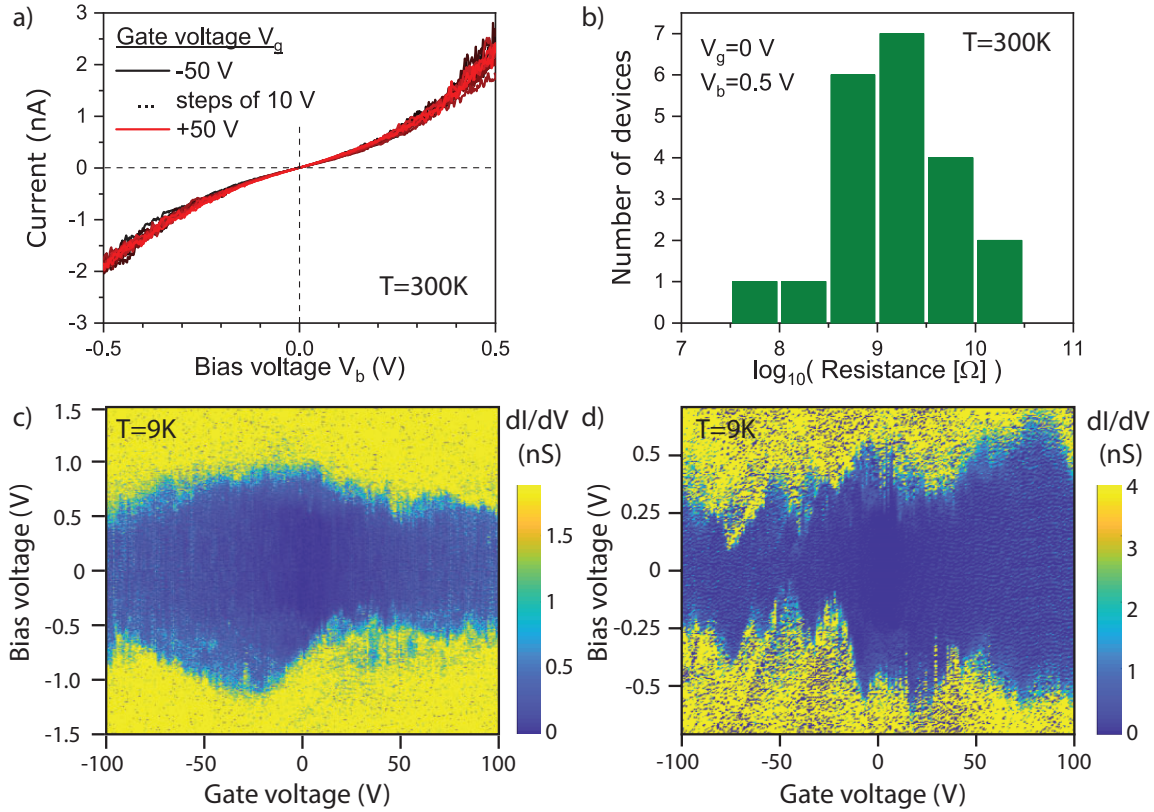


Figure 5.12 Electrical characterization of pyrene-GNR contacted with e-beam gaps. **a)** I-V characteristics of a typical device at various applied gate voltages, recorded at 300 K. **b)** Histogram of the room temperature resistance of 21 devices at $V_b = 0.5\text{ V}$ and $V_g = 0\text{ V}$. **c)** dI/dV -map as a function of applied bias and back gate voltages of a device recorded at 9 K. **d)** dI/dV -map as a function of applied bias and back gate voltages of a device after thermal annealing recorded at 9 K.

diamonds do not close completely, pointing towards an electronic transport barrier being present in the system. This is attributed to kink defects in the pyrene-GNRs that occur on average every 5-10 nm and are predicted to disrupt the transport channels (see Appendix 5.5).

We hence transferred pyrene-GNRs on nanogaps that are formed by electrical breakdown of a 400 nm wide prepatterned graphene channel, resulting in electrode separations of only a few nanometers (see Chapter 3 for details on the electrical breakdown technique).^{30,106} As the nanogap size is smaller than the average length of straight ribbon segments (see Figure 5.15), this allows us to probe transport properties we deem to be representative of the intrinsic ribbon properties.

Figure 5.13c) displays transport measurements at low temperature (9 K). In the I-V curves, we observe Coulomb blockade of charge transport at low bias voltages. The onset of current at higher bias voltages is tunable via the applied gate voltage. This is attributed to transport channels of the pyrene-GNRs entering the bias window. We observe currents of up to 10 nA at a bias voltage of 0.7 V which we assume to be limited by coupling of the graphene electrodes to the pyrene-GNR channel. Figure 5.13d)

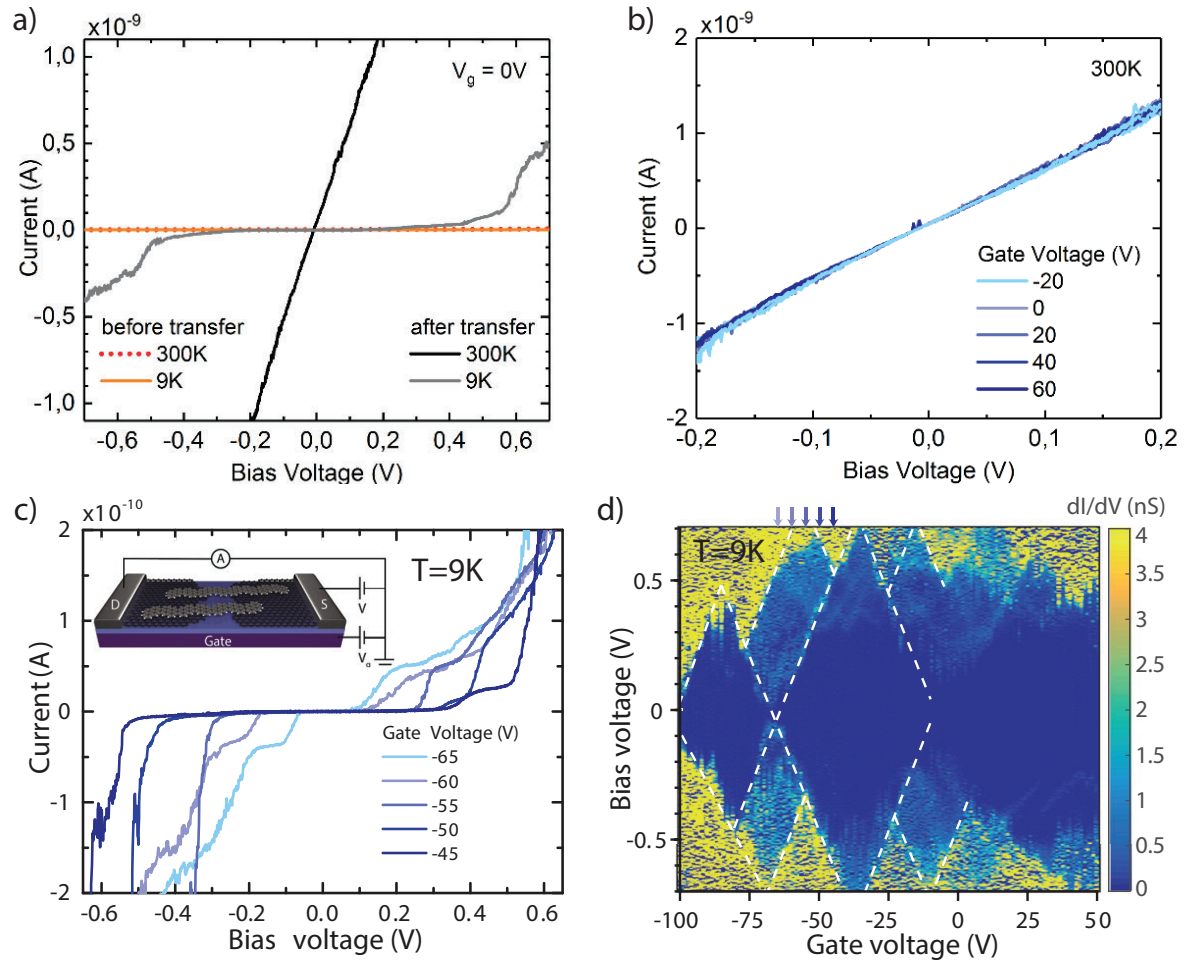


Figure 5.13 Electrical characterization of pyrene-GNRs contacted with electrical breakdown gaps. a) Current-voltage traces before and after transfer of pyrene-GNRs on predefined electrodes. b) Current-voltage traces of a pyrene-GNR device at room temperature and various applied gate voltages. c) Current-voltage traces at multiple selected gate voltages for a device recorded at 9 K. The gate voltages at which these curves were recorded are marked with arrows in panel d). The inset shows the schematic of the device and measurement layout. d) dI/dV -map of the device in c) as a function of applied bias and back gate voltages. Gate-bias ranges showing blocked charge transport are observed. White dashed lines are guides to the eye. Figure adapted from Sun et al.¹⁹

shows the corresponding charge stability diagram (differential conductance dI/dV as a function of bias and gate voltages) in which diamond-like features are visible.^{180,181} These Coulomb diamonds are characteristic of weakly coupled quantum dots, while the presence of multiple overlapping diamonds suggests that transport occurs through several pyrene-GNRs.¹⁸² The observed blockade regions range from ~ 0.2 to ~ 0.75 V bias. This agrees well with the range of transport gaps expected for pyrene-GNRs if one uses the GW approximation to account for electron-electron interaction, the insulating substrate and the range of observed ribbon lengths.

GNR type	5	5, kinked	9	17	pyrene
Armchair family	3p+2	3p+2	3p	3p+2	-
Band gap DFT (eV)	0.43 ³¹	0.43 ³¹	0.73 ³¹	0.13 ^{31,116}	0.18 ¹⁹
Band gap STS (eV)	0.85 ¹¹⁸ 0.29 ^a	0.85	1.40 ¹¹⁵	0.17 ¹¹⁶	0.23 ¹⁹
Range of addition energy (eV)	0.1 - 0.3 ¹⁵	0.08 - 0.12	0.03 - 0.15 ^b	(0.7 - 1.0) ^c	0.2 - 0.7 ¹⁹

Table 5.1 Overview of electronic properties of measured GNRs.

^aEnd-states within the band gap as reported by Lawrence et al.¹¹⁸

^bIn multi-gate geometry, see Chapter 6.

^cNo closing diamonds observed.

5.5 Conclusion and outlook

To summarize, we have shown that graphene electrodes can be used to probe the electronic properties of GNRs of various width and edge structures. Transport measurements on films of 9-AGNRs revealed a strong temperature and density dependence. Using temperature- and time-dependence measurements we showed that at high temperatures a different transport mechanism is at play than at low temperatures. Measurements at cryogenic temperatures showed that in low band gap GNRs quantum dot behavior is observed. Using spectroscopy we extracted addition energies of several hundreds of millielectronvolts. The transport results for devices where only few GNRs were contacted are presented in Table 5.1.

We see that the results on the 5-AGNRs, 17-AGNRs, and pyrene-GNRs are in good agreement with the results obtained by other means and the theoretical prediction. On the kinked 5-AGNRs and the 9-AGNRs the obtained energies show some discrepancies to the predicted value. Potentially, the transport is limited by the present kink defects and could be overcome by using the electrical breakdown gaps, probing only the straight segment, similar as in the case of the pyrene-GNRs. The overall quantum dot behavior at low temperatures leads to the conclusion that the picture of a 1D-transport through GNRs has to be revised and rather the picture of an electronic island is confirmed. Further, the large addition energies have shown to allow for observing quantum dot behavior at room temperatures. This might be used for applications in future electronic devices or in the field of energy harvesting.

However, if the electronic barriers at the graphene/GNR interface could be reduced, the picture of GNRs as 0D objects might be revised. A possible way could be by introducing add-atoms at this sensitive interface, similar as it was shown theoretically, to improve the transmission of carbon nanotube networks.¹⁸³ Having only a global gate certainly limited the presented studies. In particular, a tuning of the charge carrier density in the graphene leads is of great interest. The controlled positioning of the gap in the graphene using electron beam lithography allows for probing GNRs with advanced gating geometries. This will be further discussed in Chapter 6. Further, the surface effects should not be underestimated. As we have seen in Chapter 4, thermal annealing

can drastically improve device performance. This is in agreement with results obtained on graphene, where protection from the environment using encapsulation with hexagonal boron nitride led to drastic improvements in the device quality.^{20,184} In Chapter 7, preliminary results in this direction are presented and discussed.

Overall, we see that contacting GNRs is challenging, and also that the here presented results indicate that graphene-based platforms can serve in the exploration and probing of novel GNRs exhibiting exciting physical properties.

Appendix 5.A. 17-AGNRs: Annealing effects

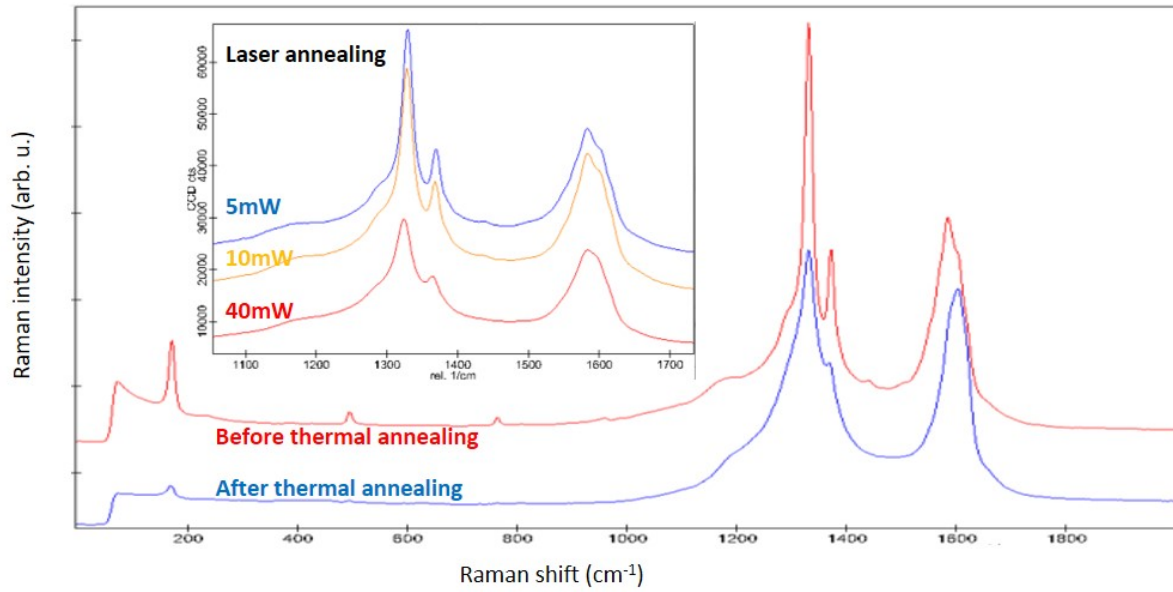


Figure 5.14 Raman characterization of transferred 17-AGNRs on device substrates. Visible are the sharp separation of the peaks in the CH/D-region ($1200\text{--}1450\text{ cm}^{-1}$) before thermal annealing at $200\text{ }^{\circ}\text{C}$ for 2 h, and their shape after thermal annealing. The inset shows Raman spectra acquired with different laser powers, leading to a local thermal annealing and hence indicating a similar degradation.

Appendix 5.B. pyrene-GNRs: Additional data

Appendix 5.B.1. kink defects in pyrene-GNRs

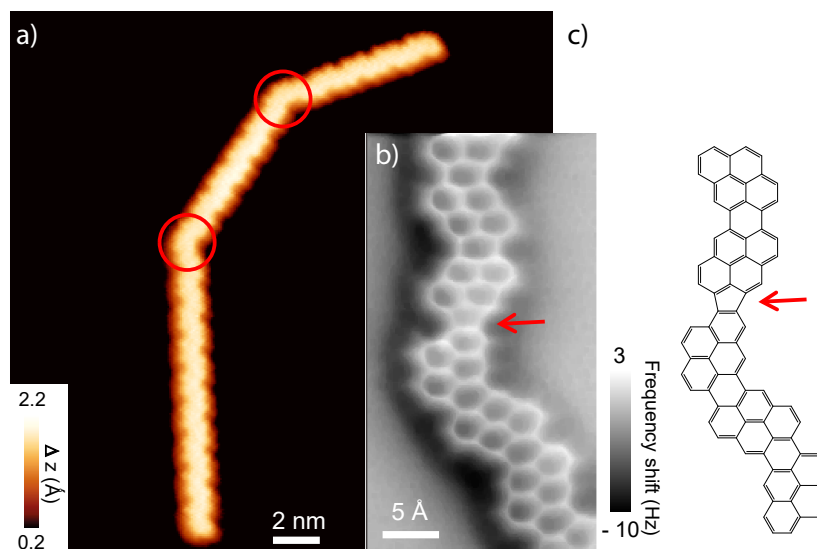


Figure 5.15 Kink defects in pyrene-GNRs. a) high-resolution STM image of a pyrene-GNR recorded at liquid helium temperatures. b) non-contact AFM image of a kink in the pyrene-GNR (indicated by red circles in a). c) Chemical structure of a pyrene-GNR around a kink. The pentagon ring (indicated with a red arrow) causing the kink of the pyrene-GNR. Figure provided by Qiang Sun.

Appendix 5.B.2. Additional transport measurements on pyrene-GNR devices

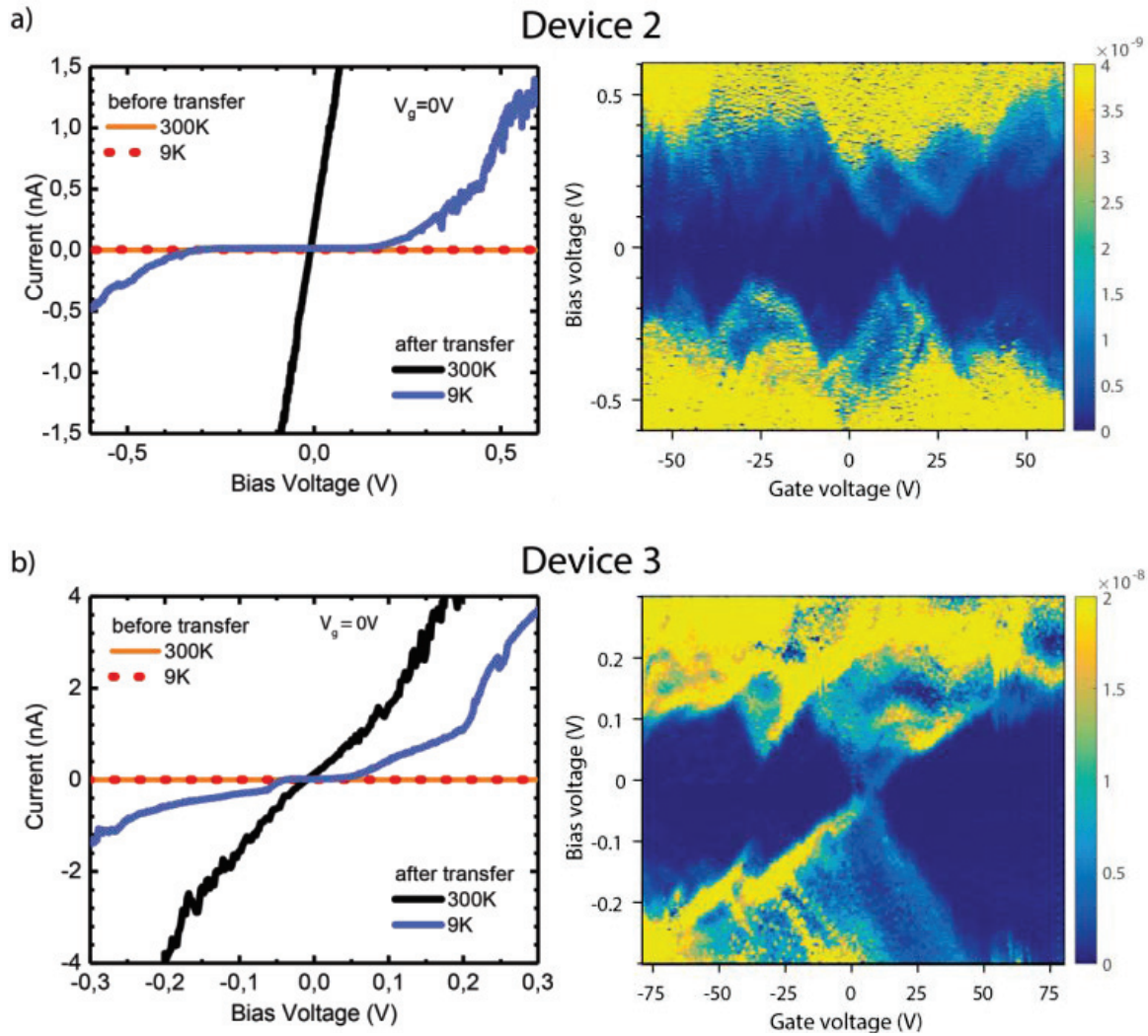


Figure 5.16 Electrical characterization of additional pyrene-GNR devices. **a)** Device 2. Left: Electrical characterization of the device before and after the electrical breakdown process at 9 K and 300K. The I-V characteristic before transfer indicates an empty gap. Right: dI/dV of the stability diagram recorded at 9 K **b)** Device 3. Same electrical characterization as described in a). Figure taken from Sun et al.¹⁹

6 Multi-gate quantum dots from 9-atom-wide armchair graphene nanoribbons

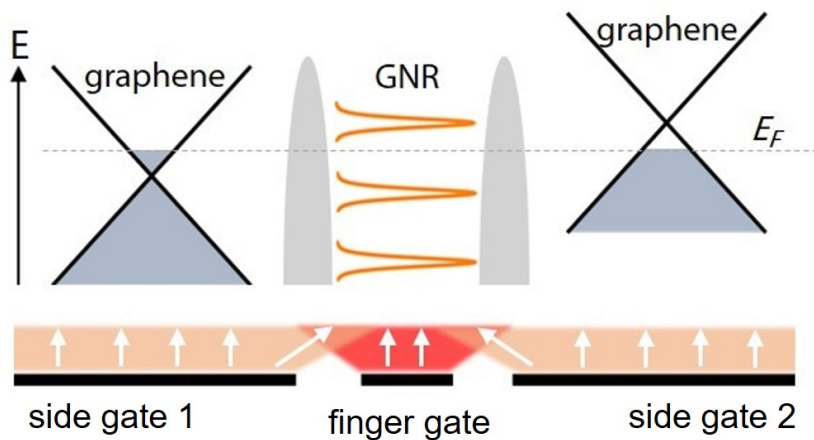


Figure 6.1 Abstract illustration of a multi-gate GNR FET device with its energy landscape. The finger gate has the strongest influence on the GNRs. The side gates influence mostly the graphene electrodes and also to some extent the GNRs.

Atomically precise graphene nanoribbons (GNRs) have attracted much interest due to their largely modifiable electronic properties, all tailored by controlling their width and edge structure during the chemical synthesis. In recent years, the exploitation of GNR properties for electronic devices has focused on their integration into field-effect-transistor (FET) geometry. However, such FET devices, due to the presence of a single gate, have limited electrostatic tunability. Here, we report on the device integration of 9-atom wide armchair graphene nanoribbons (9-AGNRs) into a multi-gate FET geometry. We use high-resolution electron beam lithography to define local gates as close as 15 nm and combine them with graphene electrodes to contact the GNRs. Low temperature transport spectroscopy measurements reveal quantum dot (QD) behaviour with addition energies of ~ 65 meV. The controlled tuning of the charge carrier density in the graphene electrodes and a separately tunable finger gate below the channel region lead to an improved gate coupling to the 9-AGNR-QDs. This experimental realization of advanced gating strategies paves the way for novel GNR-based electronic building blocks.

Contributions:

O.B., J.O., J.Z., M.L.P. and M.C. conceived the experiments. J.Z. and O.B. fabricated the devices and performed the measurements with help from M.P. The data analysis was done by J.Z. with input from O.B. M.L.P. and M.C. J.O. and M.P. did the finite-element calculations. K.M. provided precursor molecules. G.B.B. and R.D. synthesized GNRs under supervision by P.R. and R.F.. M.S. carried out SEM and TEM analysis. A.O. did the EBL. M.C. supervised the study.

6.1 Introduction

Bottom-up synthesized GNRs have attracted considerable interest as one of these future electronic building blocks. This is mainly due to the fact their chemical structure can be controlled with atomic precision, a property which top-down etched GNRs lack.^{10–12} Bottom-up synthesized GNRs can therefore be regarded as a *Designer Quantum Material*, where the material properties can be designed by selecting the appropriate chemical precursors and synthetic routes. As such, one can vary their band gap,¹³ form *pn*-junctions within a heterogeneous single ribbon,¹⁴ form quantum dots¹⁵ and even exhibit topologically non-trivial phases.^{16–19} However, many challenges remain in the device integration of these materials, especially regarding contacting and gating strategies. To date, trivial armchair graphene nanoribbons of different widths have been contacted, either using metal electrodes¹³ or graphene electrodes^{15,90,149}. Moreover, only field-effect-transistor devices with a single gate have been implemented. For more advanced device functionalities additional control over the electrostatic landscape of the device would be highly desirable, in particular for ultrashort transistors¹⁸⁵, or for the definition of multi-quantum dot systems. Given the small size of the GNRs, this requires a very high control over the fabrication of the gates, the electrodes, and the alignment between them.

Here, we report on the integration of GNRs into a multi-gate field-effect transistor with graphene electrodes. Our approach consists of a narrow finger gate and two additional side gates, which yields improved gating capabilities allowing for the individual tuning of the electrostatic potential in the nanogap and the charge carrier density in the graphene electrodes. The narrow gate is ~ 10 nm in width, leading to a gated channel length < 15 nm, fabricated using CMOS-compatible processing steps. The graphene electrodes are defined using EBL, allowing for exact control of the nanogap position and a proper alignment with the underlying gates. This is in contrast to electrodes created using the electric breakdown procedure that has been commonly used for graphene.^{15,19,30,107} Moreover, our fabrication protocol allows for the integration of the GNRs at the very last stage of device fabrication. Similar approaches with the sensitive material as final step have been shown to lead to major improvements in the device performance, as demonstrated for example for MoS₂.^{170,171} The design of the devices is supported by finite-element method (FEM) calculations for optimizing the various geometrical parameters and maximizing the effective potential at the GNRs. Furthermore, low-temperature transport spectroscopy measurements reveal quantum dot (QD) behaviour with addition energies of ~ 65 meV, and transport characteristics that are tunable using the two side gates. The presented results are a major step forward to the successful device integration of atomically precise graphene nanoribbons and pave the way for exploration of GNRs with more exotic edge structures.

6.2 Device design and fabrication

A schematic of the proposed device architecture is shown in Figure 6.2A. The finger gate (FG) with nanometer scale dimensions is patterned under the 9-AGNRs junction, while two side gates (SG1 and SG2) are defined under the source and drain graphene

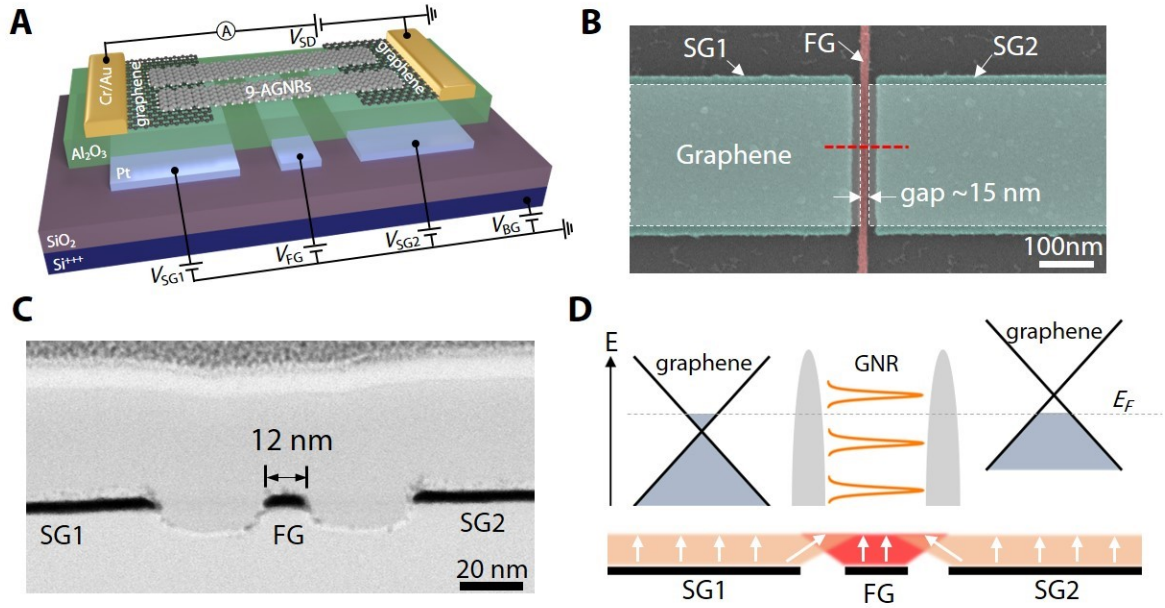


Figure 6.2 Multi-gate 9-AGNRs quantum dot device. (A) Artistic illustration of the device. The schematic circuit diagram indicates which terminals are used to apply the voltages and measure the current. (B) False-colored SEM image of a device prior to GNR transfer showing FG (red), SG1 and SG2 (turquoise) below graphene (white dashed line). (C) High resolution TEM cross-section through a device revealing the FG size and the separation to the sidegates. (D) Schematic drawing of the electrostatic landscape.

electrodes, respectively. We use HSQ as a resist to define the etch mask. This resist turns into SiO_2 after EBL exposure and development leading to a very etch resistive mask. A subsequent Ar^+ -ion milling step transfers the etch mask feature to the metal film, separating the finger from the side gates. This process leads to very sharp features as it is not limited by grain sizes or artificially enhanced edges as is common when using electron-beam evaporation with lift-off processes. This results in a finger gate with a width of 10-15 nm and length of 500 nm. The nanometer scale dimension of the FG ($< d$) creates an ultra-short effective channel length while minimizing parasitic gate to source-drain capacitance. The 9-AGNRs junction is electrically isolated from the metal gates using a 30 nm thick aluminum oxide (Al_2O_3). The device is fabricated on a highly doped silicon (Si) carrier chip with a 285 nm thick silicon dioxide (SiO_2). The Si substrate serves as a global back gate (BG). The graphene electrodes are separated by a nanogap formed with high-resolution patterning using electron-beam lithography, as reported in Chapter 4.⁹⁰ Here the electrode separation d is set to be ~ 15 nm in order to eliminate a direct tunneling current between the electrodes. In Appendix 6.4 a more detailed description of the fabrication process is given.

We note that the interplay between the gate length, gate oxide thickness and the applied potentials in order to achieve a homogeneous electrostatic potential over the complete channel length is very delicate. Thinner oxides lead to higher gate coupling but also lower breakdown voltages between the various gates. Moreover, reducing

the distance between the gate also increase the screening of the gate potential by the neighboring gates. To investigate this balance, we performed finite-element-method (FEM) calculations using Comsol Multiphysics. In Appendix 6.4, we present the effective potential at the GNRs for various thicknesses of the Al_2O_3 and the gate separation. Graphene is modelled as a surface charge density, its value is calculated using the voltage applied to the gate located below the respective electrode, and the sum of quantum capacitance and geometric capacitance.

In Appendix 6.4 we show using finite-element calculations that smaller oxides are generally more beneficial, down to 12 nm. A further result is that downsizing the FG size is beneficial, but only down to 10 nm. Beyond that point, the field strength exceeds 1 V/nm, a strength where breakdown of the oxide is risked.¹⁸⁶ A scanning electron micrograph (SEM) of the final device before GNR transfer is presented in Figure 6.2(B), alongside a transmission electron micrograph (TEM) in Figure 6.2(C). The image shows that the FG size is ~ 12 nm, and the separation between the gates ~ 30 nm.

The energy diagram of the junction containing the three gates and the density of states of the GNRs and graphene is presented in Figure 6.2D. As the electronic coupling between the GNRs and the graphene is weak, we anticipate the formation of quantum dots (QD) at low temperatures. This is represented in the schematic energy diagram by the two tunneling barriers and broadened discrete energy levels between the barriers. In such a geometry, the FG is strongly capacitively coupled to the QD and can be used to tune the chemical potential of the QD. Using one of the side gates (SG1 or SG2), the Fermi energy of the graphene electrodes (source or drain) can be tuned into the n -region or p -region. Moreover, as both side gates are located close to the nanojunction, they will also introduce an asymmetric electric field that will couple to the QD.

6.3 Quantum dot formation at low temperature

6.3.1 Characterization of the QDs with zero applied side gate voltage

Prior to the deposition of the GNRs, the nanogaps were electrically characterized to ensure a clear separation between the electrodes. Devices with currents >10 pA at $V_{\text{SD}} = 4$ V were excluded from further characterization (See Appendix 6.A.1.) Uniaxially aligned low-density 9-AGNRs were synthesized on a Au(788) single crystal under ultra-high vacuum conditions (See Appendix 6.4).¹²⁵ 9-AGNRs were then transferred to the multi-gate device substrate with the predefined and precharacterized graphene electrodes using a PMMA-based electrochemical delamination process.^{88,89,121} In order to improve the device performance, a thermal annealing step is performed as proposed in Chapter 4.⁹⁰ After this thermal annealing step the integrity of the 9-AGNRs and their alignment with respect to the source-drain axis is confirmed using polarization dependent Raman spectroscopy (See Appendix 6.4).

To evaluate the electrical properties of the 9-AGNRs after device integration, we recorded stability diagrams (current-voltage characteristics (IV) for varying FG voltage V_{FG} at $T = 9$ K for various values of the side gate voltages).

Figure 6.3A shows a stability diagram recorded with the voltages on SG1, SG2 and

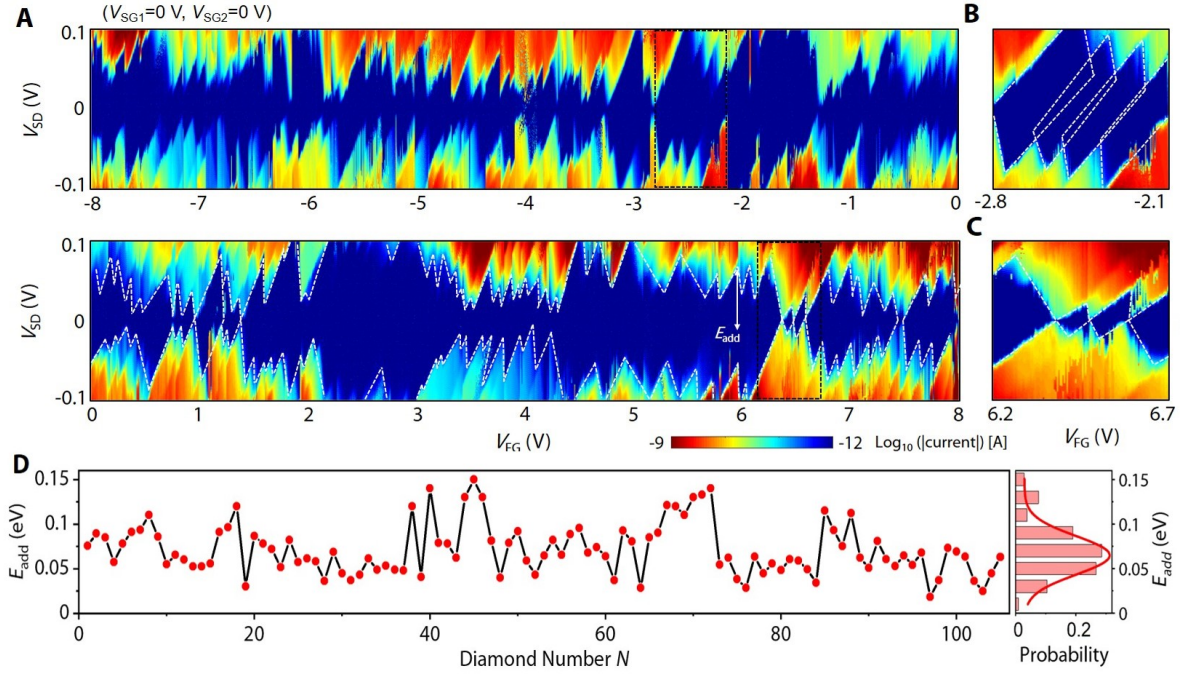


Figure 6.3 Coulomb diamonds in multi-gate 9-AGNRs device at low temperature. (A) Current as a function of bias, V_{SD} , and finger gate voltage, V_{FG} , recorded at $T = 9$ K. Coulomb diamonds are visible over a gate range of 16 V. High resolution Coulomb diamonds, where dotted white lines indicate the diamond edges. (B) Non-closing Coulomb diamonds and (C) closing Coulomb diamonds. (D) Addition energy, E_{add} , as a function of diamond number, N . The histogram shows the distribution of the addition energy values.

BG all set as 0 V. The plot shows irregular and aperiodic Coulomb diamonds (CD) over a FG voltage range of 16 V, with addition energies (E_{add}) varying between 20 meV and 150 meV. For a large portion of the FG range, no crossing of the corresponding energy level with the Fermi energy of the electrodes is observed, i.e., no resonance is visible at zero bias. This behavior is highlighted in Figure 6.3B for a gate range from -2.8 V to -2.1 V and is attributed to transport through two weakly-coupled QDs in series. Here, the serial QDs either correspond to different GNRs, or to the formation of localized charge states within a single GNR due to local confinement potentials.¹⁸⁷ In other gate regimes, for example in Figure 6.3C, the Coulomb diamonds are closing, indicating that in that gate range a single QD is dominating transport. Also in this case, multiple overlapping diamonds with different addition energies are visible, suggesting that charge transport occurs through two parallel QDs, presumably two GNRs, with different quantum dot size.¹⁸⁸ In Figure 6.3D we plot the addition energy E_{add} as function of diamond number N for the full V_{FG} range of Figure 6.3A (-8 V to 8 V), alongside a histogram of E_{add} . Interestingly, we find that the observed E_{add} is well described by Gaussian unitary distribution, revealing the GNRs still maintain Dirac billiard distribution, as observed for quantum dots carved out of graphene with a dimension smaller than 100 nanometers.¹⁸⁹ The average addition energy for the overall system, $E_0 = 65$ meV, is simply determined by the peak position of a Gaussian fit to the distribution.

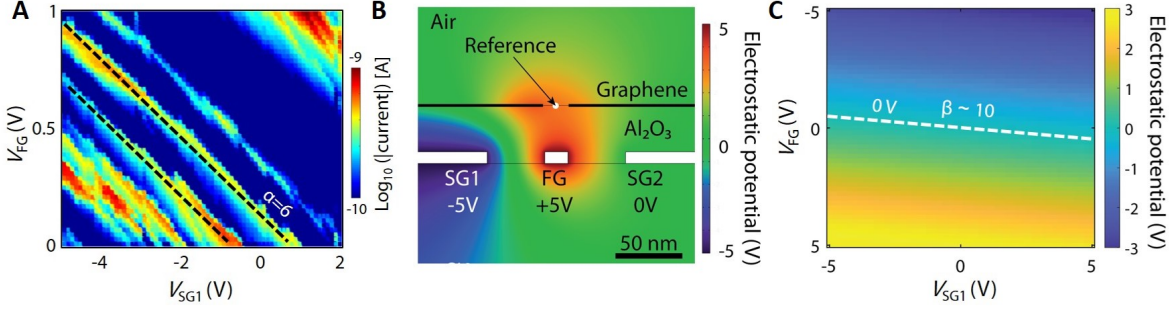


Figure 6.4 Gate coupling strengths. (A) Measured current at a fixed bias voltage of $V_{\text{SD}} = 0.1$ V as a function of applied finger gate and side gate voltage. Dashed black lines are guides to the eye. (B) Device crosssection with modeled electrostatic potential for $V_{\text{SG1}} = -5$ V, $V_{\text{SG2}} = 0$ V and $V_{\text{FG}} = +5$ V. (C) Electrostatic potential at the reference point in (B) as a function of side gate 1 and finger gate voltage. Dashed line indicates equipotential line at 0 V.

This addition energy corresponds to an effective dot size $L \simeq 10.9$ nm. The size of the quantum dots were calculated according to Shylau et al.¹⁹⁰ using $E_c = \frac{e^2}{4\pi\epsilon_0\epsilon_r L / \ln(4h/w)}$ with E_c the charging energy, ϵ_0 the electric constant, ϵ_r the relative permittivity of Al_2O_3 and h the thickness of the Al_2O_3 (30 nm) assuming a 1-dimensional GNR with a width of 11.5 Å (9-atom-wide GNR backbone including C-H bond).

We have also performed temperature-dependent measurement on this device. As shown in Appendix 6.4, the device exhibits QD behavior up to $T = 100$ K, after which it transitions to semiconductor-like behavior. The figure also shows a strong increase of the overall current through the device for the elevated temperatures. We attribute this behavior to a hopping-like mechanism through the GNR film.¹⁴³

6.3.2 Gating efficiency

To investigate the gating efficiency of the side gate versus the finger gate, we recorded a map of the current as a function of V_{FG} and V_{SG1} for a fixed source-drain voltage V_{SD} of 100 mV, as shown in Figure 6.4A. The plot displays multiple areas of high current that shift with the gate voltages. Two representative lines of enhanced current are marked with black dashed lines. From the slopes we extract the relative gate coupling α between FG and SG1 and find $\alpha = \alpha_{\text{FG}}/\alpha_{\text{SG}} \sim 5.98$.

As a comparison, we performed finite-element calculations (Comsol Multiphysics) to investigate the electrostatics of the multi-gate GNR devices. Figure 6.4B shows the geometry overlaid with the corresponding electrostatic potential for $V_{\text{FG}} = 5$ V, $V_{\text{SG1}} = -5$ V, and $V_{\text{SG2}} = 0$ V, highlighting the device geometry and the reference point at which the potential is computed. Figure 6.4C shows the potential of the reference point versus the FG and SG1. Here, a slope β of around ~ 10 is observed, close to the experimentally observed value of ~ 6 . The difference between experiment and theory may be caused by local defects in the gate oxide or a slight misalignment of the graphene gap with respect to the finger gate. Here, the relative gate coupling between the individual gates is estimated to be $\alpha_{\text{FG}}/\alpha_{\text{SG1}}/\alpha_{\text{SG2}}/\alpha_{\text{BG}} = 211.7 : 35.4 : 23.0 : 1$.

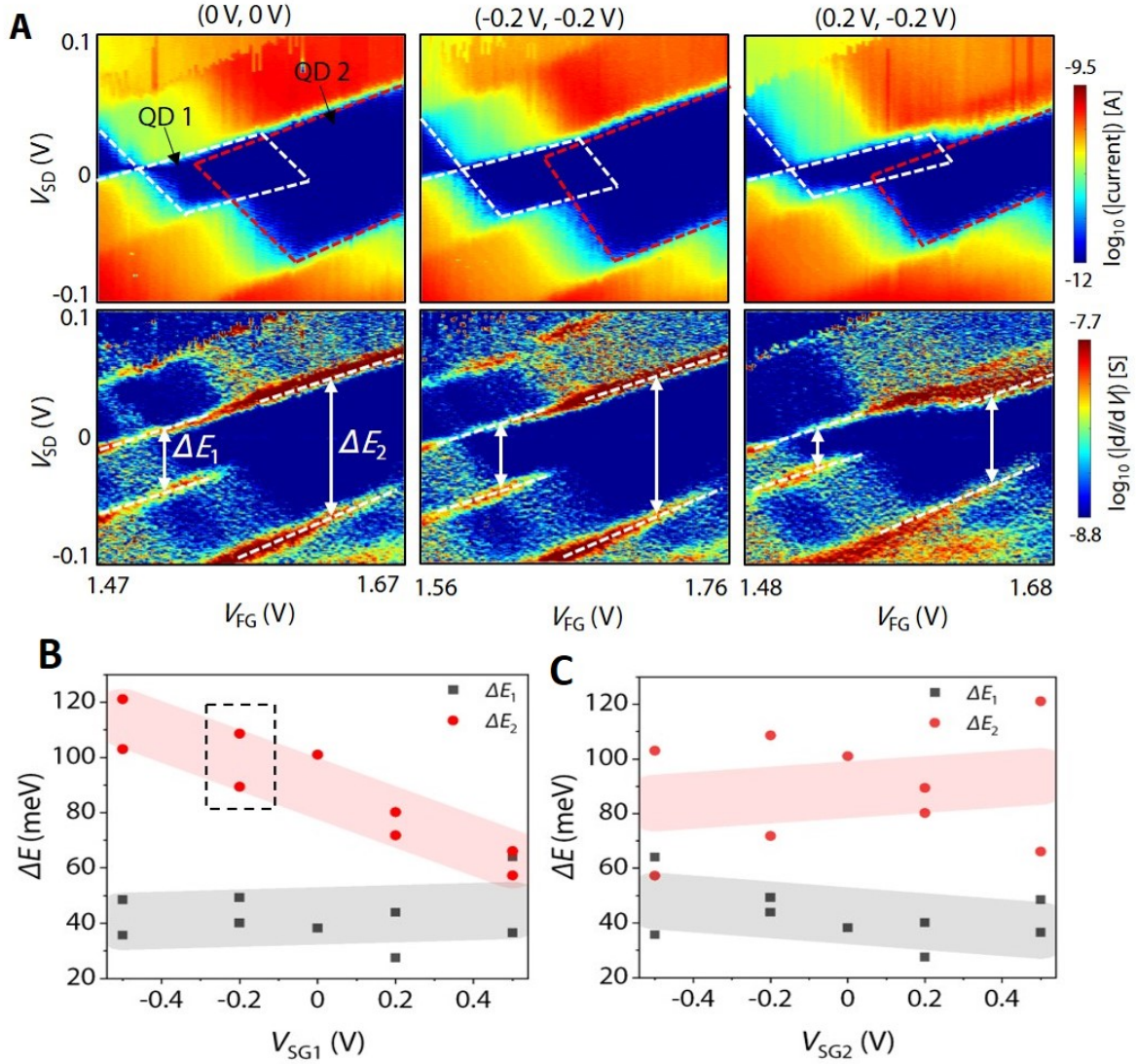


Figure 6.5 Quantum dot behaviour with individually gated electrodes. (A) Top panels: Current as a function of bias and finger gate voltage, for three different side gate voltage configurations measured at $T = 9$ K. The side gate voltages are indicated in brackets on top (V_{SG1} , V_{SG2}). Edges of QD 1 and QD 2 are indicated with dashed white and red lines, respectively. Bottom panels: Corresponding dI/dV maps. Extracted energies ΔE for various voltages V_{SG} applied to (B) side gate 1 and (C) side gate 2.

6.3.3 Tunable QD energies using side gates

To further characterize the QDs formed in the device and their addition energies, we focus on a gate range which possesses two overlapping diamonds, originating from two QDs in parallel. To do so, we measure the current I as a function of the finger gate voltage V_{FG} for different side gate voltages V_{SG1} and V_{SG2} (later indicated in brackets). In Figure 6.5A, we explore all side gate voltages combinations with ± 0.2 V and ± 0.5 V applied to the side gates. Only the full stability diagrams of $(-0.2$ V ; -0.2 V) and $(0.2$ V ; -0.2 V) are shown for illustrative purposes. The data for $V_{SG} = \pm 0.5$ V is presented in

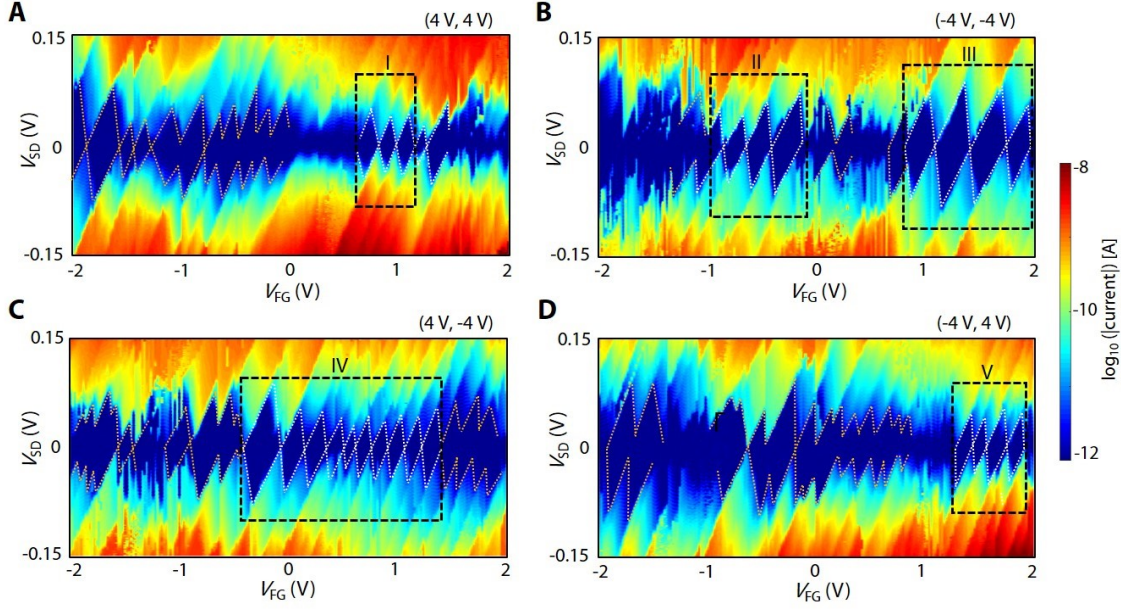


Figure 6.6 Quantum dot behavior with strongly gated electrodes. Current as a function of bias and finger gate voltage, measured at $T = 9$ K. The side gate voltages are indicated in brackets (V_{SG1} , V_{SG2}) and varied as shown in (A) 4 V, 4 V (B) -4 V, -4 V (C) 4 V, -4 V (D) -4 V, 4 V. Black dashed boxes are guides to the eye, see main text for discussion.

Appendix 6.4. In the finger gate voltage range around 1.6 V, two diamonds of different sizes overlap, indicating two QDs with different physical size are weakly coupled and contacted in parallel. In order to extract the relative gating of the two QDs by the side gates, we extract from the dI/dV plots (lower panels of Figure 6.5A) the energy difference between energy levels for different dots, as indicated by ΔE_1 and ΔE_2 . We note that these energies do not correspond to the addition energies of the two QDs. In Figure 6.5(C and D), we plot the energy difference ΔE_1 and ΔE_2 as a function of V_{SG1} and V_{SG2} , respectively. The plots shows that V_{SG1} strongly modulates ΔE_2 while having an almost negligible effect on ΔE_1 . In addition, V_{SG2} only slightly modulates ΔE_1 and ΔE_2 . These two observations suggest that QD2 is closer to SG1 than QD1, and that as a result differential gating of one QD versus the other is possible.

6.3.4 Single QD formation for strongly gated electrodes

When we apply higher/lower voltages (± 4 V) to the side gates, a few regimes with closed diamonds are observed, indicating transport through a single QD rather than serial QDs. As shown in Figure 6.6, 5 regions with single QD behavior are marked with black dashed boxes and numbered with roman letters I-V. From these diamonds, we estimate the charging energies E_c and calculate the total capacitances by $C_{\text{total}} = e_2/E_c$. In a constant interaction model, the positive and negative slopes of the diamonds are given by $+C_{FG}/(C_{\text{total}} - C_S)$ and $-C_{FG}/C_S$, with $C_{\text{total}} = C_{FG} + C_S + C_D$.^{36,37} From these expressions, we obtain the capacitances listed in Table 6.1 for the individual QDs. The

Parameter	I	II	III	IV	V
E_C [meV]	33	40	69	40	42
C_{total} [aF]	4.85	4.01	2.32	4.01	3.81
C_{FG} [aF]	1.01	0.99	0.67	1.00	1.15
C_S [aF]	1.21	0.50	0.39	1.50	0.54
C_D [aF]	2.63	2.52	1.26	1.51	2.12
C_D/C_S	2.17	5.04	3.23	1.01	3.93
Gate coupling $\alpha(\text{FG})$	0.208	0.248	0.289	0.250	0.301
Effective dot size [nm]	21.6	17.8	10.3	17.8	17.0

Table 6.1 Extracted capacities from the QDs in Figure 6.6.

gate coupling of the FG and the effective dot size are also calculated accordingly.

6.4 Conclusion and outlook

Aligned 9-AGNRs are integrated in a multi-gate FET geometry and contacted using graphene electrodes. The advanced gating architecture is motivated by finite-element calculations of the electrostatic potential for achieving homogeneous and strong gate coupling to the 9-AGNRs. Temperature dependent transport measurements show film-like hopping of charge-carriers through the GNR networks at room temperature. At low temperatures, Coulomb blockade and single electron tunneling is observed. In order to benchmark and characterize the working principle of the advanced multi-gate architecture, we investigated the Coulomb diamond shapes in a selected finger-gate region by modulating the side gate voltages. The extracted relative gate couplings of the gates illustrate that the introduction of a local finger gate leads to a massive increase in gate coupling by a factor >200 . These measurements further reveal information about the spatial position of the transport dominating quantum dots, showing that the side gate has a limited influence on the QDs if they are positioned closer to the opposite side gate. This illustrates the challenges in the exact positioning of the nanoscale gates, nanogaps and GNRs with respect to each other. The quantum dots observed with strongly gated graphene electrodes reveal dot sizes slightly below 20 nm. This size is larger than the graphene electrode separation of <15 nm,⁹⁰ but still only half the average 9-AGNRs length of 40-45 nm,¹²⁵ indicating that the confinement of the electrons in the GNRs extends within the GNRs partially on top of the graphene electrodes. The observed addition energies of ~ 0.065 eV are in discrepancy to the DFT-calculated band gap of 0.73 eV³¹ as well as the measured band gap using STS of 1.40 eV¹¹⁵. This highlights that the substrate effects need to be better understood and controlled e.g. via encapsulation (see Chapter 7). Overall, the differential gating of the QDs using multiple gates is a major step forward in the exploration of the transport characteristics of GNRs. Our approach might be further pushed towards ultimate narrow gating strategies as they have been demonstrated for MoS₂-FETs using carbon nanotubes as gate.¹⁹¹

Appendix 6.A. Device fabrication and electrostatic potential

6.A.1 Device fabrication and precharacterization

Figure 6.7 shows the detailed process flow for the device fabrication. We use a cleaned silicon/silicon dioxide (285 nm) with predefined alignment markers as substrate (A). A platinum layer (6 nm) with a chromium adhesion layer (1 nm) is deposited on the substrate using electron-beam evaporation (EBE) (B). The metalized chip is spin-coated with the negative resist hydrogen silsesquioxane (HSQ, Dow Corning) resist with a thickness of 30 nm (B). After drying in air for a few hours, the resist is then exposed using electron beam lithography (EBL, EBPG5200, Raith GmbH) at 100 keV with an electron dose of $350 \mu\text{C}/\text{cm}^2$. Then the exposed resist is developed in a salty developer for 1 min at room temperature. Afterward, the chip is dipped in DI-water for 30 s and blown dry with N_2 (C). The developed HSQ is used as etch mask for the subsequent Ar^+ -ion milling step, by which the surrounding metal layer is removed (D). The remaining HSQ-layer is gently removed by buffered hydrogen fluoride (BHF) for 5 s (E). This results in a finger gate with a width of 10-15 nm and a length of 500 nm. The great advantage of our process is that we use a high resolution resist so that we can accurately control the geometry of the structures and achieve high reproducibility. Also, the final gate electrodes are subtractively crafted from a smooth continuous film, thus not showing artificially enhanced edges, as it is common when using lift-off processes. Then we fabricate GNR junctions on top of the multi-gate structures. A pair of Cr/Au electrodes, used as the contacts to the graphene electrodes, are fabricated by standard EBL and lift-off processes (F). An Al_2O_3 dielectric layer (30 nm) is deposited using atomic layer deposition (ALD) serving as a gate oxide (G). We spin-coated a 120 nm thick PMMA 950K (AR-P 672.02, Allresist GmbH) layer on the Al_2O_3 and used EBL to define an etch mask. A wet etching step of 30 minutes at room temperature using MF321 (DOW Chemical) opened the oxide on top of the contacts and gates. The PMMA-based etch mask is removed using acetone and isopropanol followed by N_2 blowdried. Afterward, a CVD-grown graphene layer is transferred on the chip and contacted with the metal bottom contacts (H). Using EBL the graphene is patterned in the desired shape and the nanogap (<15 nm) separating the two graphene electrodes is formed as reported elsewhere.⁹⁰

This approach yields clean and well-separated graphene electrodes (I). Finally, a film of aligned 9-AGNRs is transferred using the PMMA assisted bubbling transfer.^{88,89,121} The PMMA is removed using acetone, isopropanol rinse, and N_2 blown-dry followed by a thermal annealing process at 200 °C as proposed by Braun et al.⁹⁰ to improve the device performance (J). Panel (K) shows the electrical characterization of the device before and after the transfer of 9-AGNRs.

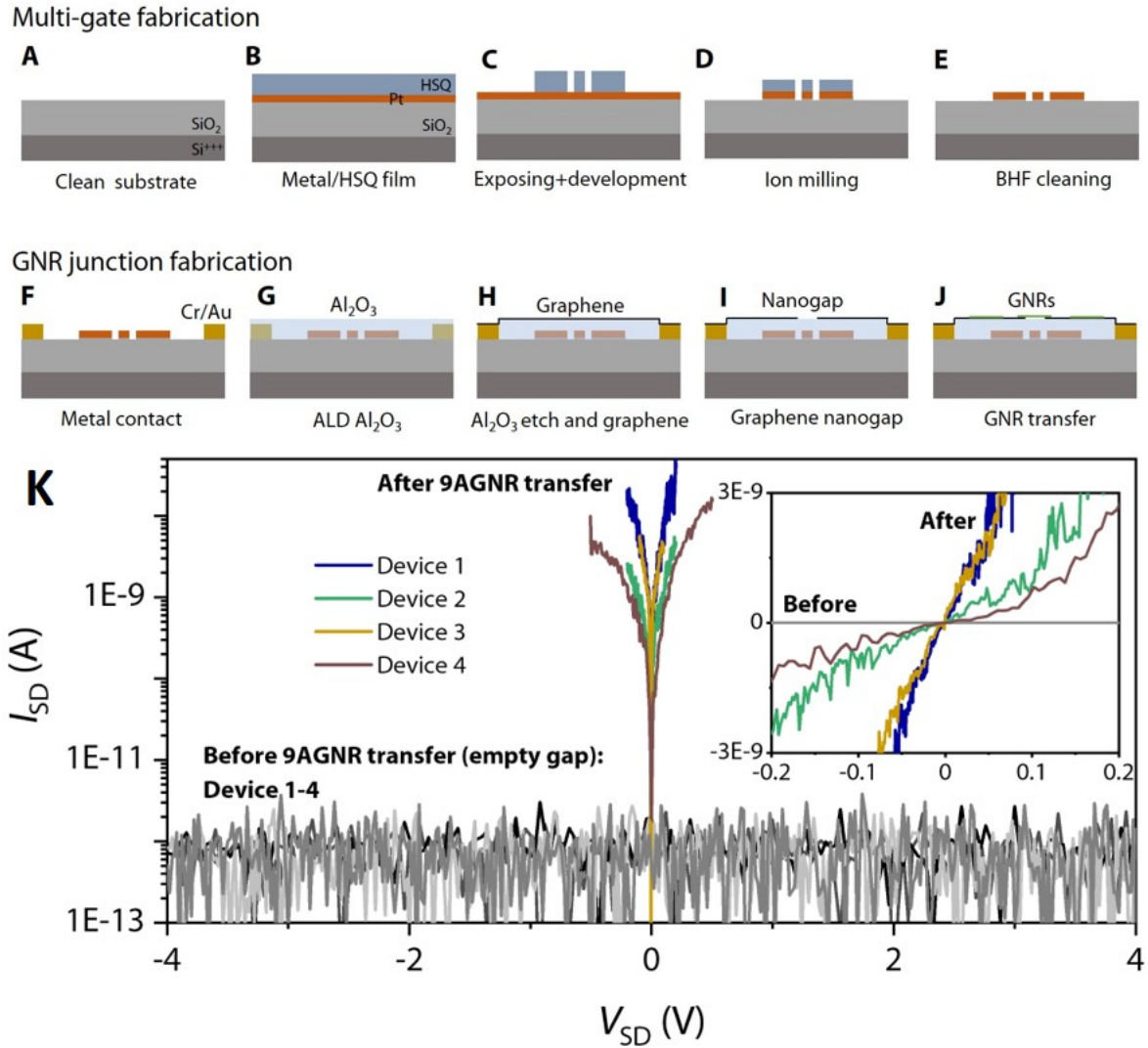


Figure 6.7 Design of multi-gate 9-AGNRs device fabrication process. Top row: Multi-gate fabrication. Bottom row: GNR junction fabrication. (A) Si/SiO₂ substrate. (B) Evaporation of Pt thin film (brown) and spin coating of HSQ resist (blue). (C) Electron beam lithography and development. (D) Ar⁺-ion milling to form local and side gates. (E) Removal of etch mask using BHF. (F) Defining and metallization of Cr/Au contacts (gold) to the graphene using EBL and subsequent lift-off process. (G) Deposition of Al₂O₃ (light blue) using ALD. (H) Wet-etching of Al₂O₃ to open the contacts and transfer of CVD-grown graphene. (I) Shaping of the graphene and nanogap formation using EBL and subsequent RIE. (J) Transfer of aligned 9-AGNRs. (K) Electrical characterization before and after 9-AGNRs transfer at room temperature.

6.A.2 FEM-calculations of the electrostatic potential

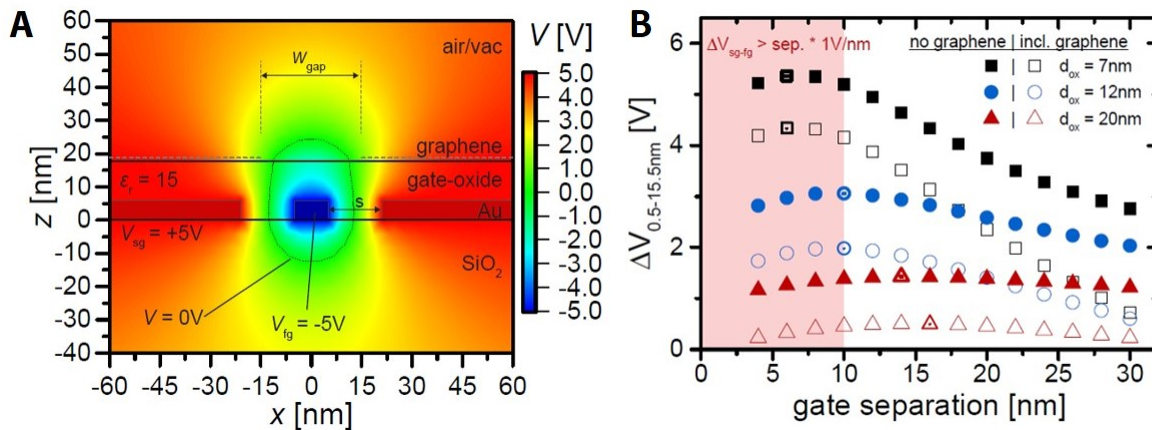


Figure 6.8 FEM calculation of the electrostatics in a finger gate configuration. (A) Electrostatic potential (V) map, with indicated zero-potential line. The graphene is not explicitly included in the simulation. (B) Electrostatic potential within the nanogap as a function of side gate to finger gate separation for various gate oxide thicknesses d_{ox} . $V_{\text{FG}} = -5$ V, $V_{\text{SG}} = +5$ V. The area in red is the area indicated where the voltage between side gate and finger gate exceeds 1 V/nm, a field strength where breakdown can occur. Figure adapted from Overbeck et al.⁹⁴

Appendix 6.B. On-surface and post-transfer characterization of GNRs

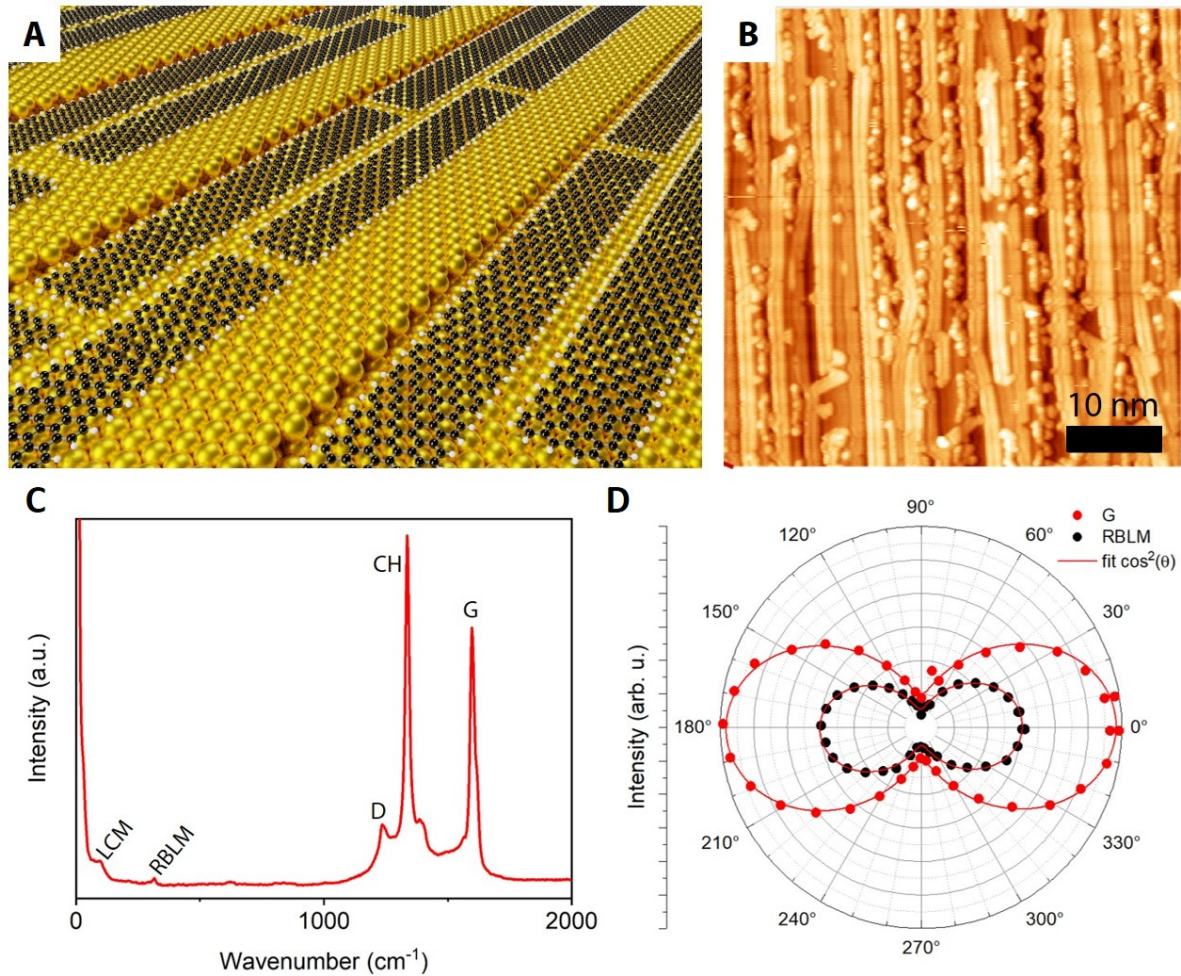


Figure 6.9 Low density aligned 9-AGNRs on Au(788). (A) Artistic illustration of low-density 9-AGNRs on Au(111) terraces of the Au(788) single-crystal growth substrate showing the well-separated GNRs. (B) Topographic scanning tunneling microscopy (STM) image of the aligned 9-AGNRs on the growth substrate. The STM scanning was taken with a Scienta Omicron VT-STM at room temperature. The experimental parameter for this constant-current STM image is -1 V sample bias and 0.03 nA set point current. (C) Raman spectra of 9-AGNRs. The presence of the characteristic peaks (D, CH, RBLM, and LCM) reveals the integrity of the 9-AGNRs upon annealing on the device substrate. (D) Polarization dependence of the G- and RBLM-peak intensity reveals almost perfect alignment with the source-drain axis.

Appendix 6.C. Device 1: Additional data

Appendix 6.C.1. Temperature dependent transport characteristics

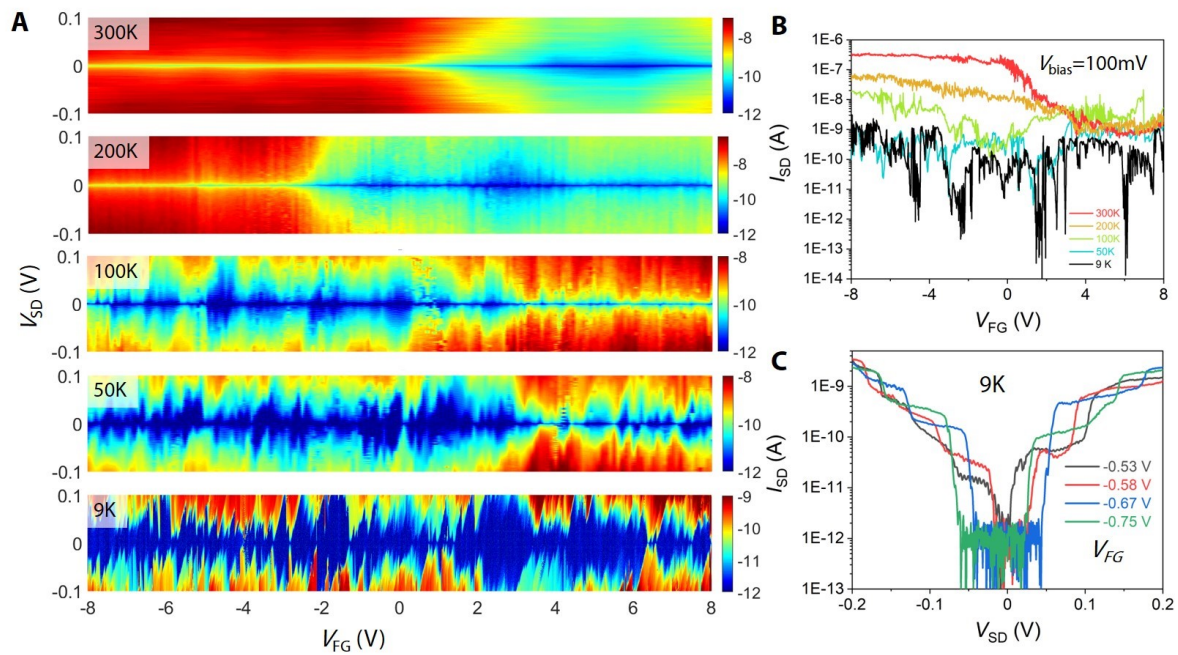


Figure 6.10 Temperature dependent transport data of device 1. (A) Current as a function of applied bias and gate voltage measured at 300 K, 200 K, 100 K, 50 K and 9 K, respectively. (B) Current as a function of gate voltage with a fixed bias voltage of 0.1 V at the same temperatures as in (A). (C) Selected I-V characteristics at various finger gate voltages recorded at 9 K.

Appendix 6.C.2. Extended data to separately gated electrodes

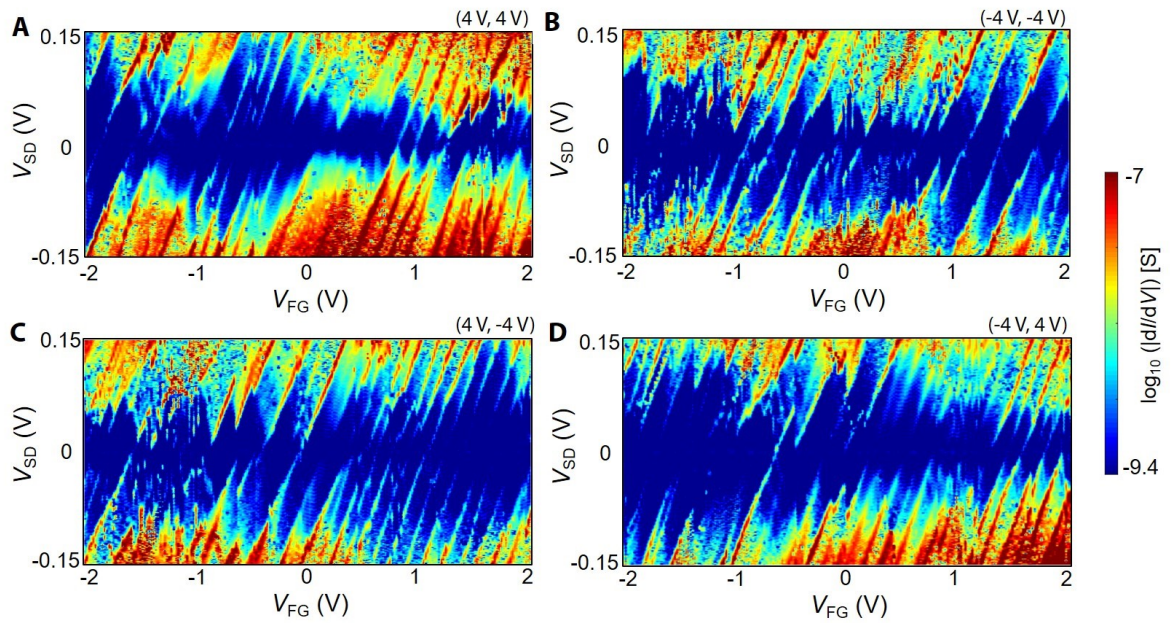


Figure 6.11 Extended data to **Figure 4** in the main text. Top panels: Current as a function of bias and finger gate voltage, for 9 different side gate voltage configurations measured at $T = 9$ K. The side gate 1, 2 voltages V_{SG1} , V_{SG2} are indicated in brackets on top. Bottom panels: Corresponding dI/dV -maps.

Appendix 6.C.3. Current and dI/dV -maps with individually gated electrodes

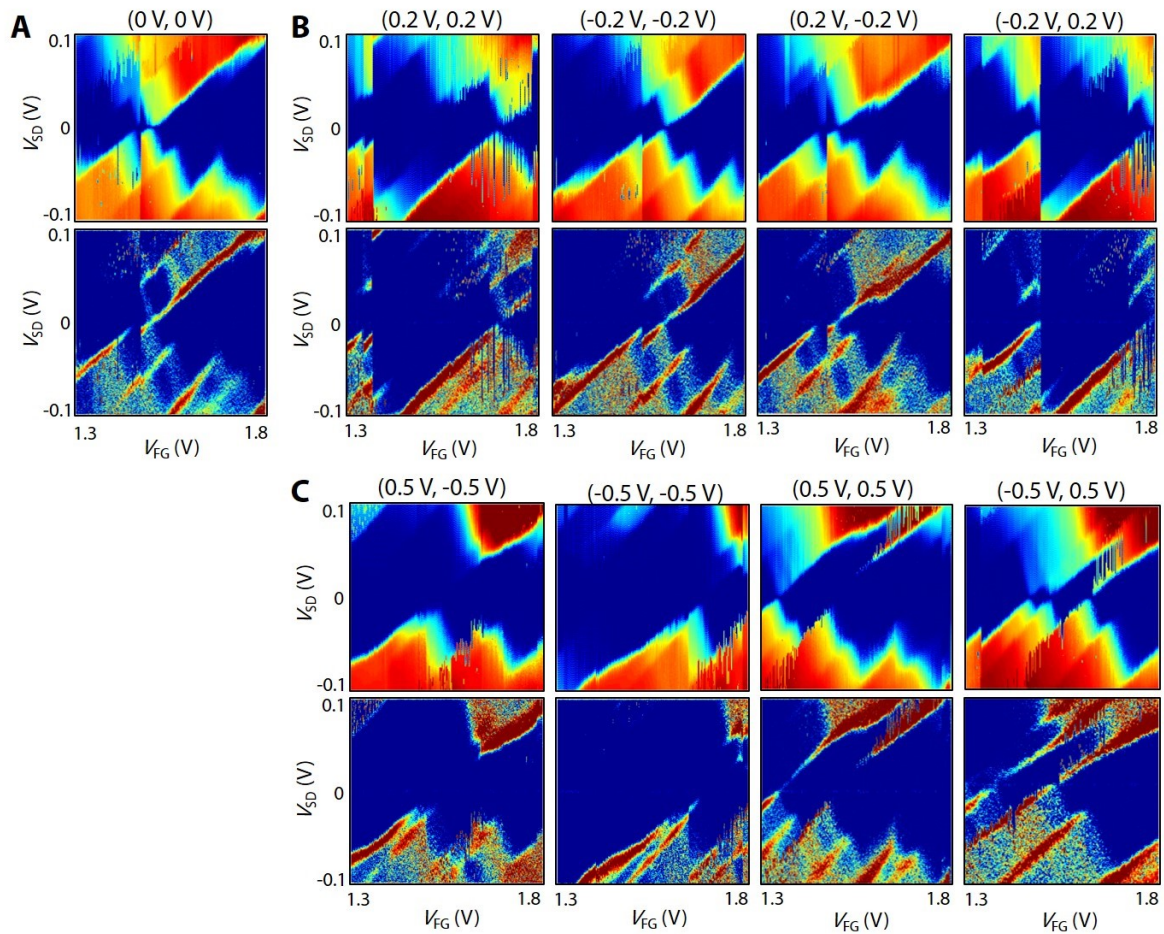


Figure 6.12 Current and dI/dV -maps with individually gated electrodes Top panels: Current as a function of bias and finger gate voltage, for three different side gate voltage configurations measured at $T = 9$ K. The side gate voltages are indicated in brackets on top (V_{SG1} , V_{SG2}). Bottom panels: Corresponding dI/dV maps. The side gate 1, 2 voltages V_{SG1} , V_{SG2} are in **A** $0V$, **B** $\pm 0.2V$ and **C** $\pm 0.5V$. The current is measured at $T = 9$ K.

Appendix 6.D. Devices 1-4: Overview of transport characteristics

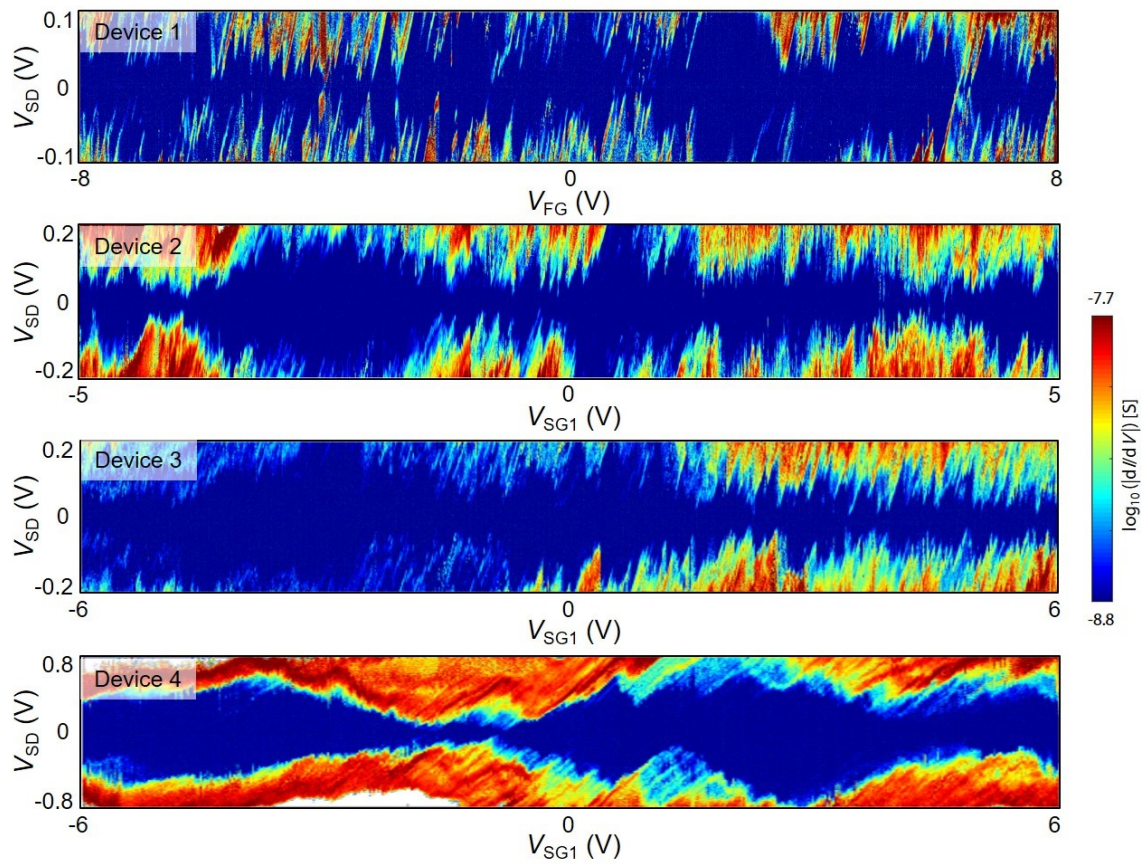


Figure 6.13 Overview of transport characteristics at low temperature of Devices 1-4. dI/dV as a function of bias and gate voltages. The device and swept voltages are indicated. All other voltages are set to zero. (A) Device 1, V_{FG} (B) Device 2, V_{SG1} (C) Device 3, V_{SG1} (D) Device 4, V_{SG1}

7 Edge contacts to graphene nanoribbons

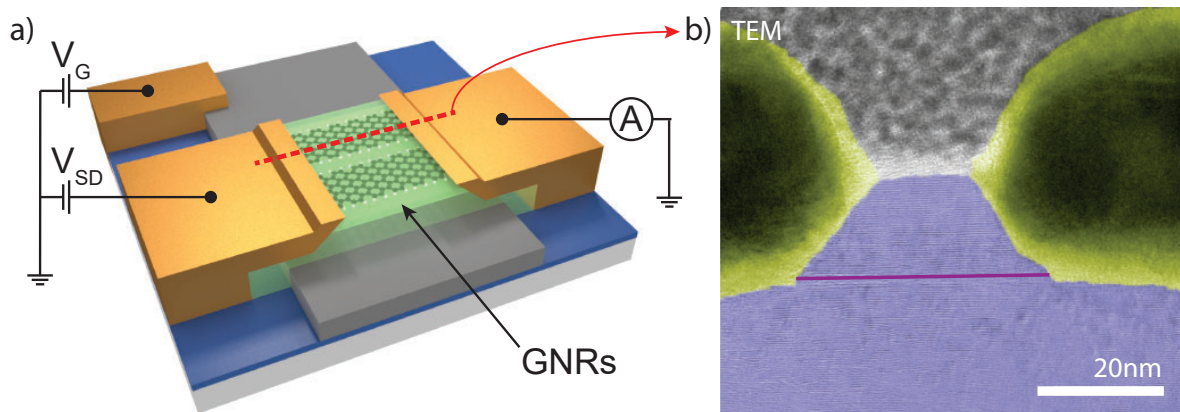


Figure 7.1 Device layout and TEM crosssection of edge contacted GNR-device. a) Artistic illustration showing edge contacted GNRs, the contacts, as well as schematically the electrical circuit. b) False colored TEM crosssection at the red dashed line in a). GNRs (purple) are embedded in hexagonal boron nitride (light blue) and contacted by metal contacts (yellow).

Encapsulating two-dimensional materials using hexagonal boron nitride and subsequently making edge contacts to the material of interest revolutionized the field of layered materials. It further enabled scientists to discover novel physical phenomena like superconductivity and opened the field of twistrionics. Here, the first encouraging results on edge-contacted GNRs are presented. We show that it is possible to contact GNRs in quasi-point contact geometry and demonstrate strong gate-dependent transport at room temperature. Temperature-dependent measurements reveal that two types of transport mechanisms are present in these structures. Finally, an outlook is given on how one can further improve the gating geometry.

Contributions:

O.B. and D.I. conceived and designed the experiments. O.B. and D.I. fabricated the devices. M.S. performed the TEM analysis. O.B. performed the Raman measurements. G.B.B and R.D. performed on-surface GNR synthesis and STM imaging, providing samples and images. Electrical, SEM, and AFM measurements were performed and analyzed by O.B., with help of M.L.P. and M.C. The Blender picture for the schematic device layout was provided by M.P. The study was supervised by M.C.

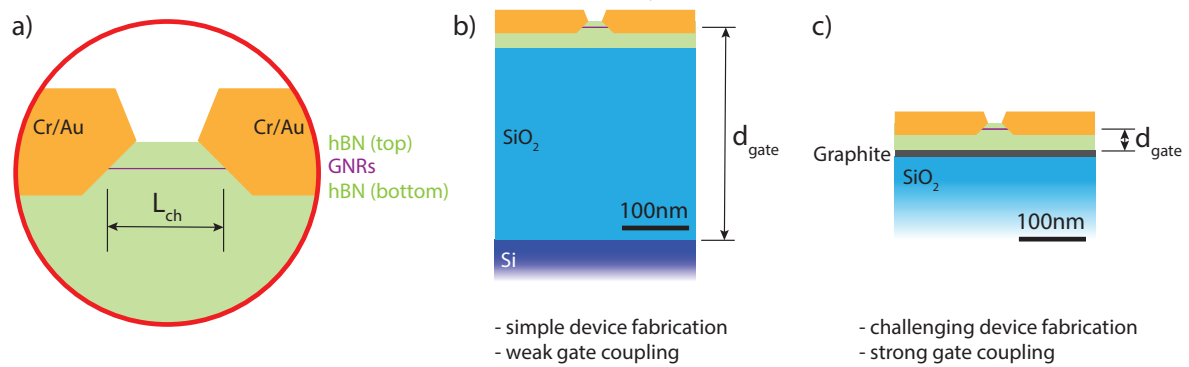


Figure 7.2 Gating geometries for edge contacted GNR-devices. a) The central cross section. Devices with different gate/gate dielectric geometries on b) Si/SiO₂ and c) on graphite. Note the drawings in b) and c) are to scale.

7.1 Introduction

Usually, graphene is contacted by evaporating metal contacts to its flat face, where there are few strong bonding sites for the metal. In contrast, the edge contacting technique makes metal contacts along its edge, where bonding orbitals of the graphene are exposed. Wang et al.²⁰ introduced in 2013 a technique to make one-dimensional contacts to a two-dimensional material. This edge contacting technique consists of encapsulating graphene (or other 2D materials) with hexagonal boron nitride sheets and etching through the top hBN to make metal contacts along the edge of the graphene.

The technique relies on high-quality hexagonal boron nitride crystals that are synthesized at the National Institute of Materials Science (NIMS) in Tsukuba, Japan, by Takashi Taniguchi and Kenji Watanabe.¹⁹² Their material is the ideal embedding material for other layered materials due to the following reasons. From a mechanical point of view, hBN crystals are layered which allows them to be cleaved into thinner flakes with atomically flat surfaces. Further, the boron and nitrogen atoms are also arranged in a hexagonal shape, although with a lattice constant 1.8% longer than that of graphene.¹⁹³ From an electronic point of view, hBN is a wide band gap material with a direct band gap of ~ 5.9 eV.¹⁹⁴ Further, high-quality hBN crystals have a reduced disorder and low charge inhomogeneity, which is favorable for high-quality gate-dielectric materials.¹⁹⁵ The two hBN sheets protect the graphene from unwanted external influences like water or contaminants. Notably, the improved electronic device characteristics, like the reported high charge carrier mobilities of $\sim 150'000$ cm²V⁻¹s⁻¹ and the low contact resistance of ~ 150 $\Omega\mu$ m for graphene at room temperature is of particular interest.²⁰ This since the high contact resistance is limiting GNR based devices in unfolding their potential.^{20,196}

Altogether, this contacting strategy is widely used by the 2D-materials community and improved the device quality and cleanliness substantially. In devices improved by this method, new physical phenomena have been observed, for example, the field of *Twistronics* has emerged, where two sheets of a 2D-material on top of each other are twisted versus each other by a small angle.¹⁹⁷ In such structures, measurements of superconductivity were reported. This effect is related to the "magic angle" twist-angle

of around 1.1° and the formed Moiré-lattice.¹⁸⁴

Motivated by this enormous potential that an embedding of the material of interest in a suited dielectric material brings, efforts to encapsulate GNRs using hBN were undertaken. An edge contacting of GNRs would result in devices that are protected from the influence of the environment during processing and measurement. Further, it would result in quasi-point contacts to a one-dimensional material.

Besides edge contacting GNRs, the gating geometry is also of crucial importance for exploring the electrical properties of the channel material. In Figure 7.2 different gating geometries are shown, where in the most simple case a highly doped silicon gate is ~ 285 nm below the channel, separated by a SiO_2 and the bottom hBN (see Figure 7.2b)). In a more advanced geometry, a ~ 10 nm thick graphite flake is used as a back gate (see Figure 7.2c)). Graphite has been shown to serve as an ideal gating material due to its flatness.¹⁹⁸

In the following, the fabrication challenges are described as well as first transport results on the two gating geometries are discussed.

7.2 Challenges in the device fabrication and proposed solutions

7.2.1 Dry transfer of 9-AGNRs

Motivated by the advantages as described in the previous section, it is obvious to test the dry transfer of GNRs from the growth substrate to the (insulating) target substrate. For a pick-up of GNRs using an hBN flake to be successful, the adhesion between GNRs and hBN has to be stronger than GNRs to Au(111). It has been reported that the GNR-Au(111) contact is almost superlubric, with kinetic and static friction force values in the range of ~ 100 pN.¹⁹⁹ However, in graphite as well as in graphene/hBN heterostructures microscale superlubricity has been reported, pointing towards a weak interaction between GNRs and the hBN flake.^{200–204} Discoveries in experimental physics frequently occur despite theory predicting challenges in their realization. In a collaboration with Dr. David Indolese from the Nanoelectronics-Group lead by Prof. Christian Schönenberger at the Department of Physics, University of Basel, we tried to pick up 9-AGNRs directly from the Au(111)/mica growth substrate. The following attempts were undertaken:

- pick-up at 40°C
- pick-up at 40°C , with mechanical force
- pick-up at 80°C
- pick-up at 80°C , with mechanical force

The added thermal energy is expected to weaken the GNR/Au(111) interaction, hence making a pick-up more likely. The additional mechanical force was applied to slightly push around the GNRs on the Au(111) surface to bring them in closer contact to the hBN and hence facilitate a pick-up. The transferred hBN flakes were pressed on a

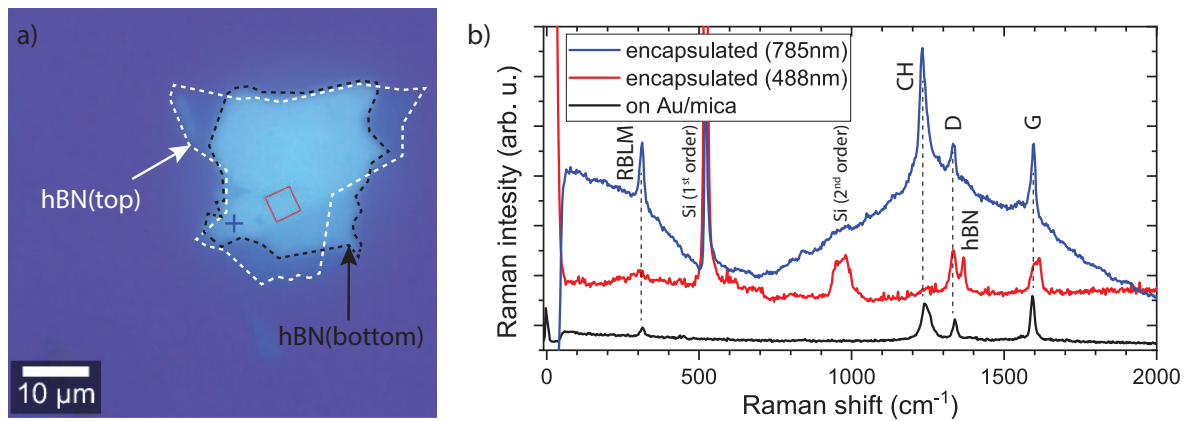


Figure 7.3 Raman signature of encapsulated 9-AGNRs. **a)** Optical micrograph showing the hBN stack on SiO_2 . The borders of the top and bottom hBN are highlighted with white and black dashed lines, respectively. Positions of where Raman spectra were taken are indicated with a blue cross and red square. **b)** Raman spectra of encapsulated 9-AGNRs acquired with an excitation wavelength of 785 nm (blue) and 488 nm (red). Raman spectra of 9-AGNRs on Au/mica growth substrate for comparison (black). Characteristic peaks are labeled (see main text for details).

Raman optimized substrate, aluminum-oxide (40 nm) grown on platinum (40 nm) on Si/SiO₂ (285 nm) for an enhanced Raman intensity and blocked Silicon background signal (for details see Chapter 3). Raman spectroscopy scans revealed that no GNRs were transferred. This negative result requires new developments in delamination techniques or intercalation of GNRs directly on the Au(111) surface for a dry-transfer to be possible.

7.2.2 Wet transfer and encapsulation of 9-AGNRs

We turned to a well-established wet-transfer of the 9-AGNR film onto Si/SiO₂ with bottom hBN-flakes.^{122–124} Subsequently, a top hBN-flake is pressed and released on a suited bottom flake, finalizing the encapsulation. The hBN pick-up and release are described in detail in Indolese et al.²⁰⁵

Raman spectra of encapsulated 9-AGNRs

The successful transfer and encapsulation of 9-AGNRs were confirmed using Raman spectroscopy measurements. Figure 7.3b) shows in blue a point spectra of encapsulated 9-AGNRs acquired with an excitation wavelength of 785 nm (1.59 eV). This excitation is used since its energy is close to the electronic excitation energy of the 9-AGNRs, which leads to a strong Raman signal, this effect is called Resonance Raman spectroscopy.^{88,206}

The characteristic Raman peaks of 9-AGNRs are visible. Namely the G-peak, caused by the C-C vibration, the edge related Ch-/D-peaks, as well as the width dependent radial-breathing-like-mode (RBLM). In the range 700-1700 cm⁻¹ (830-905 nm, 1.49-1.37 eV) a photoluminescence (PL) signal is present. Assigning the origin of this PL background is not trivial. It has been reported that in hBN single-photon emitters, from different point defects and stacking faults, give rise to a PL signal in the range

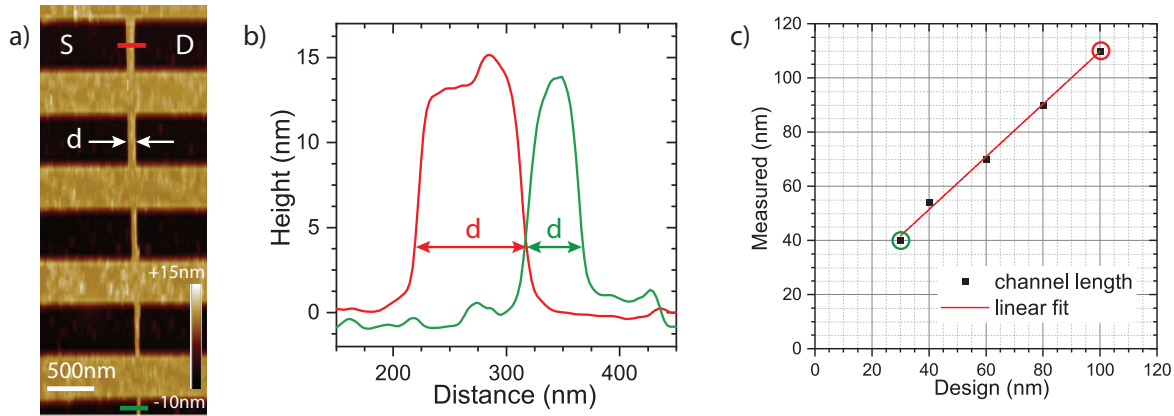


Figure 7.4 hBN etching for edge contacted GNR-devices. a) AFM height profile of an hBN flake where different source-drain separation were etched. b) Selected height profiles indicated in a) with the corresponding color, red and green, respectively. The arrow indicates where the channel would be (~ 10 nm from the top). c) Comparison of the designed and measured channel length.

570–750 nm.^{207,208} GNRs can also become photoluminescent themselves if functionalized such that sp^3 -type of defects are present.¹²¹ It has been reported that by encapsulating a material using hBN, its photoluminescence intensity is enhanced compared to non-encapsulated.²⁰⁹ A characteristic peak of the hBN, located at 1366 cm^{-1} , is only visible in the spectra acquired with a 488 nm excitation.²¹⁰ This due to the closer to resonance excitation energy. Overall, Raman spectroscopy confirms the presence of the GNRs in between the two hBN flakes, although the signal-to-noise ratio is low. The low intensity is caused by the positioning of the GNRs above the SiO_2 surface, given by the thickness of the bottom-hBN, in combination with the covering of the GNRs with the top-hBN.

hBN etching for minimal channel length

Before the spin coating of the resist that serves as an etch mask, the sample is exposed to an oxygen plasma for 15 s to etch away all the GNRs that are not protected by the top hBN. To contact the 9-AGNRs, one has to etch through the top-hBN. This etching procedure results in an hBN-etch profile of 45° . This particular profile is the key for making edge contacts, but also the limiting factor for the channel length. To keep the 9-AGNRs channel length below 40 nm, the top hBN has to be thinner than 20 nm. For our devices, we chose hBN-flakes between 5–10 nm thick. Additionally, the etch mask is chosen to be only 60 nm thick to achieve the high-resolution EBL to separate the source and drain edge contacts. After etching through the top hBN flake, the same resist mask is used for the metallization with Cr/Au. This leads to a self-alignment of the contacts to the opened GNR edges.

A high-resolution transmission electron microscope crosssection of a representative device is shown in Figure 7.1b), revealing the edge contact geometry, the clear electrode separation, and the slanted hBN profile.

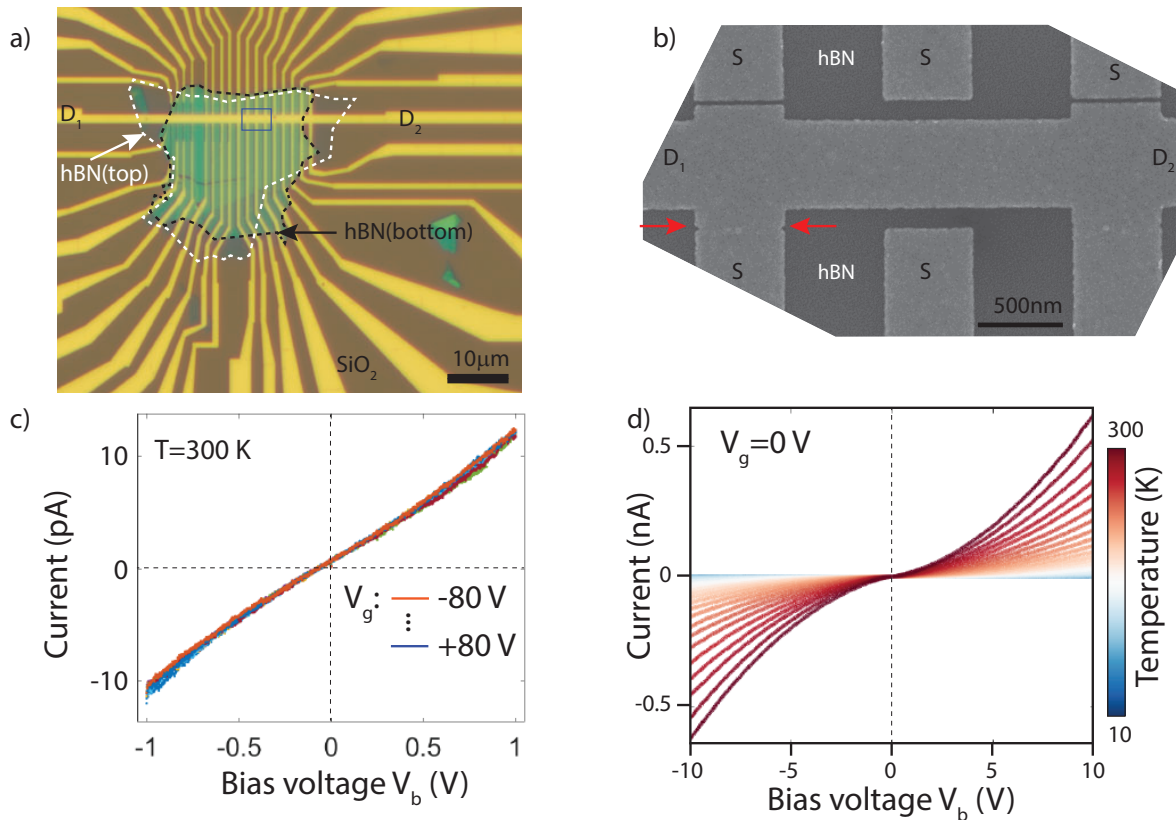


Figure 7.5 Electrical characterization of an edge contacted 9-AGNRs device on SiO₂. **a)** Optical micrograph showing the hBN stack on SiO₂ as well as the Cr/Au leads. The borders of the top and bottom hBN are highlighted with white and black dashed lines, respectively. **b)** SEM image of the region indicated with a blue square in **a)** after metalization of the source (S) and drain (D) contacts. The red arrows indicate where the contact separation was not successful during lift-off. **c)** Current-voltage characteristics for various gate voltages at room temperature. **d)** Temperature-dependent current-voltage characteristics.

7.3 Transport results of edge-contacted 9-AGNRs using a silicon gate

First devices were successfully fabricated on Si/SiO₂ (285 nm) substrates. In Figure 7.5a) a typical device is shown with a high-resolution SEM image in **b)** showing the contact separation in detail. The contacts D₁ and D₂ serve as a common drain, while all other contacts are source contacts (not labeled). This geometry has the benefit of providing more than two dozen devices out of one hBN/GNRs/hBN-heterostructure. Such a high number is needed due to a low device yield since the embedded 9-AGNRs are non-aligned. Figure 7.5c) shows I-V curves obtained on a typical device at room temperature, revealing almost linear behavior in the bias voltage range <1 V. No gate dependence is observed, in contrast to previous measurements on this type of GNR.^{13,90} This can be explained by the geometrical aspect ratio between the channel length (~40 nm) and the distance to the gate (bottom hBN+SiO₂ ~ 300 nm). Further, the

metal electrodes screen the electrostatic field substantially. With an increased bias voltage highly non-linear I-V curves are observed, see Figure 7.5d). There, the I-V curves obtained at different temperatures are shown, indicating a strong temperature dependence. The I-V characteristics are similar to GNRs contacted using graphene as well as palladium electrodes, although much lower in current.^{13,90}

7.3.1 Interpretation of the temperature-dependent transport data

The observation of non-zero current in the I-V characteristics shows that a metal/GNRs/metal junction has been formed. The low current shows that one or multiple barriers are present in the system. In metal/carbon nanotube/metal FETs it has been shown that a Schottky barrier is formed at the metal/carbon interface.²¹¹ Due to the quasi-point contact, it is questionable if the same barrier is formed. To identify the present transport mechanism in these metal/GNR/metal junctions, it can be of significant interest to look at both the temperature and voltage dependence of the I-V curves. Direct tunneling and Fowler-Nordheim tunneling, through and above the barrier in a metal/GNR junction, are temperature-independent transport mechanisms. The Fowler-Nordheim tunneling has a characteristic voltage dependence as follows:^{212,213}

$$\ln\left(\frac{J}{V^2}\right) \sim \frac{1}{V} \quad (7.1)$$

where J is the current density and V the bias voltage. On the other hand, transport mechanisms that do show a strong dependence are thermionic emission as well as hopping conduction.

For hopping conduction the following temperature dependence has been identified:²¹³

$$\ln\left(\frac{J}{V}\right) \sim \frac{1}{T} \quad (7.2)$$

where T is the system temperature. For thermionic emission, the following temperature dependence has been identified:²¹³

$$\ln\left(\frac{1}{T^2}\right) \sim \frac{1}{T} \quad (7.3)$$

To deepen the understanding of the observed strong temperature-dependent charge transport, we start our analysis by representing the data for a fixed bias voltage in an Arrhenius plot as shown in Figure 7.6a). It is observed that only the data in the temperature range 200-300 K can be directly fitted as shown in Figure 7.6b) pointing to a hopping type of transport. Following the same procedure as described in Subsection 5.2.1, an activation energy E_{act} of ~ 96 meV can be extracted. This is a bit more than a factor 2 lower than the there extracted ~ 230 meV. Reasons could be that the contact resistances are lower due to the edge contacts that cut the GNRs or that as described in Subsection 5.2.1 additional barriers are present in GNR films.

Surprisingly, the data obtained from measurements between 10-80 K can be fitted to Equation 7.3, pointing towards thermionic emission as the dominant transport mechanism. Following the interpretation of Björk et al.²¹⁴, an activation energy E_{act} of ~ 2 meV can be extracted. The difference in activation energies between the high and low temperature

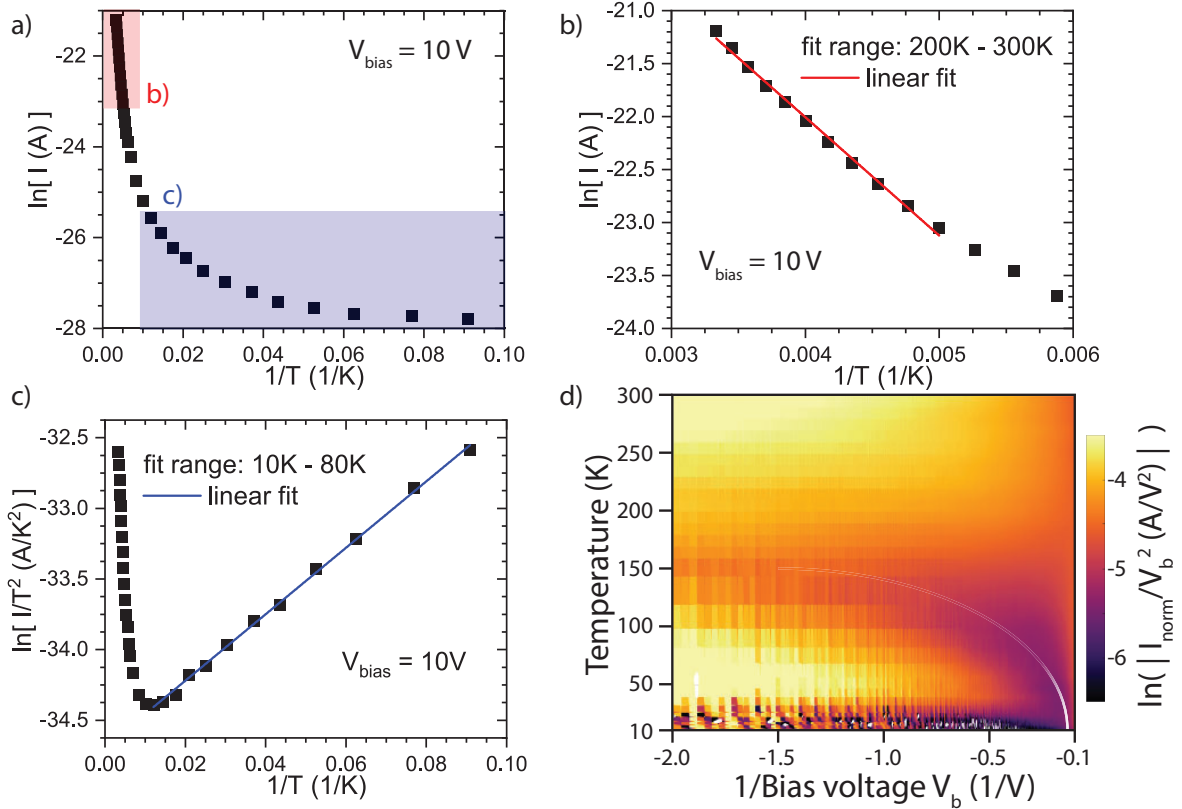


Figure 7.6 Arrhenius and transmission voltage spectroscopy analysis. a) Arrhenius plot. The data points fitted in b) and c) are highlighted in red and blue, respectively. b) Arrhenius plot of the high temperature currents. c) Arrhenius like plot with I/T^2 . d) Fowler-Nordheim plot with normalized currents at different temperatures as used in transmission voltage spectroscopy. The white fading line as a guide to the eye.

is quite striking and points towards different transport mechanisms being present in the two temperature regimes. To better understanding these transport mechanisms and in particular the transition between them, we turn towards transition voltage spectroscopy (TVS). It has been shown that in metal/molecule/metal junctions, the I-V characteristics, if plotted in a Fowler-Nordheim manner (see Equation 7.1), exhibit an inflection point.^{212,215} This is consistent with the change in transport mechanism from direct tunneling to field emission. TVS has also helped observe molecular orbital gating as shown by Song et al.²¹⁶ However, TVS is a method that is also under debate since the discrimination between metal/molecule/metal and metal/vacuum/metal junction is not as trivial as initially suggested.²¹⁷

In Figure 7.6d) we show the Fowler-Nordheim plot (with normalized currents for comparison) at various temperatures, revealing that the transition voltage changes and even disappears with increasing temperature, indicated by the white fading line for better visualization. This thermally activated process is more consistent with a hopping type of transport mechanism rather than a coherent transport picture. Hence, we interpret the presented data such that the film of 9-AGNRs is contacted with the charge carrier

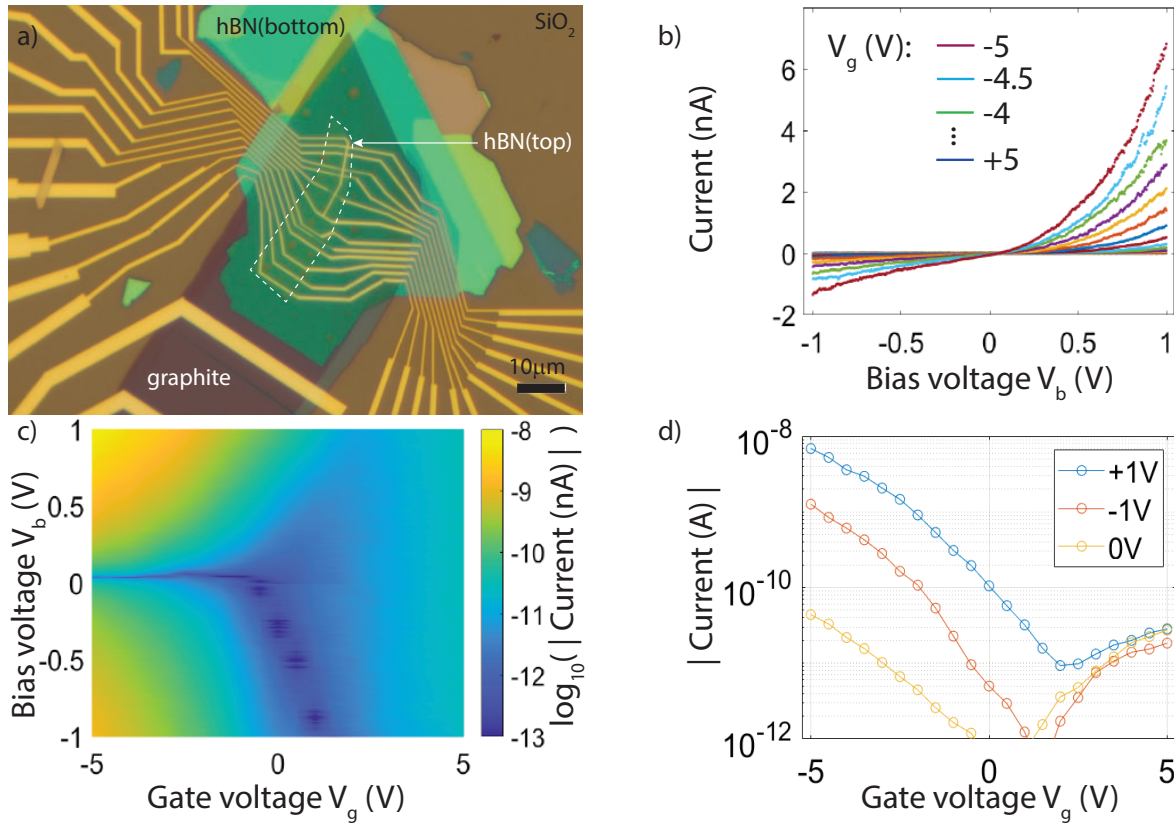


Figure 7.7 Electrical characterization of an edge contacted 9-AGNRs device on graphite at room temperature. **a)** Optical micrograph showing the hBN stack on graphite as well as the leads. The borders of the top hBN are highlighted with a white dashed line. **b)** Current-voltage characteristics for various gate voltages applied to the graphite back-gate. **c)** Absolute current values as a function of bias and gate voltage on logarithmic scale. **d)** Cuts in c) at 3 selected bias voltages $V_b = +1$ V, 0 V and -1 V, respectively.

injection at the GNR-edges. In the next section, transport results obtained on a device fabricated with a graphite back-gate to achieve higher gate coupling are presented.

7.4 Transport results of edge-contacted 9-AGNRs using a graphite gate

Figure 7.7 shows the device geometry with a graphite back-gate. The various colors of the bottom hBN arise from thickness variations in the nanometer range. A careful design of the leads is necessary. Besides avoiding going over hBN edges that are higher than the lead thickness to avoid interrupting them, one has to design the leads around the graphite flakes since it would shorten neighboring leads.

The electrical characterization revealed highly non-linear I-V characteristics at room temperature and a strong gate dependence over three orders of magnitude (see Figure 7.7b) and c), respectively). The asymmetric I-Vs show rectification behavior.

Although the device is designed symmetrically, an asymmetrical contact can be present. By plotting the current versus gate voltage at a fixed bias voltage, as shown in Figure 7.7d), it can be seen that there is also a current at $V_b = 0$ V. This can be interpreted as leakage current between the gate and the drain contact. Although a pre-resistor in front of the gate electrode is used to limit the leakage current, the resistance R_{pre} must be much smaller than the resistance between the graphite and the drain contact, otherwise, it serves as a voltage-divider and hence limits the gate voltage range. This leakage can be explained by the following. The bottom hBN was chosen to be rather thin (~ 20 nm) to have a strong gate coupling, this in combination with the direct band gap of hBN of ~ 5.9 eV, leads to a detectable leakage current at moderate gate voltages. These results demonstrate the gating of encapsulated and edge-contacted 9-AGNRs at room temperature. Unfortunately, due to a human error in the setting up of the wiring of the electric circuit for the temperature-dependent measurement, the sample was damaged and no further measurements could be taken.

7.5 Conclusion and outlook

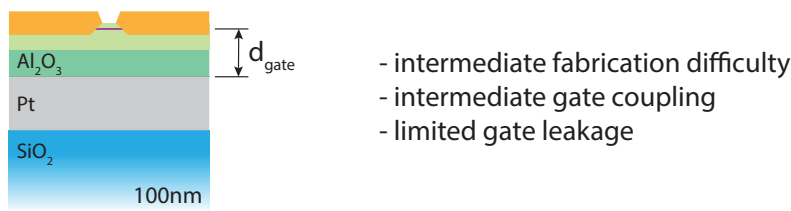


Figure 7.8 Next generation gating geometry. An intermediate geometry where a metal gate is separated by a 40 nm aluminum-oxide from the hBN/GNRs/hBN stack combining the advantages of having a close gate with limited gate leakage.

In conclusion, we have demonstrated the encapsulation and edge contacting of 9-AGNRs in two types of gating geometries. The gate-dependent transport was limited in the case where the distance between the gate and the channel was much larger than the channel length. However, in the case of a close graphite back-gate, a strong gate dependence of the charge transport could be observed, although limited by the resulting gate leakage currents. These results are encouraging for further exploration in slightly different geometries. In Figure 7.8 such a next-generation gating geometry is depicted. By choosing the aluminum oxide thickness to be ~ 40 nm thick one could bring the metallic back-gate rather close to the channel, while its thickness and dielectric properties would limit the leakage currents substantially. The present photoluminescence signal of encapsulated GNRs should be understood more clearly. Therefore, temperature-dependent measurements are suggested. The superlattice, that is formed between graphene and hBN has, due to the slight lattice constant mismatch, a maximum lattice constant of ~ 14 nm.²¹⁸ It is hence possible that the GNRs on hBN also form a superlattice, possibly resulting in interesting physical phenomena, for example band band gap engineering. However, a dry transfer of GNRs from the

growth substrate combined with subsequent encapsulation and edge-contacting would be favorable. Currently, investigations in this direction are being undertaken in the group of Prof. Roman Fasel at Empa.

8 Seebeck coefficient of nanoscale devices

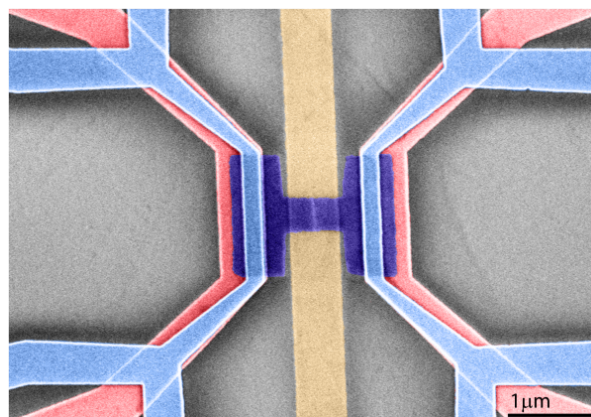


Figure 8.1 SEM image of the platform for thermoelectrical characterization. Heaters (red), thermometers (blue), gate (yellow) and graphene electrodes (violet) are highlighted in colors.

Ever since the reporting of the thermoelectric effect by Thomas Johann Seebeck in 1822, physicists have wanted to make efficient use of this energy conversion process.⁴ After exploring the thermoelectric properties of bulk materials for more than 100 years, two papers by L. D. Hicks and M. S. Dresselhaus in 1993 pointed out that quantization effects in nanostructures could be a way of designing new thermoelectric materials.^{8,9} This is mostly because the dimension reduction leads to a decoupling of the thermal and electrical conductivity, a key ingredient for improving the conversion efficiency. Motivated by this work, new efforts were undertaken to study the Seebeck coefficient of nanoscale materials. Nevertheless, it was only in 2007 that the first values for the Seebeck coefficient in a molecular junction were reported by Reddy et al.²¹⁹, highlighting the experimental challenges one has to overcome. It took another 7 years of research until electrostatic control over thermoelectricity in a molecular junction was also achieved.²²⁰ Only recently, the complete mapping of the thermoelectric properties of a single molecule was reported by Gehring et al.²²¹

This shows that determining the Seebeck coefficient of nanoscale devices is a new field that still faces many experimental hurdles due to the nanometer-scale dimensions of the objects under test. In this chapter, the Seebeck coefficients of Au-nanoparticle arrays, graphene, and films of graphene nanoribbons are determined and the experimental procedures thereof are described. Two different device architectures and measurement schemes were employed. With the first generation of measurement devices, we characterized nanoparticle arrays. Based

on the challenges we faced, we developed a second generation of devices and measurement schemes, with which we characterized graphene and films of graphene nanoribbons.

Contributions:

O.B., M.L.P., and M.C. conceived and designed the experiments. R.Fu. performed the graphene growth. M.S. and O.B. fabricated the devices. V.M., under guidance by J.L., performed NP synthesis. D.B. derived the temperature distribution reported at pages 117-119. G.B.B. and R.D., under the supervision of R.F. and P.R., performed the on-surface GNR synthesis and STM-imaging, providing samples and images. Electrical, SEM, AFM, and Raman measurements were performed and analyzed by O.B., with help of M.L.P. and M.C. Comsol simulations were performed by M.L.P. The Blender picture for the schematic device layout was provided by M.L.P.

8.1 Introduction and motivation

The Seebeck coefficient, as introduced in Chapter 2, can be expressed in the following form:

$$S = -\frac{\Delta V}{\Delta T} \quad (8.1)$$

As can be seen from Equation 8.1, to determine the Seebeck coefficient of a material, one has to determine the electrostatic potential difference ΔV that builds up between a hot and a cold side of a material with a temperature difference ΔT between them. As a result, to study this effect, a temperature gradient needs to be generated. At the macroscale, this is done, for example, by placing one side of the material in an ice water bath, as in the very early days. When it comes to the nanoscale this is more delicate due to the length scales that are involved. Local, controlled heating, similar to determining the thermal conductivity, has been achieved using optical methods,^{57,58,130} self-heating effects in nanostructures by passing a current through them,⁷⁰⁻⁷³ or indirectly by passing a current through a nearby placed heater^{82,221-223}. The most suited approach depends on the measurement scheme and sample geometry, which need to be adapted to the specific needs. For example, in the nanoelectronics community, where it is desirable to have the electronic temperature as close as possible to the cryostat temperature to enable spectroscopy measurements, the self-heating method is avoided. Therefore, fabricating micro-heater(s) nearby is the method of choice, but this requires additional electrodes, which increases the fabrication complexity. This may reduce the number of devices on a chip or may even be unfeasible due to limitations on the chip itself.

Thermoelectricity in nanoscale objects has been studied by several groups. For example, the thermoelectric properties of graphene have been reported in pioneering work by the Kim group, reporting values for S of $\approx 100 \mu\text{V}/\text{K}$.^{224,225} In the field of nanowires, the Linke group explored the feasibility of using single nanowires in the context of heat engines using a quantum dot as energy filters.^{222,223} In a single nanowire device, Roddaro et al.⁸² reported values for S exceeding $\approx 120 \mu\text{V}/\text{K}$ and Yazji et al.²²⁶ reported $S \approx 300 \mu\text{V}/\text{K}$, showing their potential for thermoelectric devices. At an even smaller scale, thermoelectric effects have also been explored in molecules, where the contributions by the Reddy group and the Venkataraman group stand out.^{219,227}

The first measurements of thermopower in molecular junctions have been reported by Reddy et al.²¹⁹ in 2007 using a modified scanning tunneling microscope. Most values of the Seebeck coefficient reported for molecular junctions have remained below $50 \mu\text{V}/\text{K}$.²²⁸ However, in 2019, by partially suppressing the electrical conductance in molecular junctions using quantum interference, a Seebeck coefficient as high as $1000 \mu\text{V}/\text{K}$ was reported by Garner et al.²²⁹ Although many STM measurements have been performed on molecular systems since 2007,^{227,230,231} it was only in 2014 that electrostatic control of thermoelectricity in molecular junctions was achieved by Kim et al.²²⁰, in a planar, solid-state, electromigration junction. In a similar planar geometry, the thermovoltage of a fullerene molecule contacted using graphene leads was measured, leading to Seebeck coefficients up to several hundreds of $\mu\text{V}/\text{K}$ at liquid nitrogen temperatures. Lately, Gehring et al.²²¹ reported on the complete mapping of the thermoelectric properties of a single molecule in a device geometry that was optimized for cryogenic

operation, in combination with an AC measurement configuration. Our methodology for obtaining results on the GNR films is based on the work by Gehring et al.²²¹ as well as Linke et al.^{222,223} with the extension that we use graphene as contact electrodes. Finally, besides measuring the Seebeck effect, in recent works from the Reddy group, Peltier cooling and thermal transport in molecular junctions have also been reported.^{65,232}

From a theoretical point of view, GNRs are ideal candidates to enhance thermoelectric performance. The narrow widths open an electronic band gap and reduce the thermal conductivity, in particular for the ultra-narrow, bottom-up synthesized GNRs. Multiple theoretical studies have been published, reporting on Seebeck coefficients reaching several hundreds of $\mu\text{V}/\text{K}$ at room temperature, depending on the particular configuration, doping level, and contacting approach.^{233–240} On the experimental side, there are only very few confirmations of these predicted values. To the best of our knowledge, only one recent publication by Li et al.²⁴¹ on ≈ 40 nm wide, as-grown suspended graphene nanoribbons, reported a Seebeck coefficient of $\approx 125 \mu\text{V}/\text{K}$ at 200 K, being only slightly above the value for single-layer graphene. Clearly, further experimental work is needed to assess the potential of GNRs for thermoelectric effects.

In this chapter, we first familiarize ourselves with the experimental aspects of measuring the Seebeck coefficient of nanomaterials by determining the Seebeck coefficient of gold nanoparticles. This is done with relatively simple, planar devices in combination with a DC measurement scheme. Based on the limitations of this approach, we motivate why a more advanced geometry in combination with an AC measurement configuration is needed and validate the method by measuring thermovoltages of a graphene based device. Finally, we present the first measurements of the Seebeck coefficient of graphene nanoribbon-based devices.

8.2 Seebeck coefficient determined using DC-method: Au-nanoparticles

For our studies of the Seebeck coefficient, we selected the method of on-chip heaters, as this allows us to accurately generate small thermal gradients and it comes the closest to a possible application in a solid-state device. On-chip heaters usually consist of a metal wire in which Joule heating occurs by pushing a current through the system. The wire is either straight or in a meandered structure. The meandered structure has the benefit of having a higher resistance which allows for a more accurate determination of the resistance increase with increasing heater current. Furthermore, the meandered structure allows for the generation of more homogeneous and larger temperature gradients, at the cost of a larger spatial extension. On the contrary, linear heaters can be placed very close to the structure under test, thereby maximizing the thermal gradient. In the planar geometry, the heater can be placed at a few hundreds of nanometers away from the contact to the material, limited by the EBL and lift-off process. Another important advantage of the line heaters is that they do not heat up the substrate significantly, allowing the heater to be switched off efficiently. This property is of utmost importance for use in the AC method as discussed later in this chapter.

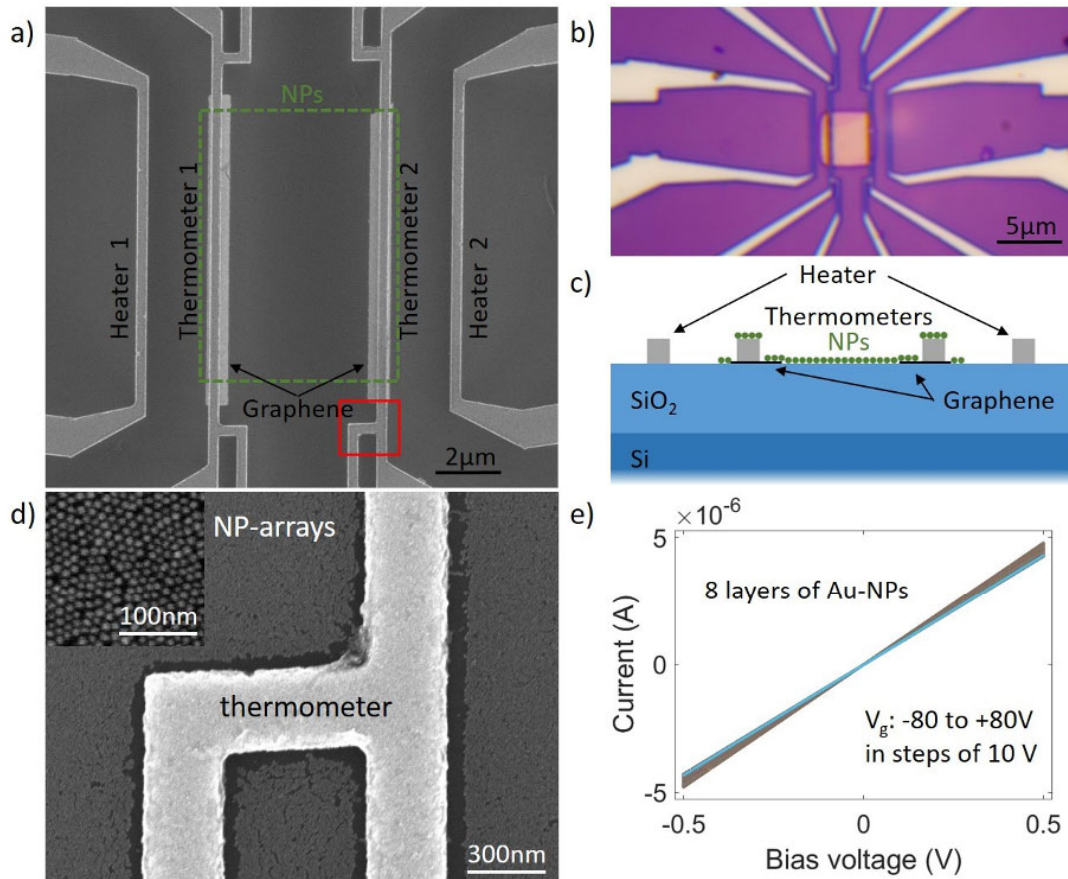


Figure 8.2 Electrical characterization of Au-nanoparticle devices. a) SEM micrograph of a substrate with graphene and metal electrodes before Au-nanoparticles stamping. b) Optical image of a device after stamping 8 layers of nanoparticles. c) Schematic crosssection through the device. d) SEM micrograph of monolayer NPs on a test structure. Inset shows zoom in on Au-NPs. e) Electrical characterization of 8 layer NPs-device at room temperature.

To explore thermoelectricity in nanoscale devices we start with a nanomaterial that is robust and well established, namely nanoparticles (NPs). Gold colloidal nanoparticles with a diameter of 10 nm can be synthesized using the method described by Slot and Geuze²⁴². A solution containing these octanethiol-capped gold nanoparticles is spread on a slightly convex water surface, leading to the self-assembly of 2D nanoparticle monolayers at the air/water interface.^{243–246} Using a stamp out of polydimethylsiloxane (PDMS), monolayers of Au-nanoparticles are picked up and the desired number of layers are simultaneously stamped at once on a substrate with predefined electrodes. This substrate consists of two thermometers, two heaters, and the silicon substrate serves as a global back gate. The alignment of the nanoparticles during the transfer of the films is challenging as the stamp is macroscopic while the electrodes are only a few hundreds of nanometers apart. Moreover, as the heaters and thermometers are all patterned in the same lithography step, the transferred (conducting) film of NPs may create an electrical short circuit between the heater and the thermometer. We solve this issue by using

graphene strips to contact the NPs, that are in turn contacted by metal electrodes, see Figure 8.2a). The metal electrodes are very thick (≈ 100 nm) leading to an interruption of the stamped NP-film close to the metal electrodes, see Figure 8.2c) and d), resulting in the graphene contacting the film of NPs.

The successful contacting was tested with electrical measurements. By recording the I-V curves between the two thermometers and between the thermometer and the corresponding heater next to it, we confirmed that they were not shorted. Figure 8.2e) shows the electrical characterization of a device at room temperature containing 8 layers of Au-NPs. The number of layers was chosen such that the film is robust and the resistance does not change further with increasing layer numbers.²⁴⁶ The I-V characteristics show linear behavior with minimal dependence on the applied gate voltage. The resistance of the shown device is ≈ 100 k Ω .

We also measured the Seebeck coefficient $S = -\Delta V/\Delta T$, requiring accurate measurement of the thermovoltage ΔV and temperature gradient ΔT . Here, the temperature gradient is generated by sourcing a DC current through the heater. To determine the temperature gradient, two separate measurements were performed. First, a 4-terminal DC measurement of the resistance of the thermometers is performed while changing the temperature of the cryostat. Figure 8.3a) shows the resistance of the thermometers R_{Thermo} as a function of cryostat temperature T_{Bath} .

The second measurement monitors the thermometer resistance while the current through the nearby heater is varied. This measurement is shown in Figure 8.3b). By combining these two, one calculates the temperature of each thermometer as a function of heater current and extracts the temperature difference, shown with the green curve in Figure 8.3b). The quadratic behavior indicates Joule heating, scaling according to $P = RI^2$. The plot shows that to obtain a temperature gradient of ≈ 1 K, approximately 4 mA of current is needed. At this current, thermometer 1 heats up by 5.5 K, while thermometer 2 heats up by 4.5 K.

Now that we have calibrated the temperature gradient, we proceed to measure the thermovoltage build-up over the NP-film using a nanovoltmeter (2182A/E - Nanovoltmeter, Keithley) as a function of heater current, shown in Figure 8.3c). Also here, a quadratic behavior is observed, indicating that the thermovoltage scales with the temperature gradient. By building the ratio between the measured thermovoltage and its corresponding temperature gradient, the Seebeck coefficient is calculated, as shown in Figure 8.3d). The plot shows that the values below a heater current of ~ 1 mA (highlighted in red) show quite some variation. This large spread is attributed to the low accuracy of the extracted (small) temperature gradient, resulting in the division through a small number when calculating the Seebeck coefficient. Hence it would be favorable to have higher temperature gradients for a more robust determination of the Seebeck coefficient.

Overall, we were able to determine the Seebeck coefficient of 8 layers of Au-nanoparticles arrays and found $S \approx 15$ $\mu\text{V}/\text{K}$ at room temperature. We have seen that the positioning of the films on top of predefined electrodes is challenging. Further, the stamping method of the films constrains the flexibility of the electrode design since they have to be thick enough to interrupt the film in order to avoid shorts. The planar geometry results in moderate temperature gradients of up to ≈ 1 K, resulting in large measurement inaccuracies at low thermal bias. The DC measurement approach was another limiting

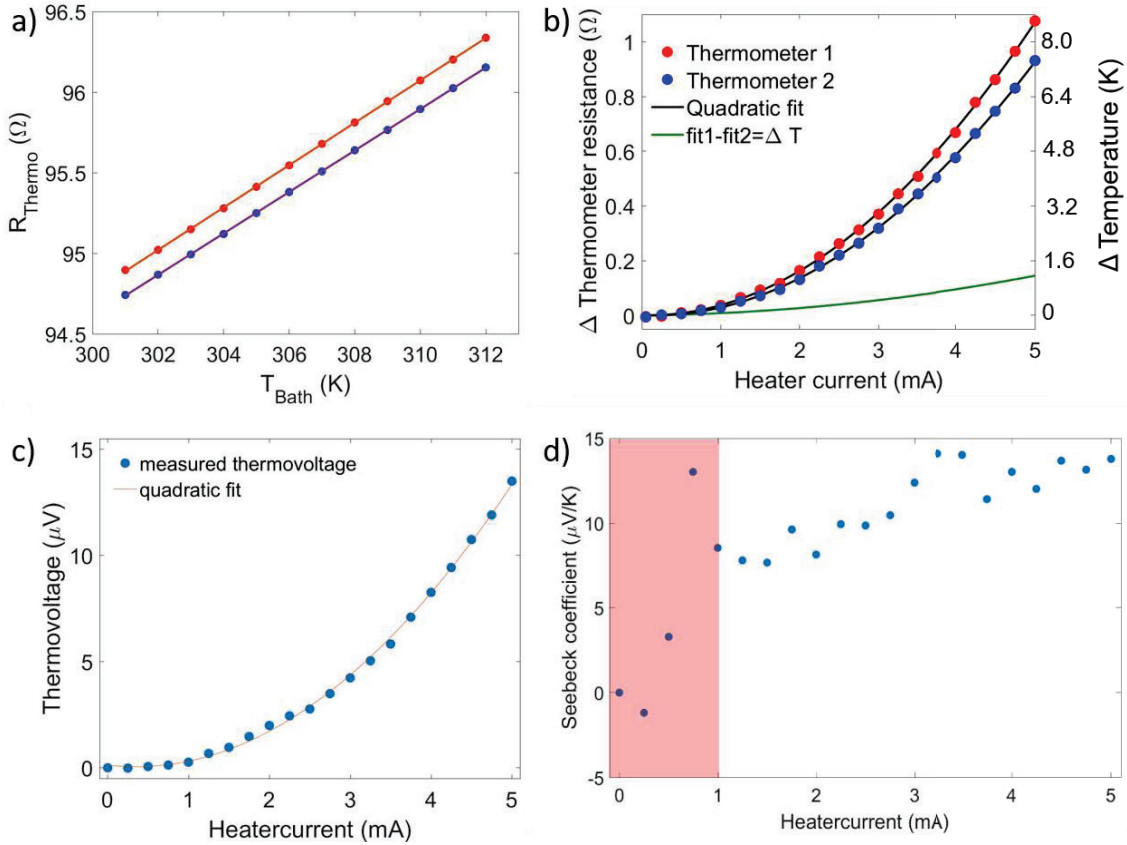


Figure 8.3 Thermoelectric characterization of 8 layer Au-NP device. **a)** Thermometer calibration. **b)** Calibration of the temperature gradient ΔT at various applied heater currents. **c)** Thermovoltage as a function of heater current. **d)** Seebeck coefficient at various applied heater currents at room temperature. The region where the value of the Seebeck coefficient is attached with large errors is highlighted in red.

factor, as with the instrumentation used it only works for devices in the mega to gigaohm regime. In the following we therefore motivate how to overcome these limitations with an improved device layout and measurement approach.

8.3 Motivation for vertical thermometer/heater structures

As we have seen in Section 8.2, four limitations of the experimental method were identified. Two are geometrical and two are about the measurement scheme:

First, as the films of nanomaterials are transferred onto predefined electrodes, one needs to make sure no electrical short exists between the thermometer and the heater.

Second, since the heater is placed rather far away from the thermometer the temperature gradient only reaches a few Kelvin at best due to the substrate acting as a heat sink. Moreover, the device itself heats up significantly, much more than the applied temperature gradient.

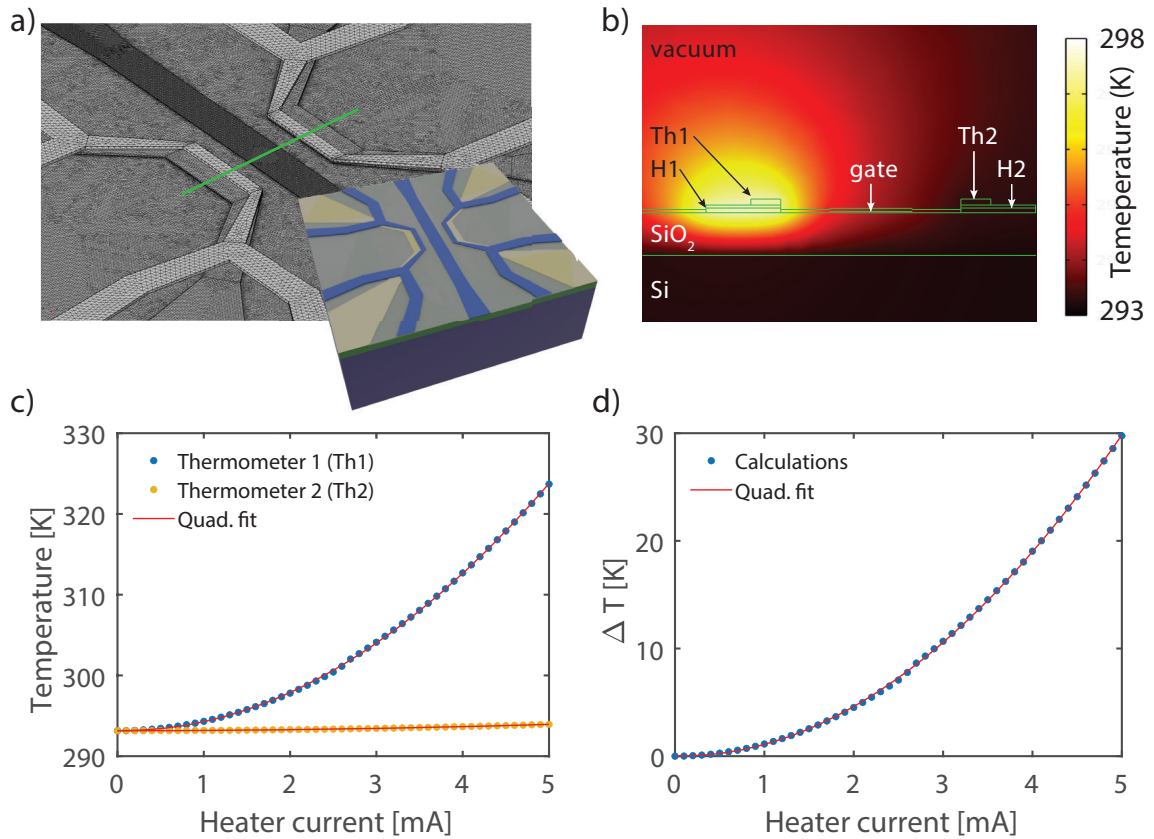


Figure 8.4 Finite element modeling of temperature profile for vertical structure. **a)** Mesh used for the FEM calculations. The inset illustrates the heaters (olive), thermometer and gate (blue) and the Si/SiO₂-substrate (blue/green). **b)** Temperature profile along the green line cut in a). A current of 2 mA is passed through Heater 1 (H1). **c)** Temperature increase at thermometer 1 and 2, respectively, for various applied heater currents to heater 1. **d)** Resulting temperature difference ΔT between thermometer 1 and 2 for various applied heater currents.

Third, a direct thermovoltage measurement was performed on rather conductive devices with 8 layers of NPs. When scaling down to 1 NP layer, the impedance of the film is equal to or even exceeds the input impedance Z_{in} of the voltage measurement instrument.

Fourth, the measured voltages have a low signal-to-noise ratio.

These limitations can be overcome by adapting the sample geometry and measurement scheme. The device is adjusted similarly to the devices proposed by the Linke group^{222,223} and also used by Gehring et al.^{221,247}

In this advanced (stacked) geometry, the heaters are placed below (or on top of) the thermometers, resulting in a much more localized heating profile. This enables larger temperature gradients across the material of interest with very limited heating of the entire sample. Furthermore, as the heaters and thermometers are separated by an oxide and electrically separated from each other, transferring a conducting film on top would not create a short circuit. In terms of measurement schemes, a

thermocurrent will be measured rather than a thermovoltage. Due to the different operating processes of a current measurement unit and a voltage measurement unit, also very small thermocurrents of highly resistive devices can be measured accurately. Moreover, an AC-modulated lock-in technique will be employed to improve the signal-to-noise ratio.

The proposed device improvements come at the cost of a more extensive device fabrication process. We didn't shy away from the fabrication effort, but to get beforehand a feeling of the temperature gradients to be expected in such the system, we used finite-element method calculations (Comsol 5.6) to model the temperature distribution and profile. This is illustrated in Figure 8.4a) showing the device schematics as well as the used mesh. A cross-section of the temperature distribution for an AC heater current of 2 mA is depicted in Figure 8.4b). The resulting temperature increase on the thermometer is shown in Figure 8.4c), with d) showing the resulting temperature difference ΔT . The plot shows that the thermometer on top of the heater heats up quite drastically, while the thermometer far away from the heater remains almost unaffected. This means the temperature gradient is strongly localized between the two thermometers, where the nanojunction is. With this modeled verification of the improved temperature gradient at a lower device heating, we fabricated the devices.

In the analysis of the measurements, we will use the resistance of the thermometers to determine the temperature gradient. We note that the extracted value for the ΔT serves as an upper limit. This results in the most conservative estimate for the Seebeck coefficient. In Gehring et al.²⁴⁷ the resulting temperature distribution is discussed extensively and also further assessed experimentally by using SThM. The resulting measurements and conclusions are presented in the following sections.

8.4 Seebeck coefficient determined using an AC-method

The core of the experimental set-up for thermoelectric characterization of nanostructures is the on-chip heaters that allow for applying a temperature gradient across the material of interest. In the present case, we study the thermoelectric performance of GNR films contacted using graphene electrodes. The device layout has been adapted from previous works with the extension of using graphene as electrode material to the film of GNRs.^{221–223,247} The resulting device is depicted in Figure 8.1, before GNR transfer. Figure 8.5a) presents the workflow of the thermoelectrical characterization experiment. The experiment is split into two separate parts. The first part determines the thermovoltage by measuring the induced thermocurrent and sample resistance, while the second part calibrates the corresponding temperature gradient.

For the first part of the experiment, a temperature gradient is established by passing an AC current \tilde{I}_h through an on-chip heater at frequency ω_1 (see Figures 8.5b) and c) for device layout). We used a voltage-controlled current source to keep the current fixed, as the heater resistance might change during the experiment. To generate a complete map of the Seebeck coefficient as a function of bias and gate voltage we applied the following voltages: One thermometer is used to apply a DC bias voltage V_{sd} and an AC bias voltage \tilde{V}_{sd} at frequency ω_2 across the GNR film. The other contact is then used to measure the DC current I_{sd} , the AC current \tilde{I}_{sd} at frequency ω_2 and the AC

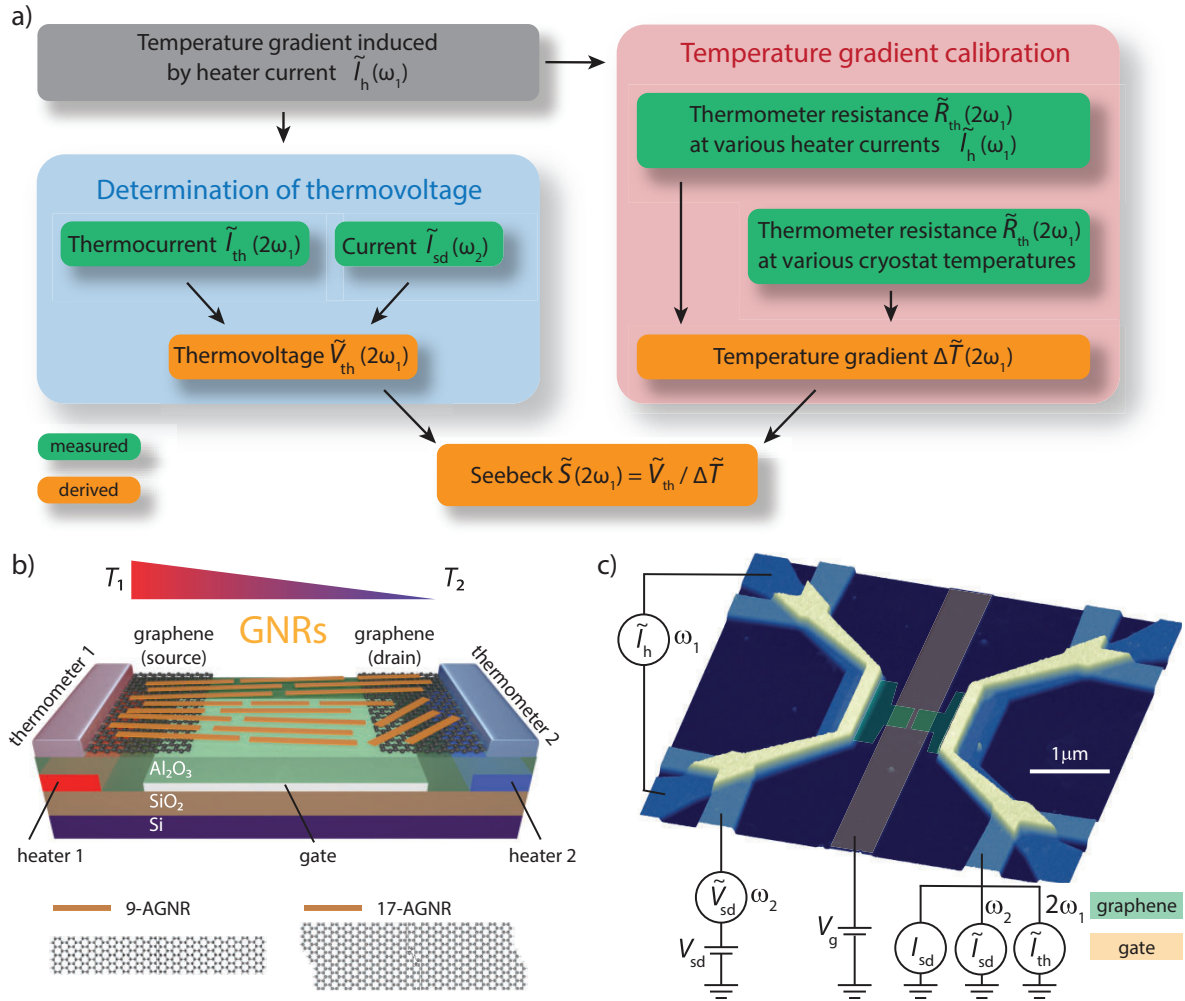


Figure 8.5 Concept of the thermoelectric characterization experiment using an AC method. **a)** Schematic process flow of the experiment. **b)** Artistic illustration of the experimental setup indicating the direction of the applied thermal gradient over graphene nanoribbons (GNRs) films. Two devices, one consisting of 9-AGNRs and one consisting of 17-AGNRs, are investigated separately and depicted as orange strips. **b)** Atomic force microscope height profile of a typical experimental device before transfer of GNRs. The graphene electrodes and the gate are highlighted in green and orange respectively. The schematic circuit diagram indicates which terminals are used to apply an AC heater current \tilde{I}_h , a DC bias voltage V_{sd} , an AC bias voltage \tilde{V}_{sd} and a gate voltage V_g , and which terminals are used to measure a DC current I_{sd} , AC current \tilde{I}_{sd} and an AC thermocurrent \tilde{I}_{th} .

thermocurrent \tilde{I}_{th} at frequency $2\omega_1$. A fixed gate voltage V_g is applied to the gate electrode to tune the electrostatic potential of the GNR film. We note that reversing the temperature gradient results in a sign-change in the thermocurrent but not in the conductance measurement. The obtained results are shown in Section 8.6.

For the second part of the experiment, the electrical wiring and connecting of the instruments to the thermometers are changed. A 4-terminal resistance measurement

configuration to each of the two thermometers is set up. Then, a constant DC bias current is pushed through each of the thermometers while the voltage drop along the central part of the thermometer is measured at frequency $2\omega_1$. The thermometer resistance \tilde{R}_{th} is then measured for various heater currents \tilde{I}_h and cryostat temperatures. Details to this part of the experiment are laid out in Subsections 8.4.1, 8.4.2 and 8.4.3.

Finally, films of GNRs (9-AGNRs or 17-AGNRs) are contacted using the graphene electrodes. The fabrication procedure and motivation for using graphene electrodes have been discussed extensively in Chapter 4 and 5. As we have pointed out in Chapter 5, the film of GNRs is conductive over length scales larger than the individual GNR length. We, therefore, separated the graphene electrodes by ≈ 100 nm. The graphene electrodes are contacted using metal wires (Ti/Pt, 5/35 nm) in a 4-terminal configuration which allows them to be used as resistance thermometers. Choosing platinum as a material for the thermometers has some advantages over other materials. First, platinum resistance temperature detectors are known for the reliability of their calibration over wide temperature ranges.²⁴⁸ Additionally, the higher resistivity of the platinum, over for example gold, results in a higher thermometer resistance leading to an improved measurement accuracy of the temperature gradient. Furthermore, it allows the transfer of transferring GNRs grown on Au(111)/mica substrates, where the transfer process involves a gold etching step that does not attack platinum. Metal heaters (Ti/Pd, 3/27 nm) are buried below the thermometers, separated by a 20 nm ALD-grown aluminum-oxide layer. Additionally, a thin gate electrode (Ti/Pd, 1/6 nm) is placed in the central region of the device. This allows for electrostatic gating of the GNRs and reduces the thermal transport between the source and drain lead. Palladium is chosen for the gate and heaters since it forms uniform thin layers with a low surface roughness.²⁴⁹ Figure 8.5c) shows the height profile of the device with the graphene electrodes and the gate highlighted using colors for better visibility, alongside a circuit diagram illustrating the use of each electrode.

8.4.1 Theoretical and experimental considerations

Theoretical considerations to the temperature distribution

This section briefly outlines the theoretical considerations for the temperature gradient generated by an alternating heater current at frequency ω . The outline follows the notation as introduced in the 1950's by Domenicali²⁵⁰ and Carslaw and Jaeger²⁵¹.

To generate a temperature gradient across the material under test, a current $I = I_0 \sin(\omega t)$ is applied to a heater that can be treated as a linear conductor with constant resistance R . The dissipated power $P(t)$ can be written as:

$$P(t) = RI^2(t) = \frac{1}{2}RI_0^2(1 - \cos(2\omega t)) \quad (8.2)$$

In the following it is assumed that the heater can be modeled as an infinitely long wire, surrounded by an electrically insulating medium. The released heat diffuses in the surrounding medium, hence inducing a space- and time-dependent variation of its temperature $T(\mathbf{r}, t)$. Starting from the three dimensional heat equation as derived by Fourier⁵⁶ with a heater $f(\mathbf{r}, t)$.

$$\frac{\partial T(\mathbf{r}, t)}{\partial t} - \alpha \nabla^2 T(\mathbf{r}, t) = \frac{f(\mathbf{r}, t)}{mc_v} \quad (8.3)$$

where $\alpha = \frac{\kappa}{c_v \rho}$, is the thermal diffusivity, depending on the thermal conductivity κ , the specific heat c_v and the mass density ρ . The fundamental solution $G(\mathbf{r}, t)$ of the three dimensional heat equation is:

$$G(\mathbf{r}, t) = \left(\frac{1}{4\pi\alpha t} \right)^{\frac{2}{3}} e^{-\frac{x^2+y^2+z^2}{4\alpha t}} \quad (8.4)$$

Therefore we can write:²⁵¹

$$T(\mathbf{r}, t) = \int \frac{f(\mathbf{r}', t')}{mc_v} G(\mathbf{r} - \mathbf{r}', t - t') dV' dt' \quad (8.5)$$

If we further assume that the infinitely long heater is lying on the z -axis we can write $f(\mathbf{r}, t) = f(r, t)\delta(x)\delta(y)$ with the Dirac delta function δ . This leads to:

$$T(\mathbf{r}, t) = \int \frac{f(z', t')}{mc_v} \left(\frac{1}{4\pi\alpha(t-t')} \right)^{\frac{2}{3}} e^{-\frac{x^2+y^2+(z-z')^2}{4\alpha(t-t')}} dz' dt' \quad (8.6)$$

by integrating over dz' from $-\infty$ to ∞ , we can write:

$$T(r, t) = \int \frac{f(t')}{mc_v} \left(\frac{1}{4\pi\kappa(t-t')} \right) e^{-\frac{r^2}{4\alpha(t-t')}} dt' \quad (8.7)$$

where $r^2 = x^2 + y^2$. By inserting the heat source term, this integral can be separated in two parts; $T = T' + T''$, with its solutions:²⁵⁰

$$T'(r, t) = -\frac{f_0}{4\pi\kappa} \text{Ei}(-\eta) \quad (8.8)$$

$$T''(r, t) = -\frac{f_0}{2\pi\kappa} \text{Re}\{e^{i2\omega t} \mathcal{K}_0(qr)\} \quad (8.9)$$

with $\eta = \frac{r^2}{4\alpha t}$, $q = \sqrt{\frac{i2\omega}{\alpha}}$, $\text{Ei}(\eta) = -\int_{-\eta}^{\infty} \frac{e^{-u}}{u} du$ and $\mathcal{K}_0(qr)$ is the Bessel functions of the second kind (0th-order).

For $\eta < 1$ one can use the approximation $\text{Ei}(-\eta) \approx \gamma + \ln(\eta) + \eta + \mathcal{O}(\eta^2)$, where γ is the Euler–Mascheroni constant. Hence, T' can be approximated as:

$$T'(r, t) \approx \frac{f_0}{4\pi\kappa} \left[\ln\left(\frac{4\alpha t}{r^2}\right) - \gamma + \frac{r^2}{4\alpha t} \right] \quad (8.10)$$

By using the Bessel-functions to evaluate T'' , one can write:

$$\text{Re}\{e^{i2\omega t} \mathcal{K}_0(qr)\} = -\sin(2\omega t) \text{Im}\{\mathcal{K}_0(qr)\} + \cos(2\omega t) \text{Re}\{\mathcal{K}_0(qr)\} \quad (8.11)$$

Hence, T'' has an in-phase and out-of-phase component, with respect to the heater current. The imaginary part of $\mathcal{K}_0(qr)$ saturates for small qr , while the real part increases. All together, and with the cryostat temperature T_{cryo} , the temperature at a distance r away from the heater at time t can be written as:

$$T(r, t) = T_{\text{cryo}} + \frac{f_0}{4\pi\kappa} \left[\ln\left(\frac{4\alpha t}{r^2}\right) - \gamma + \frac{r^2}{4\alpha t} + 2\sin(2\omega t)\text{Im}\{\mathcal{K}_0(qr)\} - 2\cos(2\omega t)\text{Re}\{\mathcal{K}_0(qr)\} \right] \quad (8.12)$$

Equation 8.12 shows that the temperature is a superposition of a temperature drift with the in-phase and out-of-phase oscillations at frequency 2ω . After a certain thermalization time, this temperature drift can be considered constant over the measurement time and hence be neglected. In this special case one can write the temperature in a very simplified form:

$$T(r, t) \approx T_{\text{cryo}} + T_{2\omega, \text{in}}(\sin(2\omega t)) + T_{2\omega, \text{out}}(\cos(2\omega t)) \quad (8.13)$$

This result means that a phase shift of $\pi/2$ between the modulation current and the temperature gradient is induced. This further implies that, if the system is driven at a too high frequency the in-phase component starts to get larger, which should be avoided. Hence, only low-frequency measurements are desirable.

We here follow also the interpretation by Gehring et al.²²¹. The measured signal of the thermocurrent has its physical signal in the out-of-phase component (Y-component) while the in-phase component (X-component) is the dephased signal due to too high measurement frequencies. In an ideal system, this component would not be present. In the next subsection, this discussion is continued but from an experimental point of view. For the calculations of the thermovoltage only the Y-component of the thermocurrent signal is considered.

The conductance measurements are carried out at the same time but at a different frequency. There the physical signal of the conductance is in the in-phase component (X-component), while on the out-of-phase component (Y-component) the capacitive contributions are reflected. For the calculations of the thermovoltage only the X-component of the conductance signal is considered.

Frequency dependence

Since an AC measurement configuration is used, we emphasize and motivate the selected parameters. The detection bandwidth of a lock-in is set by the low pass filter time constant τ and the roll-off. If not stated otherwise, we used a time constant of 3 s with 24 dB/oct roll-off. The filter output settles at the new value after a certain time has passed, called the settling time. Depending on the experimentalists' accuracy needs, this time varies and can be looked up in any lock-in instrument manual.²⁵² With our settings, a settling time of $\approx 10 \times \tau$ is needed to reach 99% of the final value. In Appendix 8.A., the frequency dependence of a film of GNRs under test is shown and discussed. Based on this measurement, we selected the heater frequency to be 3.123 Hz since it is a compromise between measurement speed and dephasing.

Probe current for resistance thermometers

To measure the resistance of the on-chip thermometers one has to find the optimum between measurement accuracy and measurement errors introduced by self-heating. In

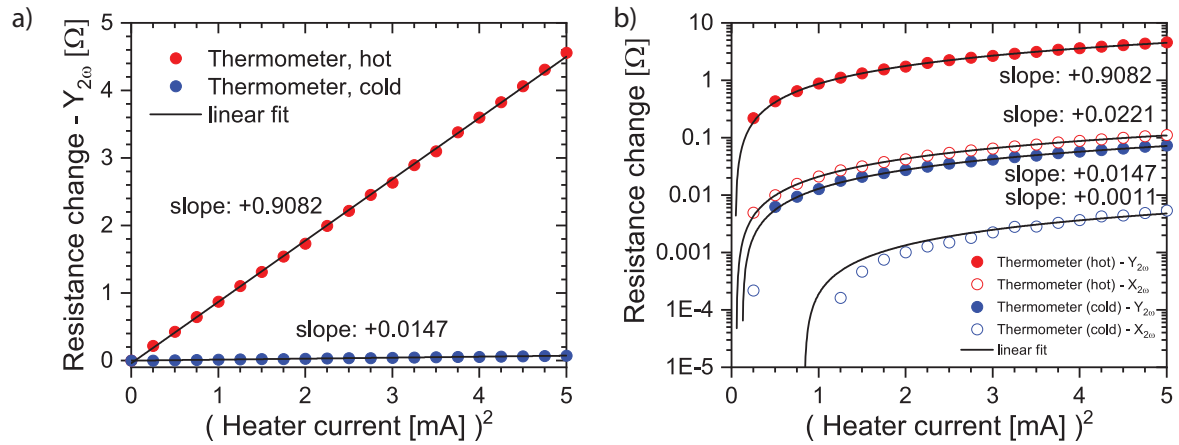


Figure 8.6 Response of the thermometer resistance to applied heater currents. The resistance of the thermometers close to the heater (hot) and away from the heater (cold) is measured at $2\omega_1$ while the heater current is driven at ω_1 . **a)** Y-component of the resistance change for various heater currents. **b)** X- and Y-component of the thermometer resistance for the for various heater currents.

Appendix 8.B., measurements for determining the ideal probe current are shown and discussed. We chose a probe current of $100 \mu\text{A}$ for all further measurements of this type.

8.4.2 Calibration: thermometer vs. heater current

To establish a thermal gradient across the material/device of interest a current is pushed through the on-chip heater. This current is applied at a frequency ω_1 and selected as described in subsection 8.4.1. The resistance of the thermometers close to the heater (hot) and away from the heater (cold) is measured at $2\omega_1$. Since the resistance measurement involves a lock-in detection, the voltage signal has an X- and Y-component (X: in-phase, Y: out-of-phase). As shown in Figure 8.6 a) the signal scales quadratically with increasing heater currents. The quadratic increase in thermometer resistance indicates Joule heating according to $P = RI^2$ where P is the power, R is the resistance of the heater and I is the heater current. The data can further be interpreted that the device is operated in the linear regime where the applied effects are reversible. As illustrated in Figure 8.6 b), the Y-component is dominating, indicating an operation in a regime where the system can follow the thermal modulation using the heater current. The data points shown in Figure 8.6 a) and b) are the averages over the last 40 s of a 120 s measurement series, as shown in Appendix 8.C. After ≈ 30 s, the system has reached a steady-state, as expected for the used lock-in settings, as discussed before in Subsection 8.4.1. The Y-component of the signal on the cold thermometer is 1.6 % of the signal on the hot thermometer. This is in contrast to the X-component, where on the cold side 5 % of the signal on the hot side is detected. This increase in difference can be explained by a much larger measurement uncertainty due to the low signal on the cold side. Overall, the very low signal on the thermometer away from the heater indicates that it does not heat up or that the heating up can be neglected in this case. This is in

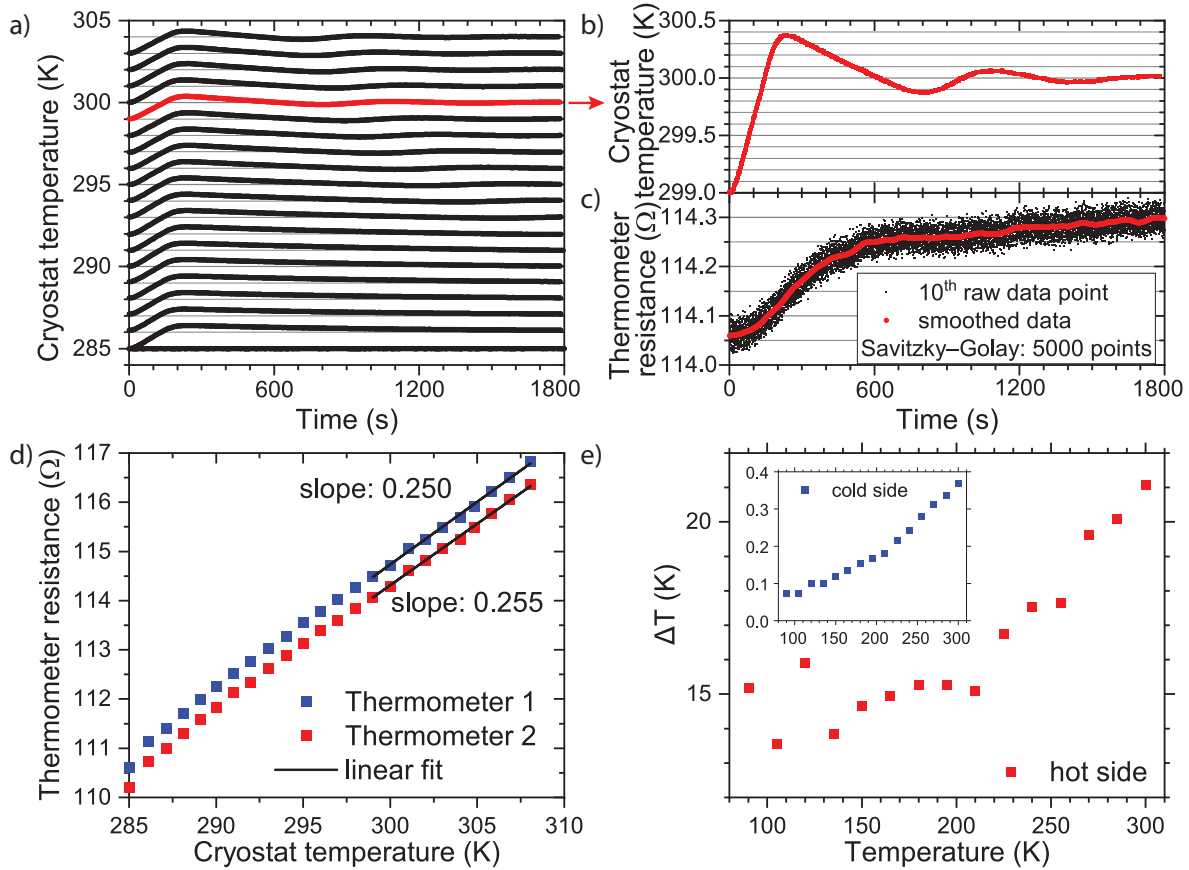


Figure 8.7 Thermalization times within the cryostat and extraction of temperature gradients. **a)** Cryostat temperature as a function of time, starting from when the set cryostat temperature is increased by 1 K. The series goes from 285 K to 304 K. **b)** Cryostat temperature as a function of time, after changing the cryostat temperature from 299 K to 300 K. The same curve is highlighted in a) in red. **c)** On-chip thermometer resistance as a function of time, after changing the cryostat temperature from 299 K to 300 K. **d)** On-chip thermometer resistance as a function of cryostat temperature. A linear fit to the data in the region 299 K to 308 K. **e)** Temperature gradient ΔT as a function of cryostat temperature for fixed applied heater current.

agreement with our finite-element methods calculations as shown in Section 8.3.

8.4.3 Calibration: thermometer vs. cryostat temperature

Besides knowledge about the timescales for the signal to stabilize on-chip, it is important for the temperature calibration to monitor the on-chip response to a change of the cryostat temperature. In Figure 8.7a), the measured cryostat temperature is shown for 30 min after a change in the set cryostat temperature by +1 K. The temperature is read out and set by a temperature controller (MercuryITC, Oxford Instruments). The response of the on-chip thermometer's resistance and the measured cryostat temperature are shown in Figure 8.7c) and b), respectively. The spread in the raw data of the on-chip thermometer is attributed to the low probe current as explained in Subsection 8.4.1 By

averaging over 5000 points an accuracy of below 0.1 % is achieved.

To extract the temperature gradient ΔT the thermometer resistance versus bath temperature curve, shown in Figure 8.7d), is combined with the thermometer resistance versus heater current curves, shown in Figure 8.6. Since the thermometers and heaters do show some temperature dependence of their resistance, the resulting temperature gradient needs to be calibrated also as a function of cryostat temperature. Figure 8.7e) depicts this temperature dependence. Since we use a voltage-controlled current source, the current is fixed, while the heater resistance decreases with decreasing temperature. This leads to an overall decrease in heater power. Additionally, there are multiple competing factors at play for thermalization. The thermal conductivity of the metal leads decreases with decreasing temperature according to the Wiedemann-Franz law⁷⁹, while the thermal conductivity of the underlying substrate increases with decreasing temperature, leading to a faster thermalization with the substrate.²⁵³⁻²⁵⁵ The extracted temperature gradients are used in the calculation of the Seebeck coefficients.

8.5 Thermoelectrical characterization of graphene films

Before applying the AC method to graphene nanoribbons, we verify the working principle on graphene. Graphene is a well-known and characterized material system with a peak Seebeck value of $\approx 100 \mu\text{V}/\text{K}$.^{224,225} Due to its unique bandstructure it is possible to tune the charge carrier majority from holes to electrons by applying an electrostatic field. This manifests by a sign change of the thermovoltage, and hence the Seebeck coefficient at the charge neutrality point (CNP). The Thermovoltage is the highest close to the CNP where the change in charge carrier density per energy change is the highest (this corresponds to where the derivative of the conductance is highest). From the sign of the thermovoltage one can deduce the type of the charge carrier majority. A negative sign corresponds to holes while a positive sign corresponds to electrons. In Figure 8.8a) a SEM image of a graphene device is shown. The graphene can be separated into three regions (labeled 1,2 and 3). In region 2, the charge carrier density in the graphene can be tuned by applying a voltage to the gate electrodes, while in regions 1 and 3 this would only be possible by applying a voltage to the silicon substrate (global gate). We probe the transport properties of the graphene by measuring the conductance as a function of gate voltage. In Figure 8.8b) this recorded curve is shown. The behavior follows the expected trend for graphene, with the CNP at $\approx -0.3 \text{ V}$. Interestingly, the conductance can be tuned only by a factor of 2. This can be understood geometrically. In regions 1 and 3, the gate voltage has little to no effect on the charge carrier density, hence only in less than half of the graphene channel, region 2, the conductance can be modulated, which is reflected in the overall device conductance modulation. Further, since CVD-graphene is usually slightly *p*-doped after the transfer, in combination with the *p*-doping of the graphene in the vicinity of the metal contacts, region 1 and 3 can be seen as slightly *p*-doped.^{256,257} This results in a doping constellation for the different graphene regions 1-2-3 of *p* – *p* – *p* in the case of a negative applied gate voltage, while in the case of a positive applied gate voltage a doping constellation of *p* – *n* – *p* arises. These two situations are illustrated in the insets of Figure 8.8c) where the solid blue line indicates the Fermi energy E_F and the energy dispersions in the

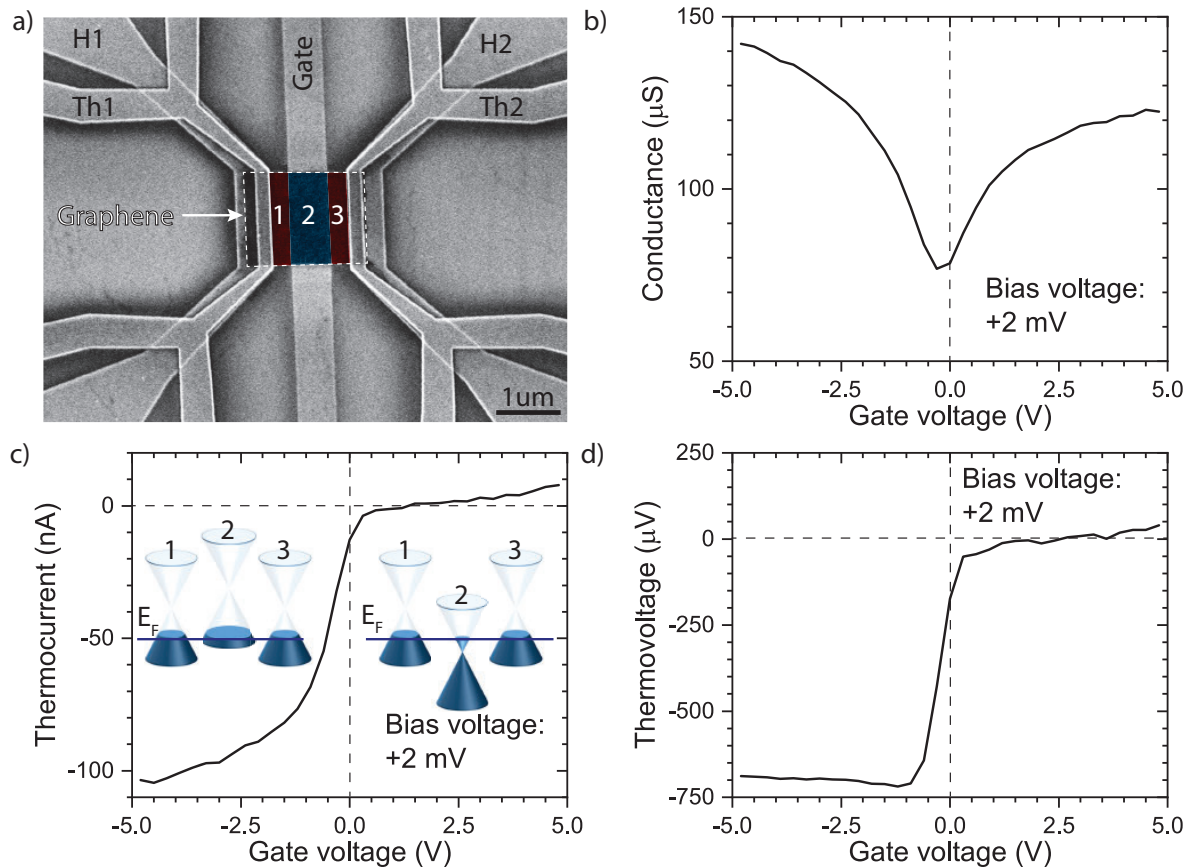


Figure 8.8 Electronic and thermoelectric characterization of graphene in vertical heater geometry at room temperature. During all measurements an AC temperature gradient of 3.8 K is applied. **a)** SEM image of a graphene device. The graphene (white dashed line) is separated into three regions (labeled 1,2 and 3). **b)** AC conductance as a function of gate voltage, measured while a DC voltage of +2 mV was applied. **c)** AC thermocurrent as a function of gate voltage, measured while a DC voltage of +2 mV was applied. Insets show the energy dispersions in the three different graphene regions for positive and negative gate voltages. **d)** Thermovoltage as a function of gate voltage, derived from the conduction and thermocurrent. (see main text for details.)

three graphene regions are depicted. The measurement of the induced thermocurrent is shown in Figure 8.8c). It is observed that the thermocurrent is negative for negative gate voltages and turns slightly positive for positive gate voltages. We interpret this observation by the $p-n-p$ junction that is formed for positive gate voltages, leading to a canceling-out of the different thermocurrents due to the change in charge carrier majorities in the different regions. From the conductance G and the thermocurrent I_{thermo} we calculate the thermovoltage V_{thermo} using $V_{\text{thermo}} = 1/G * I_{\text{thermo}}$. The resulting curve is plotted in Figure 8.8d). We see the maximum of the thermovoltage peaking at ≈ -1 V in gate voltage, as expected and reasoned above. We did not further calculate a Seebeck coefficient from this data since we think that the local temperature gradient in

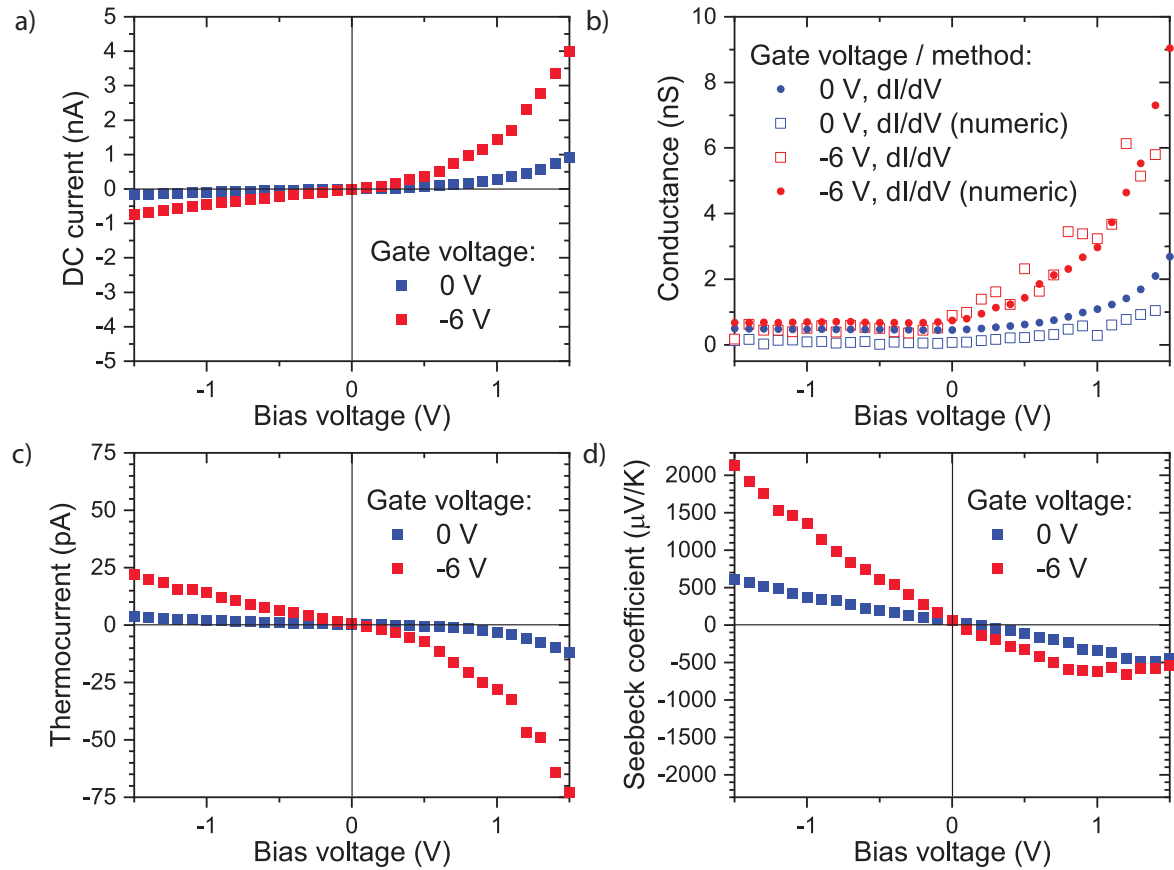


Figure 8.9 Electronic and thermoelectric characterization of 9-AGNR films at room temperature. During all measurements an AC temperature gradient of 15.2 K is applied. **a)** Current as a function of DC bias voltage characterization. **b)** Differential conductance determined with a direct measurement using a lock-in and numerically from the data shown in a). **c)** AC thermocurrent as a function of DC bias voltage. **d)** Seebeck coefficient as a function of DC bias voltage.

the three different regions would need to be taken into account instead of the overall thermal gradient. However, these measurements confirmed the correctness and working principle of the AC method and therefore have been sufficiently analyzed to proceed with the measurements on graphene nanoribbon-based devices as discussed in the next section.

8.6 Thermoelectrical characterization of GNR films

8.6.1 Conductance and thermocurrent measurements

Now we turn towards the second part of the experiment. For the first time films of GNRs are characterized thermoelectrically.

As a reminder, the graphene electrodes are separated by ≈ 100 nm. This is larger than the average GNR length of 40 to 45 nm in the case of 9-AGNRs and < 20 nm in the

case of 17-AGNRs.

The thermoelectric characterization of GNR films is performed as outlined in Section 8.4. A temperature gradient is applied by passing an AC current at frequency ω_1 through an on-chip heater. The resulting thermocurrent, the device conductance, and the DC current are measured simultaneously. The frequencies are $2\omega_1$ and ω_2 for the thermocurrent and the conductance, respectively. In Figure 8.9a) the current-voltage characteristics of a high-density 9-AGNRs films at room temperature are shown. The I-Vs are highly nonlinear and have a slightly asymmetric behavior. Qualitatively, they agree with the results on graphene electrodes separated by <15 nm, as discussed in Chapter 4.

Since we measure both the differential conductance as well as the DC current, we can cross-check their agreement. Figure 8.9b) shows a comparison between the measured dI/dV and the numerically derived dI/dV from the I-V characteristics. The numerical dI/dV has a much larger spread but is still in good agreement with the lock-in measurement. This numerical differential conductance serves therefore as a reference and is not used further on.

The thermocurrent is measured at various applied DC biases and gate voltages. For two selected gate voltages, this is depicted in Figure 8.9c). Using Ohm's law the corresponding thermovoltage is calculated from the conductance and the thermocurrent. Together with the ΔT calibration, as done in Subsection 8.4.3, the Seebeck coefficient can be derived. Figure 8.9d) shows the Seebeck coefficient at various bias voltages for two selected gate voltages. We see that the Seebeck coefficient scales with increasing bias voltage. We further see that the ranges with lower conductance exhibit higher Seebeck coefficient values, this behavior will be discussed later on. However, in order to gain a better overview of the measured device characteristics, we show in Figure 8.10 the simultaneously measured quantities of the films of GNRs, namely the DC source-drain current (I_{sd}), the AC conductance (G_{sd}) and the AC thermocurrent (\tilde{I}_{sd}), as a function of applied DC bias and gate voltage, (V_{sd} and V_g), respectively.

The temperature gradient ΔT for this particular data set is 15.2 K. The top row depicts the results on films of 9-AGNRs, while in the bottom row the results on 17-AGNRs are shown. Note the slightly different bias and gate voltage ranges.

In the case of the 9-AGNRs, a strong gate and bias voltage dependence of the source-drain current is observed, in accordance with results presented earlier in this thesis.

At $V_g = -6$ V, the conductance as well as the thermocurrent show the highest values, reaching 8 nS and -60 pA at $V_{sd} = +1.5$ V, respectively. The sign of the thermocurrent depends on the type of the majority charge carrier as well as the direction of the temperature gradient. In the presented case the heater below the drain contact was heated, leading to a negative sign at positive bias voltages. In the case of the 17-AGNRs, depicted in the bottom row of Figure 8.10, the gate voltage dependence is less pronounced, in accordance with the results described in Chapter 5. The overall higher conductance correlates with the slightly lower values in thermocurrent.

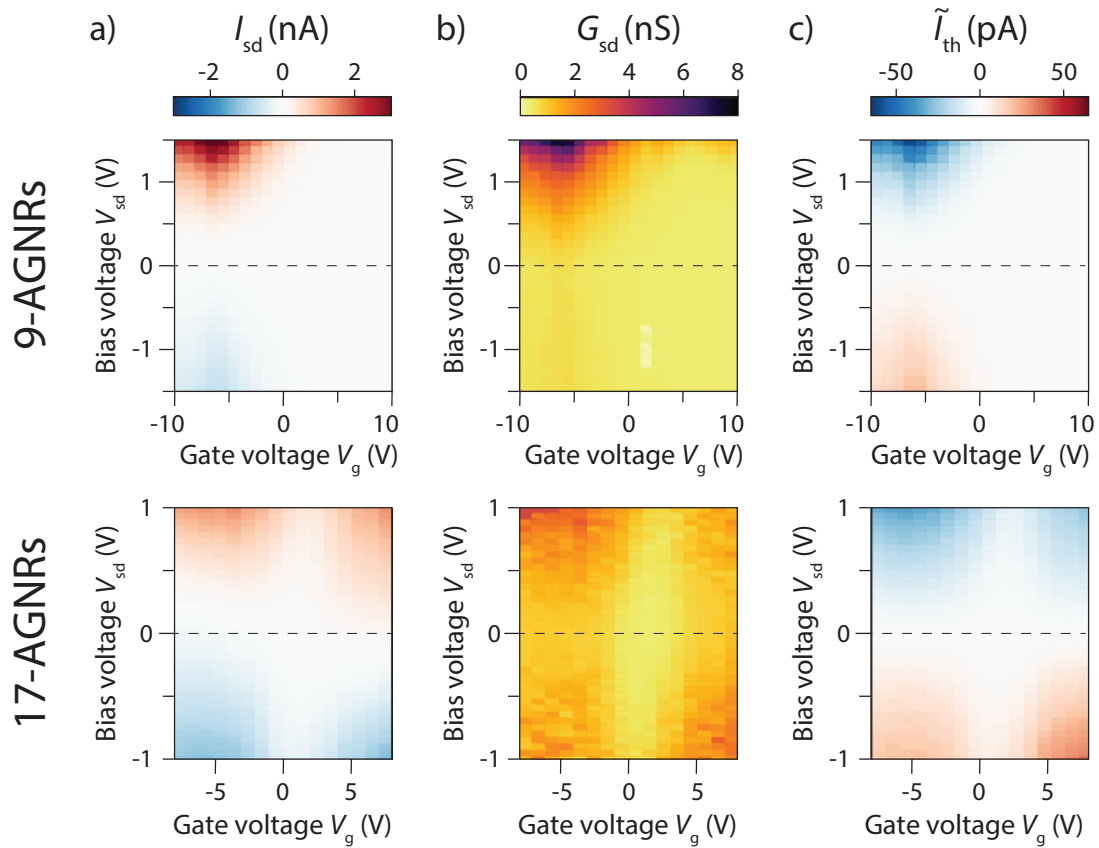


Figure 8.10 Electronic and thermoelectric properties of GNR films at room temperature. Measurements on 9-AGNRs and 17-AGNRs are shown in the top and bottom row, respectively. In columns are maps of **a)** DC current I_{sd} , **b)** differential conductance G_{sd} and **c)** AC thermocurrent \tilde{I}_{th} of GNR films measured simultaneously as a function of bias and gate voltage, V_{sd} and V_g , respectively.

8.6.2 Seebeck coefficient and power factor of GNRs

To further interpret the observed data, we apply a conversion from the thermocurrent and the conductance to the thermovoltage (not shown) as proposed by Gehring et al.²²¹:

$$S = -\frac{\tilde{V}_{th}}{\Delta\tilde{T}} = -\frac{\tilde{I}_{th}}{G_{sd}} \cdot \frac{1}{\Delta\tilde{T}} \quad (8.14)$$

Using Equation 8.14 we extract from the data shown in Figure 8.10 the corresponding Seebeck coefficient S and the resulting power factor $PF = GS^2$. Additionally, we take into account that the temperature gradient is applied in opposite to the source-drain direction. This is accounted for by a sign change of the thermocurrent. These two parameters are shown in Figure 8.11. The obtained values for the Seebeck coefficient reach $-560 \mu\text{V}/\text{K}$ and $+2120 \mu\text{V}/\text{K}$ in the case of the 9-AGNRs films and for the 17-AGNRs films $-1350 \mu\text{V}/\text{K}$ and $+1400 \mu\text{V}/\text{K}$. These extraordinary high values result in a corresponding power factor PF of $3.05 \cdot 10^{-15} \text{SV}^2/\text{K}^2$ and $3.15 \cdot 10^{-15} \text{SV}^2/\text{K}^2$ for the 9-AGNRs and 17-AGNRs, respectively.

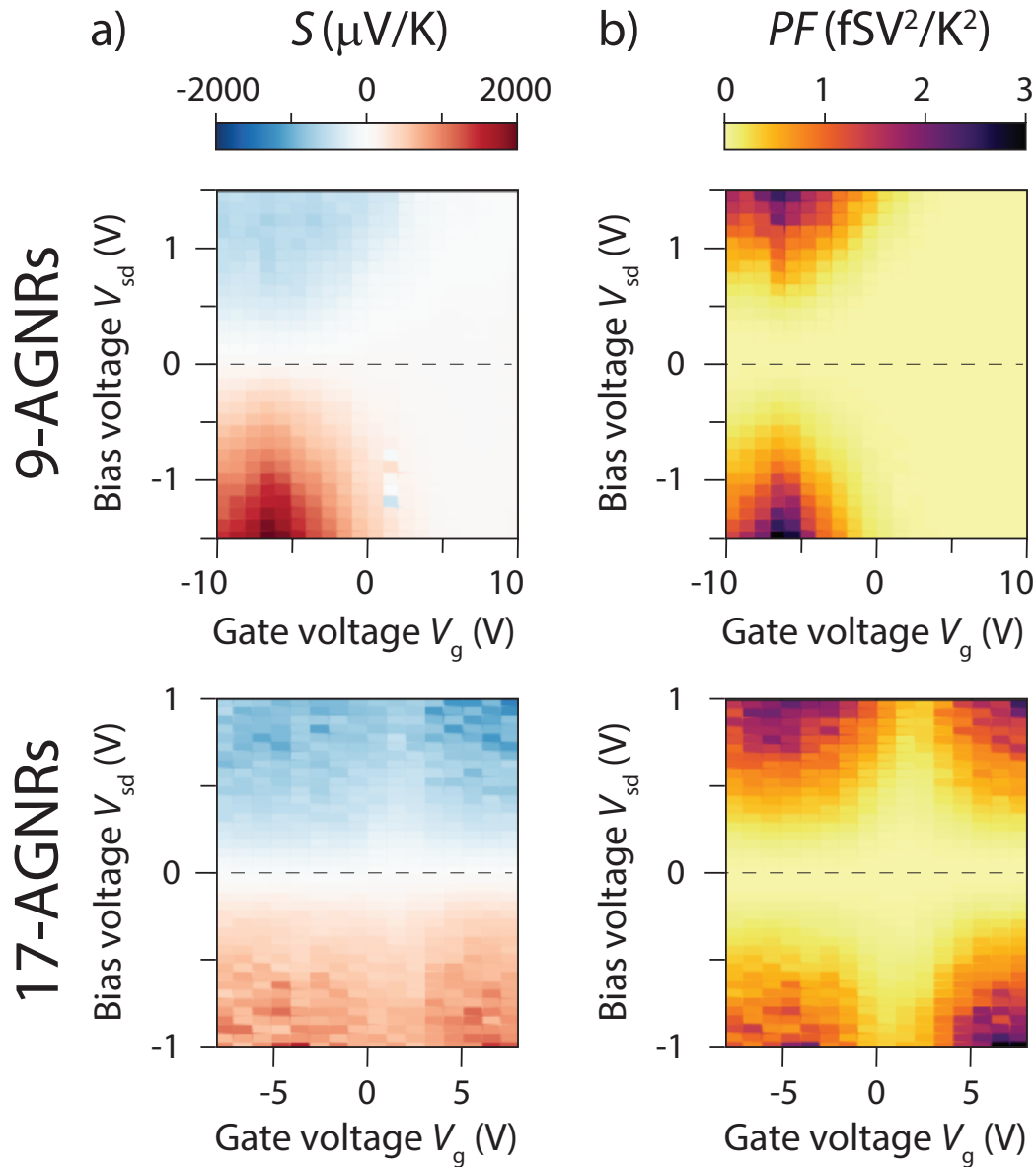


Figure 8.11 Seebeck coefficient and power factor of GNR films at room temperature. The measured conductance and thermocurrent data are used to extract the presented values. Results for 9-AGNRs and 17-AGNRs are shown in the top and bottom row, respectively. In columns are maps of **a)** the Seebeck coefficient S and **b)** the power factor PF as a function of bias and gate voltage, V_{sd} and V_g , respectively.

8.6.3 Seebeck coefficient at various heater currents

To further verify the high Seebeck values, we performed the same measurement under various temperature gradients. In Appendix 8.D. the measured thermocurrent measurements are shown. To see their scaling behavior we extracted the corresponding map of the Seebeck coefficients and show them in Figure 8.12. Operating in the linear response regime, the Seebeck coefficient should stay constant since it reflects a material property. We observe this up to a temperature gradient of ≈ 20 K. With higher temperature

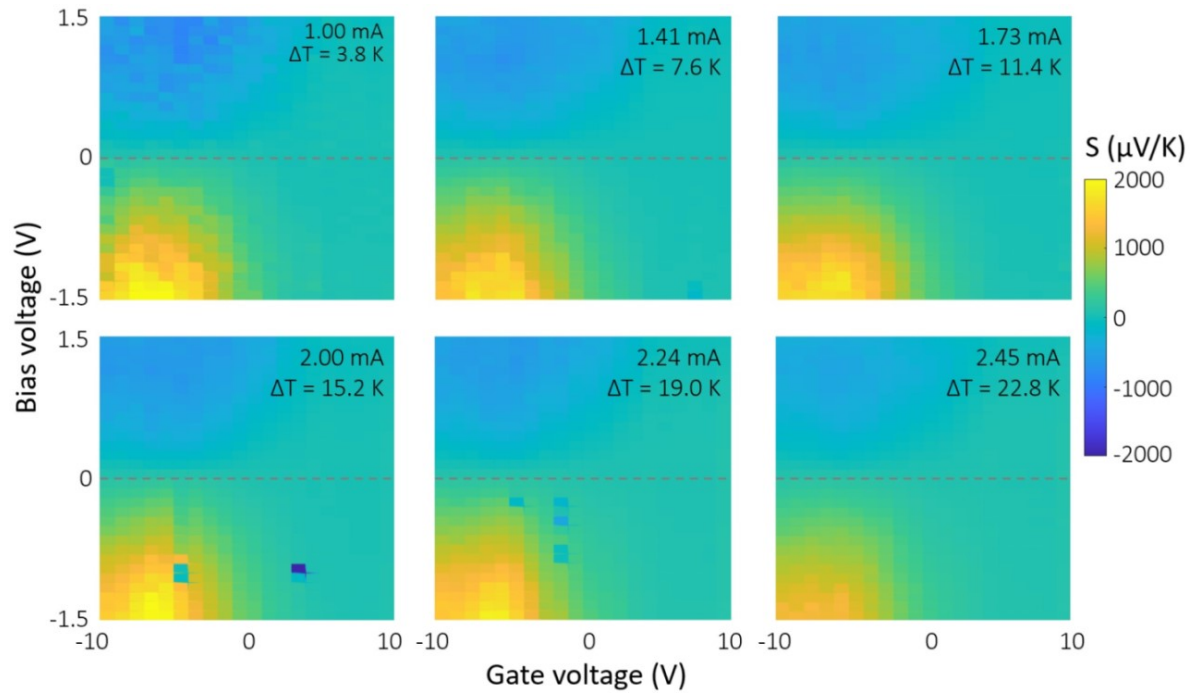


Figure 8.12 Seebeck coefficient of 9-AGNRs with various ΔT . Seebeck coefficient S as a function of bias and gate voltage with various applied heater currents. The heater currents and corresponding temperature gradients are indicated in the top right corner. Dashed lines as guides to the eye.

gradients, we observe a deviation, resulting in lower Seebeck coefficients. This can be understood intuitively as the electrical conductance of the film of GNRs increases with temperature hence leading to lower thermocurrents.

8.7 Conclusion and outlook

The Seebeck coefficient of Au-nanoparticles and GNRs has been determined. With the planar geometry implemented for Au-nanoparticles, we saw that limitations of the planar device geometry arise, resulting in a small thermal gradient and hence a less accurate determination of S for the smallest thermal gradients. To better understand the system it would be desirable to perform a systematic study on how the Seebeck coefficient scales with the number of layers. This would be interesting to see how the transition from a 3D material to a 2D material similarly influences the observed thermovoltages as it has been reported for the electrical conductivity.²⁴⁶

The first measurements of the Seebeck coefficient of atomically precise graphene nanoribbon films obtained here are encouraging. Values of S up to 2000 $\mu\text{V}/\text{K}$ at room temperature are exceeding the reported value for high S materials, e.g. selenium with $\approx 1000 \mu\text{V}/\text{K}$.²⁵⁸ Our measurements with various applied temperature gradients further indicate that we operate in the linear response regime probing the material property. However, to further confirm the high Seebeck values, a direct measurement of the thermovoltage is desirable due to several reasons. The current flowing through the device can disturb the temperature gradient by generating additional temperature differences via the Peltier effect.⁶⁵ Additionally, the temperature dependence of the device resistance has to be investigated further. This is also of interest from a purely analytical standpoint. If one defines the Seebeck as follows:

$$S = -\frac{V}{dT} \quad (8.15)$$

where V is the measured thermovoltage and T the temperature increase. Now, by assuming that not only the voltage but also the resistance is temperature dependent (indicated in brackets), then the measured thermocurrent can be expressed as follows:

$$\frac{dI(T)}{dT} = \frac{d}{dT} \frac{V(T)}{R(T)} = \frac{1}{R} \cdot \frac{dV}{dT} - \frac{1}{R^2} \cdot \frac{dR}{dT} \cdot V \quad (8.16)$$

We see that from the first term the Seebeck coefficient can be derived as we have done in this chapter. However, the second term has two competing contributions and does not necessarily vanish, and should therefore be taken into account. The mentioned temperature dependent resistance of the GNR film is therefore essential and needed to confirm the obtained results.

To summarize, the first results and analysis procedures are highly encouraging and motivate further studies on thermoelectricity in GNR based systems as well as in the context of energy harvesting.

Appendix 8.A. Frequency dependence of the thermocurrent

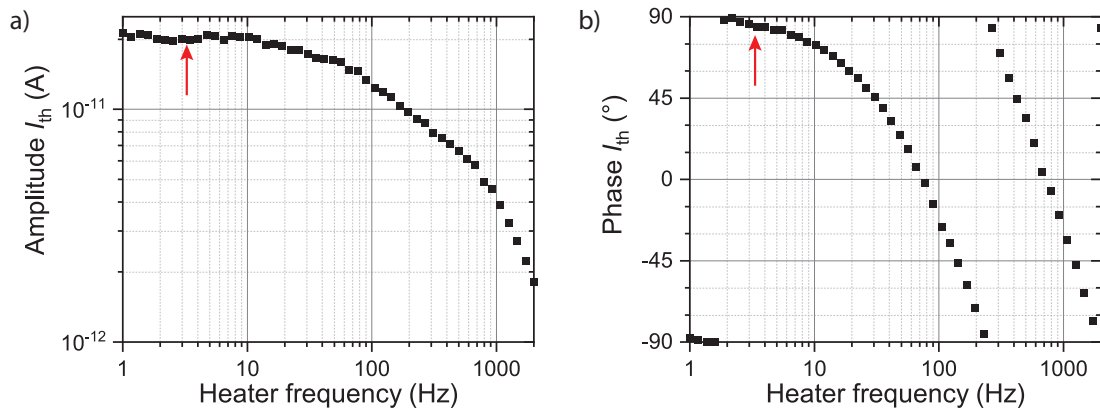


Figure 8.13 Frequency dependence of the thermocurrent. a) Amplitude of the thermocurrent as a function of applied heater frequency. b) Phase of the thermocurrent as a function of applied heater frequency. Red arrow indicates the selected heater frequency of 3.123 Hz.

Experiments that involve measurements of modulated signals require a careful determination of the used frequencies. This in order to not measure outside of the bandwidth of the device under test, which would lead to unphysical properties/a probing of the measurement instrumentation. Such a calibration is of particular interest in the case of thermoelectric characterization of nanoscale devices, since there thermalization effects are also significant.

In Figure 8.13 the amplitude and phase of the thermocurrent signal as a function of applied heater frequency is displayed. The measurement is performed on a typical 9-AGNR film sample with an applied, fixed, bias- and gate voltage of 1 V and -8 V, respectively and a heater amplitude of 2 mA. These parameters were chosen to be in a regime with a strong thermocurrent signal. For each frequency, the plotted data points each represent the average of the data acquired during the last 20 s of a 150 s long measurement.

In Figure 8.13a) one sees clearly that the signal amplitude starts to drop at a heater frequency >10 Hz. This behaviour can be explained by the thermal equilibrium time of the system as outlined in Subsection 8.4.1. On the other side, the corresponding phase shown in Figure 8.13 b) already starts to drift below 10 Hz. Note, the phase jumps slightly below 2 Hz by π , this change is arbitrary and has no direct physical consequences. Our observations are in accordance with results reported by Gehring et al.²⁴⁷, where the thermal response of the system is illustrated by presenting the scanning thermal microscopy (SThM) signal on the hot contact and shows deviations from the DC signal at a frequency above ≈ 3 Hz. Taking the above mentioned considerations into account, we selected the heater frequency at 3.123 Hz since it seems to be a good compromise between measurement speed and accuracy.

Appendix 8.B. Probe current for resistance thermometers

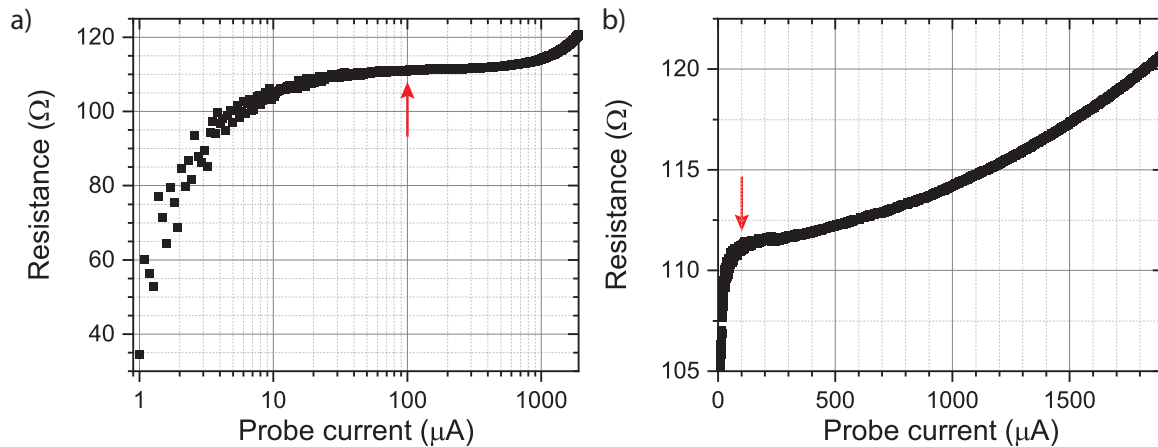


Figure 8.14 Thermometer resistance versus different probe currents. The resistance of the on-on chip thermometer is probed in a 4-terminal configuration using different probe currents. The right panel shows the same data on linear scale. The used probe current of $100 \mu\text{A}$ is indicated with red arrows.

For measuring the resistance of the on-chip thermometers one has to find the optimum between measurement accuracy and self heating. To achieve a very accurate value for the resistance, the probe current of the 4-terminal measurement needs to be as high as possible. On the other side, it should be as low as possible to keep the effect of joule heating on the resistance negligible. In Figure 8.14 the resistance of a typical on-chip thermometer is plotted for different DC probe currents. A probe current below $10 \mu\text{A}$ leads to a large spread in resistance values. The resistance value gets more and more accurate with increasing probe current but also starts to increase quadratically above $\approx 200 \mu\text{A}$, which points to joule heating. This effect is sometimes referred as self-heating. Taking above points into consideration we chose a probe current of $100 \mu\text{A}$ for all further measurements of this type.

Appendix 8.C. Thermometer response

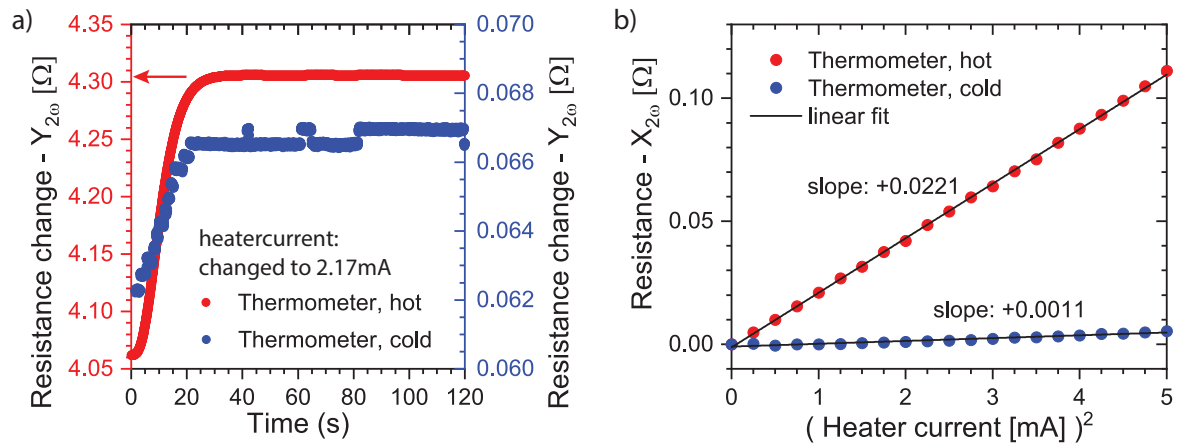


Figure 8.15 Response of the thermometer resistance to heater currents. The resistance of the thermometers close to the heater (hot) and away from the heater (cold) is measured at $2\omega_1$ while the heater current is driven at ω_1 . **a)** Y-component of the resistance over time after a change of heater current to 2.17 mA. **b)** X-component of the resistance for various heater currents.

The data points shown in Figure 8.15b) are the last 40 s of a 120 s measurement series as shown in Figure 8.15a). After ≈ 30 s the system has reached steady state again. Whether this effect is due to the established thermal gradient or the instrument requiring such long settling times is difficult to judge and would need further quantification by using other methods like for example scanning thermal microscopy (SThM).

Appendix 8.D. Thermocurrents at various heater currents

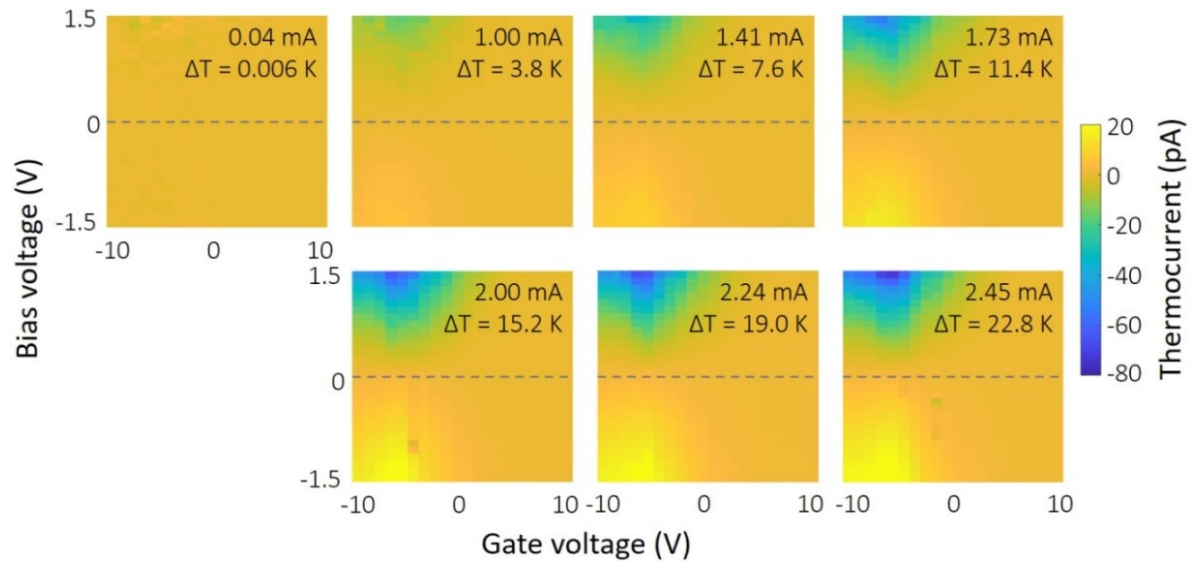


Figure 8.16 Thermocurrent of films of 9-AGNRs at room temperature. Thermocurrents as function of bias and gate voltage for various heater currents. The heater currents with the corresponding temperature gradient are indicated in the top right corner.

9 Spatially mapping thermal transport in graphene by an opto-thermal method

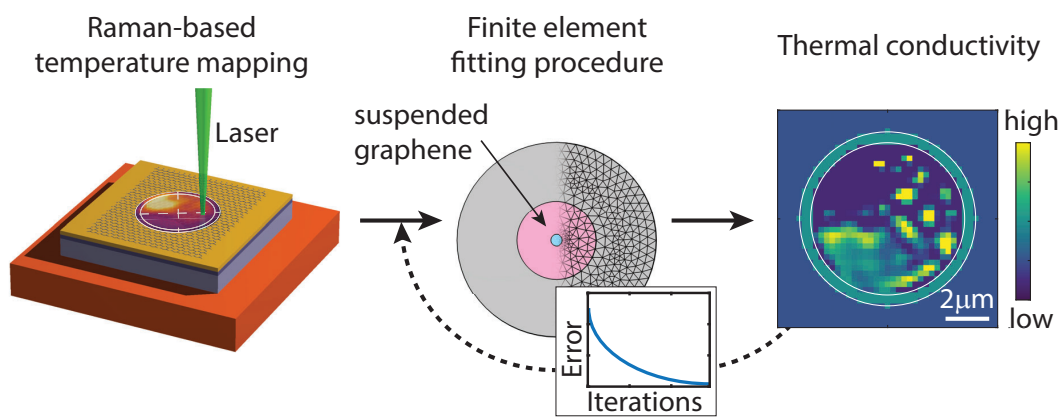


Figure 9.1 Schematic illustration of the method for obtaining a spatially resolved map of the thermal conductivity of suspended graphene. Figure taken from Braun et al.⁹⁰

Mapping the thermal transport properties of materials at the nanoscale is of critical importance for optimizing heat conduction in nanoscale devices. Several methods to determine the thermal conductivity of materials have been developed, most of them yielding an average value across the sample, thereby disregarding the role of local variations. Here, we present a method for the spatially-resolved assessment of the thermal conductivity of suspended graphene by using a combination of confocal Raman thermometry and a finite-element calculations-based fitting procedure. We demonstrate the working principle of our method by extracting the two-dimensional thermal conductivity map of one pristine suspended single-layer graphene sheet and one irradiated using helium ions. In the last section, a clustering approach developed by us is applied to the defect-engineered graphene membrane to identify spectrally separated regions without *a priori* know-how of Raman spectra modifications. Our method paves the way for spatially resolving the thermal conductivity of other types of layered materials. This is particularly relevant for the design and engineering of nanoscale thermal circuits (e.g. thermal diodes).

Contributions:

O.B., I.S., M.C., and M.L.P. conceived and designed the experiments. K.T. developed the graphene growth recipe and transfer process used in this study. R.Fu. performed the graphene growth. O.B and I.S. prepared the SiN frame and performed the defect engineering using a focused ion beam. O.B. performed the Raman measurements. O.B., M.L.P., M.C., and I.Z. did the Raman spectroscopy analysis. P.B. developed the finite-element model to calculate the temperature distribution for a single laser spot position. M.L.P. extended the model to construct the temperature map upon illumination by the Raman laser and developed the procedure to fit the thermal conductivity. M.L.P. performed all finite-element calculations. M.L.P. performed the machine learning analysis, with input from O.B., M.E., J.O., M.C, H.v.d.Z.

The first part of this chapter has been submitted as an article and is adapted from Braun et al.⁹⁰. Section 9.6 is adapted from El Abbassi et al.¹¹³

9.1 Introduction

Thermal properties of materials are of crucial importance for optimizing heat management in nanoscale devices, with thermal conductivity as a key material property.^{49,259} The thermal conductivity is typically determined by monitoring the sample temperature and/or heat flow in response to a local heat source, in combination with an analytical expression or a numerical model. For instance, for bulk materials, the well known 3ω technique^{260,261} is used, while for nanoscale materials, methods such as the thermal bridge method^{226,262,263} and micro-Raman spectroscopy^{59,60,264,265} provide the thermal conductivity of the material.

Of particular interest are the thermal properties of layered materials. Due to their broad range of conductivity values and their atomically thin nature, such materials are highly relevant for heat management at the nanoscale.^{266,267} One of the most appealing materials is graphene, with extraordinarily high thermal conductivity values. However, extracting the thermal properties of 2D materials is challenging, in particular when suspended to reduce the influence of the substrate. For example, time-domain thermoreflectance cannot be applied to 2D materials as the material is too thin²⁶⁸. Scanning thermal probe microscopy, on the other hand, despite possessing nanometer resolution, is highly delicate to perform on suspended 2D materials. Moreover, both techniques rely on on-chip heaters to channel heat into the system. Raman spectroscopy can overcome these difficulties, as it can utilize the excitation laser to locally heat the device, while at the same time measuring the local temperature. Moreover, Raman spectroscopy can be conveniently performed on suspended graphene films to eliminate the influence of the substrate. Using Raman spectroscopy, Balandin and Ghosh et al.^{57,269} determined the thermal conductivity of suspended graphene to be as high as $\sim 5000 \text{ Wm}^{-1}\text{K}^{-1}$ at room temperature. Their opto-thermal method, measuring the shift of the Raman G-band upon laser irradiation to estimate the local temperature, has been extensively used in literature since. Alternatives based on the intensity ratio of Stokes to anti-Stokes Raman scattering²⁷⁰ or the Raman 2D-band²⁷¹ have also been reported.

Using this opto-thermal method, the influence of the quality and structure of the graphene, as well as the environment have been extensively investigated. For instance, Cai et al.¹¹⁴ reported values for κ exceeding $\sim 2500 \text{ Wm}^{-1}\text{K}^{-1}$ for suspended graphene grown by chemical vapor deposition (CVD), and Chen et al.²⁷² studied the influence of environment on thermal conductivity of graphene. Isotopically pure ^{12}C (0.01 % ^{13}C) graphene has been shown to exhibit $\kappa = 4000 \text{ Wm}^{-1}\text{K}^{-1}$, a factor of two higher than κ in graphene composed of a 1:1 mixture of ^{12}C and ^{13}C .⁵⁸ Also, the influence of CVD-graphene's polycrystallinity on the thermal conductivity was studied by Lee et al.²⁷³ and Ma et al.²⁷⁴, revealing that smaller grain sizes drastically reduce κ due to grain boundary scattering. Along similar lines, wrinkles²⁷⁵, oxygen-plasma induced defects²⁷⁶, and electron beam irradiation²⁷⁷ have been shown to reduce the thermal conductivity.

In all the above-mentioned studies, the one-dimensional heat equation is used to fit the experimental temperature and extract the thermal conductivity. However, such approaches yield an average for the thermal conductivity value, not a spatially resolved map. This implies that local variations caused by defects, folds, contaminants, etc. are

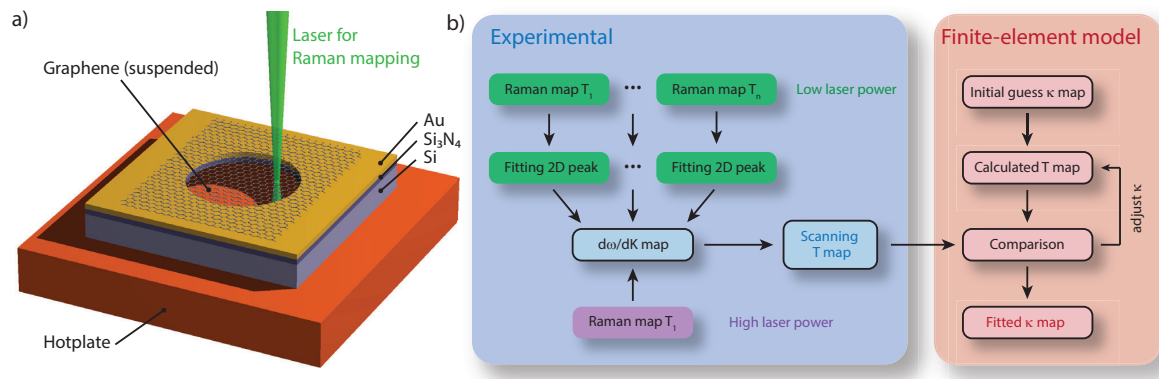


Figure 9.2 Experimental and Finite Element Method description. a) Schematic drawing of the suspended graphene membrane. b) Experimental workflow to obtain a temperature map upon laser illumination and computational workflow to fit the corresponding thermal conductivity map. Figure taken from Braun et al.⁹⁰

neglected.

To go beyond the average material property value, approaches mapping the temperature distribution in the sample are necessary, combined with a multidimensional analytical-numerical model. A range of techniques has been developed for nanoscale thermometry, such as time-domain thermoreflectance²⁷⁸, Raman spectroscopy^{57,269}, scanning thermal probe microscopy^{66,67,279}, polymer imprint thermal mapping²⁸⁰ and electron energy loss spectroscopy²⁸¹.

Here, we introduce an opto-thermal method that allows for two-dimensional mapping of the thermal conductivity of suspended graphene membranes. The presented method relies on a combination of scanning μ -Raman spectroscopy with finite-element method (FEM) calculations. The workflow for our approach is presented in Figure 9.2. In the first experimental stage, a series of two-dimensional Raman spectroscopy maps are used to construct a temperature map of the membrane upon illumination. More specifically, Raman maps are recorded for various hotplate temperatures and at a low laser power. This series of maps is used to construct a calibration map of the Raman peak shifts with temperature. Then, another Raman map is recorded at high-laser power, which, combined with the calibration map, is used to construct a temperature map of the membrane upon laser heating.

The constructed experimental temperature map is then used as an input for the FEM-based fit procedure. For a given initial guess of the thermal conductivity, the lattice temperature upon laser illumination is calculated. The thermal conductivity is then iteratively adjusted until the computed temperature map matches the experimental one. We apply this fit procedure to extract the thermal conductivity of a pristine graphene membrane that is suspended over a silicon nitride frame. Finally, we demonstrate that the thermal conductivity of the graphene membrane can be tuned in a controlled way by the introduction of helium-ion (He^+ -ion) induced defects in the membrane.

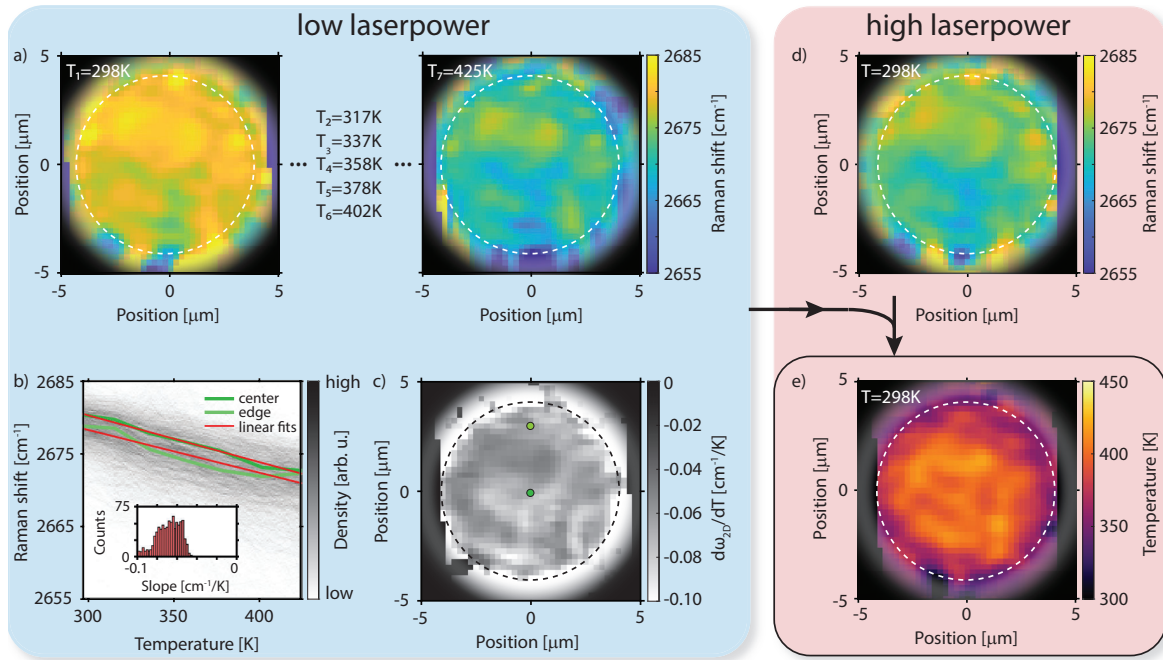


Figure 9.3 Experimental determination of temperature map. Spatially resolved mapping of laser-induced temperature rise of graphene. **a)** Raman 2D-peak position obtained with $P_{\text{laser}} = 0.25$ mW at different hot plate temperatures T_1 and T_7 . The dashed circle is a guide to the eye for the support edge. **b)** Density plot of the temperature evolution of the 2D-peak frequency. Two spatial points (center and edge, see dots in panel c)) are highlighted to represent the method. The inset shows a histogram of $d\omega_{2D}/dT$ of the complete membrane. **c)** Spatial distribution of change in Raman shift per temperature change $d\omega_{2D}/dT$ obtained from linear fits to the data shown in b). **d)** Raman 2D-peak position obtained with $P_{\text{laser}} = 4$ mW at 297 K. **e)** Temperature distribution obtained by combining the results from c) and d). Figure taken from Braun et al.⁹⁰

9.2 Experimental temperature maps

The CVD-graphene membranes are prepared as described in the methods section. We applied Raman spectroscopy to obtain the lattice temperature of the suspended graphene membranes (for details see Appendix 9.A.). Here, we focus on the 2D-band due to its high sensitivity to temperature changes^{272,273} of around -0.07 cm^{-1}/K . Alternatively, one can also rely on the G-peak due to its high linearity in peak shift versus temperature.^{114,269,282}

Figure 9.3a) presents maps of the Lorentzian-fitted 2D-peaks were acquired at temperatures T_1 - T_7 ranging between 298 K and 425 K. The Raman spectra have been acquired at low laser power (0.25 mW) to limit any heating effects using a 532 nm excitation laser (for details see Appendix 9.B.). For each pixel, the peak shift with hot plate temperature ($d\omega_{2D}/dT$) is fitted using a first-order polynomial, as shown in Figure 9.3b). The inset presents a histogram of the slopes, showing a Gaussian distribution centered around -0.07 cm^{-1}/K . The spatial distribution of the peak shifts with temperature is displayed in Figure 9.3c), showing substantial spatial variations.

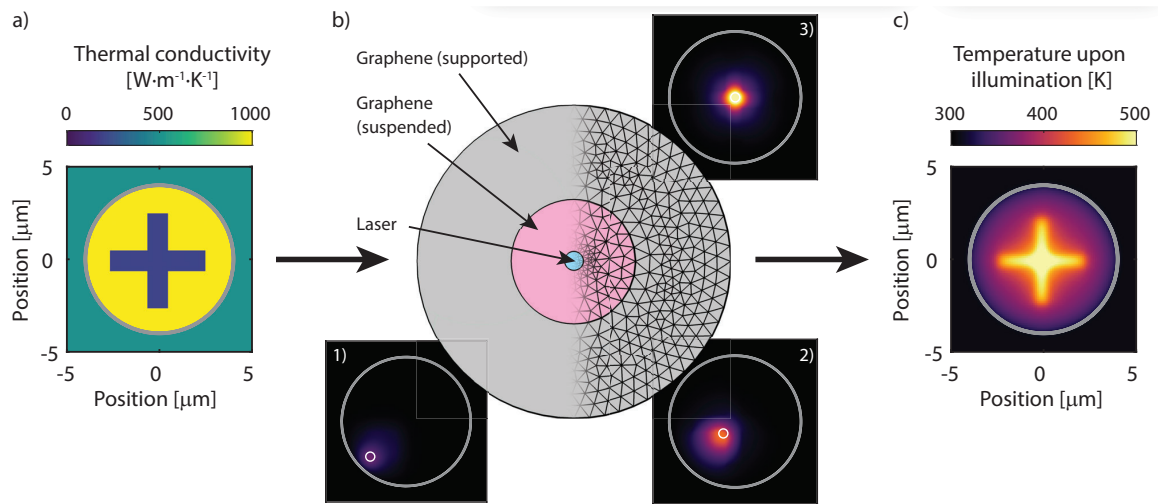


Figure 9.4 Finite Element Method description. a) Input thermal conductivity map. b) Schematic representation of the sample and the calculation mesh. Temperature profiles of the graphene membrane with the heating laser spot at three different positions 1)-3). c) Temperature profile upon laser illumination. Figure taken from Braun et al.⁹⁰

Once this calibration map is acquired, a Raman map of the graphene membrane is acquired at high laser power (4 mW), as shown in Figure 9.3d). The high laser power causes the graphene to locally heat, resulting in a shift in the Raman peak position. By combining this high-power measurement with the $d\omega_{2D}/dT$ map obtained at low laser power, a map of the average temperature within the laser spot is obtained for each laser position, as shown in Figure 9.3b). We note that local variations in the temperature upon illumination on the order of 50-100 K are observed, highlighting the importance of spatially mapping the temperature, superior to other techniques that extract thermal conductivity from a single spot.

9.3 FEM calculations

FEM calculations are employed for the computation of the temperature map of the system upon laser illumination for a given spatial thermal conductivity distribution. This concept is illustrated in Figure 9.4. As an input, a two-dimensional map of the thermal conductivity is provided, of which an example is shown in Figure 9.4a). Figure 9.4b) presents the layout of the system (not to scale). A more detailed description of the FEM calculation is shown in Appendix 9.C. and 9.D.. While scanning the laser across the membrane, the full temperature distribution is calculated for each laser spot position on the membrane (three examples are provided in Figure 9.4b). For each of these temperature distributions, the average temperature within the laser spot is calculated, from which all values are combined to obtain a two-dimensional map of the graphene temperature upon illumination. This induced-temperature map is presented in Figure 9.4c) and represents the same temperature map that is obtained experimentally upon illumination of the sample with high laser power.

To obtain the thermal conductivity map, an iterative minimization procedure is

employed. More information can be found in Appendix 9.D., in which we also validate the numerical method on a simulated system with a known thermal conductivity map. The starting point is an initial (typically uniform) guess of the thermal conductivity. In each iteration of the process, the corresponding induced temperature map is compared to the experimental temperature map, after which the thermal conductivity is adjusted pixel-wise according to the temperature difference. This process is repeated until convergence is reached.

9.4 Thermal conductivity map based on fitted experimental temperature map

The induced temperature map obtained in Figure 9.3 is used as input for the iterative procedure to obtain the thermal conductivity map. Here, as clarified in Appendix 9.8, we use a uniform absorption of 2.7 % for the suspended graphene and double that value (5.4 %) for the supported graphene. Moreover, all the employed model parameters are summarized in Table 1 of Appendix 9.8. Importantly, in the model, a diffraction-limited spot size of 300 nm is assumed. Moreover, the thermal conductivity of graphene on the supported part, the thermal coupling to the substrate, as well as the convection parameter are taken from literature.¹¹⁴ Finally, we note that it is challenging to model the transition from the suspended graphene to the supported graphene once the laser spot is in the vicinity of the edge due to 1) reflections of the laser excitation at the edges of the support may lead to an increase in the deposited laser power, 2) quenching of the Raman scattered light on the substrate may lead to an overestimation of the local temperature as the 2D peak of the suspended graphene is more pronounced than that of the supported graphene. To circumvent this issue, the thermal conductivity of the first 0.5 μm of the membranes away from the support are not fitted and kept at a fixed value. Finally, the thermal conductivity is fitted for 100 iterations, after which the absorption is fitted for the same number of cycles. More details about this procedure can be found in Supplementary Note 2 of Braun et al.¹³⁰ For numerical stability reasons, we use a lower value for the thermal conductivity at $100 \text{ Wm}^{-1}\text{K}^{-1}$.

Figure 9.5a) presents the experimental temperature map, as obtained in Figure 9.3e), alongside the fitted temperature map in Figure 9.5b). The two maps closely resemble each other. The corresponding thermal conductivity map is presented in Figure 9.5c). We find that the local thermal conductivity values range from 500 to $2000 \text{ Wm}^{-1}\text{K}^{-1}$ with an average value of $1007 \pm 450 \text{ Wm}^{-1}\text{K}^{-1}$ highlighting the importance of spatially resolving the thermal conductivity. The average value is in agreement with values reported previously as well as by other methods.^{283,284} In Figure 9.5e), we present a histogram of the fitted thermal conductivity map for increasing hot plate temperatures. The bar plots show that for increasing temperature a gradual decrease in thermal conductivity is observed. This behavior follows the trend observed by others.^{58,272,273}

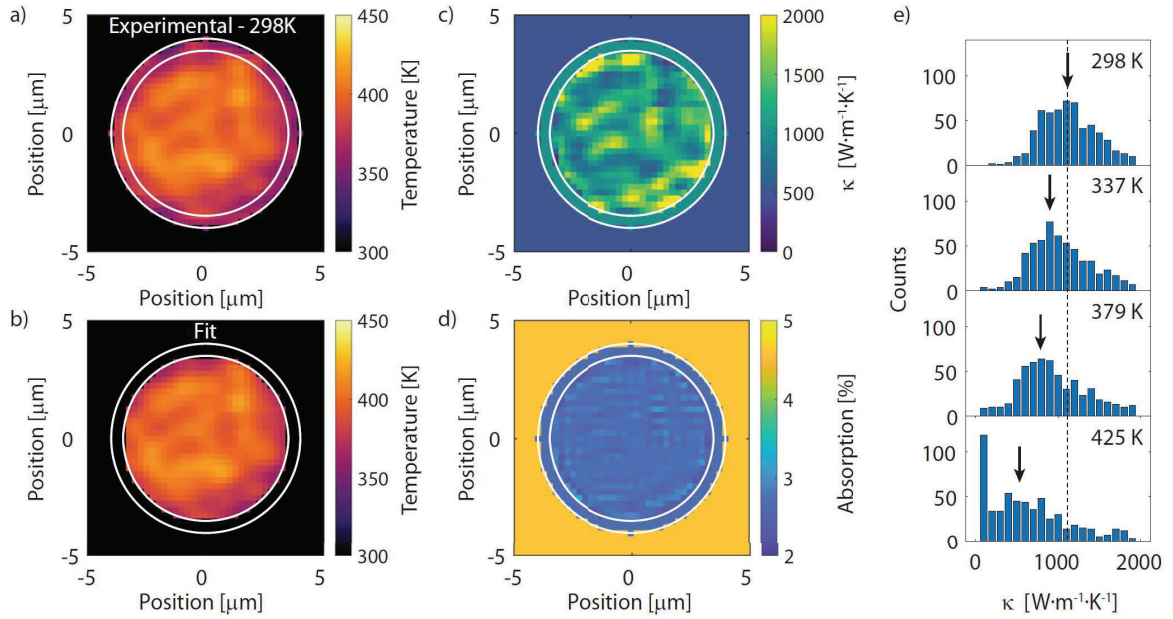


Figure 9.5 Thermal conductivity map based on fitted experimental data. **a)** Experimentally determined temperature map. **b)** Fitted temperature map. **c)** Fitted thermal conductivity map. **d)** Converged absorption map. **e)** Histogram of the thermal conductivity for various hot plate temperatures. Arrows indicate the mode of the smoothed distributions. Figure taken from Braun et al.⁹⁰

9.5 Thermal conductivity of defect-engineered graphene

As a final demonstration of the capability of the presented method, we study the thermal conductivity of a graphene membrane that is exposed to He^+ -ions using focused ion beam lithography. As shown previously, He^+ -ions can be used to induce, in a controlled fashion, defects in suspended graphene membranes and other two-dimensional materials.^{129,285}

Figure 9.6a) presents the exposure pattern as well as the used irradiation doses. The membrane is divided into four quadrants, with the He^+ -ion irradiation steadily increasing in the counterclockwise direction, starting in the lower left with no He^+ -ion dose. Manually selected representative Raman spectra of each quadrant are presented in Appendix 9.A., exhibiting all the characteristic graphene peaks. Upon an increase of the He^+ -ion dose, the D-band intensity steadily increases. The intensity ratio of the D and D' band $I(\text{D})/I(\text{D}')$ upon irradiation, is indicative of the type of defect.²⁸⁶ We extract this ratio by fitting the ratios $I(\text{D})/I(\text{G})$ versus $I(\text{D}')/I(\text{G})$ for various He^+ -ion doses. We find an intensity ratio of ~ 11.7 for the defect-engineered graphene. This value is comparable to the reported intensity ratio of ~ 13 for sp^3 type of defects (see Appendix 9.A.). We employ the same procedure as presented in Figures 9.3 for the extraction of the temperature. Figure 9.6b) presents the induced temperature map upon a 4 mW laser illumination. In this plot, the four quadrants are visible, with the lowest temperatures recorded in the (unexposed) lower left section of the membrane, and the highest one in the upper left (most exposed). This temperature map is used as input for the iterative FEM-based fitting procedure, resulting in the fitted thermal

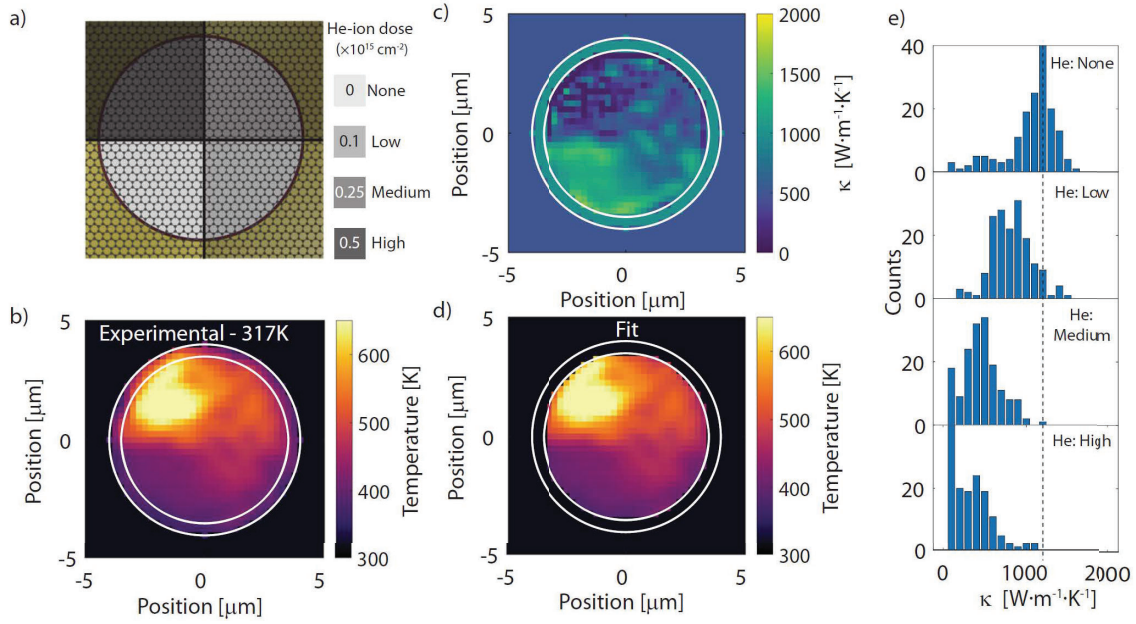


Figure 9.6 Thermal conductivity of defect engineered graphene. a) Schematic image of a suspended graphene membrane. The areas where the membrane was exposed to He^+ -ions and their corresponding dose is indicated with different colors. b) Experimentally observed temperature map. c) Fitted thermal conductivity map. d) Fitted temperature map. e) Histogram of the thermal conductivity for various defect densities. Figure taken from Braun et al.⁹⁰

conductivity map in Figure 9.6c) and the corresponding fitted temperature map shown in Figure 9.6d). Figure 9.6e) presents a histogram of the thermal conductivity of each of the four quadrants. A steady decrease in average conductivity is observed, from $\sim 1000 \text{ Wm}^{-1}\text{K}^{-1}$ for the no He^+ -ion irradiation, and $\sim 100 \text{ Wm}^{-1}\text{K}^{-1}$ for the highest He^+ -ion dose. This decrease in thermal conductivity with increasing defect density is in agreement with previous reports.^{276,277}

In this study, based on extensive literature, it was known beforehand which peaks are relevant for graphene (D, G, 2D), that the 2D peak is sensitive to damage, and also where the He^+ damage has been introduced. However, such knowledge is not always available, and in such cases, unsupervised machine learning algorithms are very useful as they aim to identify structures in datasets, without any beforehand knowledge of the system. Given the high quality of this dataset and the precision with which the He^+ -ion irradiation occurred, this system forms a nice benchmark for investigating such algorithms. As shown in Section 9.6 and reported in El Abbassi et al.¹¹³, we have investigated such clustering approaches and applied them to this Raman data set.

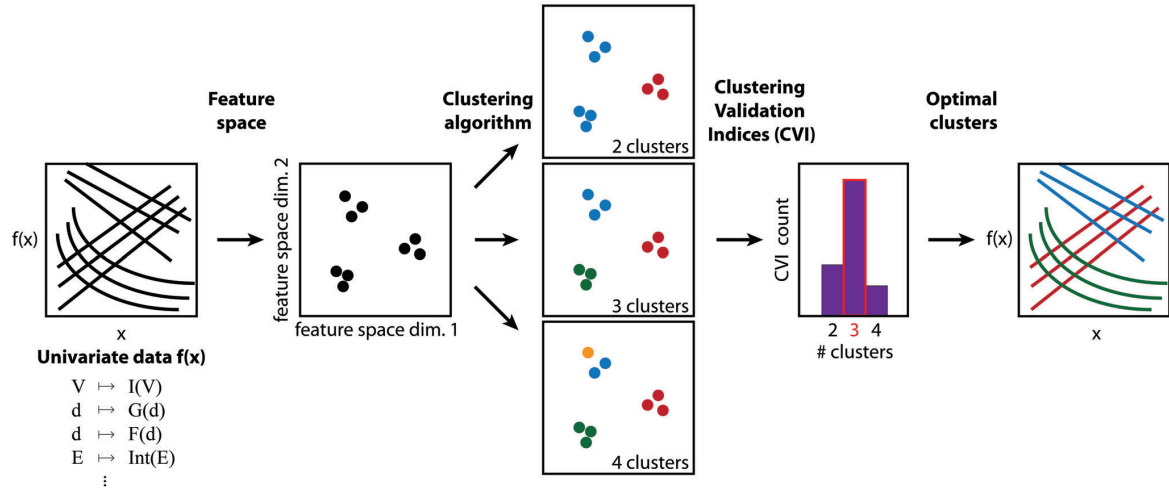


Figure 9.7 Concept of our approach for univariate data classification. Any dataset in which the data depends on a single variable (for instance current I vs. bias voltage V , conductance G vs. electrode displacement d , force F vs. displacement d , intensity Int vs. energy E , etc.) can be converted into a feature vector. The feature space spanning the entire dataset is then split into clusters (represented using different colors) using a clustering algorithm. Finally, cluster validation indices (CVIs) are used to estimate the optimal number of clusters (NoC). Figure taken from El Abbassi et al.¹¹³

9.6 Unsupervised classification of Raman spectrum in maps of defect engineered graphene

Unsupervised machine learning, and in particular data clustering, is a powerful approach for the analysis of datasets and identification of characteristic features occurring throughout a dataset. It is gaining popularity across scientific disciplines and is particularly useful for applications without a priori knowledge of the data structure. As published in El Abbassi et al.¹¹³ we introduced an approach for unsupervised data classification of any dataset consisting of a series of univariate measurements, among them Raman measurements. The effect of He^+ -ion-induced defects on the Raman spectrum of graphene is known from literature^{129,287}, but for our analysis here we explicitly do not rely on any a priori knowledge of the system, i.e., we do not need to know beforehand which Raman bands will be altered by the irradiation and by what spatial pattern the graphene has been irradiated. Instead, we use our clustering approach to identify the different types of Raman spectra present in the sample from which we infer the spatial distribution of He -irradiation doses and their effect on the graphene spectrum.

Our three-step approach consists of: 1) the feature space construction, 2) the clustering algorithm, and 3) the internal validation to define the optimum number of clusters (NoC). A schematic of the workflow for the unsupervised classification of univariate measurements is depicted in Figure 9.7, starting from a dataset consisting of N univariate and discrete functions $f(x_i)$, $i \in [1, N]$. Each measurement curve is converted into an M -dimensional feature vector, resulting in a feature space containing $M \times N$ data points. After this step, a clustering algorithm is applied. As the number of classes is

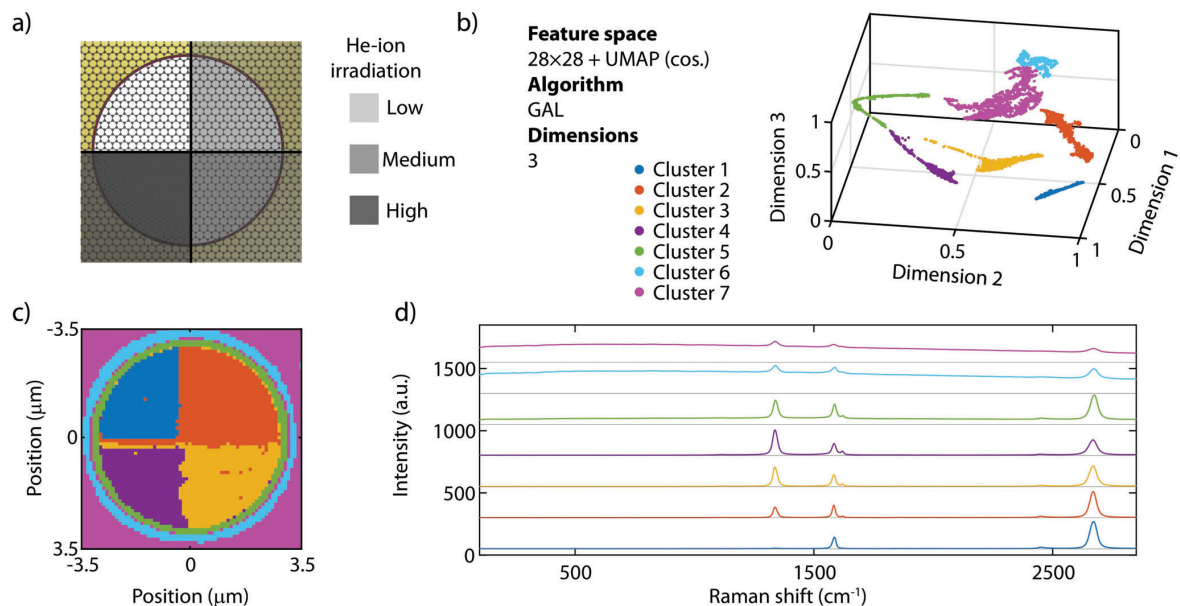


Figure 9.8 Application of the method on Raman spectra. **a)** Sample layout: suspended graphene membrane irradiated with four different He^+ -ion doses. **b)** Partitioned feature space, constructed with $28 \times 28 +$ uniform manifold approximation and projection (UMAP) using the cosine (cos.) distance metric and the graph average linkage (GAL) clustering algorithm. **c)** Spatial map of the extracted clusters. **d)** Average Raman spectrum of each cluster. Figure taken from El Abbassi et al.¹¹³

not known a priori, this clustering step is repeated for a range of cluster numbers (in this illustration for 2–4 clusters).

Based on an extensive benchmark to rank the different clusters, we find that the feature spaces $28 \times 28 +$ t-distributed stochastic neighbor embedding (t-SNE)²⁸⁸ and $28 \times 28 +$ uniform manifold approximation and projection (UMAP)²⁸⁹ feature spaces perform the best. For both approaches, the Raman spectra are first reduced to a 28×28 histogram, after which dimensionality reduction is performed (UMAP or t-SNE). After this step, we compare various clustering algorithms using cluster validation indices. The graph average linkage (GAL) algorithm²⁹⁰ performs best, separating the dataset into 7 clusters (see Supplementary Note 8 of El Abbassi et al.¹¹³ for more details).

Figure 9.8b) presents the partitioned feature space, containing several well-separated clusters. From this partitioning, we construct a two-dimensional map of the clusters to investigate their spatial distribution (see Figure 9.8c). The plot shows that the extracted clusters match well the physical topology of the sample: Clusters 1–4 are located on the suspended graphene membrane, reproducing the four quadrants. Clusters 5–7 form concentric rings located at the edge of the boundary between the SiN/Ti/Au support and the hole and on the support itself. Figure 9.8d) shows the average spectrum obtained per cluster from the which the following characteristics can be evoked:

Cluster 1 shows a flat background, with pronounced peaks at 1585 cm^{-1} and 2670 cm^{-1} . For Clusters 2 to 4 (corresponding to increasing He^+ -ion-doses), a peak at 1340 cm^{-1} appears with steadily increasing intensity while the intensity of the peak at 2670 cm^{-1} , decreases.

Cluster 5, located at the edge of the support possesses all three above-mentioned peaks, while for Clusters 6 and 7 a broad fluorescence background originating from the gold is present and all graphene-related peaks drastically decrease in prominence. Interestingly, the four quadrants have only been identified as distinct clusters on the suspended part, but not on the substrate. This implies that the clustering algorithm identifies spectral changes upon He⁺-ion irradiation as characteristic features of the freely suspended material, whereas the additional fluorescence background from the gold is a more characteristic attribute of the supported material than the variation between quadrants. Nevertheless, when inspecting Clusters 6 and 7, some substructure is still visible, and performing clustering on that subset may reveal additional structure.

The three observed peaks correspond to the well-known D-, G- and 2D-peak and follow the behavior expected for progressive damage to graphene by He⁺-ion irradiation^{129,287}. We would like to stress that our approach allowed us to extract the increase of the D peak and the decrease of the 2D-peak after introducing defects in graphene, without any beforehand knowledge of the system: neither the type of Raman spectra under consideration nor where on the sample the He⁺-ion irradiation occurred.

9.7 Discussion

The FEM calculations employed here assume that the heat transport through the system is following Fourier's Law. This assumption implies that the phonon mean free path is much smaller than the membrane size. Indeed, ballistic phonon transport has been reported in several nanosystems at room temperature: In substrate-supported graphene the phonon mean free path is ~ 100 nm²⁹¹; for suspended graphene discs, the transition from ballistic to diffusive transport occurs at ~ 775 nm²⁹² while in ultrathin nanowires phonon mean free paths of several micrometers have been observed.²⁹³ Therefore, the resolution of the presented method is limited by the phonon mean free path as a spatial mapping of the thermal conductivity below this length scale would require a heat transport description based on the Boltzmann transport equation.⁸⁴⁻⁸⁶ Given this boundary condition, the resolution of 250 nm used in this study is close to the ultimate resolution this FEM-based method allows.

A limitation of the presented method is the time consumption of the temperature calibration, reducing its use in high-throughput applications. As the laser power is low, acquiring the two-dimensional Raman map at each temperature requires several hours. This long acquisition time can also lead to a drift in the sample position during the measurement. To reduce this drift, clamping of the sample and a good thermalization of the sample with the environment is crucial. Furthermore, as changing the hot plate temperature leads to shifts of the sample position, the Raman maps acquired at various temperatures need to be aligned one versus the other.

A second limitation is the fixed value for the absorption of 2.7 % that is used for the first 100 cycles of the fitting procedure, after which the absorption is fitted as well. The accuracy of the model may be improved by experimentally determining the absorption at the various hot plate temperatures. Ideally, the absorption would be measured by simultaneously monitoring the transmitted, and reflected laser power while scanning across the sample. We stress that simultaneously measuring both components is crucial,

as contaminations and residues on the membrane may scatter the laser light, leading to a reduction in the transmitted light, but not to an increase in absorption. However, such a measurement is challenging and technically unfeasible in our current setup.

Despite the previously mentioned limitations, our method is well suited for studying the thermal properties of two-dimensional materials, in particular for materials with an anisotropic thermal conductivity.^{294–296} The method can also be extended to characterize van der Waals materials consisting of multiple layers. Furthermore, the method is extensible from two to three dimensions, allowing for modeling of more complex device geometries, including, for instance, stacks of 2D materials, or the presence of contact electrodes of finite thickness. As such, it could be used for assessing the material quality after device integration. Also, as the individual two-dimensional materials in a stacked geometry each have a distinct Raman signature, it is possible to investigate the subsurface thermal properties of materials, such as, for instance, graphene embedded in a thin hexagonal boron nitride layer. Alternatively, when the material under study is on a substrate or thick enough, other means of determining the temperature map may be used, like time-domain thermoreflectance, for reduced measurement time and improve throughput.

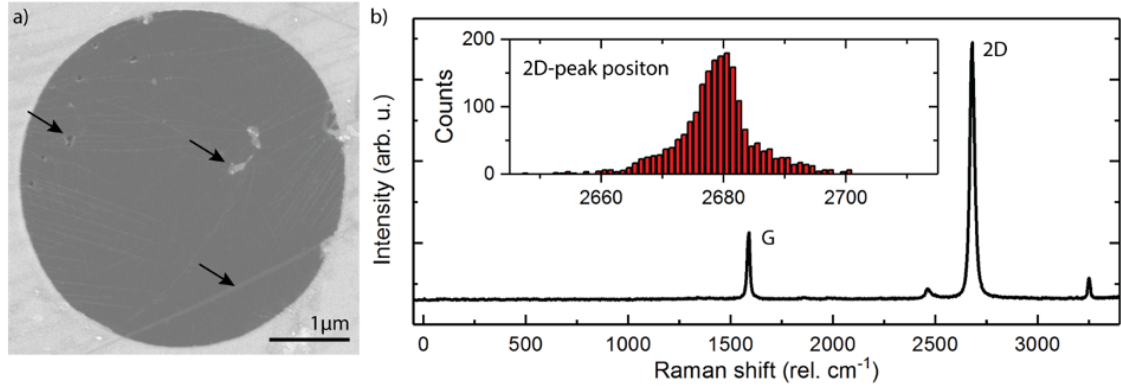
9.8 Conclusion and outlook

We have introduced a method for spatially mapping the thermal conductivity of single-layer graphene using a combination of Raman spectroscopy and finite-element calculations at ultimate resolution. We anticipate that this method can be applied to other single- and few-layer materials. We applied the method to obtain the thermal conductivity of a pristine and He⁺-ion patterned suspended single-layer graphene film. For the unpatterned film, large variations of the extracted thermal conductivity are observed and attributed to local irregularities such as contamination, defects, or folds. These findings highlight the importance of spatial mapping of the thermal conductivity, in contrast to measurement approaches that yield a thermal conductivity averaged across the entire sample. On the patterned membrane, we demonstrate controlled engineering of the thermal conductivity by He⁺-ion irradiation. As Raman spectroscopy is widely used in the two-dimensional materials community, our method is ideally suited to study the thermal properties of other layered materials. Moreover, the working principle of the FEM method can easily be extended to more complex geometries or interfaces, in particular, combined with alternative measurement techniques for providing a temperature map. Our method enables spatially resolving the thermal conductivity of atomically thin materials, a prerequisite for optimizing and engineering thermal stewardship in nanoscale devices.

We have also shown that Raman datasets acquired on precisely patterned nanostructures can form an ideal benchmark for testing unsupervised machine learning algorithms. Such machine learning approaches can reveal substructures, hidden even for the trained and experienced observer. It further facilitates the data interpretation and removes a big portion of the human bias to data treatment. This gives hope that novel insights in experiments with large data sets can be gained from approaches as introduced here.

Appendix 9.A. Raman spectra of pristine and defect engineered graphene

Pristine graphene membrane



Defect engineered graphene membrane

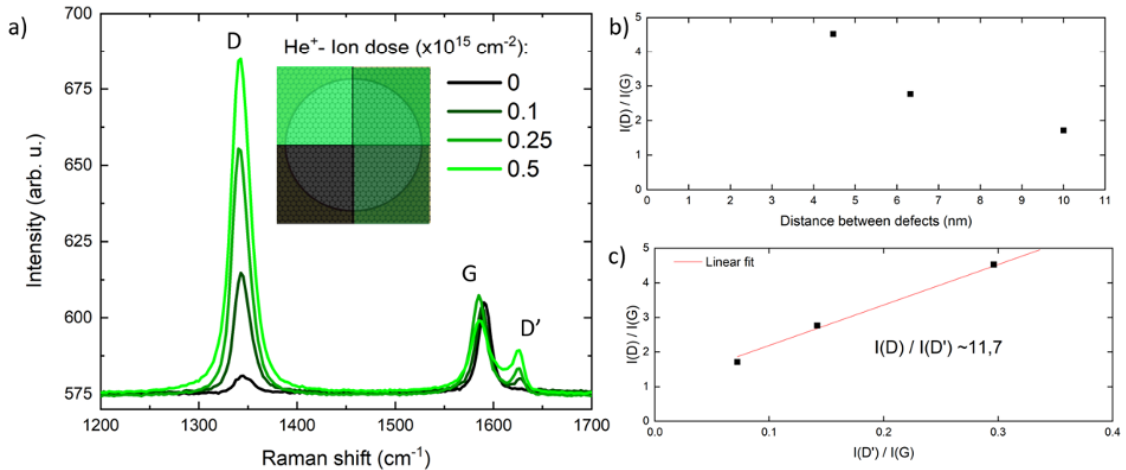


Figure 9.9 Raman spectra graphene membranes. **Top row:** pristine graphene membrane. **a)** Scanning electron micrograph of a representative suspended graphene membrane. Arrows indicate defects (holes, contaminations, folds). **b)** Representative Raman spectra in the center of the same graphene membrane. The typical Raman bands, G and 2D, are labeled. The absence of the D-band indicates high graphene quality. The inset shows a histogram of fitted 2D-peak positions of Raman spectra obtained from a spatial 2D-mapping of the same device. The spread in 2D-peak position is attributed to different levels of strain, doping or defects. **Bottom row:** Defect engineered graphene membrane. **a)** Raman spectra of He⁺-ion irradiated suspended graphene. The inset shows the He⁺-ion doses on the membrane. **b)** Intensity ratio $I(D)/I(G)$ at different average distances between defects. **c)** Intensity ratio $I(D)/I(G)$ versus $I(D')/I(G)$ leads to $I(D)/I(D')$ of ~ 11.7 .

Appendix 9.B. Laser power and absorption

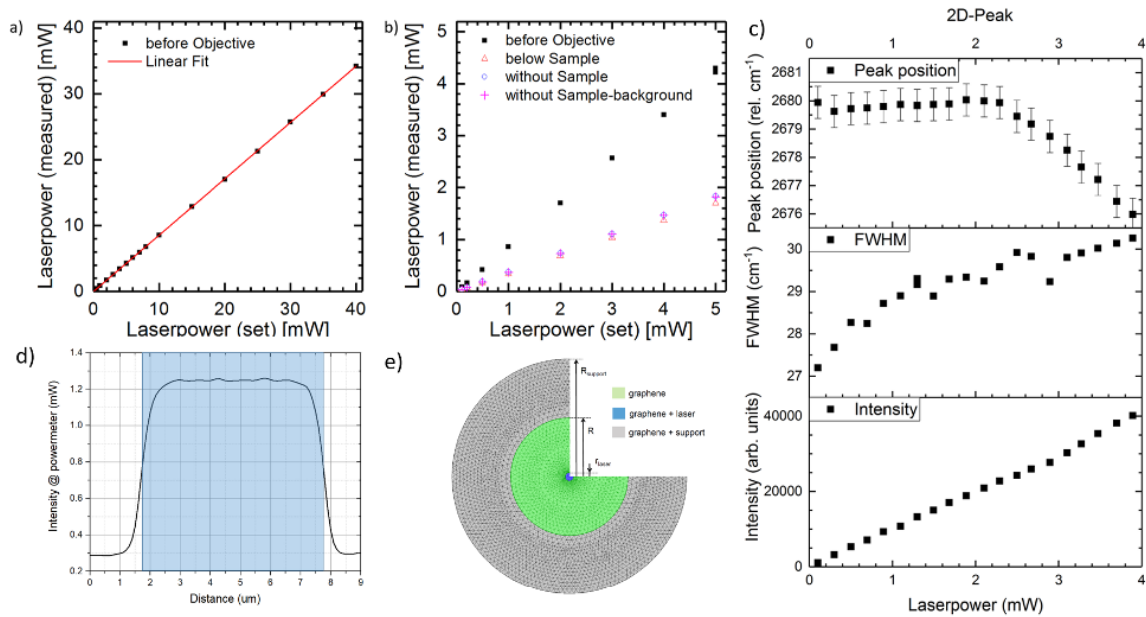


Figure 9.10 Influence of laser power. a) Correlation between set and measured laser power before the objective. b) Measured laser power at different positions in the experimental setup. c) 2D peak evolution for different laser powers. Peak properties extracted from Lorentz fit to the spectra. Spectra taken with a grating of 1800 g/mm. d) Measured laser power below sample while performing line scan over sample. In blue the hole size in the SiN membrane is indicated. e) Geometry used for finite element calculations. Graphene, where suspended/supported, is indicated in green/gray respectively. The position of the laser spot is indicated with blue. The mesh used for finite element calculations is indicated with thin black triangles.

Appendix 9.C. Laser spot size, beam profile and FEM parameters

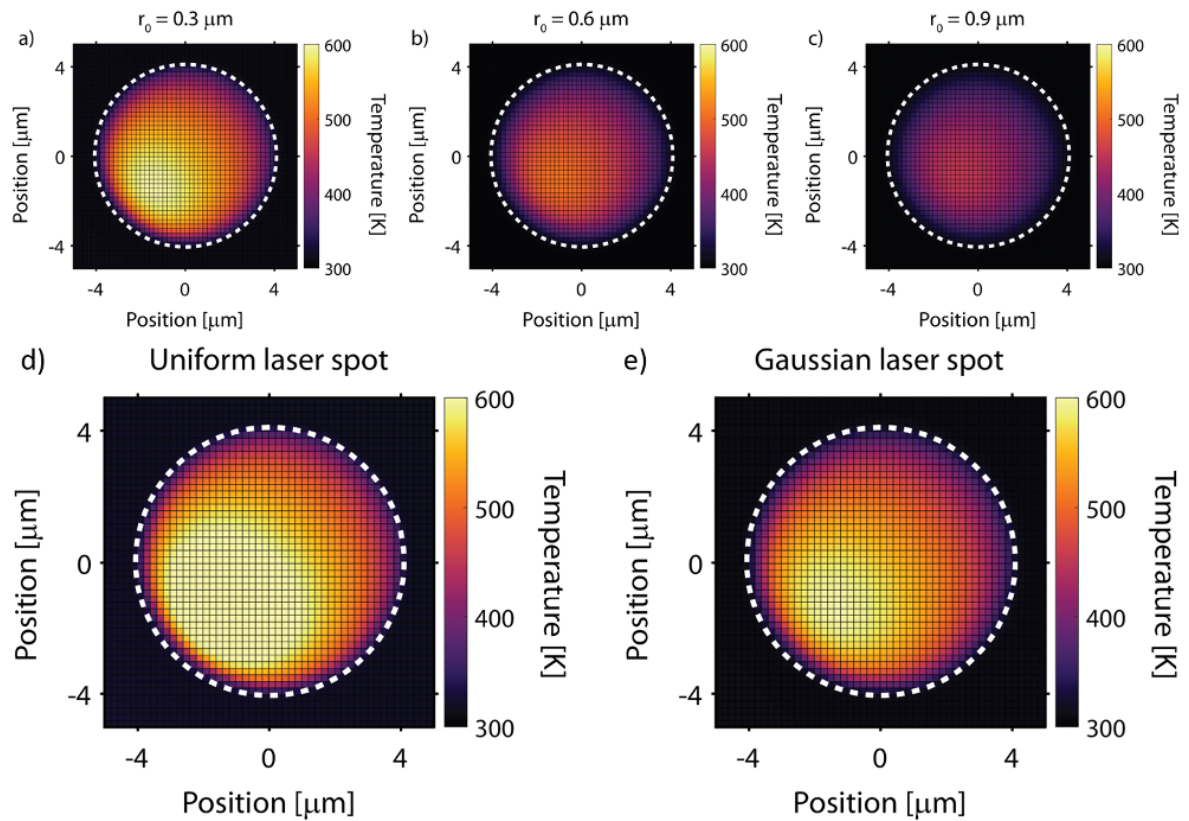


Figure 9.11 Influence of laser spot size and beam profile. a)-c) Influence of spot size in calculations. d) and e) Constructed temperature map upon illumination for comparing a Gaussian and uniform beam profile.

Parameter	short	unit	value
Radius of suspended graphene	R	um	3.5
Radius of supported graphene	R_{supp}	um	8
Radius of beam spot	r_0	nm	300
Thickness of graphene	t_{gr}	nm	0.353
Absorbed laser power	Q_{abs}	mW	4
Ambient temperature	T_0	K	298
Convection coefficient graphene to air	h_{conv}	$\text{Wm}^{-2}\text{K}^{-1}$	2.9×10^4
Interface thermal conductance between graphene and Au/Si ₃ N ₄ substrate	g	$\text{Wm}^{-2}\text{K}^{-1}$	2.8×10^7
Comsol Multiphysics adaptive mesh	-	tetrahedrall	

Table 9.1 Parameters used in finite element calculations

Appendix 9.D. Validation of method

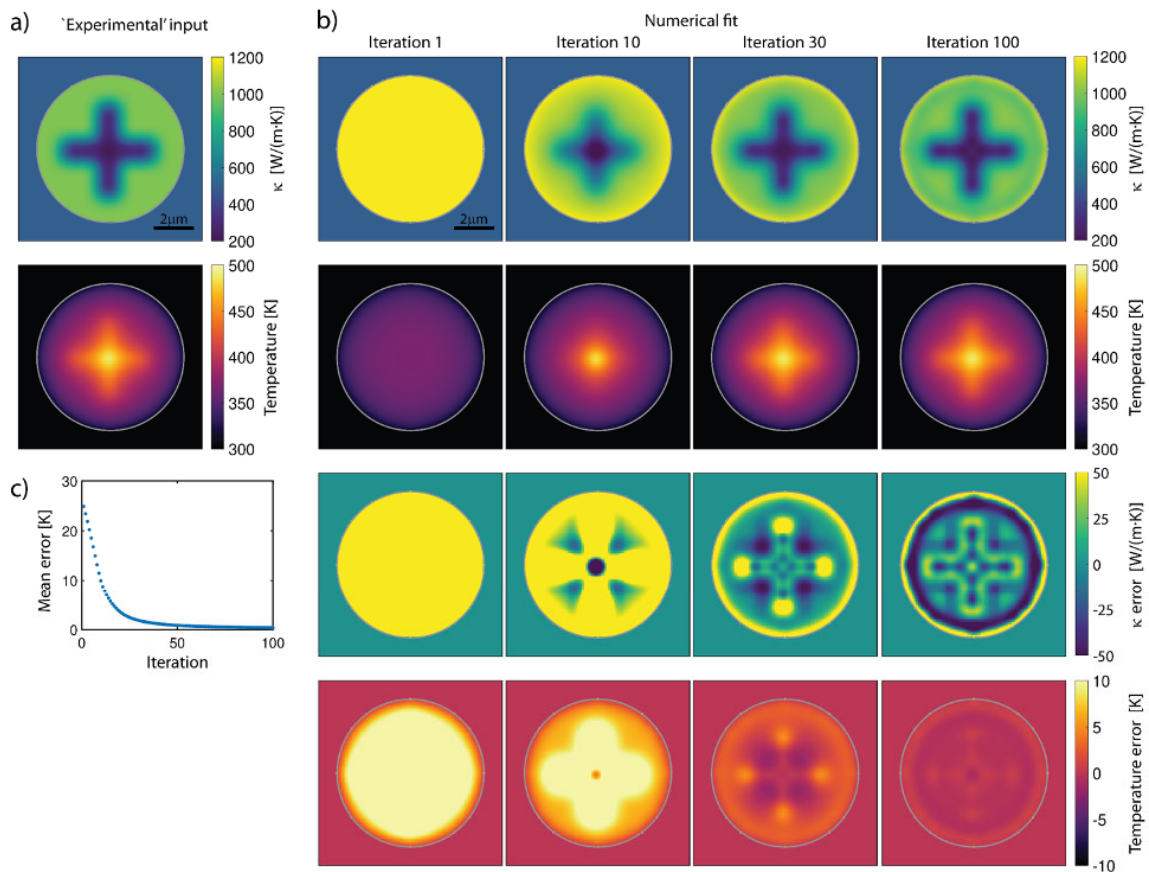


Figure 9.12 Validation of method. Demonstration of iterative calculation procedure in order to obtain a map of the thermal conductivity of defect engineered graphene.

We validate our numerical method on a simulated system with a known thermal conductivity map, as shown in Fig. 9.12a). The thermal conductivity of the suspended

graphene is set to $1000 \text{ Wm}^{-1}\text{K}^{-1}$, while only $500 \text{ Wm}^{-1}\text{K}^{-1}$ is used on the support. In the center of the membrane, a cross of low thermal conductivity values is defined. The temperature map upon illumination is also shown in the left panel, in which the cross in low conductivity values results in a cross of high temperatures. This temperature map will be fit using our iterative approach.

The procedure starts with a uniform distribution of the thermal conductivity. For each iteration, the induced temperature is calculated, as well as the error between the 'experimental' map and the calculated map. The error is used to adjust the thermal conductivity. For a series of iterations, the thermal conductivity, calculated temperature, and temperature error are shown in Fig. 9.12. For an increasing number of iterations, the original cross is steadily recovered in the thermal conductivity map, although with rounded edges, an effect that is attributed to the convolution of the thermal conductivity map with the Gaussian beam distribution. At the same time, the temperature error map is being monitored, with the mean temperature error shown in Fig. 9.12c).

10 Conclusion & outlook

This dissertation entitled *Thermoelectric Effects in Nanoscale Devices* describes the results of a Ph.D. project with the aim to fabricate and investigate devices based on nanomaterials. Thermoelectric materials generate electricity from temperature gradients. To quantify their efficiency, three main aspects have to be considered: the electrical and thermal transport as well as the Seebeck effect. All these aspects have been investigated throughout this work.

10.1 Results and conclusions

First, the basic concepts, materials and methods were elaborated in Chapters 2 and 3. We introduced the fundamentals of charge transport and thermoelectricity as well as thermal transport. We emphasize the interplay of these three aspects and discuss measurement techniques to quantify them in nanoscale objects. A strong focus is given to the introduction of bottom-up synthesized graphene nanoribbons, which are the basic material system under investigation in this thesis.

Next, we turn towards the investigation of charge transport properties of GNRs with a variety of edge and width structures. The characterization of GNRs outside of ultra-high vacuum conditions has only recently begun and therefore is still at a very early stage of adoption. A particular challenge is to make reliable contacts to these nano objects. In Chapter 4 an optimized procedure to fabricate graphene electrodes for contacting GNRs is presented. The procedure uses standard top-down processes at their limits to make graphene electrodes separated by down to <15 nm. Additionally, we show that a final thermal annealing step drastically improves the device performance in 9-AGNR-FETs due to local rearrangements and residue removal. In Chapter 5, these newly developed graphene electrodes serve as a platform to probe charge transport in GNRs of various widths and edge structures. In cases where the GNRs are shorter than 15 nm we use graphene electrodes separated by only a few nanometers, formed by applying the electric breakdown procedure. After transferring films of GNRs, we find that hopping of charge carriers can occur over distances several times longer than the average GNR lengths. This effect is studied as a function of GNR density and temperature, revealing strong charging effects.

In devices with a small electrode separation, we found that at room temperature this film behavior dominates the charge transport as well. However, at low temperatures, Coulomb blockade, and single-electron tunneling were observed in these devices. This proved that it is possible to contact a (few) GNR(s) using graphene electrodes. Although their aspect ratio points towards 1D objects, GNRs behave electronically like 0D objects. For the first time, the device integration of GNRs with partially zigzag-edges in a FET

geometry is realized. This is astonishing since the zigzag edges are much more reactive than their armchair counterparts. The particular edge structure of these pyrene-based GNRs gives rise to a very low band gap with electronic states near a topological phase boundary. In Chapter 6 we extend the standard FET geometry by multiple gates, allowing the graphene electrodes and the GNR channel to be independently gated. Preliminary results on such devices are presented, showing the formation of multiple quantum dots in 9-AGNRs at low temperatures and differential gating thereof. This advanced gating architecture is promising to fully unleash the potential of GNR based devices. Besides advanced gating architectures, the contacts play an important role to achieve this. We investigate the contacts to GNRs in Chapter 7. There we apply the in the graphene community well-established edge-contacting technique to encapsulated GNRs. This undertaking is highly challenging since the etching process of the top-hBN geometrically limits the minimum channel length. First, results show that it is possible to establish electrical contact to the GNRs, and at room temperature, hopping transport is present while at low temperatures thermionic emission is the main charge transport mechanism.

After that, we extended the electrical measurements on GNR based devices by a thermoelectrical characterization. In Chapter 8, we report on the first measurements of the Seebeck coefficient of films of GNRs, namely 9-AGNRs and 17-AGNRs. We found astonishingly high values of up to $2000 \mu\text{V}/\text{K}$. These measurements were carried out in a thermocurrent, rather than thermovoltage, measurement scheme, therefore have to be taken with a pinch of salt and will need further confirmation and control measurements to exclude any contributing effects from other thermoelectric effects like the Peltier effect and/or Thomson effect, or being caused by thermovoltages that build up at the metal/graphene electrode interface. The presented results are encouraging and hold the potential for impacting the field of nanoscale thermoelectricity.

Finally, Chapter 9 presents a novel approach to map the thermal conductivity. The developed method is based on a temperature profile, measured using Raman spectroscopy that is then iteratively evaluated using a finite-element methods fitting procedure. We demonstrate the working principle by mapping the thermal conductivity of pristine and defect-engineered graphene. This is of high interest in the context of thermal management, e.g. for thermal diodes. The method is extendable to other systems such as films of GNRs.

To conclude, we have investigated all three aspects of the thermoelectric figure of merit. This by investigating contacting approaches to GNRs, revealing the potential of graphene electrodes for GNR based electronic devices and fundamental investigation of GNRs. The first-of-its-kind measurements of Seebeck coefficients of GNRs are highly encouraging for further investigation from both a fundamental research and a technological point of view. Mapping thermal conductivity is certainly an important tool for optimizing and engineering thermal stewardship in nanoscale devices.

10.2 Outlook

Bottom-up synthesized graphene nanoribbons will serve as a capable platform for novel physical phenomena. This due to the increasing variety of width and edge structures.²⁹⁷

Contacting these nano objects remains a challenging task. The presented contacting approaches using graphene electrodes have shown that major improvements can be achieved by using advanced gating geometries or thermal annealing. Further, an encapsulation of the GNRs is possible but certainly limited to GNRs of sufficient length constrained by the top-hBN and etching profile. The developed scalable contacting platforms allow future investigation of GNRs with topologically protected modes.^{17,18,118} Material systems exhibiting such modes are believed to be a key building block for the realization of a scalable quantum computer. However, for the near term future, contact resistances play a dominating role and should be further investigated. To tackle this, contact electrodes out of semimetals like e.g. bismuth could lead to further improvements as it has been shown for MoS₂ recently.²⁹⁸

The experimental thermoelectric characterization of GNRs is reported for the first time in this Ph.D. thesis. Therefore, it needs careful cross-validation and will certainly be discussed by the thermoelectricity community. One of these further control measurements will be to verify the results using direct measurements of the thermovoltage with improved electronic equipment. Certainly, a detailed investigation of the contribution of the Peltier and Thomson effect will be needed. Further, it will be exciting to see how the edge structure of the GNRs influences the Seebeck coefficient of GNR based devices. To boost the zT of GNRs, it could be very interesting to investigate GNRs with changing width along their axis, this could lead to an enhanced phonon scattering while keeping the electrical and thermoelectrical properties unaffected.

Mapping thermal conductivity is certainly of great interest in existing and novel nanoscale devices. In particular since the in Chapter 9 presented method is applicable to other methods that record a temperature profile, it shows a certain universality.

Overall, the investigation of thermoelectric effects in nanoscale devices is a broad topic that covers a variety of fields, from advanced nano fabrication over charge transport to thermal transport. The findings in this thesis will certainly accelerate the implementation of GNRs into devices and has hopefully convinced the reader that by starting from molecules one can generate even more exciting nano objects, the GNRs!

Bibliography

- ¹ Shell International BV. World Energy Model - A view to 2100. pages 1–32, 2017.
- ² International Energy Agency. Energy Technology Perspectives 2020 - Special Report on Clean Energy Innovation. 2020.
- ³ S. Carnot. Réflexions sur la puissance motrice du feu et sur les machines propres à développer cette puissance. *Annales de l'Ecole Normale*, 2e Série(Tome 1.):393–457, 1824.
- ⁴ T. J. Seebeck. Magnetische Polarisation der Metalle und Erze durch Temperatur-Differenz. *Abhandlungen der Koeniglichen Akademie der Wissenschaften zu Berlin.*, 1822.
- ⁵ G. J. Snyder and A. H. Snyder. Figure of merit ZT of a thermoelectric device defined from materials properties. *Energy & Environmental Science*, 10(11):2280–2283, 2017. doi: 10.1039/C7EE02007D.
- ⁶ National Aeronautics and Space Administration. Multi-Mission Radioisotope Thermoelectric Generator (MMRTG). 2020.
- ⁷ C. B. Vining. An inconvenient truth about thermoelectrics. *Nature materials*, 8(2):83–85, 2009. doi: 10.1038/nmat2361.
- ⁸ L. D. Hicks and M. S. Dresselhaus. Effect of quantum-well structures on the thermoelectric figure of merit. *Physical Review B*, 47(19):12727, 1993.
- ⁹ L. D. Hicks and M. S. Dresselhaus. Thermoelectric figure of merit of a one-dimensional conductor. *Physical Review B*, 47(24):16631, 1993.
- ¹⁰ D. Gunlycke, H. M. Lawler, and C. T. White. Room-temperature ballistic transport in narrow graphene strips. *Physical Review B*, 75(8):1704, 2007. doi: 10.1103/PhysRevB.75.085418.
- ¹¹ C. Stampfer, J. Güttinger, S. Hellmüller, F. Molitor, K. Ensslin, and T. Ihn. Energy gaps in etched graphene nanoribbons. *Physical review letters*, 102(5):056403, 2009. doi: 10.1103/PhysRevLett.102.056403.
- ¹² P. Ruffieux, J. Cai, N. C. Plumb, L. Patthey, D. Prezzi, A. Ferretti, E. Molinari, X. Feng, K. Müllen, C. A. Pignedoli, and R. Fasel. Electronic structure of atomically precise graphene nanoribbons. *ACS nano*, 6(8):6930–6935, 2012. doi: 10.1021/nn3021376.
- ¹³ J. P. Llinas, A. Fairbrother, G. Borin Barin, W. Shi, K. Lee, S. Wu, B. Yong Choi, R. Braganza, J. Lear, N. Kau, W. Choi, C. Chen, Z. Pedramrazi, T. Dumslaff, A. Narita, X. Feng, K. Müllen, F. Fischer, A. Zettl, P. Ruffieux, E. Yablonovitch, M. Crommie, R. Fasel, and J. Bokor. Short-channel field-effect transistors with 9-atom and 13-atom wide graphene nanoribbons. *Nature communications*, 8(1):633, 2017. doi: 10.1038/s41467-017-00734-x.

- ¹⁴ J. Cai, C. A. Pignedoli, L. Talirz, P. Ruffieux, H. Söde, L. Liang, V. Meunier, R. Berger, R. Li, X. Feng, K. Müllen, and R. Fasel. Graphene nanoribbon heterojunctions. *Nature nanotechnology*, 9(11):896–900, 2014. doi: 10.1038/nnano.2014.184.
- ¹⁵ M. El Abbassi, M. L. Perrin, G. B. Barin, S. Sangtarash, J. Overbeck, O. Braun, C. J. Lambert, Q. Sun, T. Prechtel, A. Narita, K. Müllen, P. Ruffieux, H. Sadeghi, R. Fasel, and M. Calame. Controlled Quantum Dot Formation in Atomically Engineered Graphene Nanoribbon Field-Effect Transistors. *ACS nano*, 14(5):5754–5762, 2020. doi: 10.1021/acsnano.0c00604.
- ¹⁶ T. Cao, F. Zhao, and S. G. Louie. Topological Phases in Graphene Nanoribbons: Junction States, Spin Centers, and Quantum Spin Chains. *Physical review letters*, 119(7):076401, 2017. doi: 10.1103/PhysRevLett.119.076401.
- ¹⁷ D. J. Rizzo, G. Veber, T. Cao, C. Bronner, T. Chen, F. Zhao, H. Rodriguez, S. G. Louie, M. F. Crommie, and F. R. Fischer. Topological band engineering of graphene nanoribbons. *Nature*, 560(7717):204–208, 2018. doi: 10.1038/s41586-018-0376-8.
- ¹⁸ O. Gröning, S. Wang, X. Yao, C. A. Pignedoli, G. B. Barin, C. Daniels, A. Cupo, V. Meunier, X. Feng, A. Narita, K. Müllen, P. Ruffieux, and R. Fasel. Engineering of robust topological quantum phases in graphene nanoribbons. *Nature*, 560(7717):209–213, 2018. doi: 10.1038/s41586-018-0375-9.
- ¹⁹ Q. Sun, X. Yao, O. Gröning, K. Eimre, C. A. Pignedoli, K. Müllen, A. Narita, R. Fasel, and P. Ruffieux. Coupled Spin States in Armchair Graphene Nanoribbons with Asymmetric Zigzag Edge Extensions. *Nano letters*, 20(9):6429–6436, 2020. doi: 10.1021/acs.nanolett.0c02077.
- ²⁰ L. Wang, I. Meric, P. Y. Huang, Q. Gao, Y. Gao, H. Tran, T. Taniguchi, K. Watanabe, L. M. Campos, D. A. Muller, J. Guo, P. Kim, J. C. Hone, K. L. Shepard, and C. R. Dean. One-dimensional electrical contact to a two-dimensional material. *Science*, 342(6158):614–617, 2013. doi: 10.1126/science.1244358.
- ²¹ A. Jorio, R. Saito, G. Dresselhaus, and M. S. Dresselhaus. *Raman spectroscopy in graphene related systems*. Wiley-VCH, Weinheim, 2011. ISBN 9783527632701. doi: 10.1002/9783527632695. URL <http://site.ebrary.com/lib/alltitles/docDetail.action?docID=10510381>.
- ²² F. Banhart, J. Kotakoski, and A. V. Krasheninnikov. Structural defects in graphene. *ACS nano*, 5(1):26–41, 2011. doi: 10.1021/nn102598m.
- ²³ C. Nef, L. Pósa, P. Makk, W. Fu, A. Halbritter, C. Schönenberger, and M. Calame. High-yield fabrication of nm-size gaps in monolayer CVD graphene. *Nanoscale*, 6(13):7249–7254, 2014. doi: 10.1039/c4nr01838a.
- ²⁴ K. S. Novoselov, A. K. Geim, S. V. Morozov, D. Jiang, Y. Zhang, S. V. Dubonos, I. V. Grigorieva, and A. A. Firsov. Electric field effect in atomically thin carbon films. *Science*, 306(5696):666–669, 2004. doi: 10.1126/science.1102896.
- ²⁵ A. K. Geim and K. S. Novoselov. The rise of graphene. *Nature materials*, 6:183–191, 2007. doi: 10.1038/nmat1849.

- ²⁶ F. Prins, A. Barreiro, J. W. Ruitenber, J. S. Seldenthuis, N. Aliaga-Alcalde, L. M. K. Vandersypen, and H. S. J. van der Zant. Room-temperature gating of molecular junctions using few-layer graphene nanogap electrodes. *Nano letters*, 11(11):4607–4611, 2011. doi: 10.1021/nl202065x.
- ²⁷ G. S. Kliros. *Graphene Science Handbook: Size-dependent properties; Chapter: Quantum Capacitance of Graphene Sheets and Nanoribbons*. CRC Press, 2016.
- ²⁸ E. Lörtscher. Wiring molecules into circuits. *Nature nanotechnology*, 8(6):381–384, 2013. doi: 10.1038/nnano.2013.105.
- ²⁹ P. Gehring, J. K. Sowa, J. Cremers, Q. Wu, H. Sadeghi, Y. Sheng, J. H. Warner, C. J. Lambert, G. A. D. Briggs, and J. A. Mol. Distinguishing Lead and Molecule States in Graphene-Based Single-Electron Transistors. *ACS nano*, 11(6):5325–5331, 2017. doi: 10.1021/acsnano.7b00570.
- ³⁰ M. El Abbassi, S. Sangtarash, X. Liu, M. L. Perrin, O. Braun, C. Lambert, H. S. J. van der Zant, S. Yitzchaik, S. Decurtins, S.-X. Liu, H. Sadeghi, and M. Calame. Robust graphene-based molecular devices. *Nature nanotechnology*, 14(10):957–961, 2019. doi: 10.1038/s41565-019-0533-8.
- ³¹ Y.-W. Son, M. L. Cohen, and S. G. Louie. Energy Gaps in Graphene Nanoribbons. *Physical review letters*, 97(21):216803, 2006. doi: 10.1103/PhysRevLett.97.216803.
- ³² V. Barone, O. Hod, and G. E. Scuseria. Electronic structure and stability of semiconducting graphene nanoribbons. *Nano letters*, 6(12):2748–2754, 2006. doi: 10.1021/nl0617033.
- ³³ P. Jarillo-Herrero, S. Sapmaz, C. Dekker, L. P. Kouwenhoven, and H. S. J. van der Zant. Electron-hole symmetry in a semiconducting carbon nanotube quantum dot. *Nature*, 429(6990):389–392, 2004. doi: 10.1038/nature02568.
- ³⁴ S. Sapmaz, P. Jarillo-Herrero, L. P. Kouwenhoven, and H. S. J. van der Zant. Quantum dots in carbon nanotubes. *Semiconductor Science and Technology*, 21(11):S52–S63, 2006. doi: 10.1088/0268-1242/21/11/S08.
- ³⁵ A. Donarini, M. Niklas, M. Schafberger, N. Paradiso, C. Strunk, and M. Grifoni. Coherent population trapping by dark state formation in a carbon nanotube quantum dot. *Nature communications*, 10(1):381, 2019. doi: 10.1038/s41467-018-08112-x.
- ³⁶ L. P. Kouwenhoven, D. G. Austing, and S. Tarucha. Few-electron quantum dots. *Reports on Progress in Physics*, 64(6):701–736, 2001.
- ³⁷ T. Ihn. *Semiconductor nanostructures: Quantum states and electronic transport*. Oxford University Press, Oxford and New York, 2010. ISBN 9780199534432.
- ³⁸ J. B. Gramich. *Andreev and Spin Transport in Carbon Nanotube Quantum Dot Hybrid Devices*. PhD thesis, University of Basel, 2016.
- ³⁹ E. Lörtscher, J. W. Ciszek, J. Tour, and H. Riel. Reversible and controllable switching of a single-molecule junction. *Small*, 2(8-9):973–977, 2006. doi: 10.1002/smll.200600101.

- ⁴⁰ F. Schwarz, G. Kastlunger, F. Lissel, C. Egler-Lucas, S. N. Semenov, K. Venkatesan, H. Berke, R. Stadler, and E. Lörtscher. Field-induced conductance switching by charge-state alternation in organometallic single-molecule junctions. *Nature nanotechnology*, 11(2): 170–176, 2016. doi: 10.1038/nnano.2015.255.
- ⁴¹ A. Batra, P. Darancet, Q. Chen, J. S. Meisner, J. R. Widawsky, J. B. Neaton, C. Nuckolls, and L. Venkataraman. Tuning rectification in single-molecular diodes. *Nano letters*, 13(12): 6233–6237, 2013. doi: 10.1021/nl403698m.
- ⁴² C. Joachim and G. Rapenne. Molecule concept nanocars: chassis, wheels, and motors? *ACS nano*, 7(1):11–14, 2013. doi: 10.1021/nn3058246.
- ⁴³ L. Venkataraman, J. E. Klare, C. Nuckolls, M. S. Hybertsen, and M. L. Steigerwald. Dependence of single-molecule junction conductance on molecular conformation. *Nature*, 442(7105):904–907, 2006. doi: 10.1038/nature05037.
- ⁴⁴ S. Ayissi, P. A. Charpentier, N. Farhangi, J. A. Wood, K. Palotás, and W. A. Hofer. Interaction of Titanium Oxide Nanostructures with Graphene and Functionalized Graphene Nanoribbons: A DFT Study. *The Journal of Physical Chemistry C*, 117(48):25424–25432, 2013. ISSN 1932-7447. doi: 10.1021/jp403835m.
- ⁴⁵ D. Krepel and O. Hod. Effects of Edge Oxidation on the Structural, Electronic, and Magnetic Properties of Zigzag Boron Nitride Nanoribbons. *Journal of chemical theory and computation*, 10(1):373–380, 2014. doi: 10.1021/ct400882q.
- ⁴⁶ J. D. Thomsen, J. Kling, D. M. A. Mackenzie, P. Bøggild, and T. J. Booth. Oxidation of Suspended Graphene: Etch Dynamics and Stability Beyond 1000 °C. *ACS nano*, 13(2): 2281–2288, 2019. doi: 10.1021/acsnano.8b08979.
- ⁴⁷ S. L. Kawahara, J. Lagoute, V. Repain, C. Chacon, Y. Girard, S. Rousset, A. Smogunov, and C. Barreateau. Large magnetoresistance through a single molecule due to a spin-split hybridized orbital. *Nano letters*, 12(9):4558–4563, 2012. doi: 10.1021/nl301802e.
- ⁴⁸ B. Kretz, D. A. Egger, and E. Zojer. A Toolbox for Controlling the Energetics and Localization of Electronic States in Self-Assembled Organic Monolayers. *Advanced science*, 2(3):1400016, 2015. doi: 10.1002/advs.201400016.
- ⁴⁹ H. Song, J. Liu, B. Liu, J. Wu, H.-M. Cheng, and F. Kang. Two-Dimensional Materials for Thermal Management Applications. *Joule*, 2(3):442–463, 2018. ISSN 25424351. doi: 10.1016/j.joule.2018.01.006.
- ⁵⁰ G. S. Nolas, J. Sharp, and J. Goldsmid. *Thermoelectrics: basic principles and new materials developments*, volume 45. Springer Science & Business Media, 2013.
- ⁵¹ C. Goupil. *Continuum theory and modeling of thermoelectric elements*. John Wiley & sons, 2015.
- ⁵² Y.-S. Liu and Y.-C. Chen. Seebeck coefficient of thermoelectric molecular junctions: First-principles calculations. *Physical Review B*, 79(19), 2009. doi: 10.1103/PhysRevB.79.193101.
- ⁵³ P. Butti, R. Brönnimann, K. Ensslin, and I. Shorubalko. Joule-heating induced thermal voltages in graphene three-terminal nanojunctions. *Applied Physics Letters*, 112(13):133501, 2018. ISSN 0003-6951. doi: 10.1063/1.5022962.

- ⁵⁴ J. C. A. Peltier. *Nouvelles expériences sur la caloricit  des courans  lectriques*. Paris, Crochard, 1834.
- ⁵⁵ W. Thomson. 4. On a Mechanical Theory of Thermo-Electric Currents. *Proceedings of the Royal Society of Edinburgh*, 3:91–98, 1857. doi: 10.1017/S0370164600027310.
- ⁵⁶ baron de Fourier, Jean Baptiste Joseph. *Th orie analytique de la chaleur*. Firmin Didot, 1822.
- ⁵⁷ A. A. Balandin, S. Ghosh, W. Bao, I. Calizo, D. Teweldebrhan, F. Miao, and C. N. Lau. Superior thermal conductivity of single-layer graphene. *Nano letters*, 8(3):902–907, 2008. doi: 10.1021/nl0731872.
- ⁵⁸ S. Chen, Q. Wu, C. Mishra, J. Kang, H. Zhang, K. Cho, W. Cai, A. A. Balandin, and R. S. Ruoff. Thermal conductivity of isotopically modified graphene. *Nature materials*, 11(3):203–207, 2012. doi: 10.1038/nmat3207.
- ⁵⁹ J. S. Reparaz, E. Chavez-Angel, M. R. Wagner, B. Graczykowski, J. Gomis-Bresco, F. Alzina, and C. M. Sotomayor Torres. A novel contactless technique for thermal field mapping and thermal conductivity determination: two-laser Raman thermometry. *The Review of scientific instruments*, 85(3):034901, 2014. doi: 10.1063/1.4867166.
- ⁶⁰ M. Soini, I. Zardo, E. Uccelli, S. Funk, G. Koblm ller, A. Fontcuberta i Morral, and G. Abstreiter. Thermal conductivity of GaAs nanowires studied by micro-Raman spectroscopy combined with laser heating. *Applied Physics Letters*, 97(26):263107, 2010. doi: 10.1063/1.3532848.
- ⁶¹ G. S. Doerk, C. Carraro, and R. Maboudian. Single nanowire thermal conductivity measurements by Raman thermography. *ACS nano*, 4(8):4908–4914, 2010. doi: 10.1021/nm1012429.
- ⁶² M. Y. Swinkels, A. Campo, D. Vakulov, W. Kim, L. Gagliano, S. E. Steinvall, H. Detz, M. de Luca, A. Lugstein, E. Bakkers, A. Fontcuberta i Morral, and I. Zardo. Measuring the Optical Absorption of Single Nanowires. *Physical Review Applied*, 14(2), 2020. doi: 10.1103/PhysRevApplied.14.024045.
- ⁶³ C. C. Williams and H. K. Wickramasinghe. Scanning thermal profiler. *Applied Physics Letters*, 49(23):1587–1589, 1986. doi: 10.1063/1.97288.
- ⁶⁴ L. Cui, W. Jeong, S. Hur, M. Matt, J. C. Kl ckner, F. Pauly, P. Nielaba, J. C. Cuevas, E. Meyhofer, and P. Reddy. Quantized thermal transport in single-atom junctions. *Science*, 355(6330):1192–1195, 2017. doi: 10.1126/science.aam6622.
- ⁶⁵ L. Cui, S. Hur, Z. A. Akbar, J. C. Kl ckner, W. Jeong, F. Pauly, S.-Y. Jang, P. Reddy, and E. Meyhofer. Thermal conductance of single-molecule junctions. *Nature*, 572:628–633, 2019. doi: 10.1038/s41586-019-1420-z.
- ⁶⁶ K. Kim, W. Jeong, W. Lee, and P. Reddy. Ultra-high vacuum scanning thermal microscopy for nanometer resolution quantitative thermometry. *ACS nano*, 6(5):4248–4257, 2012. doi: 10.1021/nm300774n.

- ⁶⁷ F. Menges, P. Mensch, H. Schmid, H. Riel, A. Stemmer, and B. Gotsmann. Temperature mapping of operating nanoscale devices by scanning probe thermometry. *Nature communications*, 7:10874, 2016. doi: 10.1038/ncomms10874.
- ⁶⁸ F. Könemann, M. Vollmann, T. Wagner, N. Mohd Ghazali, T. Yamaguchi, A. Stemmer, K. Ishibashi, and B. Gotsmann. Thermal Conductivity of a Supported Multiwalled Carbon Nanotube. *The Journal of Physical Chemistry C*, 123(19):12460–12465, 2019. doi: 10.1021/acs.jpcc.9b00692.
- ⁶⁹ A. Harzheim, C. Evangeli, O. V. Kolosov, and P. Gehring. Direct mapping of local Seebeck coefficient in 2D material nanostructures via scanning thermal gate microscopy. *2D Materials*, 7(4):041004, 2020. doi: 10.1088/2053-1583/aba333.
- ⁷⁰ D. G. Cahill and R. O. Pohl. Thermal conductivity of amorphous solids above the plateau. *Physical Review B*, 35(8):4067–4073, 1987.
- ⁷¹ D. G. Cahill. Thermal conductivity measurement from 30 to 750 K: the 3 omega method. *Review of Scientific Instruments*, 61(2):802–808, 1990. ISSN 0034-6748. doi: 10.1063/1.1141498.
- ⁷² D. G. Cahill, M. Katiyar, and J. R. Abelson. Thermal conductivity of a-Si:H thin films. *Physical Review B*, 50(9):6077–6081, 1994.
- ⁷³ T. Tong and A. Majumdar. Reexamining the 3-omega technique for thin film thermal characterization. *Review of Scientific Instruments*, 77(10):104902, 2006. ISSN 0034-6748. doi: 10.1063/1.2349601.
- ⁷⁴ J. P. Heremans, M. S. Dresselhaus, L. E. Bell, and D. T. Morelli. When thermoelectrics reached the nanoscale. *Nature nanotechnology*, 8(7):471–473, 2013. doi: 10.1038/nnano.2013.129.
- ⁷⁵ J.-F. Li, W.-S. Liu, L.-D. Zhao, and M. Zhou. High-performance nanostructured thermoelectric materials. *NPG Asia Materials*, 2(4):152–158, 2010. ISSN 1884-4049. doi: 10.1038/asiamat.2010.138.
- ⁷⁶ D. Narducci. Do we really need high thermoelectric figures of merit? A critical appraisal to the power conversion efficiency of thermoelectric materials. *Applied Physics Letters*, 99(10):102104, 2011. doi: 10.1063/1.3634018.
- ⁷⁷ L. Shi. Thermal and Thermoelectric Transport in Nanostructures and Low-Dimensional Systems. *Nanoscale and Microscale Thermophysical Engineering*, 16(2):79–116, 2012. ISSN 1556-7265. doi: 10.1080/15567265.2012.667514.
- ⁷⁸ J. Baxter, Z. Bian, G. Chen, D. Danielson, M. S. Dresselhaus, A. G. Fedorov, T. S. Fisher, C. W. Jones, E. Maginn, U. Kortshagen, A. Manthiram, A. Nozik, D. R. Rolison, T. Sands, L. Shi, D. Sholl, and Y. Wu. Nanoscale design to enable the revolution in renewable energy. *Energy & Environmental Science*, 2(6):559, 2009. ISSN 1754-5692. doi: 10.1039/b821698c.
- ⁷⁹ R. Franz and G. Wiedemann. Über die Wärme-Leitungsfähigkeit der Metalle. *Annalen der Physik*, 165(8):497–531, 1853.
- ⁸⁰ G. T. Craven and A. Nitzan. Wiedemann-Franz Law for Molecular Hopping Transport. *Nano letters*, 20(2):989–993, 2020. doi: 10.1021/acs.nanolett.9b04070.

- ⁸¹ C. Kittel and P. McEuen. *Introduction to solid state physics*, volume 8. Wiley New York, 1996.
- ⁸² S. Roddaro, D. Ercolani, M. A. Safeen, S. Suomalainen, F. Rossella, F. Giazotto, L. Sorba, and F. Beltram. Giant thermovoltage in single InAs nanowire field-effect transistors. *Nano letters*, 13(8):3638–3642, 2013. doi: 10.1021/nl401482p.
- ⁸³ P. M. Wu, J. Gooth, X. Zianni, S. F. Svensson, J. G. Gluschke, K. A. Dick, C. Thelander, K. Nielsch, and H. Linke. Large thermoelectric power factor enhancement observed in InAs nanowires. *Nano letters*, 13(9):4080–4086, 2013. doi: 10.1021/nl401501j.
- ⁸⁴ G. Fugallo, A. Cepellotti, L. Paulatto, M. Lazzeri, N. Marzari, and F. Mauri. Thermal conductivity of graphene and graphite: collective excitations and mean free paths. *Nano letters*, 14(11):6109–6114, 2014. doi: 10.1021/nl502059f.
- ⁸⁵ A. Cepellotti, G. Fugallo, L. Paulatto, M. Lazzeri, F. Mauri, and N. Marzari. Phonon hydrodynamics in two-dimensional materials. *Nature communications*, 6:6400, 2015. doi: 10.1038/ncomms7400.
- ⁸⁶ M. Simoncelli, N. Marzari, and A. Cepellotti. Generalization of Fourier’s Law into Viscous Heat Equations. *Physical Review X*, 10(1):66, 2020. doi: 10.1103/PhysRevX.10.011019.
- ⁸⁷ C. A. Perroni and G. Benenti. Theoretical approaches for nanoscale thermoelectric phenomena. *arXiv preprint arXiv:2007.01407v1*, (2007.01407v1):1–20, 2020. URL <http://arxiv.org/pdf/2007.01407v1>.
- ⁸⁸ J. W. Overbeck. *Nanojunctions from molecules to graphene nanoribbons: optical characterization and transport properties*. Doctoral Thesis, University of Basel, 2019.
- ⁸⁹ J. Overbeck, G. Borin Barin, C. Daniels, M. L. Perrin, L. Liang, O. Braun, R. Darawish, B. Burkhardt, T. Dumsflaff, X.-Y. Wang, A. Narita, K. Müllen, V. Meunier, R. Fasel, M. Calame, and P. Ruffieux. Optimized Substrates and Measurement Approaches for Raman Spectroscopy of Graphene Nanoribbons. *physica status solidi (b)*, 256(12):1900343, 2019. doi: 10.1002/pssb.201900343.
- ⁹⁰ O. Braun, J. Overbeck, M. El Abbassi, S. Käser, R. Furrer, A. Olziersky, A. Flasby, G. Borin Barin, R. Darawish, K. Müllen, P. Ruffieux, R. Fasel, I. Shorubalko, M. L. Perrin, and M. Calame. Optimized Graphene Electrodes for contacting Graphene Nanoribbons. *arXiv preprint*, arXiv:2102.13033, 2021.
- ⁹¹ C. V. Raman. A new radiation. *Indian Journal of Physics*, 2:387–398, 1928.
- ⁹² C. V. Raman and K. S. Krishnan. The Negative Absorption of Radiation. *Nature*, 122:12–13, 1928. doi: 10.1038/122012b0.
- ⁹³ G. Landsberg and L. Mandelstam. Über die Lichtzerstreuung in Kristallen. *Zeitschrift für Physik*, 50:769–780, 1928. doi: 10.1007/BF01339412.
- ⁹⁴ J. Overbeck, G. B. Barin, C. Daniels, M. L. Perrin, O. Braun, Q. Sun, R. Darawish, M. de Luca, X.-Y. Wang, T. Dumsflaff, A. Narita, K. Müllen, P. Ruffieux, V. Meunier, R. Fasel, and M. Calame. A Universal Length-Dependent Vibrational Mode in Graphene Nanoribbons. *ACS nano*, 13(11):13083–13091, 2019. doi: 10.1021/acsnano.9b05817.

- ⁹⁵ Q. Yu, J. Lian, S. Siriponglert, H. Li, Y. P. Chen, and S.-S. Pei. Graphene segregated on Ni surfaces and transferred to insulators. *Applied Physics Letters*, 93(11):113103, 2008. doi: 10.1063/1.2982585.
- ⁹⁶ L. G. de Arco, Y. Zhang, A. Kumar, and C. Zhou. Synthesis, Transfer, and Devices of Single- and Few-Layer Graphene by Chemical Vapor Deposition. *IEEE Transactions on Nanotechnology*, 8(2):135–138, 2009. ISSN 1536-125X. doi: 10.1109/TNANO.2009.2013620.
- ⁹⁷ A. Reina, X. Jia, J. Ho, D. Nezich, H. Son, V. Bulovic, M. S. Dresselhaus, and J. Kong. Large area, few-layer graphene films on arbitrary substrates by chemical vapor deposition. *Nano letters*, 9(1):30–35, 2009. doi: 10.1021/nl801827v.
- ⁹⁸ K. S. Kim, Y. Zhao, H. Jang, S. Y. Lee, J. M. Kim, K. S. Kim, J.-H. Ahn, P. Kim, J.-Y. Choi, and B. H. Hong. Large-scale pattern growth of graphene films for stretchable transparent electrodes. *Nature*, 457(7230):706–710, 2009. doi: 10.1038/nature07719.
- ⁹⁹ X. Li, W. Cai, J. An, S. Kim, J. Nah, D. Yang, R. Piner, A. Velamakanni, I. Jung, E. Tutuc, S. K. Banerjee, L. Colombo, and R. S. Ruoff. Large-area synthesis of high-quality and uniform graphene films on copper foils. *Science*, 324(5932):1312–1314, 2009. doi: 10.1126/science.1171245. URL 10.1126/science.1171245.
- ¹⁰⁰ K. Thodkar, M. El Abbassi, F. Lüönd, F. Overney, C. Schönenberger, B. Jeanneret, and M. Calame. Comparative study of single and multi domain CVD graphene using large-area Raman mapping and electrical transport characterization. *physica status solidi (RRL)*, 10(11):807–811, 2016. doi: 10.1002/pssr.201600211.
- ¹⁰¹ K. Thodkar, D. Thompson, F. Lüönd, L. Moser, F. Overney, L. Marot, C. Schönenberger, B. Jeanneret, and M. Calame. Restoring the Electrical Properties of CVD Graphene via Physisorption of Molecular Adsorbates. *ACS applied materials & interfaces*, 9(29):25014–25022, 2017. doi: 10.1021/acsami.7b05143.
- ¹⁰² J.-Y. Hong, Y. C. Shin, A. Zubair, Y. Mao, T. Palacios, M. S. Dresselhaus, S. H. Kim, and J. Kong. A Rational Strategy for Graphene Transfer on Substrates with Rough Features. *Advanced materials*, 28(12):2382–2392, 2016. doi: 10.1002/adma.201505527.
- ¹⁰³ J. E. Lee, G. Ahn, J. Shim, Y. S. Lee, and S. Ryu. Optical separation of mechanical strain from charge doping in graphene. *Nature communications*, 3:1024, 2012. doi: 10.1038/ncomms2022.
- ¹⁰⁴ N. Bendiab, J. Renard, C. Schwarz, A. Reserbat-Plantey, L. Djévahirdjian, V. Bouchiat, J. Coraux, and L. Marty. Unravelling external perturbation effects on the optical phonon response of graphene. *Journal of Raman Spectroscopy*, 49(1):130–145, 2018. ISSN 03770486. doi: 10.1002/jrs.5267.
- ¹⁰⁵ F. Schwierz. Graphene transistors. *Nature nanotechnology*, 5(7):487–496, 2010. doi: 10.1038/nnano.2010.89.
- ¹⁰⁶ L. Pósa, M. El Abbassi, P. Makk, B. Sánta, C. Nef, M. Csontos, M. Calame, and A. Halbritter. Multiple Physical Time Scales and Dead Time Rule in Few-Nanometers Sized Graphene-SiO_x-Graphene Memristors. *Nano letters*, 17(11):6783–6789, 2017. doi: 10.1021/acs.nanolett.7b03000.

- ¹⁰⁷ M. El Abbassi, L. Pósa, P. Makk, C. Nef, K. Thodkar, A. Halbritter, and M. Calame. From electroburning to sublimation: substrate and environmental effects in the electrical breakdown process of monolayer graphene. *Nanoscale*, 9(44):17312–17317, 2017. doi: 10.1039/c7nr05348g.
- ¹⁰⁸ S. G. Sarwat, P. Gehring, G. Rodriguez Hernandez, J. H. Warner, G. A. D. Briggs, J. A. Mol, and H. Bhaskaran. Scaling Limits of Graphene Nanoelectrodes. *Nano letters*, 17(6):3688–3693, 2017. doi: 10.1021/acs.nanolett.7b00909.
- ¹⁰⁹ J. G. Simmons. Generalized Formula for the Electric Tunnel Effect between Similar Electrodes Separated by a Thin Insulating Film. *Journal of Applied Physics*, 34(6):1793–1803, 1963. ISSN 0021-8979. doi: 10.1063/1.1702682.
- ¹¹⁰ A. Barreiro, H. S. J. van der Zant, and L. M. K. Vandersypen. Quantum dots at room temperature carved out from few-layer graphene. *Nano letters*, 12(12):6096–6100, 2012. doi: 10.1021/nl3036977.
- ¹¹¹ P. Gehring, A. Harzheim, J. Spièce, Y. Sheng, G. Rogers, C. Evangeli, A. Mishra, B. J. Robinson, K. Porfyakis, J. H. Warner, O. V. Kolosov, G. A. D. Briggs, and J. A. Mol. Field-Effect Control of Graphene-Fullerene Thermoelectric Nanodevices. *Nano letters*, 17(11):7055–7061, 2017. doi: 10.1021/acs.nanolett.7b03736.
- ¹¹² P. Gehring, H. Sadeghi, S. Sangtarash, C. S. Lau, J. Liu, A. Ardavan, J. H. Warner, C. J. Lambert, G. A. D. Briggs, and J. A. Mol. Quantum Interference in Graphene Nanoconstrictions. *Nano letters*, 16(7):4210–4216, 2016. doi: 10.1021/acs.nanolett.6b01104.
- ¹¹³ M. El Abbassi, J. Overbeck, O. Braun, M. Calame, H. S. J. van der Zant, and M. L. Perrin. Benchmark and application of unsupervised classification approaches for univariate data. *Communications Physics*, 4(1):85, 2021. doi: 10.1038/s42005-021-00549-9.
- ¹¹⁴ W. Cai, A. L. Moore, Y. Zhu, X. Li, S. Chen, L. Shi, and R. S. Ruoff. Thermal transport in suspended and supported monolayer graphene grown by chemical vapor deposition. *Nano letters*, 10(5):1645–1651, 2010. doi: 10.1021/nl9041966.
- ¹¹⁵ L. Talirz, H. Söde, T. Dumschlaff, S. Wang, J. R. Sanchez-Valencia, J. Liu, P. Shinde, C. A. Pignedoli, L. Liang, V. Meunier, N. C. Plumb, M. Shi, X. Feng, A. Narita, K. Müllen, R. Fasel, and P. Ruffieux. On-Surface Synthesis and Characterization of 9-Atom Wide Armchair Graphene Nanoribbons. *ACS nano*, 11(2):1380–1388, 2017. doi: 10.1021/acsnano.6b06405.
- ¹¹⁶ J. Yamaguchi, H. Hayashi, H. Jippo, A. Shiotari, M. Ohtomo, M. Sakakura, N. Hieda, N. Aratani, M. Ohfuchi, Y. Sugimoto, H. Yamada, and S. Sato. Small bandgap in atomically precise 17-atom-wide armchair-edged graphene nanoribbons. *Communications Materials*, 1(1):17954, 2020. doi: 10.1038/s43246-020-0039-9.
- ¹¹⁷ Z. Chen, H. I. Wang, N. Bilbao, J. Teyssandier, T. Prechtel, N. Cavani, A. Tries, R. Biagi, V. de Renzi, X. Feng, M. Kläui, S. de Feyter, M. Bonn, A. Narita, and K. Müllen. Lateral Fusion of Chemical Vapor Deposited N = 5 Armchair Graphene Nanoribbons. *Journal of the American Chemical Society*, 139(28):9483–9486, 2017. doi: 10.1021/jacs.7b05055.

- ¹¹⁸ J. Lawrence, P. Brandimarte, A. Berdonces-Layunta, M. S. G. Mohammed, A. Grewal, C. C. Leon, D. Sánchez-Portal, and D. G. de Oteyza. Probing the Magnetism of Topological End States in 5-Armchair Graphene Nanoribbons. *ACS nano*, 14(4):4499–4508, 2020. doi: 10.1021/acsnano.9b10191.
- ¹¹⁹ L. Talirz, H. Söde, S. Kawai, P. Ruffieux, E. Meyer, X. Feng, K. Müllen, R. Fasel, C. A. Pignedoli, and D. Passerone. Band Gap of Atomically Precise Graphene Nanoribbons as a Function of Ribbon Length and Termination. *Chemphyschem : a European journal of chemical physics and physical chemistry*, 20(18):2348–2353, 2019. doi: 10.1002/cphc.201900313.
- ¹²⁰ S. Linden, D. Zhong, A. Timmer, N. Aghdassi, J. H. Franke, H. Zhang, X. Feng, K. Müllen, H. Fuchs, L. Chi, and H. Zacharias. Electronic structure of spatially aligned graphene nanoribbons on Au(788). *Physical review letters*, 108(21):216801, 2012. doi: 10.1103/PhysRevLett.108.216801.
- ¹²¹ B. V. Senkovskiy, M. Pfeiffer, S. K. Alavi, A. Bliesener, J. Zhu, S. Michel, A. V. Fedorov, R. German, D. Hertel, D. Haberer, L. Petaccia, F. R. Fischer, K. Meerholz, P. H. M. van Loosdrecht, K. Lindfors, and A. Grüneis. Making Graphene Nanoribbons Photoluminescent. *Nano letters*, 17(7):4029–4037, 2017. doi: 10.1021/acs.nanolett.7b00147.
- ¹²² A. Fairbrother, J.-R. Sanchez-Valencia, B. Lauber, I. Shorubalko, P. Ruffieux, T. Hintermann, and R. Fasel. High vacuum synthesis and ambient stability of bottom-up graphene nanoribbons. *Nanoscale*, 9(8):2785–2792, 2017. doi: 10.1039/c6nr08975e.
- ¹²³ G. Borin Barin, A. Fairbrother, L. Rotach, M. Bayle, M. Paillet, L. Liang, V. Meunier, R. Hauert, T. Dumsclaff, A. Narita, K. Müllen, H. Sahabudeen, R. Berger, X. Feng, R. Fasel, and P. Ruffieux. Surface-Synthesized Graphene Nanoribbons for Room Temperature Switching Devices: Substrate Transfer and ex Situ Characterization. *ACS Applied Nano Materials*, 2(4):2184–2192, 2019. ISSN 2574-0970. doi: 10.1021/acsanm.9b00151.
- ¹²⁴ C. Backes, A. M. Abdelkader, C. Alonso, A. Andrieux-Ledier, R. Arenal, J. Azpeitia, N. Balakrishnan, L. Banszerus, J. Barjon, R. Bartali, S. Bellani, C. Berger, R. Berger, M. M. B. Ortega, C. Bernard, P. H. Beton, A. Beyer, A. Bianco, P. Bøggild, F. Bonaccorso, G. B. Barin, C. Botas, R. A. Bueno, D. Carriazo, A. Castellanos-Gomez, M. Christian, A. Ciesielski, T. Ciuk, M. T. Cole, J. Coleman, C. Coletti, L. Crema, H. Cun, D. Dasler, D. de Fazio, N. Díez, S. Drieschner, G. S. Duesberg, R. Fasel, X. Feng, A. Fina, S. Forti, C. Galiotis, G. Garberoglio, J. M. García, J. A. Garrido, M. Gibertini, A. Gözlhäufer, J. Gómez, T. Greber, F. Hauke, A. Hemmi, I. Hernandez-Rodriguez, A. Hirsch, S. A. Hodge, Y. Huttel, P. U. Jepsen, I. Jimenez, U. Kaiser, T. Kaplas, H. Kim, A. Kis, K. Papagelis, K. Kostarelos, A. Krajewska, K. Lee, C. Li, H. Lipsanen, A. Liscio, M. R. Lohe, A. Loiseau, L. Lombardi, M. Francisca López, O. Martin, C. Martín, L. Martínez, J. A. Martin-Gago, J. Ignacio Martínez, N. Marzari, Á. Mayoral, J. McManus, M. Melucci, J. Méndez, C. Merino, P. Merino, A. P. Meyer, E. Miniussi, V. Miseikis, N. Mishra, V. Morandi, C. Munuera, R. Muñoz, H. Nolan, L. Ortolani, A. K. Ott, I. Palacio, V. Palermo, J. Parthenios, I. Pasternak, A. Patane, M. Prato, H. Prevost, V. Prudkovskiy, N. Pugno, T. Rojo, A. Rossi, P. Ruffieux, P. Samorì, L. Schué, E. Setijadi, T. Seyller, G. Speranza, C. Stampfer, I. Stenger, W. Strupinski, Y. Svirko, S. Taioli, K. B. K. Teo, M. Testi, F. Tomarchio, M. Tortello, E. Treossi, A. Turchanin, E. Vazquez, E. Villaro, P. R. Whelan, Z. Xia, R. Yakimova, S. Yang, G. R. Yazdi, C. Yim, D. Yoon, X. Zhang, X. Zhuang, L. Colombo, A. C. Ferrari,

- and M. Garcia-Hernandez. Production and processing of graphene and related materials. *2D Materials*, 7(2):022001, 2020. ISSN 1064-8208. doi: 10.1088/2053-1583/ab1e0a.
- ¹²⁵ M. Di Giovannantonio, O. Deniz, J. I. Urgel, R. Widmer, T. Dienel, S. Stolz, C. Sánchez-Sánchez, M. Muntwiler, T. Dumslaff, R. Berger, A. Narita, X. Feng, K. Müllen, P. Ruffieux, and R. Fasel. On-Surface Growth Dynamics of Graphene Nanoribbons: The Role of Halogen Functionalization. *ACS nano*, 12(1):74–81, 2018. doi: 10.1021/acs.nano.7b07077.
- ¹²⁶ M. Pizzochero, K. Čerņevičs, G. Borin Barin, S. Wang, P. Ruffieux, R. Fasel, and O. V. Yazyev. Quantum Electronic Transport Across "Bite" Defects in Graphene Nanoribbons. *2D Materials*, 8:035025, 2021. doi: 10.1088/2053-1583/abf716.
- ¹²⁷ F. Neese. The ORCA program system. *WIREs Computational Molecular Science*, 2(1):73–78, 2012. doi: 10.1002/wcms.81.
- ¹²⁸ K. Celebi, J. Buchheim, R. M. Wyss, A. Droudian, P. Gasser, I. Shorubalko, J.-I. Kye, C. Lee, and H. G. Park. Ultimate permeation across atomically thin porous graphene. *Science*, 344(6181):289–292, 2014. doi: 10.1126/science.1249097.
- ¹²⁹ J. Buchheim, R. M. Wyss, I. Shorubalko, and H. G. Park. Understanding the interaction between energetic ions and freestanding graphene towards practical 2D perforation. *Nanoscale*, 8(15):8345–8354, 2016. doi: 10.1039/c6nr00154h.
- ¹³⁰ O. Braun, R. Furrer, P. Butti, K. R. Thodkar, I. Shorubalko, I. Zardo, M. Calame, and M. L. Perrin. Spatially mapping the thermal conductivity of graphene by an opto-thermal method. *arXiv preprint*, arXiv:2101.12238v2, 2021. URL <http://arxiv.org/pdf/2101.12238v2>.
- ¹³¹ S. Iijima. Helical microtubules of graphitic carbon. *Nature*, 354(6348):56–58, 1991.
- ¹³² S. J. Tans, M. H. Devoret, H. Dai, A. Thess, R. E. Smalley, L. J. Geerligs, and C. Dekker. Individual single-wall carbon nanotubes as quantum wires. *Nature*, 386(6624):474–477, 1997.
- ¹³³ D. Mann, A. Javey, J. Kong, Q. Wang, and H. Dai. Ballistic Transport in Metallic Nanotubes with Reliable Pd Ohmic Contacts. *Nano letters*, 3(11):1541–1544, 2003. doi: 10.1021/nl034700o.
- ¹³⁴ J. Sann, J. Gramich, A. Baumgartner, M. Weiss, and C. Schönenberger. Optimized fabrication and characterization of carbon nanotube spin valves. *Journal of Applied Physics*, 115(17):174309, 2014. ISSN 0021-8979. doi: 10.1063/1.4874919.
- ¹³⁵ G. Hills, C. Lau, A. Wright, S. Fuller, M. D. Bishop, T. Srimani, P. Kanhaiya, R. Ho, A. Amer, Y. Stein, D. Murphy, Arvind, A. Chandrakasan, and M. M. Shulaker. Modern microprocessor built from complementary carbon nanotube transistors. *Nature*, 572(7771):595–602, 2019. doi: 10.1038/s41586-019-1493-8.
- ¹³⁶ R. G. Treuting and S. M. Arnold. Orientation habits of metal whiskers. *Acta Metallurgica*, 5(10):598, 1957.
- ¹³⁷ S. Gangadharaiah, B. Braunecker, P. Simon, and D. Loss. Majorana Edge States in Interacting One-Dimensional Systems. *Physical review letters*, 107(3):819, 2011. doi: 10.1103/PhysRevLett.107.036801.

- ¹³⁸ C. Kloeffer and D. Loss. Prospects for Spin-Based Quantum Computing in Quantum Dots. *Annual Review of Condensed Matter Physics*, 4(1):51–81, 2013. ISSN 1947-5454. doi: 10.1146/annurev-conmatphys-030212-184248.
- ¹³⁹ Y. Cui, Z. Zhong, D. Wang, W. U. Wang, and C. M. Lieber. High Performance Silicon Nanowire Field Effect Transistors. *Nano letters*, 3(2):149–152, 2003. doi: 10.1021/nl025875l.
- ¹⁴⁰ Z. Chen, W. Zhang, C.-A. Palma, A. Lodi Rizzini, B. Liu, A. Abbas, N. Richter, L. Martini, X.-Y. Wang, N. Cavani, H. Lu, N. Mishra, C. Coletti, R. Berger, F. Klappenberger, M. Kläui, A. Candini, M. Affronte, C. Zhou, V. de Renzi, U. Del Pennino, J. V. Barth, H. J. Räder, A. Narita, X. Feng, and K. Müllen. Synthesis of Graphene Nanoribbons by Ambient-Pressure Chemical Vapor Deposition and Device Integration. *Journal of the American Chemical Society*, 138(47):15488–15496, 2016. doi: 10.1021/jacs.6b10374.
- ¹⁴¹ P. Ruffieux, S. Wang, B. Yang, C. Sánchez-Sánchez, J. Liu, T. Dienel, L. Talirz, P. Shinde, C. A. Pignedoli, D. Passerone, T. Dumslaff, X. Feng, K. Müllen, and R. Fasel. On-surface synthesis of graphene nanoribbons with zigzag edge topology. *Nature*, 531(7595):489–492, 2016. doi: 10.1038/nature17151.
- ¹⁴² A. Keerthi, B. Radha, D. Rizzo, H. Lu, V. Diez Cabanes, I. C.-Y. Hou, D. Beljonne, J. Cornil, C. Casiraghi, M. Baumgarten, K. Müllen, and A. Narita. Edge Functionalization of Structurally Defined Graphene Nanoribbons for Modulating the Self-Assembled Structures. *Journal of the American Chemical Society*, 139(46):16454–16457, 2017. doi: 10.1021/jacs.7b09031.
- ¹⁴³ N. Richter, Z. Chen, A. Tries, T. Prechtel, A. Narita, K. Müllen, K. Asadi, M. Bonn, and M. Kläui. Charge transport mechanism in networks of armchair graphene nanoribbons. *Scientific reports*, 10(1):1988, 2020. doi: 10.1038/s41598-020-58660-w.
- ¹⁴⁴ M. L. Perrin, C. J. O. Verzijl, C. A. Martin, A. J. Shaikh, R. Eelkema, J. H. van Esch, J. M. van Ruitenbeek, J. M. Thijssen, H. S. J. van der Zant, and D. Dulić. Large tunable image-charge effects in single-molecule junctions. *Nature nanotechnology*, 8(4):282–287, 2013. doi: 10.1038/nnano.2013.26.
- ¹⁴⁵ M. L. Perrin, E. Burzurí, and H. S. J. van der Zant. Single-molecule transistors. *Chemical Society reviews*, 44(4):902–919, 2015. doi: 10.1039/c4cs00231h.
- ¹⁴⁶ K. Moth-Poulsen and T. Bjørnholm. Molecular electronics with single molecules in solid-state devices. *Nature nanotechnology*, 4(9):551–556, 2009. doi: 10.1038/nnano.2009.176.
- ¹⁴⁷ W. J. Yu, Y. Liu, H. Zhou, A. Yin, Z. Li, Y. Huang, and X. Duan. Highly efficient gate-tunable photocurrent generation in vertical heterostructures of layered materials. *Nature nanotechnology*, 8(12):952–958, 2013.
- ¹⁴⁸ Y. Liu, H. Wu, H.-C. Cheng, S. Yang, E. Zhu, Q. He, M. Ding, D. Li, J. Guo, N. O. Weiss, Y. Huang, and X. Duan. Toward barrier free contact to molybdenum disulfide using graphene electrodes. *Nano letters*, 15(5):3030–3034, 2015. doi: 10.1021/nl504957p.
- ¹⁴⁹ L. Martini, Z. Chen, N. Mishra, G. B. Barin, P. Fantuzzi, P. Ruffieux, R. Fasel, X. Feng, A. Narita, C. Coletti, K. Müllen, and A. Candini. Structure-dependent electrical properties of graphene nanoribbon devices with graphene electrodes. *Carbon*, 146(14):36–43, 2019. ISSN 00086223. doi: 10.1016/j.carbon.2019.01.071.

- ¹⁵⁰ A. Candini, L. Martini, Z. Chen, N. Mishra, D. Convertino, C. Coletti, A. Narita, X. Feng, K. Müllen, and M. Affronte. High Photoresponsivity in Graphene Nanoribbon Field-Effect Transistor Devices Contacted with Graphene Electrodes. *The Journal of Physical Chemistry C*, 121(19):10620–10625, 2017. ISSN 1932-7447. doi: 10.1021/acs.jpcc.7b03401.
- ¹⁵¹ V. M. García-Suárez, A. García-Fuente, D. J. Carrascal, E. Burzurí, M. Koole, H. S. J. van der Zant, M. El Abbassi, M. Calame, and J. Ferrer. Spin signatures in the electrical response of graphene nanogaps. *Nanoscale*, 10(38):18169–18177, 2018. doi: 10.1039/c8nr06123h.
- ¹⁵² S. Thoms and D. S. Macintyre. Investigation of CSAR 62, a new resist for electron beam lithography. *Journal of Vacuum Science & Technology B, Nanotechnology and Microelectronics: Materials, Processing, Measurement, and Phenomena*, 32(6):06FJ01, 2014. ISSN 2166-2746. doi: 10.1116/1.4899239.
- ¹⁵³ Y. Chen, X.-L. Gong, and J.-G. Gai. Progress and Challenges in Transfer of Large-Area Graphene Films. *Advanced science*, 3(8):1500343, 2016. doi: 10.1002/advs.201500343.
- ¹⁵⁴ P.-C. Chen, C.-P. Lin, C.-J. Hong, C.-H. Yang, Y.-Y. Lin, M.-Y. Li, L.-J. Li, T.-Y. Yu, C.-J. Su, K.-S. Li, Y.-L. Zhong, T.-H. Hou, and Y.-W. Lan. Effective N-methyl-2-pyrrolidone wet cleaning for fabricating high-performance monolayer MoS₂ transistors. *Nano Research*, 12(2):303–308, 2019. ISSN 1998-0124. doi: 10.1007/s12274-018-2215-5.
- ¹⁵⁵ B. Zhuang, S. Li, S. Li, and J. Yin. Ways to eliminate PMMA residues on graphene-super-clean graphene. *Carbon*, 173(5696):609–636, 2021. ISSN 00086223. doi: 10.1016/j.carbon.2020.11.047.
- ¹⁵⁶ H. Schmidt, T. Lüdtke, P. Barthold, E. McCann, V. I. Fal’ko, and R. J. Haug. Tunable graphene system with two decoupled monolayers. *Applied Physics Letters*, 93(17):172108, 2008. doi: 10.1063/1.3012369.
- ¹⁵⁷ P. Rickhaus, M.-H. Liu, M. Kurpas, A. Kurzmann, Y. Lee, H. Overweg, M. Eich, R. Pisoni, T. Taniguchi, K. Watanabe, K. Richter, K. Ensslin, and T. Ihn. The electronic thickness of graphene. *Science advances*, 6(11):eaay8409, 2020.
- ¹⁵⁸ Z. Cheng, Q. Zhou, C. Wang, Q. Li, C. Wang, and Y. Fang. Toward intrinsic graphene surfaces: a systematic study on thermal annealing and wet-chemical treatment of SiO₂-supported graphene devices. *Nano letters*, 11(2):767–771, 2011. doi: 10.1021/nl103977d.
- ¹⁵⁹ Y. Hong, S. Wang, Q. Li, X. Song, Z. Wang, X. Zhang, F. Besenbacher, and M. Dong. Interfacial icelike water local doping of graphene. *Nanoscale*, 11(41):19334–19340, 2019. doi: 10.1039/c9nr05832j.
- ¹⁶⁰ S. Bailey, D. Visontai, C. J. Lambert, M. R. Bryce, H. Frampton, and D. Chappell. A study of planar anchor groups for graphene-based single-molecule electronics. *The Journal of chemical physics*, 140(5):054708, 2014. doi: 10.1063/1.4861941.
- ¹⁶¹ B. J. Robinson, S. W. D. Bailey, L. J. O’Driscoll, D. Visontai, D. J. Welsh, A. B. Mostert, R. Mazzocco, C. Rabot, S. P. Jarvis, O. V. Kolosov, M. R. Bryce, and C. Lambert. Formation of Two-Dimensional Micelles on Graphene: Multi-Scale Theoretical and Experimental Study. *ACS nano*, 11(3):3404–3412, 2017. doi: 10.1021/acsnano.7b01071.

- ¹⁶² H. Sadeghi, S. Sangtarash, and C. Lambert. Robust Molecular Anchoring to Graphene Electrodes. *Nano letters*, 17(8):4611–4618, 2017. doi: 10.1021/acs.nanolett.7b01001.
- ¹⁶³ A. Tries, N. Richter, Z. Chen, A. Narita, K. Müllen, H. I. Wang, M. Bonn, and M. Kläui. Hysteresis in graphene nanoribbon field-effect devices. *Physical chemistry chemical physics : PCCP*, 22(10):5667–5672, 2020. doi: 10.1039/d0cp00298d.
- ¹⁶⁴ P. Jangid, D. Pathan, and A. Kottantharayil. Graphene nanoribbon transistors with high Ion/Ioff ratio and mobility. *Carbon*, 132(7419):65–70, 2018. ISSN 00086223. doi: 10.1016/j.carbon.2018.02.030.
- ¹⁶⁵ L. Xie, M. Liao, S. Wang, H. Yu, L. Du, J. Tang, J. Zhao, J. Zhang, P. Chen, X. Lu, G. Wang, G. Xie, R. Yang, D. Shi, and G. Zhang. Graphene-Contacted Ultrashort Channel Monolayer MoS2 Transistors. *Advanced materials*, 29(37), 2017. doi: 10.1002/adma.201702522.
- ¹⁶⁶ A. Behnam, F. Xiong, A. Cappelli, N. C. Wang, E. A. Carrion, S. Hong, Y. Dai, A. S. Lyons, E. K. Chow, E. Piccinini, C. Jacoboni, and E. Pop. Nanoscale phase change memory with graphene ribbon electrodes. *Applied Physics Letters*, 107(12):123508, 2015. ISSN 0003-6951. doi: 10.1063/1.4931491.
- ¹⁶⁷ X. Liu, G. Li, A. Lipatov, T. Sun, M. Mehdi Pour, N. R. Aluru, J. W. Lyding, and A. Sinitskii. Chevron-type graphene nanoribbons with a reduced energy band gap: Solution synthesis, scanning tunneling microscopy and electrical characterization. *Nano Research*, 13(6):1713–1722, 2020. doi: 10.1007/s12274-020-2797-6.
- ¹⁶⁸ IEEE. International roadmap for devices and systems (IRDS), 2020. URL <https://irds.ieee.org/editions/2020>.
- ¹⁶⁹ M. de Cervantes. *El ingenioso hidalgo don Quixote de la Mancha*. Francisco de Robles, Habsburg Spain, 1605.
- ¹⁷⁰ B. Radisavljevic, A. Radenovic, J. Brivio, V. Giacometti, and A. Kis. Single-layer MoS2 transistors. *Nature nanotechnology*, 6(3):147–150, 2011. doi: 10.1038/nnano.2010.279.
- ¹⁷¹ G. M. Marega, Y. Zhao, A. Avsar, Z. Wang, M. Tripathi, A. Radenovic, and A. Kis. Logic-in-memory based on an atomically thin semiconductor. *Nature*, 587(7832):72–77, 2020. doi: 10.1038/s41586-020-2861-0.
- ¹⁷² Q. Sun, O. Gröning, J. Overbeck, O. Braun, M. L. Perrin, G. Borin Barin, M. El Abbassi, K. Eimre, E. Ditler, C. Daniels, V. Meunier, C. A. Pignedoli, M. Calame, R. Fasel, and P. Ruffieux. Massive Dirac Fermion Behavior in a Low Bandgap Graphene Nanoribbon Near a Topological Phase Boundary. *Advanced materials*, 32(12):e1906054, 2020. doi: 10.1002/adma.201906054.
- ¹⁷³ K. Sun, P. Ji, J. Zhang, J. Wang, X. Li, X. Xu, H. Zhang, and L. Chi. On-Surface Synthesis of 8- and 10-Armchair Graphene Nanoribbons. *Small*, 15(15):e1804526, 2019. doi: 10.1002/smll.201804526.
- ¹⁷⁴ L. A. Ponomarenko, R. Yang, R. V. Gorbachev, P. Blake, A. S. Mayorov, K. S. Novoselov, M. I. Katsnelson, and A. K. Geim. Density of states and zero Landau Level probed through capacitance of graphene. *Physical review letters*, 105(13):136801, 2010. doi: 10.1103/PhysRevLett.105.136801.

- ¹⁷⁵ S. Arrhenius. Über die Reaktionsgeschwindigkeit bei der Inversion von Rohrzucker durch Säuren. *Zeitschrift für Physikalische Chemie*, 4U(1), 1889. URL [10.1515/zpch-1889-0416](https://doi.org/10.1515/zpch-1889-0416).
- ¹⁷⁶ S. M. Sze, Y. Li, and K. K. Ng. *Physics of semiconductor devices*. John Wiley & sons, 2021.
- ¹⁷⁷ J. M. Thijssen and H. S. J. van der Zant. Charge transport and single-electron effects in nanoscale systems. *physica status solidi (b)*, 245(8):1455–1470, 2008. doi: [10.1002/pssb.200743470](https://doi.org/10.1002/pssb.200743470).
- ¹⁷⁸ F. S. Thomas, A. Baumgartner, L. Gubser, C. Jünger, G. Fülöp, M. Nilsson, F. Rossi, V. Zannier, L. Sorba, and C. Schönenberger. Highly symmetric and tunable tunnel couplings in InAs/InP nanowire heterostructure quantum dots. *Nanotechnology*, 31(13):135003, 2019. doi: [10.1088/1361-6528/ab5ce6](https://doi.org/10.1088/1361-6528/ab5ce6).
- ¹⁷⁹ S. Gustavsson, R. Leturcq, B. Simovic, R. Schleser, T. Ihn, P. Studerus, K. Ensslin, D. C. Driscoll, and A. C. Gossard. Counting statistics of single electron transport in a quantum dot. *Physical review letters*, 96(7):076605, 2006. doi: [10.1103/PhysRevLett.96.076605](https://doi.org/10.1103/PhysRevLett.96.076605).
- ¹⁸⁰ M. Y. Han, J. C. Brant, and P. Kim. Electron transport in disordered graphene nanoribbons. *Physical review letters*, 104(5):056801, 2010. doi: [10.1103/PhysRevLett.104.056801](https://doi.org/10.1103/PhysRevLett.104.056801).
- ¹⁸¹ X. Wang, Y. Ouyang, L. Jiao, H. Wang, L. Xie, J. Wu, J. Guo, and H. Dai. Graphene nanoribbons with smooth edges behave as quantum wires. *Nature nanotechnology*, 6(9):563–567, 2011. doi: [10.1038/nnano.2011.138](https://doi.org/10.1038/nnano.2011.138).
- ¹⁸² J. A. Mol, C. S. Lau, W. J. M. Lewis, H. Sadeghi, C. Roche, A. Cnossen, J. H. Warner, C. J. Lambert, H. L. Anderson, and G. A. D. Briggs. Graphene-porphyrin single-molecule transistors. *Nanoscale*, 7(31):13181–13185, 2015. doi: [10.1039/c5nr03294f](https://doi.org/10.1039/c5nr03294f).
- ¹⁸³ E. Y. Li and N. Marzari. Improving the electrical conductivity of carbon nanotube networks: a first-principles study. *ACS nano*, 5(12):9726–9736, 2011. doi: [10.1021/nn2032227](https://doi.org/10.1021/nn2032227).
- ¹⁸⁴ Y. Cao, V. Fatemi, S. Fang, K. Watanabe, T. Taniguchi, E. Kaxiras, and P. Jarillo-Herrero. Unconventional superconductivity in magic-angle graphene superlattices. *Nature*, 556(7699):43–50, 2018. doi: [10.1038/nature26160](https://doi.org/10.1038/nature26160).
- ¹⁸⁵ A. D. Franklin. Nanomaterials in transistors: From high-performance to thin-film applications. *Science*, 349(6249):aab2750, 2015. doi: [10.1126/science.aab2750](https://doi.org/10.1126/science.aab2750).
- ¹⁸⁶ Y. Q. Wu, H. C. Lin, P. D. Yea, and G. D. Wilk. Current transport and maximum dielectric strength of atomic-layer-deposited ultrathin Al₂O₃ on GaAs. *Applied Physics Letters*, 90(7):072105, 2007. doi: [10.1063/1.2535528](https://doi.org/10.1063/1.2535528).
- ¹⁸⁷ P. Gallagher, K. Todd, and D. Goldhaber-Gordon. Disorder-induced gap behavior in graphene nanoribbons. *Physical Review B*, 81(11):115409, 2010. doi: [10.1103/PhysRevB.81.115409](https://doi.org/10.1103/PhysRevB.81.115409).
- ¹⁸⁸ I. Ionica, L. Montès, J. Zimmermann, L. Saminadayar, and V. Bouchiat. Influence of the Geometry on the Coulomb Blockade in Silicon Nanostructures. 2005. URL http://perso.neel.cnrs.fr/vincent.bouchiat/page_personnelle_de_Vincent_Bouchiat/publications_files/IONICA_IMEP_ESSDERC05_1.pdf.

- ¹⁸⁹ L. A. Ponomarenko, F. Schedin, M. I. Katsnelson, R. Yang, E. W. Hill, K. S. Novoselov, and A. K. Geim. Chaotic Dirac Billiard in Graphene Quantum Dots. *Science*, 320(5874): 356–358, 2008. doi: 10.1126/science.1154663.
- ¹⁹⁰ A. A. Shylau, J. W. Klos, and I. V. Zozoulenko. Capacitance of graphene nanoribbons. *Physical Review B*, 80(20):205402, 2009. doi: 10.1103/PhysRevB.80.205402.
- ¹⁹¹ S. B. Desai, S. R. Madhvapathy, A. B. Sachid, J. P. Llinas, Q. Wang, G. H. Ahn, G. Pitner, M. J. Kim, J. Bokor, C. Hu, H.-S. P. Wong, and A. Javey. MoS₂ transistors with 1-nanometer gate lengths. *Science*, 354(6308):99–102, 2016. doi: 10.1126/science.aah4698.
- ¹⁹² M. Zastrow. Meet the crystal growers who sparked a revolution in graphene electronics. *Nature*, 572(7768):429–433, 2019. doi: 10.1038/d41586-019-02472-0.
- ¹⁹³ L. Liu, Y. P. Feng, and Z. X. Shen. Structural and electronic properties of h-BN. *Physical Review B*, 68(10):582, 2003. ISSN 2469-9950. doi: 10.1103/PhysRevB.68.104102.
- ¹⁹⁴ K. Watanabe, T. Taniguchi, and H. Kanda. Direct-bandgap properties and evidence for ultraviolet lasing of hexagonal boron nitride single crystal. *Nature materials*, 3(6):404–409, 2004. doi: 10.1038/nmat1134.
- ¹⁹⁵ C. R. Dean, A. F. Young, I. Meric, C. Lee, L. Wang, S. Sorgenfrei, K. Watanabe, T. Taniguchi, P. Kim, K. L. Shepard, and J. Hone. Boron nitride substrates for high-quality graphene electronics. *Nature nanotechnology*, 5(10):722–726, 2010. doi: 10.1038/nnano.2010.172.
- ¹⁹⁶ V. Saraswat, R. M. Jacobberger, and M. S. Arnold. Materials Science Challenges to Graphene Nanoribbon Electronics. *ACS nano*, 2021. doi: 10.1021/acsnano.0c07835.
- ¹⁹⁷ S. Carr, D. Massatt, S. Fang, P. Cazeaux, M. Luskin, and E. Kaxiras. Twistronics: Manipulating the electronic properties of two-dimensional layered structures through their twist angle. *Physical Review B*, 95(7):075420, 2017. ISSN 2469-9950. doi: 10.1103/PhysRevB.95.075420.
- ¹⁹⁸ M. Eich, F. Herman, R. Pisoni, H. Overweg, A. Kurzmann, Y. Lee, P. Rickhaus, K. Watanabe, T. Taniguchi, M. Sigrist, T. Ihn, and K. Ensslin. Spin and Valley States in Gate-Defined Bilayer Graphene Quantum Dots. *Physical Review X*, 8(3), 2018. ISSN 1063-7761. doi: 10.1103/PhysRevX.8.031023.
- ¹⁹⁹ S. Kawai, A. Benassi, E. Gnecco, H. Söde, R. Pawlak, X. Feng, K. Müllen, D. Passerone, C. A. Pignedoli, P. Ruffieux, R. Fasel, and E. Meyer. Superlubricity of graphene nanoribbons on gold surfaces. *Science*, 351(6276):957–961, 2016. doi: 10.1126/science.aad9041.
- ²⁰⁰ G. S. Verhoeven, M. Dienwiebel, and J. W. M. Frenken. Model calculations of superlubricity of graphite. *Physical Review B*, 70(16):905, 2004. doi: 10.1103/PhysRevB.70.165418.
- ²⁰¹ M. H. Müser. Structural lubricity: Role of dimension and symmetry. *Europhysics Letters*, 66(1):97–103, 2004. doi: 10.1209/epl/i2003-10139-6.
- ²⁰² I. Leven, D. Krepel, O. Shemesh, and O. Hod. Robust Superlubricity in Graphene/h-BN Heterojunctions. *The journal of physical chemistry letters*, 4(1):115–120, 2013. ISSN 1948-7185. doi: 10.1021/jz301758c.

- ²⁰³ D. Mandelli, I. Leven, O. Hod, and M. Urbakh. Sliding friction of graphene hexagonal-boron nitride heterojunctions: a route to robust superlubricity. *Scientific reports*, 7(1):10851, 2017. doi: 10.1038/s41598-017-10522-8.
- ²⁰⁴ Y. Song, D. Mandelli, O. Hod, M. Urbakh, M. Ma, and Q. Zheng. Robust microscale superlubricity in graphite/hexagonal boron nitride layered heterojunctions. *Nature materials*, 17(10):894–899, 2018. doi: 10.1038/s41563-018-0144-z.
- ²⁰⁵ D. I. Indolese, R. Delagrangé, P. Makk, J. R. Wallbank, K. Wanatabe, T. Taniguchi, and C. Schönenberger. Signatures of van Hove Singularities Probed by the Supercurrent in a Graphene-hBN Superlattice. *Physical review letters*, 121(13):137701, 2018. doi: 10.1103/PhysRevLett.121.137701.
- ²⁰⁶ D. P. Strommen and K. Nakamoto. Resonance raman spectroscopy. *Journal of Chemical Education*, 54(8):474, 1977.
- ²⁰⁷ N. Chejanovsky, M. Rezai, F. Paolucci, Y. Kim, T. Rendler, W. Rouabeh, F. Fávaro de Oliveira, P. Herlinger, A. Denisenko, S. Yang, I. Gerhardt, A. Finkler, J. H. Smet, and J. Wrachtrup. Structural Attributes and Photodynamics of Visible Spectrum Quantum Emitters in Hexagonal Boron Nitride. *Nano letters*, 16(11):7037–7045, 2016. doi: 10.1021/acs.nanolett.6b03268.
- ²⁰⁸ S. Castelletto, F. A. Inam, S.-I. Sato, and A. Boretti. Hexagonal boron nitride: a review of the emerging material platform for single-photon sources and the spin-photon interface. *Beilstein journal of nanotechnology*, 11:740–769, 2020. ISSN 2190-4286. doi: 10.3762/bjnano.11.61.
- ²⁰⁹ Y. Hoshi, T. Kuroda, M. Okada, R. Moriya, S. Masubuchi, K. Watanabe, T. Taniguchi, R. Kitaura, and T. Machida. Suppression of exciton-exciton annihilation in tungsten disulfide monolayers encapsulated by hexagonal boron nitrides. *Physical Review B*, 95(24), 2017. doi: 10.1103/PhysRevB.95.241403.
- ²¹⁰ R. V. Gorbachev, I. Riaz, R. R. Nair, R. Jalil, L. Britnell, B. D. Belle, E. W. Hill, K. S. Novoselov, K. Watanabe, T. Taniguchi, A. K. Geim, and P. Blake. Hunting for monolayer boron nitride: optical and Raman signatures. *Small*, 7(4):465–468, 2011. doi: 10.1002/sml.201001628.
- ²¹¹ A. Hazeghi, T. Krishnamohan, and H.-S. P. Wong. Schottky-Barrier Carbon Nanotube Field-Effect Transistor Modeling. *IEEE Transactions on Electron Devices*, 54(3):439–445, 2007. ISSN 0018-9383. doi: 10.1109/TED.2006.890384.
- ²¹² L. Nordheim and R. H. Fowler. Electron emission in intense electric fields. *Royal Society Proceedings*, 119:173–181, 1928.
- ²¹³ J. C. Cuevas and E. Scheer. *Molecular electronics: an introduction to theory and experiment*, volume 15. World Scientific, 2017. ISBN 978-981-3226-02-9.
- ²¹⁴ M. T. Björk, B. J. Ohlsson, T. Sass, A. I. Persson, C. Thelander, M. H. Magnusson, K. Deppert, L. R. Wallenberg, and L. Samuelson. One-dimensional Steeplechase for Electrons Realized. *Nano Letters*, 2(2):87–89, 2002. ISSN 1530-6984. doi: 10.1021/nl010099n.

- ²¹⁵ J. M. Beebe, B. Kim, J. W. Gadzuk, C. D. Frisbie, and J. G. Kushmerick. Transition from direct tunneling to field emission in metal-molecule-metal junctions. *Physical review letters*, 97(2):026801, 2006. doi: 10.1103/PhysRevLett.97.026801.
- ²¹⁶ H. Song, Y. Kim, Y. H. Jang, H. Jeong, M. A. Reed, and T. Lee. Observation of molecular orbital gating. *Nature*, 462(7276):1039–1043, 2009. doi: 10.1038/nature08639.
- ²¹⁷ M. L. Trouwborst, C. A. Martin, R. H. M. Smit, C. M. Guédon, T. A. Baart, S. J. van der Molen, and J. M. van Ruitenbeek. Transition voltage spectroscopy and the nature of vacuum tunneling. *Nano letters*, 11(2):614–617, 2011. doi: 10.1021/nl103699t.
- ²¹⁸ C. R. Dean, L. Wang, P. Maher, C. Forsythe, F. Ghahari, Y. Gao, J. Katoch, M. Ishigami, P. Moon, M. Koshino, T. Taniguchi, K. Watanabe, K. L. Shepard, J. Hone, and P. Kim. Hofstadter’s butterfly and the fractal quantum Hall effect in moiré superlattices. *Nature*, 497(7451):598–602, 2013. doi: 10.1038/nature12186.
- ²¹⁹ P. Reddy, S.-Y. Jang, R. A. Segalman, and A. Majumdar. Thermoelectricity in molecular junctions. *Science*, 315(5818):1568–1571, 2007. doi: 10.1126/science.1137149.
- ²²⁰ Y. Kim, W. Jeong, K. Kim, W. Lee, and P. Reddy. Electrostatic control of thermoelectricity in molecular junctions. *Nature nanotechnology*, 9(11):881–885, 2014. doi: 10.1038/nnano.2014.209.
- ²²¹ P. Gehring, J. K. Sowa, C. Hsu, J. de Bruijckere, M. van der Star, J. J. Le Roy, L. Bogani, E. M. Gauger, and H. S. J. van der Zant. Complete mapping of the thermoelectric properties of a single molecule. *Nature nanotechnology*, 2021. doi: 10.1038/s41565-021-00859-7.
- ²²² M. Josefsson, A. Svilans, A. M. Burke, E. A. Hoffmann, S. Fahlvik, C. Thelander, M. Leijnse, and H. Linke. A quantum-dot heat engine operating close to the thermodynamic efficiency limits. *Nature nanotechnology*, 13(10):920–924, 2018. doi: 10.1038/s41565-018-0200-5.
- ²²³ A. Svilans, M. Josefsson, A. M. Burke, S. Fahlvik, C. Thelander, H. Linke, and M. Leijnse. Thermoelectric Characterization of the Kondo Resonance in Nanowire Quantum Dots. *Physical review letters*, 121(20):206801, 2018. doi: 10.1103/PhysRevLett.121.206801.
- ²²⁴ Y. M. Zuev, W. Chang, and P. Kim. Thermoelectric and magnetothermoelectric transport measurements of graphene. *Physical review letters*, 102(9):096807, 2009. doi: 10.1103/PhysRevLett.102.096807.
- ²²⁵ F. Ghahari, H.-Y. Xie, T. Taniguchi, K. Watanabe, M. S. Foster, and P. Kim. Enhanced Thermoelectric Power in Graphene: Violation of the Mott Relation by Inelastic Scattering. *Physical review letters*, 116(13):136802, 2016. doi: 10.1103/PhysRevLett.116.136802.
- ²²⁶ S. Yazji, M. Y. Swinkels, M. de Luca, E. A. Hoffmann, D. Ercolani, S. Roddaro, G. Abstreiter, L. Sorba, E. P. A. M. Bakkers, and I. Zardo. Assessing the thermoelectric properties of single InSb nanowires: the role of thermal contact resistance. *Semiconductor Science and Technology*, 31(6):064001, 2016. doi: 10.1088/0268-1242/31/6/064001.
- ²²⁷ S. V. Aradhya and L. Venkataraman. Single-molecule junctions beyond electronic transport. *Nature nanotechnology*, 8(6):399–410, 2013. doi: 10.1038/nnano.2013.91.

- ²²⁸ L. Rincón-García, C. Evangeli, G. Rubio-Bollinger, and N. Agrait. Thermopower measurements in molecular junctions. *Chemical Society reviews*, 45(15):4285–4306, 2016. doi: 10.1039/c6cs00141f.
- ²²⁹ M. H. Garner, H. Li, Y. Chen, T. A. Su, Z. Shangguan, D. W. Paley, T. Liu, F. Ng, H. Li, S. Xiao, C. Nuckolls, L. Venkataraman, and G. C. Solomon. Comprehensive suppression of single-molecule conductance using destructive sigma-interference. *Nature*, 558(7710): 415–419, 2018. doi: 10.1038/s41586-018-0197-9.
- ²³⁰ J. R. Widawsky, P. Darancet, J. B. Neaton, and L. Venkataraman. Simultaneous determination of conductance and thermopower of single molecule junctions. *Nano letters*, 12(1): 354–358, 2012. doi: 10.1021/nl203634m.
- ²³¹ C. Evangeli, K. Gillemot, E. Leary, M. T. González, G. Rubio-Bollinger, C. J. Lambert, and N. Agrait. Engineering the thermopower of C60 molecular junctions. *Nano letters*, 13(5):2141–2145, 2013. doi: 10.1021/nl400579g.
- ²³² L. Cui, R. Miao, K. Wang, D. Thompson, L. A. Zotti, J. C. Cuevas, E. Meyhofer, and P. Reddy. Peltier cooling in molecular junctions. *Nature nanotechnology*, 13(2):122–127, 2018. doi: 10.1038/s41565-017-0020-z.
- ²³³ F. Mazzamuto, V. Hung Nguyen, Y. Apertet, C. Caër, C. Chassat, J. Saint-Martin, and P. Dollfus. Enhanced thermoelectric properties in graphene nanoribbons by resonant tunneling of electrons. *Physical Review B*, 83(23), 2011. doi: 10.1103/PhysRevB.83.235426.
- ²³⁴ H. Zheng, H. J. Liu, X. J. Tan, H. Y. Lv, L. Pan, J. Shi, and X. F. Tang. Enhanced thermoelectric performance of graphene nanoribbons. *Applied Physics Letters*, 100(9): 093104, 2012. doi: 10.1063/1.3689780.
- ²³⁵ L. Rosales, C. D. Nunez, M. Pacheco, A. Latgé, and P. A. Orellana. Graphene nanoribbon thermopower as a tool for molecular spectroscopy. *Journal of Applied Physics*, 114(15): 153711, 2013. ISSN 0021-8979. doi: 10.1063/1.4826266.
- ²³⁶ A. S. Nissimagoudar and N. S. Sankeshwar. Electronic thermal conductivity and thermopower of armchair graphene nanoribbons. *Carbon*, 52(1):201–208, 2013. ISSN 00086223. doi: 10.1016/j.carbon.2012.09.021.
- ²³⁷ B. Zhou, B. Zhou, Y. Zeng, G. Zhou, and T. Ouyang. Seebeck effects in a graphene nanoribbon coupled to two ferromagnetic leads. *Journal of Applied Physics*, 115(11):114305, 2014. ISSN 0021-8979. doi: 10.1063/1.4868322.
- ²³⁸ H. Rezanian and A. Valizadeh Ghorlivand. Seebeck coefficient and thermal conductivity of doped armchair graphene nanoribbon in the presence of magnetic field. *Materials Research Bulletin*, 99:18–22, 2018. ISSN 00255408. doi: 10.1016/j.materresbull.2017.10.023.
- ²³⁹ Y. Dong, Y. Wu, X. Wang, X. Yang, and Y. Liu. Nanoporous Graphene Nanoribbons: Robust Spin-Semiconducting Property and Perfect Spin Seebeck Effects. *The Journal of Physical Chemistry C*, 123(48):29126–29132, 2019. ISSN 1932-7447. doi: 10.1021/acs.jpcc.9b08092.
- ²⁴⁰ Y.-B. Dai, K. Luo, and X.-F. Wang. Thermoelectric properties of graphene-like nanoribbon studied from the perspective of symmetry. *Scientific reports*, 10(1):9105, 2020. doi: 10.1038/s41598-020-66073-y.

- ²⁴¹ Q.-Y. Li, T. Feng, W. Okita, Y. Komori, H. Suzuki, T. Kato, T. Kaneko, T. Ikuta, X. Ruan, and K. Takahashi. Enhanced Thermoelectric Performance of As-Grown Suspended Graphene Nanoribbons. *ACS nano*, 13(8):9182–9189, 2019. doi: 10.1021/acsnano.9b03521.
- ²⁴² J. W. Slot and H. J. Geuze. A new method of preparing gold probes for multiple-labeling cytochemistry. *European journal of cell biology*, 38(1):87–93, 1985.
- ²⁴³ J. Liao, Y. Zhang, W. Yu, L. Xu, C. Ge, J. Liu, and N. Gu. Linear aggregation of gold nanoparticles in ethanol. *Colloids and Surfaces A: Physicochemical and Engineering Aspects*, 223(1-3):177–183, 2003. ISSN 09277757. doi: 10.1016/S0927-7757(03)00156-0.
- ²⁴⁴ J. Liao, L. Bernard, M. Langer, C. Schönenberger, and M. Calame. Reversible Formation of Molecular Junctions in 2D Nanoparticle Arrays. *Advanced materials*, 18(18):2444–2447, 2006. doi: 10.1002/adma.200601001.
- ²⁴⁵ J. Liao, M. A. Mangold, S. Grunder, M. Mayor, C. Schönenberger, and M. Calame. Interlinking Au nanoparticles in 2D arrays via conjugated dithiolated molecules. *New Journal of Physics*, 10(6):065019, 2008. doi: 10.1088/1367-2630/10/6/065019.
- ²⁴⁶ Y. Wang, C. Duan, L. Peng, and J. Liao. Dimensionality-dependent charge transport in close-packed nanoparticle arrays: from 2D to 3D. *Scientific reports*, 4:7565, 2014. doi: 10.1038/srep07565.
- ²⁴⁷ P. Gehring, M. van der Star, C. Evangeli, J. J. Le Roy, L. Bogani, O. V. Kolosov, and H. S. J. van der Zant. Efficient heating of single-molecule junctions for thermoelectric studies at cryogenic temperatures. *Applied Physics Letters*, 115(7):073103, 2019. doi: 10.1063/1.5118861.
- ²⁴⁸ W. Betteridge, D. W. Rhys, and D. F. Withers. Laboratory Control of Production of Platinum for Thermometry. *Temperature; Its Measurement and Control in Science and Industry, Volume 1*, page 263, 1962.
- ²⁴⁹ S. Nazarpour, A. Cirera, and M. Varela. Material properties of Au–Pd thin alloy films. *Thin Solid Films*, 518(20):5715–5719, 2010. ISSN 00406090. doi: 10.1016/j.tsf.2010.05.054.
- ²⁵⁰ C. A. Domenicali. Irreversible Thermodynamics of Thermoelectricity. *Reviews of modern Physics*, 26(2):237–275, 1954.
- ²⁵¹ H. S. Carslaw and J. C. Jaeger. *Conduction of heat in solids*, Clarendon, 1959.
- ²⁵² Z. Instruments. Principles of lock-in detection and the state of the art. *White Paper*, pages 1–10, 2016. URL <https://www.zhinst.com/ch/en/resources/principles-of-lock-in-detection>.
- ²⁵³ H. R. Shanks, P. D. Maycock, P. H. Sidles, and G. C. Danielson. Thermal Conductivity of Silicon from 300 to 1400 K. *Physical Review*, 130(5):1743–1748, 1963.
- ²⁵⁴ C. J. Glassbrenner and G. A. Slack. Thermal Conductivity of Silicon and Germanium from 3°K to the Melting Point. *Physical Review*, 134(4A):A1058, 1964.
- ²⁵⁵ G. S. Nolas and H. J. Goldsmid. *Thermal conductivity of semiconductors*. Springer, 2004.

- ²⁵⁶ G. Giovannetti, P. A. Khomyakov, G. Brocks, V. M. Karpan, J. van den Brink, and P. J. Kelly. Doping Graphene with Metal Contacts. *Physical review letters*, 101(2):026803, 2008. doi: 10.1103/PhysRevLett.101.026803.
- ²⁵⁷ S. Goniszewski, M. Adabi, O. Shaforost, S. M. Hanham, L. Hao, and N. Klein. Correlation of p-doping in CVD Graphene with Substrate Surface Charges. *Scientific reports*, 6:22858, 2016. doi: 10.1038/srep22858.
- ²⁵⁸ H. W. Henkels. Thermoelectric Power and Mobility of Carriers in Selenium. *Physical Review*, 77(5):734–736, 1950.
- ²⁵⁹ L. Shi, C. Dames, J. R. Lukes, P. Reddy, J. Duda, D. G. Cahill, J. Lee, A. Marconnet, K. E. Goodson, J.-H. Bahk, A. Shakouri, R. S. Prasher, J. Felts, W. P. King, B. Han, and J. C. Bischof. Evaluating Broader Impacts of Nanoscale Thermal Transport Research. *Nanoscale and Microscale Thermophysical Engineering*, 19(2):127–165, 2015. ISSN 1556-7265. doi: 10.1080/15567265.2015.1031857.
- ²⁶⁰ O. M. Corbino. Thermal oscillations in lamps of thin fibers with alternating current flowing through them and the resulting effect on the rectifier as a result of the presence of even-numbered harmonics. *Physikalische Zeitschrift*, 11:413–417, 1910.
- ²⁶¹ O. M. Corbino. Periodic resistance changes of fine metal threads which are brought together by alternating streams as well as deduction of their thermo characteristics at high temperatures. *Physikalische Zeitschrift*, 12:292–295, 1911.
- ²⁶² J. H. Seol, I. Jo, A. L. Moore, L. Lindsay, Z. H. Aitken, M. T. Pettes, X. Li, Z. Yao, R. Huang, D. Broido, N. Mingo, R. S. Ruoff, and L. Shi. Two-dimensional phonon transport in supported graphene. *Science*, 328(5975):213–216, 2010. doi: 10.1126/science.1184014.
- ²⁶³ M. Y. Swinkels, M. R. van Delft, D. S. Oliveira, A. Cavalli, I. Zardo, R. W. van der Heijden, and E. P. A. M. Bakkers. Diameter dependence of the thermal conductivity of InAs nanowires. *Nanotechnology*, 26(38):385401, 2015. doi: 10.1088/0957-4484/26/38/385401.
- ²⁶⁴ V. V. Deshpande, S. Hsieh, A. W. Bushmaker, M. Bockrath, and S. B. Cronin. Spatially resolved temperature measurements of electrically heated carbon nanotubes. *Physical review letters*, 102(10):105501, 2009. doi: 10.1103/PhysRevLett.102.105501.
- ²⁶⁵ S. Neogi, J. S. Reparaz, L. F. C. Pereira, B. Graczykowski, M. R. Wagner, M. Sledzinska, A. Shchepetov, M. Prunnila, J. Ahopelto, C. M. Sotomayor-Torres, and D. Donadio. Tuning thermal transport in ultrathin silicon membranes by surface nanoscale engineering. *ACS nano*, 9(4):3820–3828, 2015. doi: 10.1021/nm506792d.
- ²⁶⁶ K. M. Shahil and A. A. Balandin. Thermal properties of graphene and multilayer graphene: Applications in thermal interface materials. *Solid State Communications*, 152(15):1331–1340, 2012. ISSN 00381098. doi: 10.1016/j.ssc.2012.04.034.
- ²⁶⁷ A. A. Balandin. Phononics of Graphene and Related Materials. *ACS nano*, 14(5):5170–5178, 2020. doi: 10.1021/acsnano.0c02718.
- ²⁶⁸ T. S. Kasirga. *Thermal Conductivity Measurements in Atomically Thin Materials and Devices*. Springer Nature, 2020.

- ²⁶⁹ S. Ghosh, I. Calizo, D. Teweldebrhan, E. P. Pokatilov, D. L. Nika, A. A. Balandin, W. Bao, F. Miao, and C. N. Lau. Extremely high thermal conductivity of graphene: Prospects for thermal management applications in nanoelectronic circuits. *Applied Physics Letters*, 92(15):151911, 2008. doi: 10.1063/1.2907977.
- ²⁷⁰ C. Faugeras, B. Faugeras, M. Orlita, M. Potemski, R. R. Nair, and A. K. Geim. Thermal conductivity of graphene in corbino membrane geometry. *ACS nano*, 4(4):1889–1892, 2010. doi: 10.1021/nn9016229.
- ²⁷¹ J.-U. Lee, D. Yoon, H. Kim, S. W. Lee, and H. Cheong. Thermal conductivity of suspended pristine graphene measured by Raman spectroscopy. *Physical Review B*, 83(8), 2011. doi: 10.1103/PhysRevB.83.081419.
- ²⁷² S. Chen, A. L. Moore, W. Cai, J. W. Suk, J. An, C. Mishra, C. Amos, C. W. Magnuson, J. Kang, L. Shi, and R. S. Ruoff. Raman measurements of thermal transport in suspended monolayer graphene of variable sizes in vacuum and gaseous environments. *ACS nano*, 5(1):321–328, 2011. doi: 10.1021/nn102915x.
- ²⁷³ W. Lee, K. D. Kihm, H. G. Kim, S. Shin, C. Lee, J. S. Park, S. Cheon, O. M. Kwon, G. Lim, and W. Lee. In-Plane Thermal Conductivity of Polycrystalline Chemical Vapor Deposition Graphene with Controlled Grain Sizes. *Nano letters*, 17(4):2361–2366, 2017. doi: 10.1021/acs.nanolett.6b05269.
- ²⁷⁴ T. Ma, Z. Liu, J. Wen, Y. Gao, X. Ren, H. Chen, C. Jin, X.-L. Ma, N. Xu, H.-M. Cheng, and W. Ren. Tailoring the thermal and electrical transport properties of graphene films by grain size engineering. *Nature communications*, 8:14486, 2017. doi: 10.1038/ncomms14486.
- ²⁷⁵ S. Chen, Q. Li, Q. Zhang, Y. Qu, H. Ji, R. S. Ruoff, and W. Cai. Thermal conductivity measurements of suspended graphene with and without wrinkles by micro-Raman mapping. *Nanotechnology*, 23(36):365701, 2012. doi: 10.1088/0957-4484/23/36/365701.
- ²⁷⁶ W. Zhao, Y. Wang, Z. Wu, W. Wang, K. Bi, Z. Liang, J. Yang, Y. Chen, Z. Xu, and Z. Ni. Defect-Engineered Heat Transport in Graphene: A Route to High Efficient Thermal Rectification. *Scientific reports*, 5:11962, 2015. doi: 10.1038/srep11962.
- ²⁷⁷ H. Malekpour, P. Ramnani, S. Srinivasan, G. Balasubramanian, D. L. Nika, A. Mulchandani, R. K. Lake, and A. A. Balandin. Thermal conductivity of graphene with defects induced by electron beam irradiation. *Nanoscale*, 8(30):14608–14616, 2016. doi: 10.1039/c6nr03470e.
- ²⁷⁸ A. Ziabari, P. Torres, B. Vermeersch, Y. Xuan, X. Cartoixà, A. Torelló, J.-H. Bahk, Y. R. Koh, M. Parsa, P. D. Ye, F. X. Alvarez, and A. Shakouri. Full-field thermal imaging of quasiballistic crosstalk reduction in nanoscale devices. *Nature communications*, 9(1):255, 2018. doi: 10.1038/s41467-017-02652-4.
- ²⁷⁹ A. Majumdar. Scanning thermal microscopy. *Annual review of materials science*, 29(1):505–585, 1999.
- ²⁸⁰ A. A. Kinkhabwala, M. Staffaroni, O. Suzer, S. Burgos, and B. Stipe. Nanoscale Thermal Mapping of HAMR Heads Using Polymer Imprint Thermal Mapping. *IEEE Transactions on Magnetics*, 52(2):1–4, 2016. ISSN 0018-9464. doi: 10.1109/TMAG.2015.2474299.

- ²⁸¹ M. Mecklenburg, W. A. Hubbard, E. R. White, R. Dhall, S. B. Cronin, S. Aloni, and B. C. Regan. Thermal measurement. Nanoscale temperature mapping in operating microelectronic devices. *Science*, 347(6222):629–632, 2015. doi: 10.1126/science.aaa2433.
- ²⁸² I. Calizo, A. A. Balandin, W. Bao, F. Miao, and C. N. Lau. Temperature dependence of the Raman spectra of graphene and graphene multilayers. *Nano letters*, 7(9):2645–2649, 2007. doi: 10.1021/nl071033g.
- ²⁸³ M. T. Pettes, I. Jo, Z. Yao, and L. Shi. Influence of polymeric residue on the thermal conductivity of suspended bilayer graphene. *Nano letters*, 11(3):1195–1200, 2011. doi: 10.1021/nl104156y.
- ²⁸⁴ X. Xu, L. F. C. Pereira, Y. Wang, J. Wu, K. Zhang, X. Zhao, S. Bae, C. Tinh Bui, R. Xie, J. T. L. Thong, B. H. Hong, K. P. Loh, D. Donadio, B. Li, and B. Özyilmaz. Length-dependent thermal conductivity in suspended single-layer graphene. *Nature communications*, 5:3689, 2014. doi: 10.1038/ncomms4689.
- ²⁸⁵ V. Iberi, L. Liang, A. V. Ievlev, M. G. Stanford, M.-W. Lin, X. Li, M. Mahjouri-Samani, S. Jesse, B. G. Sumpter, S. V. Kalinin, D. C. Joy, K. Xiao, A. Belianinov, and O. S. Ovchinnikova. Nanoforging Single Layer MoSe₂ Through Defect Engineering with Focused Helium Ion Beams. *Scientific reports*, 6:30481, 2016. doi: 10.1038/srep30481.
- ²⁸⁶ A. Eckmann, A. Felten, A. Mishchenko, L. Britnell, R. Krupke, K. S. Novoselov, and C. Casiraghi. Probing the nature of defects in graphene by Raman spectroscopy. *Nano letters*, 12(8):3925–3930, 2012. doi: 10.1021/nl300901a.
- ²⁸⁷ I. Shorubalko, L. Pillatsch, and I. Utke. Direct-write milling and deposition with noble gases. In *Helium Ion Microscopy*, pages 355–393. Springer, 2016.
- ²⁸⁸ L. van der Maaten and G. Hinton. Visualizing Data using t-SNE. *Journal of machine learning research*, 9(11):2579–2605, 2008.
- ²⁸⁹ L. McInnes, J. Healy, N. Saul, and L. Großberger. UMAP: Uniform Manifold Approximation and Projection. *Journal of Open Source Software*, 3(29):861, 2018. doi: 10.21105/joss.00861.
- ²⁹⁰ Y. Zhang, L. Zhang, and C. Zhou. Review of chemical vapor deposition of graphene and related applications. *Accounts of chemical research*, 46(10):2329–2339, 2013. doi: 10.1021/ar300203n.
- ²⁹¹ M.-H. Bae, Z. Li, Z. Aksamija, P. N. Martin, F. Xiong, Z.-Y. Ong, I. Knezevic, and E. Pop. Ballistic to diffusive crossover of heat flow in graphene ribbons. *Nature communications*, 4:1734, 2013. doi: 10.1038/ncomms2755.
- ²⁹² A. El Sachat, F. Könenmann, F. Menges, E. Del Corro, J. A. Garrido, C. M. Sotomayor Torres, F. Alzina, and B. Gotsmann. Crossover from ballistic to diffusive thermal transport in suspended graphene membranes. *2D Materials*, 6(2):025034, 2019. ISSN 1064-8208. doi: 10.1088/2053-1583/ab097d.
- ²⁹³ D. Vakulov, S. Gireesan, M. Y. Swinkels, R. Chavez, T. Vogelaar, P. Torres, A. Campo, M. de Luca, M. A. Verheijen, S. Koelling, L. Gagliano, J. E. M. Haverkort, F. X. Alvarez, P. A. Bobbert, I. Zardo, and E. P. A. M. Bakkers. Ballistic Phonons in Ultrathin Nanowires. *Nano letters*, 20(4):2703–2709, 2020. doi: 10.1021/acs.nanolett.0c00320.

- ²⁹⁴ Z. Luo, J. Maassen, Y. Deng, Y. Du, R. P. Garrelts, M. S. Lundstrom, P. D. Ye, and X. Xu. Anisotropic in-plane thermal conductivity observed in few-layer black phosphorus. *Nature communications*, 6:8572, 2015. doi: 10.1038/ncomms9572.
- ²⁹⁵ J. S. Kang, H. Wu, and Y. Hu. Thermal Properties and Phonon Spectral Characterization of Synthetic Boron Phosphide for High Thermal Conductivity Applications. *Nano letters*, 17(12):7507–7514, 2017. doi: 10.1021/acs.nanolett.7b03437.
- ²⁹⁶ A. Islam, A. van den Akker, and P. X.-L. Feng. Anisotropic Thermal Conductivity of Suspended Black Phosphorus Probed by Opto-Thermomechanical Resonance Spectromicroscopy. *Nano letters*, 18(12):7683–7691, 2018. doi: 10.1021/acs.nanolett.8b03333.
- ²⁹⁷ R. S. K. Houtsma, J. de La Rie, and M. Stöhr. Atomically precise graphene nanoribbons: interplay of structural and electronic properties. *Chemical Society reviews*, 6:183, 2021. doi: 10.1039/D0CS01541E.
- ²⁹⁸ P.-C. Shen, C. Su, Y. Lin, A.-S. Chou, C.-C. Cheng, J.-H. Park, M.-H. Chiu, A.-Y. Lu, H.-L. Tang, M. M. Tavakoli, G. Pitner, X. Ji, Z. Cai, N. Mao, J. Wang, V. Tung, J. Li, J. Bokor, A. Zettl, C.-I. Wu, T. Palacios, L.-J. Li, and J. Kong. Ultralow contact resistance between semimetal and monolayer semiconductors. *Nature*, 593:211–217, 2021. doi: 10.1038/s41586-021-03472-9.

Acknowledgments

Direct contributions

Michel Calame (M.C.), Mickael L. Perrin (M.P.), Jan Overbeck (J.O.), Gabriela Borin Barin (G.B.B.), Rimah Darawish (R.D.), Qiang Sun (Q.S.), Maria El Abbassi (M.E.A.), Jian Zhang (J.Z.), Silvan Käser (S.K.), Kishan Thodkar (K.T.), Roman Furrer (R.Fu.), Roman Fasel (R.F.), Pascal Ruffieux (P.R.), Nicolo Bassi (N.B.), Klaus Müllen (K.M.), Ivan Shorubalko (I.S.), Ilaria Zardo (I.Z.), Pascal Butti (P.B.), David Indolese (D.I.), Christian Schönenberger (C.S.), Herre van der Zant (H.v.d.Z.), Valentin Matton (V.M.), Jianhui Liao (J.L.), Michael Stiefel (M.S.), Davide Beretta (D.B.)

First, I would like to thank my PhD advisor, Prof. Michel Calame, for his support, the many inspiring discussions, and for giving me the freedom to work on challenging and rewarding projects. Thanks to you, I got many valuable insights to the carbon based electronics and profited from your expertise in the field of molecular electronics.

Prof. Ilaria Zardo, I would like to thank for your guidance and the hospitality in your group in the transition phase from Basel to Empa. It was a pleasure to exchange and learn in the familiar atmosphere you created. *A me mi piace!*

Thanks to Prof. Pramod Reddy and Prof. Pascal Gehring for carefully reading the present thesis, giving valuable feedback and taking the time to be part of the defense committee.

The work presented here is the result of a large, international collaboration.

Thanks to the whole Transport at Nanoscale Interfaces Laboratory at Empa lead by Prof. Michel Calame. In particular I want to thank its members who directly contributed to the work presented here: Mickael L. Perrin, Jan Overbeck, Jian Zhang, Maria El Abbassi, Ivan Shorubalko, Roman Furrer, Michael Stiefel, Wenhao Huang, Tathagata Paul, Omar Vögele, Angela Hunziker, Yves Mermoud, Alexander Flasby, Silvan Käser, Kishan Thodkar, Anton Vladyka, Oliver Schmuck, Jacopo Oswald, Nadia Jimenez-Olalla, Gökhan Kara, Davide Beretta, Bobby Kunz, Rico Muff, Prof. Jianhui Liao, Valentin Matton.

I want to express my gratitude to the people who made the graphene nanoribbons and their precursor molecules, in particular: Gabriela Borin Barin, Rimah Darawish, Qiang Sun, Pascal Ruffieux, Prof. Klaus Müllen and Prof. Roman Fasel.

Further, I'm thankful for discussions and received advice from current and former members of two groups at the physics department of the university of Basel.

The Nanophononics group lead by Prof. Ilaria Zardo. In particular: Marta De Luca, Milo Y. Swinkles, Alessio Campo, Claudia Fasola, Lukas Gubser, Gerard Gadea Diez

and Kamiar Davallou.

The Nanoelectronics group lead by Prof. Christian Schönenberger. In particular its members: David Indolese, Lujun Wang, Peter Makk, Roy Haller, Simon Zihlmann, Clevin Handschin, Andreas Baumgartner, Minkyung Jung, Christian Jünger and Barbara Kammermann.

I want to thank Peter Rickhaus, Bernd Gotsmann, Prof. Hatef Sadeghi, Prof. Colin Lambert, Prof. Milena Grifoni and Prof. Herre van der Zant for inspiring discussions.

I want to thank Empa and the European Union for their financial support through the QuIET-project and for providing a interdisciplinary, stimulating environment. To the staff of the labs and offices I worked in, including the staff of the BRNC and FIRST cleanrooms, in particular Antonis Olziersky, Diana Davila Pineda and Ute Drechsler. Thank you for your tireless efforts in keeping the labs running as smoothly as possible.

Thanks goes also to the physics study group DPW from the University of Basel, for the exchange and the great time together.

I want to also thank Anna, my friends, family, and loved ones for all their support throughout my academic career.

About the Author

Oliver Braun, born on February 5th 1989 in Neuwied (Germany)
Place of origin, Herznach (AG).

Education

- 12/2016 - 07/2021 **Doctor of Philosophy (PhD) in Physics**
University of Basel, Switzerland
Thermoelectric Effects in Nanoscale Devices
Prof. Dr. Michel Calame
Prof. Dr. Ilaria Zardo
- 09/2014 - 06/2016 **Master of Science (MSc) in Physics**
University of Basel, Switzerland
Thermoelectric Effects in Graphene
PD Dr. Michel Calame
Prof. Dr. Christian Schönenberger
- 09/2011 - 07/2014 **Bachelor of Science (BSc) in Physics**
University of Basel, Switzerland
- 08/2010 - 08/2011 **Supplementary Examination Passerelle**
Gymnasium Kirschgarten, Basel, Switzerland
- 08/2008 - 06/2009 **Vocational Baccalaureate**
Berufsschule Aarau, Switzerland

Work experience

- 12/2016 - 06/2021 **Research Assistant, Empa**
Transport at Nanoscale Interfaces Laboratory
- 08/2014 - 09/2014 **Consultant, Imecon GmbH**
Brewery Industry
- 04/2010 - 07/2012 **Draftsman (60%), KSL Ingenieurbüro AG**
Civil engineering
- 07/2009 - 04/2010 **Military Service, Swiss Army**
- 08/2004 - 08/2008 **Draftsman Apprenticeship,
KSL Ingenieurbüro AG**
Civil engineering

Publications

- „*Thermoelectric characterization of atomically precise graphene nanoribbons*“
O. Braun*, M.L. Perrin*, M. Stiefel, R. Furrer, G. Borin Barin, R. Darawish, J. Zhang, A. Olziersky, K. Müllen, O. Gröning, P. Ruffieux, R. Fasel, H. Sadeghi and M. Calame
in preparation
- „*Highly tunable quantum dots from 9-atom-wide armchair graphene nanoribbons using multi-gate architecture*“
J. Zhang*, **O. Braun***, J. Overbeck, G. Borin Barin, R. Darawish, M. Stiefel, A. Olziersky, K. Müllen, I. Shorubalko, P. Ruffieux, R. Fasel, M. L. Perrin and M. Calame
in preparation
- „*On surface synthesis, Raman characterization and device integration of low bandgap 17-AGNRs*“
G. Borin Barin, **O. Braun**, N. Bassi, M. L. Perrin, M. Stiefel, R. Furrer, A. Narita, V. Meunier, K. Müllen, M. Calame, R. Fasel and P. Ruffieux
in preparation
- „*Edge-contacts to atomically precise graphene nanoribbons*“
O. Braun, D.I. Indolese, M.L. Perrin, M. Stiefel, G. Borin Barin, R. Darawish, J. Overbeck, A. Olziersky, K. Müllen, P. Ruffieux, R. Fasel, C. Schönenberger and M. Calame
in preparation
- „*Spatially mapping thermal transport in graphene by an optothermal method*“
O. Braun, R. Furrer, P. Butti, K. Thodkar, I. Shorubalko, I. Zardo, M. Calame and M.L. Perrin
npj 2D Materials and Applications, **2022**, 6, 6
- „*Radial gradients in PET monofilaments: A Raman mapping and SAXS tomography study*“
E. Perret, K. Chen, **O. Braun**, R. Muff and R. Hufenus
Polymer, **2022**, 238, 124422
- „*Optimized graphene electrodes for contacting graphene nanoribbons* “
O. Braun, J. Overbeck, M. El Abbassi, S. Käser, R. Furrer, A. Olziersky, A. Flasby, G. Borin Barin, R. Darawish, K. Müllen, P. Ruffieux, R. Fasel, I. Shorubalko, M.L. Perrin and M. Calame
Carbon, **2021**, 184, 331-339

- „*High-resolution 2D Raman mapping of mono- and bicomponent filament cross-sections* “
E. Perret*, **O. Braun***, K. Sharma, S. Tritsch, R. Muff and R. Hufenus
Polymer, **2021**, *229*, 124011
- „*2D Raman, ATR-FTIR, WAXD, SAXS and DSC data of PET mono- and PET/PA6 bicomponent filaments* “
K. Sharma, **O. Braun**, S. Tritsch, R. Muff, R. Hufenus and E. Perret
Data in Brief, **2021**, *38*, 107416
- „*Benchmark and application of unsupervised classification approaches for univariate data*“
M. El Abbassi, J. Overbeck, **O. Braun**, M. Calame, H.S.J. van der Zant and M.L. Perrin
Communications Physics, **2021**, *4*, 50
- „*Combining polarized Raman spectroscopy and micropillar compression to study microscale structure-property relationships in mineralized tissues*“
T. Kochetkova, C. Peruzzi, **O. Braun**, J. Overbeck, A.K. Maurya, A. Neels, M. Calame, J. Michler, P. Zysset and J. Schwiedrzik
Acta Biomaterialia, **2021**, *119*, 390-404
- „*Epoxy-graphene related material composites: Nanostructure characterization and release quantification*“
T. Hammer, W. Netkueakul, P. Zolliker, C. Schreiner, J. Hubeli, R. Figi, **O. Braun** and J. Wang
NanoImpact, **2020**, *20*, 100266
- „*Controlled Quantum Dot Formation in Atomically Engineered Graphene Nanoribbon Field-Effect Transistors*“
M. El Abbassi, M.L. Perrin, G. Borin Barin, S. Sangtarash, J. Overbeck, **O. Braun**, C. Lambert, Q. Sun, T. Prectl, A. Narita, K. Müllen, P. Ruffieux, H. Sadeghi, R. Fasel and M. Calame
ACS Nano, **2020**, *14*, 5, 5754–5762
- „*Release of graphene-related materials from epoxy-based composites: characterization, quantification and hazard assessment in vitro*“
W. Netkueakul, D. Korejwo, T. Hammer, S. Chortarea, P. Rupper, **O. Braun**, M. Calame, B. Rothen-Rutishauser, T. Buerki-Thurnherr, P. Wick and J. Wang
Nanoscale, **2020**, *12*, 10703
- „*Massive Dirac Fermion Behavior in a Low Bandgap Graphene Nanoribbon Near a Topological Phase Boundary*“
Q. Sun, O. Gröning, J. Overbeck, **O. Braun**, M.L. Perrin, G. Borin Barin, M. El Abbassi, K. Eimre, E. Ditler, C. Daniels, V. Meunier, C.A. Pignedoli, M. Calame, R. Fasel and P. Ruffieux
Advanced Materials, **2020**, *32*, 12, 1906054

-
- „*A Universal Length-Dependent Vibrational Mode in Graphene Nanoribbons*“
J. Overbeck, G. Borin Barin, C. Daniels, M.L. Perrin, **O. Braun**, Q. Sun, R. Darawish, M. de Luca, X.-Y. Wang, T. Dumslaff, A. Narita, K. Müllen, P. Ruffieux, V. Meunier, R. Fasel and M. Calame
ACS nano, **2019**, *13*, 13083
 - „*Optimized Substrates and Measurement Approaches for Raman Spectroscopy of Graphene Nanoribbons*“
J. Overbeck, G. Borin Barin, C. Daniels, M.L. Perrin, L. Liang, **O. Braun**, R. Darawish, B. Burkhardt, T. Dumslaff, X.-Y. Wang, A. Narita, K. Müllen, V. Meunier, R. Fasel, M. Calame and P. Ruffieux
physica statatus solidi (b), **2019**, *256*, 1900343
 - „*Robust graphene-based molecular devices*“
M. El Abbassi, S. Sangtarash, X. Liu, M.L. Perrin, **O. Braun**, C. Lambert, H.S.J. van der Zant, S. Yitzchaik, S. Decurtins, S.-X. Liu, H. Sadeghi and M. Calame
Nature Nanotechnology, **2019**, *14*, 957–961

* These authors contributed equally.

Talks

- „*Device integration of atomically precise graphene nanoribbons*“, Materials Research Society: Spring meeting, (online), April 2021
- „*Device integration of atomically precise graphene nanoribbons*“, American Physical Society: March meeting, (online), March 2021
- „*From quantum transport to bone stability*“, Lab visit by Prof. G.-L. Bona (CEO Empa), Dübendorf (Switzerland), September 2020
- „*Device integration of atomically precise graphene nanoribbons*“ Empa-Department „Material meets life“PhD Symposium, (online), June 2020
- „*Device integration of atomically precise graphene nanoribbons*“, International Conference on Molecular-Scale Charge and Thermal Transport, Engelberg (Switzerland), January 2020
- „*Device integration of atomically precise graphene nanoribbons*“, Empa PhD Symposium, St. Gallen (Switzerland), November 2019
Best Talk Prize
- „*Thermoelectric effects in nanoscale devices*“ Empa-Department „Material meets life“PhD Symposium, St. Gallen (Switzerland), June 2017

Poster contributions

- „*Characterization of atomically precise graphene nanoribbons by Raman spectroscopy*“, 33th International Winterschool on Electronic Properties of Novel Materials, Kirchberg in Tirol (Austria), February 2019
- „*Spatially resolved mapping of graphene’s thermal conductivity*“, Nanoscale and Microscale Heat Transfer VI – Eurotherm 111, Levi (Finland), December 2018
- „*Spatially resolved mapping of graphene’s thermal conductivity*“, Empa PhD-Symposium, Dübendorf (Switzerland), November 2018
- „*Thermoelectric effects in graphene*“, 20th International Winterschool on new developments in solid state physics, Mauterndorf (Austria), February 2018
- „*InAs nanowire arrays as thermoelectric devices*“, 1st Workshop on Thermo-Electric Transport in Nanowires, Eindhoven (Netherlands), December 2017

Supervised student projects

- „*Electric Field Effect Tuning of Electron-Phonon Coupling in 9-atom-wide armchair Graphene Nanoribbons (9-AGNRs)*“
Master project Angela Hunziker, July - September 2020
- „*Graphene Electrodes for Contacting Atomically Precise Graphene Nanoribbons*“
Master thesis Alexander Flasby, April - September 2019
- „*Raman and Electrical Characterization of graphene/graphene nanoribbon-based junctions*“
Master project Silvan Käser, April - July 2018
- „*Fabrication and performance characterization of a thermoelectric device based on nanowire arrays*“
Master thesis Kamiar Davallou, November 2017 - September 2018